

A Priori Knowledge-Based Post-Doppler STAP for Traffic Monitoring with Airborne Radar

Zur Erlangung des akademischen Grades eines

DOKTOR-INGENIEURS

von der Fakultät für
Elektrotechnik und Informationstechnik
des Karlsruher Instituts für Technologie (KIT)

genehmigte

DISSERTATION

von

M.Sc. André Barros Cardoso da Silva
geb. in Taubaté, São Paulo, Brasilien

Tag der mündlichen Prüfung:

25.10.2019

Referent:

Prof. Dr.-Ing. habil. Alberto Moreira

Korreferent:

Prof. Dr. Pierfrancesco Lombardo

Acknowledgements

Time is the most precious resource that a person owns to spend. Once time is gone, it is unrecoverable.

This doctoral thesis is the conclusion of a personal life project that demanded not only my time and effort, but especially the time and effort of several people of good will that directly and indirectly contributed to the accomplishment of this work. For the precious time contribution of those people, I express my deepest gratitude and respect.

First of all, I am very grateful to my advisor Prof. Dr. Alberto Moreira for his trust in giving me the opportunity to conduct my research activities in his very prestigious team, which is an honor. I extend my gratitude to Prof. Dr. Gerhard Krieger and Prof. Dr. Marwan Younis for their expert support and advice that greatly improved the quality of this doctoral thesis. I am especially thankful to my supervisor Dr. Stefan V. Baumgartner for the uncountable meetings and fruitful discussions that lead to the successful accomplishment of this doctoral work. I am also very thankful to my co-advisor Prof. Dr. Pierfrancesco Lombardo for his valuable feedback and thesis review.

I acknowledge all my colleagues from DLR for their great support, pleasant company and very warm atmosphere. You are all an immense part of my achievements.

I express deep gratitude to my family (Edson, Alzira and Luciano) for understanding and supporting the reasons why I am far from home pursuing my dreams. Thank you for always backing me up and comforting me when I need to feel at home.

Finally, in the same level of gratitude and in the same sentence, I acknowledge God and my beloved wife Juliana not only for keeping my life in a perfect balance, but especially for showing me every single day how stunning and meaningful life is!

Oberpfaffenhofen, November 2019

André Barros Cardoso da Silva.

Contents

Acknowledgements	ii
Contents	iii
Zusammenfassung.....	vii
Abstract.....	ix
List of Symbols and Acronyms	x
1 Introduction	1
1.1 Background and Motivation.....	1
1.2 State-of-the-Art GMTI Algorithms and Systems.....	4
1.3 Main Objectives	7
1.4 Scope and Major Contributions	8
1.5 Outline.....	9
2 SAR Principles.....	11
2.1 Chapter Overview	11
2.2 Brief History of SAR.....	11
2.3 SAR Terminology and Acquisition Geometry.....	12
2.4 Signal Model for Stationary Point-Like Targets.....	15
2.5 Pulse Compression	17
2.6 SAR Image Formation	18
2.7 Moving Target Effects on SAR Imagery	19
2.8 Chapter Summary.....	21
3 Space-Time Adaptive Processing (STAP).....	23
3.1 Chapter Overview	23
3.2 The Need for STAP.....	23
3.3 Post-Doppler STAP.....	24
3.3.1 Data Segmentation	25
3.3.2 Signal Model and Test Statistics	27
3.3.3 Clutter Cancellation and Moving Target Pre-Detection	29
3.3.4 Moving Target Parameter Estimation	31
3.4 Clutter Model	35
3.4.1 Homogeneous Terrain.....	36

3.4.2	Heterogeneous Terrain	37
3.5	Performance Model	40
3.5.1	SNR and CNR	41
3.5.2	Detection Performance	42
3.5.3	Position and Velocity Estimation Accuracy	43
3.5.4	Simulation Results	44
3.6	Main Limitations	48
3.6.1	DOA Angle Ambiguities	48
3.6.2	Blind Velocities	50
3.7	Coherent Processing Interval Length	51
3.8	Position and Velocity Errors	54
3.9	Chapter Summary	57
4	PD STAP Processor with Different Modes	59
4.1	Chapter Overview	59
4.2	Mode 1: Conventional PD STAP	60
4.3	Mode 2: A Priori Knowledge-Based PD STAP	62
4.4	Mode 3: Fast A Priori Knowledge-Based PD STAP	64
4.5	Chapter Summary	66
5	Positioning Error Models and Decision	67
5.1	Chapter Overview	67
5.2	Positioning Error Model for Targets	68
5.3	Positioning Error Model for Road Points	71
5.4	Decision	74
5.4.1	General Form of an Ellipse	74
5.4.2	Target's Positioning Error Ellipse	75
5.4.3	Road Point's Positioning Error Ellipse	77
5.4.4	Intersection of Positioning Error Ellipses	78
5.4.5	Procedure for Decision	81
5.5	Target's Positioning Error Contributions	83
5.5.1	Impact of Error Sources	83
5.5.2	Impact of Platform's Heading Angle	86
5.6	Experimental Results	89
5.7	Chapter Summary	92

6	Data Calibration.....	95
6.1	Chapter Overview	95
6.2	Introduction	95
6.3	Structure of the Algorithm	96
6.4	Antenna Aperture Switching Correction.....	97
6.5	Parameters Estimation.....	98
6.5.1	Antenna Patterns	98
6.5.2	Magnitude Offsets.....	98
6.5.3	Along-Track Baselines.....	99
6.6	Doppler Centroid.....	101
6.6.1	Aircraft's Motion	101
6.6.2	Squint Angle and Doppler Centroid Estimation	103
6.6.3	Attitude Angle Offsets	105
6.7	ATI Phase Correction.....	108
6.8	GMTI Results from Data Take 1.....	110
6.9	Chapter Summary.....	112
7	Training Data Selection Strategies and Experimental Results	113
7.1	Chapter Overview	113
7.2	Introduction	113
7.3	Real-World Effects.....	115
7.4	Algorithms for Training Data Selection and Update	117
7.4.1	Algorithm 1 (Conventional).....	117
7.4.2	Algorithm 2 (Conventional).....	118
7.4.3	Algorithm 3 (Novel).....	120
7.4.4	Algorithm 4 (Novel).....	121
7.4.5	Module for Moving Target Signal Rejection (MTSR).....	122
7.5	Experimental Results.....	124
7.5.1	Experimental Setup.....	124
7.5.2	Moving Window Parameters	125
7.5.3	Impact of MTSR on Clutter Model.....	127
7.5.4	GMTI Results for Data Take 1.....	128
7.5.5	Quantitative Comparisons for Data Takes 1 to 3	134
7.5.6	GMTI Results for Data Take 4.....	137
7.5.7	GMTI Results Using the Fast PD STAP Processor	139
7.6	Chapter Summary.....	143

8	Conclusion.....	145
8.1	Discussion and Summary of Results.....	145
8.2	Outlook of Future Work.....	147
	Appendix A: F-SAR System.....	151
A.1	Overview	151
A.2	GMTI Configuration	153
A.3	Flight Campaigns	154
	Appendix B: Log of Roads in Germany.....	159
	Bibliography	161
	Curriculum Vitae.....	176

Zusammenfassung

Die Verkehrsüberwachung gewinnt aufgrund des weltweiten Anstiegs der Verkehrsteilnehmer immer mehr an Bedeutung. Sicherer und effizienter Straßenverkehr erfordert detaillierte Verkehrsinformationen. Häufig sind diese lediglich stationär, räumlich stark begrenzt und meist nur auf Hauptverkehrsstraßen verfügbar. In dieser Hinsicht ist ein Ausfall des Telekommunikationsnetzes, beispielsweise im Falle einer Katastrophe, und der damit einhergehende Informationsverlust als kritisch einzustufen. Flugzeuggetragene Radarsysteme mit synthetischer Apertur (eng. Synthetic Aperture Radar - SAR) können für dieses Szenario eine Lösung darstellen, da sie großflächig hochauflösende Bilder generieren können, unabhängig von Tageslicht und Witterungsbedingungen. Sie ermöglichen aufgrund dieser Charakteristik die Detektion von Bewegtzielen am Boden (eng. ground moving target indication – GMTI).

Moderne GMTI-Algorithmen und -Systeme, die prinzipiell für die Verkehrsüberwachung verwendbar sind, wurden in der Literatur bereits diskutiert. Allerdings ist die Robustheit dieser Systeme oft mit hohen Kosten, hoher Hardwarekomplexität und hohem Rechenaufwand verbunden. Diese Dissertation stellt einen neuartigen GMTI-Prozessor vor, der auf dem Radar-Mehrkanalverfahren *post-Doppler space-time adaptive processing* (PD STAP) basiert. Durch die Überlagerung einer Straßenkarte mit einem digitalen Höhenmodell ist es mithilfe des PD STAP möglich, Falschdetektionen zu erkennen und auszuschließen sowie die detektierten Fahrzeuge ihren korrekten Straßenpositionen zuzuordnen. Die präzisen Schätzungen von Position, Geschwindigkeit und Bewegungsrichtung der Fahrzeuge können mit vergleichsweise geringerer Hardware-Komplexität zu niedrigeren Kosten durchgeführt werden.

Ferner wird im Rahmen dieser Arbeit ein effizienter Datenkalibrierungsalgorithmus erläutert, der das Ungleichgewicht zwischen den Empfangskanälen sowie die Variation des Dopplerschwerpunkts über Entfernung und Azimut korrigiert und so das Messergebnis verbessert. Darüber hinaus werden neue und automatisierte Strategien

zur Erhebung von Trainingsdaten vorgestellt, die für die Schätzung der Clutter-Kovarianzmatrix wegen ihres direkten Einflusses auf die Clutter-Unterdrückung und Zieldetektion essentiell für PD STAP sind.

Der neuartige PD STAP Prozessor verfügt über drei verschiedene Betriebsarten, die für militärische und zivile Anwendungen geeignet sind, darunter ein schneller Verarbeitungsalgorithmus der das Potential für eine zukünftige Echtzeit-Verkehrsüberwachung hat. Alle Betriebsarten wurden erfolgreich mit Radar-Mehrkanaldaten des flugzeuggetragenen F-SAR-Radarsensors des DLR getestet.

Abstract

Traffic monitoring is currently a trending topic due to the worldwide increase of road users. Safe and efficient roadway operations require detailed traffic information that relies on stationary ground infrastructure often available only for the major highways. Particularly in case of catastrophes (when mobile internet and phone communication are impossible), the actual road systems could fail altogether due to extensive power blackouts or ground infrastructure damages, resulting in complete lack of information. Synthetic aperture radar (SAR) offers a remarkable solution for this scenario due to its unique capability in providing high-resolution images independent of daylight and weather conditions, allowing applications in ground moving target indication (GMTI).

State-of-the-art GMTI algorithms have been proposed in the literature using a priori knowledge information, whereas their robustness is often achieved with high costs, high hardware complexity and high computational effort. This doctoral thesis presents a GMTI processor based on the powerful multi-channel technique post-Doppler space-time adaptive processing (PD STAP). This GMTI processor blends a road map with a digital elevation model in order to recognize and to reject false detections, and to assign the detected vehicles to their correct positions on the roads. Accurate position, velocity and moving direction estimates of the vehicles are obtained with decreased processing hardware complexity and low costs compared to state-of-the-art systems.

This doctoral thesis also includes an efficient data calibration algorithm that corrects the channel imbalances and the Doppler centroid variations over range and azimuth. In addition, novel and automatic training data selection strategies are presented for the clutter covariance matrix estimation, which is essential for the PD STAP processor, since it impacts directly its clutter cancellation and target detection capabilities.

The novel PD STAP processor has three operational modes designed for military and civilian applications, including a fast processing mode that paves the way for real-time traffic monitoring. All modes were tested on multi-channel data acquired by DLR's airborne system F-SAR, containing scenarios with controlled vehicles and real-traffic.

List of Symbols and Acronyms

List of Constants

c	Speed of light in vacuum	2.99792458×10^8 [m/s]
k_B	Boltzmann constant	$1.38064852 \times 10^{-23}$ [J/K]
π	Pi (ratio of a circle's circumference to its diameter)	3.14159265359

Mathematical Notations, Symbols and Functions

In this work no distinction in notation is made between real and complex quantities.

$ \cdot $	Absolute value
$[\cdot]^*$	Complex conjugate
$[\cdot]^H$	Hermitian operator (complex conjugate transposition)
$[\cdot]^T$	Transpose operator
*	Convolution
\hat{a}	Estimated value
\bar{a}	Mean value
\mathbf{a}	Vector nomenclature
\mathbf{A}	Matrix nomenclature
$\cos^{-1}(\theta)$	Inverse cosine function
$\cos(\theta)$	Cosine function
$\sin(\theta)$	Sine function
$\text{sinc}(x) = \frac{\sin(x)}{x}$	Sinus Cardinalis (sinc) function
$e^{j\theta}, \exp(j \cdot \theta)$	Complex exponential
j	Imaginary unit $j = \sqrt{-1}$
\mathbb{C}	Set of complex numbers
\mathbb{Z}	Set of integer numbers
∂	Partial derivative
$\Gamma[\cdot]$	Gamma function
$\gamma[\cdot]$	Incomplete gamma function
$\sum_k a_k$	Sum versus the summands a_k
${}_2F_1[\cdot]$	Gaussian hypergeometric function
$\arg[\cdot]$	Argument of a function
$\text{rect}[\cdot]$	Unity rectangular function
$\text{sgn}[\cdot]$	Sign function
$E[\cdot]$	Expectation operator
$I_0[\cdot]$	Modified zero-order Bessel function of the first kind
$\text{Re}\{\cdot\}, \text{Im}\{\cdot\}$	Real and imaginary part of complex quantity

Acronyms

1-D	One dimensional
2-D	Two-dimensional
ADC	Analog-to-Digital Converter
AMF	Adaptive Matched Filter
AS	Aperture Switching
ATI	Along-Track Interferometry
CCM	Clutter Covariance Matrix
CDF	Cumulative Distribution Function
CFAR	Constant False Alarm Rate
CNR	Clutter-to-Noise Ratio
CPI	Coherent Processing Interval
CRB	Cramér-Rao Bound
CR	Corner Reflector
CUT	Cell Under Test
dB	Decibel
DBF	Digital Beamforming
DCB	Digital Channel Balancing
DEM	Digital Elevation Model
DGPS	Differential Global Positioning System
DLR	Deutsches Zentrum für Luft und Raumfahrt (German Aerospace Center)
DOA	Direction-of-Arrival
DoF	Degree of Freedom
DPCA	Displaced Phase Center Antenna
E-KAPE	Enhanced Knowledge-Aided Parametric Covariance Estimation
FFT	Fast Fourier Transform
GIP	Generalized Inner Product
GMTI	Ground Moving Target Indication
GPS	Global Positioning System
HRWS	High Resolution Wide Swath
IDL	Interactive Data Language
IMU	Inertial Measurement Unit
ISAR	Inverse Synthetic Aperture Radar
KA	Knowledge-Aided
KAPE	Knowledge-Aided Parametric Covariance Estimation
KML	Keyhole Markup Language
LFM	Linear Frequency Modulated
LLA	Left-Looking Antenna
LTE	Long Term Evolution
MDV	Minimum Detectable Velocity
MTSR	Moving Target Signal Rejection
OSM	OpenStreetMap
PD STAP	Post-Doppler Space-Time Adaptive Processing

PDF	Probability Distribution Function
PRF	Pulse Repetition Frequency
PRI	Pulse Repetition Interval
PSD	Power Spectral Density
RADAR	Radio Detection and Ranging
RAR	Real Aperture Radar
RC	Range-Compressed
RCMC	Range Cell Migration Correction
RCS	Radar Cross Section
RDA	Range-Doppler Algorithm
RF	Radiofrequency
RLA	Right-Looking Antenna
ROI	Region of Interest
RX	Reception
SAR	Synthetic Aperture Radar
SCNR	Signal-to-Clutter plus Noise Ratio
SMI	Sample Matrix Inverse
SNR	Signal-to-Noise Ratio
SRTM	Shuttle Radar Topography Mission
STAP	Space-Time Adaptive Processing
STDDEV	Standard Deviation
STOL	Short Take-Off and Landing
SWMF	Stationary World Matched Filter
TanDEM-X	TerraSAR-X Add-On for Digital Elevation Measurement
TOPS	Terrain Observation by Progressive Scans
TX	Transmission
UTC	Coordinated Universal Time
UTM	Universal Transverse Mercator
WGS84	World Geodetic System 1984

Lower Case Letters

(a, b)	Semi-axes of a generic ellipse
a_s	Complex reflectivity of a scatterer
b_a	Along-track separation between two adjacent antenna centers
c	Clutter vector in time domain
d	Beamforming or DOA vector
d_a	Effective along-track separation between two adjacent antenna centers
d_u	First derivative of the DOA vector d
f_a	Doppler frequency
$f_{a,CPI}$	Number of Doppler frequency samples contained in one CPI
$f_{chirp}(\tau)$	Instantaneous frequency of the range chirp signal

f_{DC}	Doppler shift or Doppler centroid
$f_{DC,ATT}(r_k, t)$	Corrected Doppler centroid of the scene
$\bar{f}_{DC,ATT,AZ}(t)$	Azimuth profile of the corrected Doppler centroid of the scene
$f_{DC,ATT,BIAS}(r_k, t)$	Biased Doppler centroid of the scene
$\bar{f}_{DC,ATT,SR}(r_k)$	Slant range profile of the corrected Doppler centroid of the scene
$f_{DC,REF}(r_k, t)$	Doppler centroid of the scene used as reference
$\bar{f}_{DC,REF,AZ}(t)$	Azimuth profile of the reference Doppler centroid of the scene
$\bar{f}_{DC,REF,SR}(r_k)$	Slant range profile of the reference Doppler centroid of the scene
f_r	Range or fast frequency
f_T	PDF of the test statistics $T = \bar{T}/E\{\bar{T}\}$ for homogeneous terrain
$f_{\bar{T}}$	PDF of the test statistics \bar{T} for homogeneous terrain
f_X	PDF of the scaled F -distribution for heterogeneous terrain
g	Number of points of the ellipse defined in the interval of $(0, 2\pi)$
h	Flight altitude of the platform above the ground
k	Range gate
k_a	Doppler slope or Doppler rate of the signal
k_r	Chirp rate
n	Effective number of looks
\mathbf{n}	Noise vector in time domain
$n_{a,CPI}$	Number of azimuth samples contained in one CPI
$n_{a,CPI,max}$	Maximum number of azimuth samples contained in one CPI
n_{lanes}	Number of road lanes
\bar{n}_{lanes}	Average number of road lanes estimated empirically
n'_r	Number of range bins used in the training data selection algorithm 4
$\mathbf{p} = [x_p, y_p, z_p]^T$	Vector containing the radar coordinates of the platform
$\mathbf{p}_{UTM} = [x_{p,UTM}, y_{p,UTM}, z_{p,UTM}]^T$	Vector containing the UTM coordinates of the platform
q	Road lane index
\mathbf{s}	Multi-channel signal vector
$s_{ATI}(t)$	ATI signal
s_{chirp}	Range chirp signal
$s_{RX}(\tau)$	Received single-channel signal in RF band
$s_{RX,b}(\tau, t)$	Received single-channel signal in baseband
$s_{TX}(\tau)$	Transmitted single-channel signal in RF band
$s_{TX,b}(\tau)$	Transmitted single-channel signal in baseband
t	Azimuth or slow time

u_0	Directional cosine steered to the broadside direction of the antenna array
u_{array}	Directional cosine measured with respect to the antenna array axis
$u_{\text{array,amb}}$	Directional cosine ambiguities
v_p	Platform (tangential) velocity
v_r	Line-of-sight velocity of the target
$v_{r,\text{blind}}$	Blind line-of-sight velocity of the target
$v_{\text{road}}, v_{\text{abs}} $	Absolute velocity of the target on the road
$v_{\text{road,GPS}}$	Velocity of the target obtained from GPS receivers
w_{lanes}	Width of the road lanes
\bar{w}_{lanes}	Average width of the road lanes estimated empirically
x	x -direction, along-track or azimuth position
x_m	Position of the antenna center in the azimuth direction with respect to the antenna array origin
$\mathbf{x}_t = [x_t, y_t, z_t]^T$	Vector containing the radar coordinates of the target
$\mathbf{x}_{t,\text{UTM}} = [x_{t,\text{UTM}}, y_{t,\text{UTM}}, z_{t,\text{UTM}}]^T$	Vector containing the UTM coordinates of the target
y	y -direction or across-track position
z	Data sample of the space-time snapshot, z -direction or altitude
$\mathbf{z}(t)$	Space-time snapshot of the received noise and clutter contaminated multi-channel signal vector in time domain
z_{ACC}	Data sample of the space-time snapshot after clutter cancellation
z_{BCC}	Data sample of the space-time snapshot before clutter cancellation

Capital Letters

A_s	Complex coefficient containing free-space attenuation, backscattering and two-way antenna pattern weighting
$A(f_a, m)$	Two-way diagram of the m -th antenna pattern in Doppler frequency domain
$A_{\text{osm,el}}$	Area of the OSM road point's positioning error ellipse
A_{res}	Ground resolution cell size
$A_{t,\text{el}}$	Area of the target's positioning error ellipse
B_r	Range or chirp bandwidth
$D_{\text{rx}}(u)$	RX antenna characteristics as a function of the directional cosine
$D_{\text{tx}}(u)$	TX antenna characteristics as a function of the directional cosine
F	System noise figure
F_T	CDF of the test statistics T for homogeneous terrain

F_X	CDF of the scaled F -distribution for heterogeneous terrain
G_{RX}	RX antenna gain
G_{TX}	TX antenna gain
\mathbf{I}_M	Identity matrix of size $M \times M$
K	Total number of range samples contained in the data set
K_{gz}	Number of range bins used as guard zones
L	Losses
L_{az}	Antenna length in azimuth direction
L_{sa}	Length of the synthetic aperture
M	Number of RX antennas or channels
$N_{a,CPI}$	Total number of azimuth samples or pulses contained in one CPI
P_d	Probability of detection
P_{fa}	Probability of false alarm
\hat{P}_{fa}	Estimated probability of false alarm
P_t	Peak transmit power
R	Generic slant range from radar to target
R_0	Slant range of minimum approximation for the target to the swath's center
$R_{0,g}$	Projection on ground of R_0
R_g	Projection on ground of R
$\hat{\mathbf{R}}_W$	Clutter-plus-noise covariance matrix estimated from the radar data
$S_{chirp}(f)$	Range chirp spectrum
$S_{chirp}^*(f)$	Matched filter of the range chirp spectrum for range compression
$T = \bar{T}/E[\bar{T}]$	Test statistics based on AMF and normalized by its expectation
\bar{T}	Test statistics based on AMF
T_0	Reference noise temperature
T_{CPI}	Coherent processing interval
T_{sa}	Synthetic aperture time
(X_0, Y_0)	Coordinates of a generic ellipse's origin
(X_{el}, Y_{el})	Coordinates of a generic ellipse
$(X_{osm,el}, Y_{osm,el})$	Coordinates of the OSM road point's positioning error ellipse
$(X_{t,el}, Y_{t,el})$	Coordinates of the target's positioning error ellipse
$\mathbf{Z}(f_a)$	Space-time snapshot of the received noise and clutter contaminated multi-channel signal vector in Doppler frequency domain

Greek Symbols

α_p	Platform moving direction with respect to the global UTM Easting axis
α_r	Road point angle with respect to the global UTM Easting axis

$\alpha_{r,az}$	Road point angle with respect to azimuth or flight direction
α_t	Moving direction of the target with respect to azimuth or flight direction
α_{wn}	Losses due to windowing applied during the range compression
β	Rotation angle of a generic ellipse
β_T	Normalized detection threshold
δ_{az}	Geometric azimuth resolution of the SAR image
$\delta_{az,raw}$	Real antenna aperture in azimuth
Δd	Minimum distance between the target and its closest OSM road point
δf_a	Doppler bandwidth or Doppler frequency spread of the moving target signal
Δf_a	Sample spacing in Doppler domain
Δf_{DC}	Doppler centroid offset
δ_r	Geometric range resolution of the SAR image
$\delta_{r,raw}$	Geometric range resolution before pulse compression
Δr	Pixel spacing in range
Δt	Generic time difference
Δt_{AS}	Time delay associated to the antenna AS
Δv_r	Maximum error of the target's line-of-sight velocity
Δv_{road}	Maximum error of the target's absolute velocity on the road
Δx	Distance between the radar and the moving target in along-track or azimuth
Δx_t	Maximum error of the target's position in azimuth
Δx_{UTM}	Distance between the radar and the moving target in UTM Easting axis
Δy_{UTM}	Distance between the radar and the moving target in UTM Northing axis
$\Delta \theta_{PITCH}$	Aircraft's pitch angle offset
$\Delta \theta_{ROLL}$	Aircraft's roll angle offset
$\Delta \theta_{YAW}$	Aircraft's yaw angle offset
$\Delta \varphi$	ATI phase difference or interferogram
$\overline{\Delta \varphi}$	Average of the ATI phase difference or interferogram
ζ	Confidence level for a Normal distribution (also known as "z-score")
η	Generic CFAR detection threshold
η_{dist}	Empirical threshold based on the distance between the moving target and its closest OSM road point
η_{hete}	CFAR detection threshold for heterogeneous clutter
η_{homo}	CFAR detection threshold for homogeneous clutter
θ_{az}	Antenna aperture in azimuth
$\theta_{az,3dB}$	Antenna 3-dB aperture in azimuth
$\bar{\theta}_{COURSE}$	Aircraft's mean flight course with respect to the true North
θ_d	Antenna depression angle

θ_{HEADING}	Aircraft's heading angle with respect to the true North
θ_i	Incidence angle
$\theta_{\text{PITCH,ANT}}$	Pitch angle of the antenna array
$\theta_{\text{PITCH,IMU}}$	Pitch angle of the aircraft obtained from the IMU system
θ_{rg}	Antenna aperture in elevation
$\theta_{\text{ROLL,ANT}}$	Roll angle of the antenna array
$\theta_{\text{ROLL,IMU}}$	Roll angle of the aircraft obtained from the IMU system
$\theta_{\text{YAW,ANT}}$	Yaw angle of the antenna array
$\theta_{\text{YAW,IMU}}$	Yaw angle of the aircraft obtained from the IMU system
κ	Clutter ambiguities
λ	Radar wavelength
ν	Texture parameter that describes the degree of heterogeneity of the scene
ξ	Empirical threshold used by the MTSR module, consisting on the number of undesired range bins to be rejected from the uncleaned training data
$\rho_{1,m}$	Magnitude offset of the m -th antenna pattern assuming RX1 as reference
σ_0	Clutter reflectivity
σ_n^2	Power of the additive thermal noise
$\sigma_{n_{\text{lanes}}}$	Standard deviation of the number of road lanes
σ_r	Standard deviation of the road lane index
σ_R	Standard deviation of the target's slant range
σ_t	Radar cross section of the target
σ_u	Standard deviation of the directional cosine
σ_{v_r}	Standard deviation of the target's line-of-sight velocity
$\sigma_{w_{\text{lanes}}}$	Standard deviation of width of the road lanes
σ_x	Standard deviation of the target's azimuth position
$\sigma_{x,\text{min}}$	Minimum expected error of the target's azimuth position
$\sigma_{x_p,\text{UTM}}$	Standard deviation of the platform's position in UTM Easting axis
$\sigma_{x_t,\text{UTM}}$	Standard deviation of the target's position in UTM Easting axis
$\sigma_{y_p,\text{UTM}}$	Standard deviation of the platform's position in UTM Northing axis
$\sigma_{y_t,\text{UTM}}$	Standard deviation of the target's position in UTM Northing axis
σ_{z_p}	Standard deviation of the platform's altitude above ground
σ_{z_t}	Standard deviation of the target's altitude
$\sigma_{x_{\text{osm}}}$	Standard deviation of the OSM road point's position in x -axis (local UTM coordinates)
$\sigma_{y_{\text{osm}}}$	Standard deviation of the OSM road point's position in y -axis (local UTM coordinates)
σ_{α_p}	Standard deviation of the platform's moving direction with respect to the global UTM Easting axis

σ_K^2	Power of clutter contributions
$\sigma_{\Psi_{\text{DOA,az,g}}}$	Standard deviation of the target's DOA angle with respect to the azimuth direction and projected on ground
τ	Range time or fast time
τ_p	Pulse duration
ϕ	Generic interferometric phase between two RX antennas or channels
$\varphi_{\text{AS}}(f_a)$	Phase ramp for correcting the antenna AS in Doppler frequency domain
χ^2	Chi-squared density function
$\Psi_{\text{DOA,array}}$	DOA angle of the target measured with respect to the antenna array axis
$\Psi_{\text{DOA,az}}$	DOA angle of the target measured with respect to azimuth or flight direction
$\Psi_{\text{DOA,az,g}}$	Projection ground of $\Psi_{\text{DOA,az}}$
Ψ_{sq}	Squint angle
$\Psi_{\text{sq,LLA}}$	Squint angle for a left-looking antenna
$\Psi_{\text{sq,RLA}}$	Squint angle for a right-looking antenna
Ψ_{tilt}	Tilt angle

Subscripts and Superscripts

$\{\cdot\}_{amb}$	Ambiguities
$\{\cdot\}_{array}$	Antenna array axis
$\{\cdot\}_b$	Baseband signal
$\{\cdot\}_{el}$	Positioning error ellipse
$\{\cdot\}_g$	Ground projection
$\{\cdot\}_m$	Index of RX antennas or channels
$\{\cdot\}_{max}$	Maximum
$\{\cdot\}_{min}$	Minimum
$\{\cdot\}_{OSM}$	OpenStreetMap (OSM)
$\{\cdot\}_p$	Platform
$\{\cdot\}_r$	Radial or line-of-sight
$\{\cdot\}_{reg}$	Coregistered
$\{\cdot\}_{RX}$	RX antenna or channel
$\{\cdot\}_{sa}$	Synthetic aperture
$\{\cdot\}_t$	Target
$\{\cdot\}_{TX}$	TX antenna or channel
$\{\cdot\}_{UTM}$	Global UTM coordinate system

1 Introduction

1.1 Background and Motivation

Road traffic management is currently a trending topic due to the worldwide increase of vehicle density over the last decades [1]–[3]. The challenges are higher in big metropolises, where roadway operations are barely able to handle everyday traffic volumes. Indeed, current road traffic information generally relies on stationary ground infrastructure, such as: traffic cameras, induction loops, pneumatic road tube counters or even people counting manually. Much information obtained from such road systems are collected, processed and interpreted by traffic management centers that adopt measures for the traffic flow's optimization [4]. Some of the main problems regarding the road systems employed nowadays for collecting traffic data are:

1. They are limited in spatial coverage due to the high costs for installation and maintenance. In reality, detailed traffic information is usually available only for major roads or highways, therefore the traffic monitoring systems are blind to the situations on minor roads;
2. They depend on the weather conditions. For instance, video systems depend on sight conditions for proper operation and pneumatic road tube counters present problems especially due to the accumulation of snow [5];
3. Lastly, they could fail altogether in case of large scale events and catastrophes due to ground infrastructure damages or extensive power blackouts, resulting in complete lack of information in major and minor roads.

An efficient and elegant solution to provide accurate traffic data for safe and efficient traffic monitoring is to use radars flying at high altitudes, for instance, synthetic aperture radar (SAR).

Generally, SAR is a side-looking imaging radar that is mounted on a moving platform, for instance an aircraft or a satellite (referred in the literature as airborne SAR and spaceborne SAR, respectively). A SAR system offers unique capability to provide high-resolution two-dimensional images (i.e., reflectivity maps commonly displayed

in terms of intensity values of each image pixel) independent of daylight, cloud coverage and weather conditions (e.g., rain, snow, fog, smog, among others) [6]–[11]. Moreover, the diverse scattering properties of materials with frequency allow the observation of different features, which is not possible with optical sensors based on visible light. Due to such remarkable features, SAR has been widely used in the last decades for plentiful applications, ranging from geoscience and climate change research, environmental and Earth system monitoring, topography and cartography analysis, change detection, security-related applications, ground moving target indication (GMTI) up to planetary exploration [12]. The SAR principles and theory are presented in Chapter 2.

Particularly, airborne SAR has been receiving growing attention for traffic monitoring of non-cooperative vehicles (i.e., vehicles not sharing their positions via Internet). From the economical point of view, it is clear that a traffic monitoring system based on airborne radar cannot compete with systems that evaluate continuously the shared geographical positions of the cooperative road users (e.g., Google Maps, Waze etc). Nevertheless, especially in case of large scale events and catastrophes (when mobile internet connection is disturbed or unavailable and the phone communication is impossible), an airborne SAR system can provide important information about the actual road traffic situation. Although not discussed in this doctoral thesis, an airborne SAR system can additionally provide high resolution SAR images, which can be used for evaluating the condition of traffic infrastructure (e.g., damages of bridges, landslides over roads, among others). Actual information about road traffic and traffic infrastructure is highly valuable for relief forces (e.g., fire department, technical emergency service, police, etc.), especially for disaster management and evacuation planning.

Nowadays, the German Aerospace Center (DLR) develops approaches for traffic management in case of large scale events and catastrophes in the frame of the project VABENE⁺⁺ [13]. One of the approaches consists in using the DLR's F-SAR system (described in detail in Appendix A), which has the challenging task to acquire and to

process the traffic data onboard the research aircraft Dornier DO228-212, and finally to transmit the relevant traffic data to the traffic management center. The general idea of this approach is depicted in **Figure 1.1**.

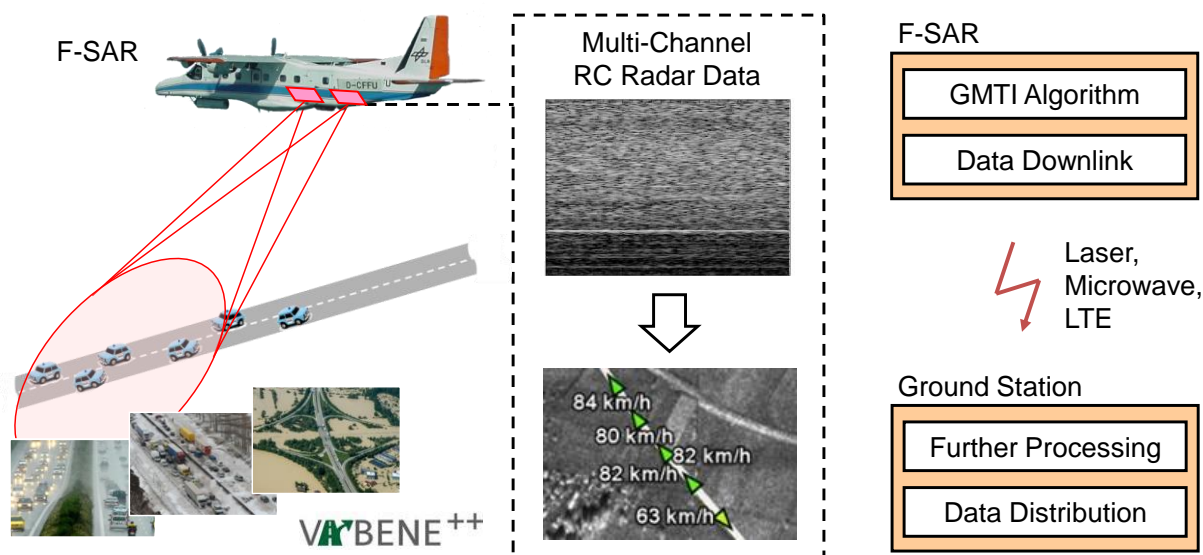


Figure 1.1. Traffic monitoring in case of large scale events and catastrophes using an airborne SAR system (e.g., F-SAR) in the frame of DLR’s project VABENE⁺⁺. The relevant traffic data are obtained after processing the multi-channel radar data using a proper GMTI algorithm (i.e., the one proposed in this doctoral thesis).

Onboard the F-SAR, a ground moving target indication (GMTI) algorithm is applied for processing the multi-channel radar data and for estimating relevant parameters of the moving vehicles, such as: positions, velocities and moving directions. Examples of state-of-the-art GMTI algorithms and systems are presented in Section 1.2.

The data downlink can be carried out using an optical laser communication link, a microwave data link, or (more recently) an existing long term evolution (LTE) infrastructure [14]–[16]. Naturally, such options present pros and cons. For instance, the communication via an existing LTE network offers the lowest costs for hardware, integration, maintenance and operation. However, if the number of LTE base stations in the disaster location is not enough, measurement gaps are expected due to loss of LTE connection. Alternatively, the communication via laser or microwave data links is especially valuable when the mobile internet connection (i.e., the LTE network) is

unavailable. The drawback is that they require fast installation of a dedicated mobile ground station close to the disaster location, which in reality might be challenging.

Indeed, the traffic data obtained from an airborne SAR system could supplement the information acquired by the road sensors and be used in research for improving traffic models or as information source for road traffic statistics [17]. Besides, it is important to mention that in some cases (e.g., in rural and primary roads without enough sensor installations or in large scale events and catastrophes) an airborne SAR system could be the only source of traffic data.

1.2 State-of-the-Art GMTI Algorithms and Systems

GMTI algorithms were originally designed for military applications with the aim to detect targets moving on the Earth's surface (land and ocean) and gained popularity nowadays also for civilian applications (e.g., road traffic monitoring).

The number of receiving antennas or channels plays an important role for GMTI. Although single-channel GMTI is possible [18]–[21], generally more sophisticated and fundamentally more powerful algorithms are based on multi-channel processing (i.e., multiple receiving antennas arranged in the flight direction and separated by a properly selected azimuth baseline) due to their capability to achieve more significant clutter cancellation, which enables the detection of even slowly moving targets [22].

The clutter cancellation can be performed by using the well-known displaced phase center antenna (DPCA) technique [23], while the target's line-of-sight velocity and position can be estimated by using the along-track interferometry (ATI) technique [24]. Both DPCA and ATI techniques were originally designed for two-channel radar systems. Nevertheless, at least a three-channel system is necessary for obtaining both clutter cancellation and accurate target's motion and position parameter estimation. For instance, the addition of a third receiving antenna allows not only the combination of the DPCA and ATI techniques for improved parameter estimation accuracy [25], but also the application of the powerful space-time adaptive processing (STAP)

techniques [26], [27]. STAP achieves very good clutter cancellation and provides accurate target's line-of-sight velocity and position estimation by successive adaption of the steering vector, whereas at the expense of a higher computational power compared to DPCA and ATI.

Numerous GMTI algorithms are available in the literature for road traffic monitoring using airborne SAR (and also using spaceborne SAR [28]–[33] or even aerial optical images [4], [34], whereas such systems are not in the scope of this doctoral thesis). For instance, an interesting three-channel GMTI algorithm is presented in [35], where the post-Doppler STAP (PD STAP) is combined with a scanning operation mode (i.e., a wide area is monitored by a narrow azimuth antenna beam width that is steered from one azimuth angle to another in a cyclic way after a certain time span). Thus, the same vehicle can be detected several times from different aspect angles. Although this algorithm achieves very good detection performance, it is pointed out that: 1) an efficient scanning operation requires an expensive and heavy phased-array antenna, which is generally not available for all state-of-the-art airborne SAR systems; and 2) no prior knowledge is used for estimating the parameters of the detected vehicles and for assigning them to their correct roads (e.g., the use of a road database).

A fast dual-channel GMTI algorithm based on a priori knowledge was presented more recently in [36], where the roads obtained from the OpenStreetMap (OSM) [37] database are mapped into the radar range-compressed (RC) data array so that only the intersections of the moving target signals are evaluated. The positions of the cars are obtained directly from the intersection between the moving target signals and the OSM road axes. Nevertheless, it is pointed out that false detections may be obtained due to signals coming from adjacent roads. In order to recognize and to discard these false detections, PD STAP is suggested in [38] for estimating the direction-of-arrival (DOA) angles of the detections. Although the PD STAP theoretical performance is presented in [38], the algorithm itself was not implemented and evaluated in detail.

The idea of using an a priori known road database is very recent. Even so, it has been combined mainly with displacement-based GMTI algorithms, where computational

time consuming SAR processing is performed. As a result, the moving vehicles appear displaced from the roads [28]–[30], [39] and their reassignments are very challenging, especially in dense traffic scenarios with several adjacent roads. This doctoral thesis follows up the framework presented in [36], [38], where the highlights are: 1) the promising combination of an a priori known road database with the powerful PD STAP; and 2) the ability to reduce potential false detections significantly.

Finally, **Table 1.1** shows an overview of some civilian state-of-the-art airborne SAR systems designed for research and environmental monitoring purposes [40]. The systems with GMTI capability are the ones principally suitable for traffic monitoring. For instance, this doctoral thesis presents results obtained from real multi-channel radar data acquired with the DLR’s F-SAR system [41] (described in detail in Appendix A). A comprehensive overview of state-of-the-art spaceborne SAR systems and their main features is presented in [12].

TABLE 1.1
STATE-OF-THE-ART AIRBORNE SAR SYSTEMS

Sensor	Frequency Band	Fully Polarimetric	Single-Pass InSAR	GMTI Capability	Institution	Country
AIRSAR [42]	P,L,C	P,L,C	C	No	NASA/JPL	USA
UAVSAR [43]	L	L	-	No	NASA/JPL	USA
AeS-1/2 [44]	X,P	P	X	No	Intermap	USA
CV-580 [45]	C,X	C,X	-	Yes	DRDC	Canada
F-SAR [41]	X,C,S,L,P	X,C,S,L,P	X,S	Yes	DLR	Germany
SmartSAR [46]	X	-	-	Yes	Cassidian	Germany
PAMIR [47]	X	-	X	Yes	FHR	Germany
AER-II [48]	X	X	X	Yes	FHR	Germany
EMISAR [49]	L,C	L,C	C	No	TUD	Denmark
Carabas-II [50]	VHF	VHF	-	No	FOI	Sweden
RAMSES [51]	W,Ka,Ku, X,C,S,L,P	Ku,X,C, S,L,P	Ku,X	Yes	ONERA	France
SETHI [52]	X,L,P	X,L,P	X	Yes	ONERA	France
Pi-SAR [53]	X,L	X,L	X	No	JAXA	Japan
Pi-SAR 2 [54]	X	X	X	Yes	JAXA	Japan

1.3 Main Objectives

This doctoral thesis presents a novel a priori knowledge-based algorithm for traffic monitoring that combines a road database with the powerful multi-channel technique PD STAP. The proposed algorithm blends two freely available databases: 1) a road network obtained from the celebrated OSM [37]; and 2) a digital elevation model (DEM) obtained from the Shuttle Radar Topography Mission (SRTM) [55], [56]. The DEM is necessary since the OSM does not provide geographical height information. Both OSM and SRTM provide the input parameters for two positioning error models that are essential for recognizing and rejecting the false detections, as well as for assigning the detected cars to their correct roads (cf. Chapter 5).

The PD STAP is chosen due to its sensitivity to both low and high line-of-sight velocities, its true clutter suppression and its accurate target position estimation capabilities. In addition, the PD STAP is a reduced-rank method which offers computational burden mitigation and improved statistical convergence (cf. Chapter 3).

By incorporating an a priori known road network into the processing chain and by ignoring vehicles moving off-road (which may be of interest for military applications but not for civilian traffic monitoring), decreased processing hardware complexity and low costs compared to the military state-of-the-art GMTI systems can be achieved. Therefore, the proposed PD STAP processor is a promising solution for detecting effectively the cars and for estimating their positions, velocities and moving directions with high accuracy.

The proposed PD STAP processor is evaluated using real four-channel aperture switching (AS) radar data acquired by the DLR's F-SAR system. The radar data takes are described in detail in Appendix A and include scenarios with controlled cars as well a real traffic on a major highway in Germany.

1.4 Scope and Major Contributions

The major concern of this doctoral thesis is to provide a complete and comprehensive description (e.g., mathematical framework, performance analysis, experimental results and limitations) of the proposed a priori knowledge-based PD STAP algorithm for traffic monitoring using the DLR's F-SAR system.

The novelties and major contributions of this work are:

1. An extensive review and overview about the main PD STAP features, such as: clutter cancellation, position and velocity estimation of the moving target, clutter models (for homogeneous and heterogeneous terrain) for estimating the constant false alarm rate (CFAR) threshold, performance model for theoretical estimations, eigenvalues obtained from the clutter covariance matrix (CCM) and the impacts of a squinted array in the radar data acquisition (cf. Chapter 3);
2. A novel PD STAP algorithm implemented in Interactive Data Language (IDL) [57] with three operational modes (cf. Chapter 4):
 - a. Conventional PD STAP (i.e., without a priori knowledge information): detects also vehicles moving off-road, being suitable especially for areas where road information is unavailable;
 - b. PD STAP with a priori knowledge information: assigns the moving vehicles to their correct roads and discards off-road vehicles (i.e., detections that lie far from roads), being suitable for non-real time traffic monitoring;
 - c. Fast PD STAP with a priori knowledge information: faster processing version of (b), being promising for real time traffic monitoring. In this case, only the relevant data around the roads are processed.
3. A novel error module for recognizing and discarding false detections, and for assigning the cars to their correct roads. This module blends two positioning error models: 1) an existing one for the moving targets [35]; and 2) a novel one for the OSM road points [58] (cf. Chapter 5);
4. A novel data calibration algorithm that is able to: 1) handle the antenna AS; 2) correct the channel imbalances; and 3) consider the 2-D Doppler centroid

change over slant range and azimuth time by using the incidence angle and the Euler angles of the aircraft (yaw, pitch and roll) - obtained from the inertial measurement unit (IMU) (cf. Chapter 6);

5. Novel and automatic training data selection strategies for the CCM estimation that can be combined with a module for moving target signal rejection (cf. Chapter 7).

A part of the experimental results presented in this doctoral thesis was published in peer-reviewed journal papers [59]–[62], in conference papers [58], [63]–[66] and in internal technical reports [67], [68].

1.5 Outline

Overall, this doctoral thesis is organized in eight chapters. Additional information is provided in two appendixes at the end of the thesis.

The structure of this doctoral thesis is delineated as follows. This first chapter introduces the need for road traffic monitoring using airborne SAR, especially in case of large scale events and catastrophes. In this sense, the benefits and limitations of renowned state-of-the-art GMTI algorithms are presented, giving support to describe the main objectives and contributions of this work. Chapter 2 reviews the principles and theory of airborne SAR with emphasis on GMTI in order to establish the necessary background. This chapter closes by introducing the benefits of the STAP technique for moving target's detection and parameters estimation. Chapter 3 gives an overview about the main features of the PD STAP technique, including the mathematical framework, performance analysis, experimental results and limitations. Chapter 4 presents the processing chain of the proposed a priori knowledge-based PD STAP processor, pointing out the main tasks carried out for each block. Chapter 5 describes the novel positioning error models that are combined in order to recognize and to reject false detections that lie far from the roads. Chapter 6 presents the workflow of the data calibration algorithm that is crucial for the GMTI operation and for the corresponding parameter extraction of the moving targets. Chapter 7 examines

novel and automatic training data selection strategies for CCM estimation along with a module for moving target signal rejection. This topic is of great importance because the quality of the training data impacts directly on the PD STAP performance. In addition, Chapter 7 presents and discusses experimental GMTI results obtained by applying the proposed PD STAP processor on four data takes considering scenarios with controlled cars and real traffic in a major highway of Germany. Chapter 8 concludes the doctoral thesis and provides an outlook on future radar-based traffic monitoring research. Appendix A addresses important information about the DLR's system F-SAR, the flight campaigns conducted for the GMTI experiments and the SAR data takes processed by the proposed PD STAP processor. Finally, Appendix B presents a log of roads in Germany that is used for estimating empirically important parameters for the novel positioning error models presented in Chapter 5.

2 SAR Principles

2.1 Chapter Overview

This chapter presents basic SAR principles for the application of STAP techniques. In this sense, the common SAR terminology is introduced together with an acquisition geometry for airborne SAR systems in stripmap mode. The signal model for stationary point-like targets is derived based on the classic frequency modulated pulse waveform known as range chirp, which is compressed along the range dimension for improving the resolution and the signal-to-noise ratio (SNR). After pulse compression, the radar data become range-compressed and are ready for STAP. This chapter concludes by pointing out important features of conventional SAR processing methods regarding SAR image formation and the effects of moving targets on SAR imagery.

2.2 Brief History of SAR

The first Radio Detection and Ranging (RADAR) system was developed by Christian Hülsmeyer (1881-1957) in 1904 for ship collision prevention, called *Telemobiloscope* [69]. In the 1930s, the radar research was intensified worldwide (e.g., Germany, Italy, the United States, the United Kingdom and the Soviet Union) for military applications motivated by the World War II [70].

In the 1950s, the principle of SAR was invented and firstly demonstrated by Carl Wiley (1918-1985) at Goodyear Aerospace Ltd [71]. Nevertheless, at that time the data recording and imaging were accomplished using optical lenses due to the lack of digital signal processors. The SAR technique was further developed in the 1960s [11], once more pursuing military applications.

Currently, SAR is in a “golden age” with several applications in vast remote sensing areas, for instance: geology, cartography, oceanography, nautical shipping, hydrology, glaciology, agriculture and forestry, environmental monitoring, GMTI, emergency management, among others [12].

2.3 SAR Terminology and Acquisition Geometry

SAR is an active sensor that uses one or more antennas for transmitting and receiving electromagnetic radiation. The transmitted radio frequency (RF) pulses strike an illuminated area on the ground containing not only the targets of interest but also several undesired objects that are known as *clutter*. All illuminated objects backscatter the transmitted RF pulses and a very small fraction of the backscattered signals is coherently received by the SAR system, amplified, down converted, digitized and stored in the mass memory [72].

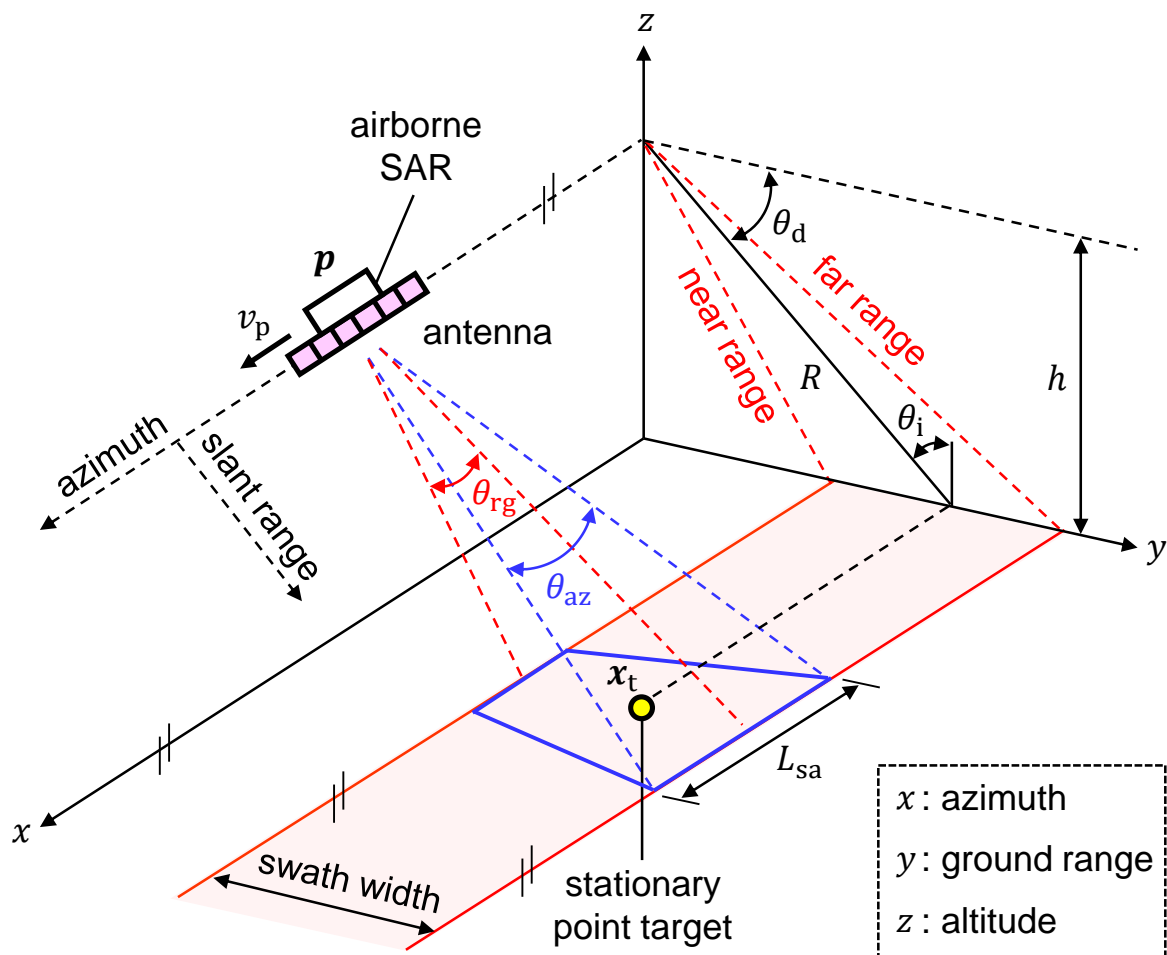


Figure 2.1. Illustration of an airborne SAR acquisition geometry in stripmap operation mode.

The SAR terminology can be introduced by means of **Figure 2.1**. In this figure, an airborne SAR system flies at constant altitude h and with constant velocity v_p along a

straight trajectory, so that a strip of a certain width is imaged on the ground. This operation mode is known as *stripmap* and the strip width imaged on the ground is denominated swath¹. The direction of flight is known as azimuth or along-track. The direction of propagation is known as slant range or line-of-sight, and its projection on the ground is known as ground range. The minimum and the maximum slant ranges are known as near range and far range, respectively. The antenna is mounted on the aircraft's fuselage in order to achieve a side looking geometry (e.g., left-looking with respect to the azimuth direction, as depicted in **Figure 2.1**), where the antenna beam is pointed perpendicular to the azimuth direction (or pointed to a certain squint angle – cf. Section 3.3.4). The antenna is tilted from the horizontal plane downwards by a certain depression angle θ_d , which is complementary to the incidence angle θ_i for a Cartesian acquisition geometry (e.g., airborne SAR acquisition). Here the flat earth assumption is used. The distance between the SAR platform $\mathbf{p} = [x_p, y_p, z_p]^T$ and the stationary point target $\mathbf{x}_t = [x_t, y_t, z_t]^T$ (where the symbol $[\cdot]^T$ terms the transpose operator) is known as target's slant range $R(t)$, which varies over azimuth time t . The SAR transmits pulses according to a certain pulse repetition frequency (PRF), which also determines the sampling frequency in the azimuth direction.

The antenna 3-dB (half power) beamwidth in elevation θ_{rg} defines the maximum swath width, while the 3 dB beamwidth in azimuth θ_{az} defines the synthetic aperture L_{sa} , which is range dependent and can be expressed by [7]

$$L_{sa} = 2 \cdot R_0 \cdot \tan\left(\frac{\theta_{az}}{2}\right), \quad (2.1)$$

where R_0 is the slant range to the swath center. The synthetic aperture time is given by

¹Traditional SAR operation modes can be applied in order to increase the swath width (*scanSAR*) or to improve the azimuth resolution (*spotlight*) comparing to the stripmap mode. In addition, modern imaging modes are also available in the literature for improving certain performance parameters (although at the expense of others), for instance: *TOPSAR* [149], *circular SAR* (in both stripmap and spotlight modes) [87], [150], *holographic SAR* [151], *staggered SAR* [152], among others. Such operation modes are generally carried out by controlling the antenna's radiation pattern, which is possible for instance by using a planar antenna [12].

$$T_{sa} = \frac{L_{sa}}{v_p} . \quad (2.2)$$

Real scenarios may contain several targets with overlapping backscattering. Without pulse compression, two targets can be generally separated in the slant range direction if their echoes are not simultaneously received. Assuming that the SAR transmits a rectangular pulse with duration τ_p , the minimum slant range distance between two neighboring targets before pulse compression can be expressed by [7]

$$\delta_{r,raw} = \frac{c}{2} \cdot \tau_p , \quad (2.3)$$

where c is the speed of light in vacuum. This expression shows that the slant range resolution is directly dependent upon the pulse duration, suggesting that very narrow pulses should be transmitted for ensuring a good slant range resolution. However, very narrow pulses require high transmitting power for receiving the echoes with a proper SNR. The trade-off between the pulse duration and the achieved slant range resolution can be solved by using matched filters (e.g., pulse compression), which improve the slant range resolution and increase the point-target SNR significantly (cf. Section 2.5).

In the azimuth dimension, the backscattered echoes from targets overlap within the azimuth footprint. For real aperture radars (RAR) with a narrow azimuth beamwidth θ_{az} , the azimuth resolution can be expressed by the approximation [7]

$$\delta_{az,raw} = L_{sa} \approx \theta_{az} \cdot R_0 \approx \left(\frac{\lambda}{L_a}\right) \cdot R_0 , \quad (2.4)$$

where λ is the wavelength and L_a is the effective length of the antenna in azimuth. This expression shows that: 1) the azimuth resolution coarses as the targets are further apart from the sensor since R_0 increases; and 2) a long antenna yields a better azimuth resolution for a given operational frequency. However, instead of using a very long antenna, all echoes received within the illumination interval of a certain target can be

coherently combined by applying signal processing techniques, so that a very large antenna aperture is synthesized in the direction of flight. This is the basic idea of SAR.

For SAR systems, the achievable azimuth resolution can be expressed as a function of the coherent processing interval (CPI) time T_{CPI} according to the approximation [73]

$$\delta_{\text{az}} \approx \frac{\lambda \cdot R_0}{2 \cdot v_p \cdot T_{\text{CPI}}}, \quad (2.5)$$

which assumes that the SAR platform velocity v_p is much higher than the maximum expected velocity of the target in azimuth. Indeed, if the complete synthetic aperture time T_{sa} is considered (so that $T_{\text{CPI}} = T_{\text{sa}}$), then the best achievable azimuth resolution can be obtained by the approximation [6]

$$\delta_{\text{az}} \approx \frac{L_{\text{az}}}{2}. \quad (2.6)$$

This expression is very important because it allows pointing out the main differences between RAR and SAR systems, for instance:

1. The SAR azimuth resolution is directly proportional to the effective length of the azimuth antenna. Consequently, the smaller the antenna length the better is the azimuth resolution, since the illumination time (and therefore the coherent integration time) is increased;
2. The SAR azimuth resolution is independent of range, which explains why even spaceborne SAR systems are able to achieve high azimuth resolution.

2.4 Signal Model for Stationary Point-Like Targets

SAR systems commonly transmit a long linear frequency modulated (LFM) pulse waveform known as *range chirp* [9] (although other pulse waveforms are possible). The signal model described in this section uses the framework presented in [22].

The SAR transmitted signal in the range direction can be expressed as

$$s_{\text{TX}}(\tau) = s_{\text{TX,b}}(\tau) \cdot \exp\left(j \cdot \frac{2\pi}{\lambda} \cdot c \cdot \tau\right), \quad (2.7)$$

where j denotes the imaginary unit, τ is known as *fast time* and represents the range direction, and $s_{\text{TX,b}}(\tau)$ is the pulse waveform in baseband, which in the case of a LFM range chirp can be expressed as

$$s_{\text{TX,b}}(\tau) = \text{rect}\left(\frac{\tau}{\tau_p}\right) \cdot \exp(\pm j \cdot \pi \cdot k_r \cdot \tau^2), \quad (2.8)$$

where $k_r = B_r/\tau_p$ denotes the chirp slope and $\text{rect}[\cdot]$ denotes the unity rectangular function.

The signal received from a point-like target can be considered as a delayed and attenuated version of the transmitted signal $s_{\text{TX}}(\tau)$, being expressed as

$$s_{\text{RX}}(\tau) = A_s \cdot s_{\text{TX}}\left[\tau - \frac{2 \cdot R(\tau)}{c}\right], \quad (2.9)$$

where A_s is a coefficient that includes the free-space attenuation, the backscattering coefficient and the weighting of the two-way antenna pattern.

Finally, the received signal $s_{\text{RX}}(\tau)$ can be expressed in baseband in a two-dimensional form as

$$s_{\text{RX,b}}(\tau, t) = A_s \cdot s_{\text{TX}}\left[\tau - \frac{2 \cdot R(\tau)}{c}\right] \cdot \exp\left[-j \frac{2\pi}{\lambda} \cdot 2 \cdot R(t)\right], \quad (2.10)$$

where t is known as *slow time* and represents the azimuth direction.

Equation (2.10) describes the collected SAR data before any processing, which is called *raw data*. Note that for each pulse in azimuth time t , an echo of duration τ is received in fast time. Since the electromagnetic waves are propagated in the speed of light (i.e., much faster than the aircraft's velocity), the aircraft can be considered static

during the transmission of a pulse and the reception of the scattered signal (known in the literature as the “stop-and-go approximation”). The collected SAR data are stored into a two-dimensional complex raw data matrix (with dimensions azimuth and range, respectively) in the mass memory of the radar system.

2.5 Pulse Compression

The pulse compression is carried out with respect to the transmitted signal in baseband (for instance, based on the LFM range chirp)

$$s_{\text{TX,b}}(\tau) = s_{\text{chirp}}(\tau) = \text{rect}\left(\frac{\tau}{\tau_p}\right) \cdot \exp(j \cdot \pi \cdot k_r \cdot \tau^2). \quad (2.11)$$

The instantaneous frequency of the range chirp can be expressed as [7]

$$f_{\text{chirp}}(\tau) = \frac{1}{2 \cdot \pi} \cdot \frac{d(\arg[s_{\text{chirp}}(\tau)])}{dt} = k_r \cdot \tau, \quad (2.12)$$

which is defined within $[-\tau_p/2, \tau_p/2]$ and varies linearly along fast time τ with either a positive or a negative angular coefficient depending on the sign of the chirp slope k_r (known as *up chirp* and *down chirp*, respectively). By using the principle of stationary phase (which is an approximation of the Fourier Integral that considers only the region where the phase varies slowly) and apart from a complex constant, the range chirp spectrum can be shown to be also a chirp [7]:

$$S_{\text{chirp}}(f) = \text{rect}\left(\frac{f}{B_r}\right) \cdot \exp\left(-j \cdot \pi \cdot \frac{f^2}{k_r}\right). \quad (2.13)$$

It is shown in [7] that the pulse compression can be achieved by multiplying the chirp spectrum from (2.13) with a matched filter $S_{\text{chirp}}^*(f)$ (where $[\cdot]^*$ denotes the complex conjugation).

After pulse compression, the best achievable slant range resolution is given by [7]

$$\delta_r = \alpha_{\text{wn}} \cdot \frac{c}{2 \cdot B_r}, \quad (2.14)$$

where α_{wn} accounts for losses due to windowing applied during processing (e.g., $\alpha_{\text{wn}} \cong 0.89$ for a rectangular window) [74]. This expression shows that the larger the chirp bandwidth B_r , the better is the slant range resolution.

2.6 SAR Image Formation

SAR processing requires high computational time for processing the raw data in order to obtain the desired information from the backscattered energy. Classical algorithms for SAR processing are based on the well-known “stationary world matched filtering” (SWMF). A prominent example in this case is the range-Doppler algorithm (RDA) [75], which basically includes three major steps (as depicted in **Figure 2.2**):

1. Range compression: a pulse compression is carried out along the range direction, (cf. **Figure 2.2b**);
2. Range cell migration correction (RCMC): the curvature of the range history is corrected (cf. **Figure 2.2c**);
3. Azimuth compression: a pulse compression is carried out along the azimuth direction (cf. **Figure 2.2d**).

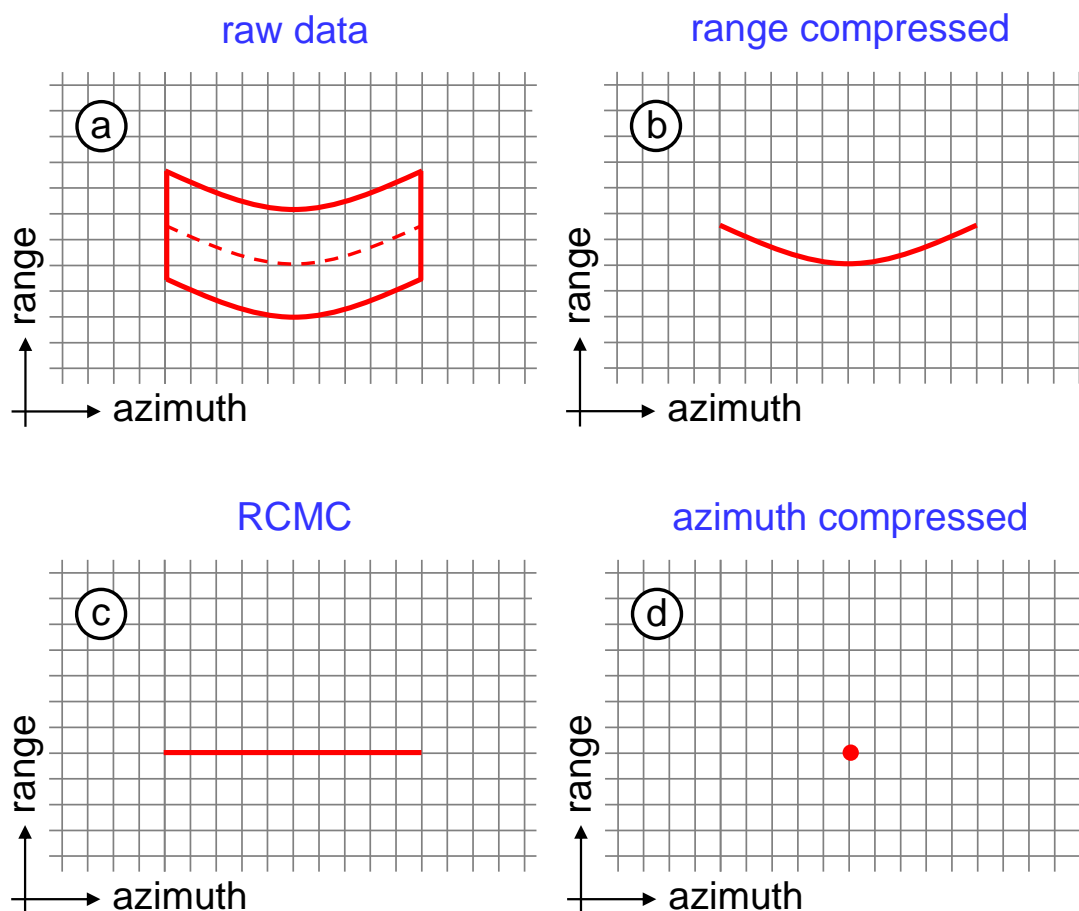


Figure 2.2. Major steps of the RDA for a single stationary point-like target: (a) SAR raw data, (b) data after range compression, (c) data after RCMC and (d) data after azimuth compression [22].

Other SAR processing approaches are possible, for instance, using algorithms based on spectral analysis or in the wavelength domain. An extensive review and overview about state-of-the-art SAR processing methodologies can be found in [7], [76].

2.7 Moving Target Effects on SAR Imagery

SAR is designed for processing stationary targets. Therefore, when moving targets are processed as static ground they might appear displaced and defocused due to their motion in both range and azimuth directions. Comprehensive tutorials are available in the literature explaining the effects of moving target's velocity and acceleration on SAR imagery [22], [77], [78]. For instance, a noticeable effect is caused by the target's velocity in range, which causes a proportional spatial displacement from its real position (especially along the azimuth direction). To demonstrate this effect, an

interesting spaceborne SAR image acquired with the German TerraSAR-X satellite [79]–[81] is shown in **Figure 2.3**, where a train moves through the Tehachapi Loop, in California, USA. In this case, both range and azimuth velocities of the train change gradually as it moves through the spiral loop. As a result, the train is detected several times with different displacements from its actual positions (i.e., on the rail track), appearing as an ellipse (shown in blue). Note that the train is only detected on the rail track when it presents zero range velocity (i.e., only azimuth velocity). In contrast, the same train is detected with a maximum azimuth displacement (in the order of 400 m) when it presents maximum range velocity (i.e., zero azimuth velocity).

Indeed, GMTI algorithms based on SAR processing need to estimate the positions and the velocities of the moving targets for correcting their displacement and defocusing in the final SAR focused image. The example shown in **Figure 2.3** gives a sense about how far a moving target can be detected from its actual position due to its velocity. Thus, one can visualize how challenging is the reassignment of moving vehicles especially in dense traffic scenarios with a number of adjacent roads.

STAP techniques are applied directly on range compressed data. In this sense, no time-consuming SAR imaging is necessary (e.g., RCMC and azimuth compression) and the aforementioned effects of moving targets on SAR imagery are not an issue. This is an important difference between SAR processing and STAP. The main STAP features and limitations are presented and discussed in detail in Chapter 3.



Figure 2.3. Spaceborne SAR image acquired with the TerraSAR-X satellite showing the Tehachapi Loop, in California, USA. A moving train is detected several times with different displacements from its actual positions (especially in azimuth), so that the detections form an ellipse (shown in blue). The azimuth displacements are proportional to the velocity of the train in the range direction.

2.8 Chapter Summary

This chapter presents basic SAR concepts, including a signal model for stationary point-like targets that employs the widely used transmitted pulse waveform known as “range chirp”, which allows the pulse compression for enhancing the resolution and the SNR significantly. Conventional SAR processing algorithms (e.g., the RDA) basically perform: range compression, RCMC and azimuth compression. Since SAR is designed for processing stationary targets, when moving targets are processed as static ground they might appear displaced and defocused due to their velocities. The PD STAP operates directly on RC data (i.e., after range pulse compression) in range-Doppler domain. Therefore, no time-consuming SAR imaging is necessary and it is

not affected by the effects caused by moving targets on SAR imagery. A detailed overview about the main PD STAP features is presented in the next chapter.

3 Space-Time Adaptive Processing (STAP)

3.1 Chapter Overview

This chapter presents an overview about the main features of the PD STAP technique, which is able to perform clutter suppression, moving target's detection and parameters estimation (e.g., position, velocity and moving direction). The moving target detection is carried out according to a CFAR threshold that is estimated from a clutter model. In this chapter, two clutter models are presented and discussed: one for homogeneous clutter and one for heterogeneous clutter. A performance model for PD STAP is also presented comprising the theoretical predictions of the detection performance, the achievable position and the velocity estimation accuracy. Finally, some of the main limitations of the PD STAP technique are addressed.

3.2 The Need for STAP

STAP is a class of linear adaptive filtering techniques that operates on space-time observations for enhancing the moving target detection [82]. The STAP definition can be explained by the need for *space-time* processing and the need for *adaptability*.

The need for *space-time* processing arises from the inherent two-dimensional nature of the ground clutter, as illustrated in **Figure 3.1**. This figure shows the distribution of the power spectral density (PSD) of the ground clutter in the angle-Doppler plan, where the normalized angle denotes the spatial dimension and the normalized Doppler denotes the temporal dimension. The ground clutter angle-Doppler region of support is described in the literature as a “ridge”, which behaves as a line for airborne SAR, opening up into an ellipse for varying degrees of the aircraft's yaw [83]. **Figure 3.1** also shows that the space-time filter is able to place a null in the angle-Doppler beam pattern where the ground clutter may compete. Hence, since the space-time filter has a narrow ground clutter notch, the depicted target falls into the pass band [84].

The need for *adaptability* arises from the numerous real-world effects that still need to be taken into account, for instance: channel mismatches, clutter heterogeneity, clutter

nonstationarity, among others. Such effects strictly limit the performance of the space-time processing and give rise to the need for adaptability - therefore *space-time adaptive processing*, or simply “STAP” [85].

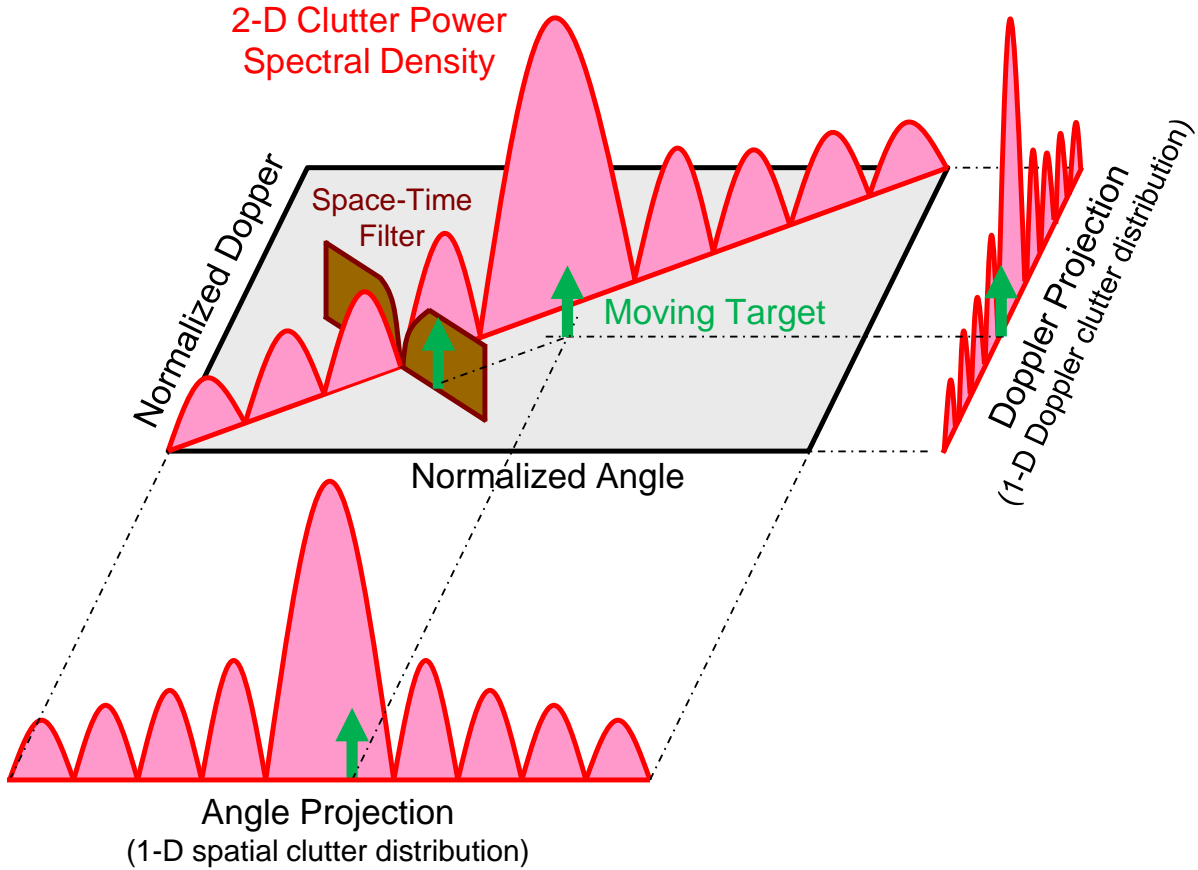


Figure 3.1. The principle of the space-time clutter filtering (modified after [22]).

3.3 Post-Doppler STAP

A number of STAP techniques are possible [26], [85], [86]. This doctoral thesis sheds light on the PD STAP, which is a reduced dimension algorithm that requires less sample support and less processing effort than the classical joint-domain STAP. Besides, similarly to other state-of-the-art STAP techniques, the PD STAP is able to perform clutter suppression as well as the moving target’s detection and parameters estimation (e.g., line-of-sight velocity, Doppler frequency and DOA angle) [82].

The main steps of the PD STAP core are summarized in **Figure 3.2** and are presented in detail in the following sections.

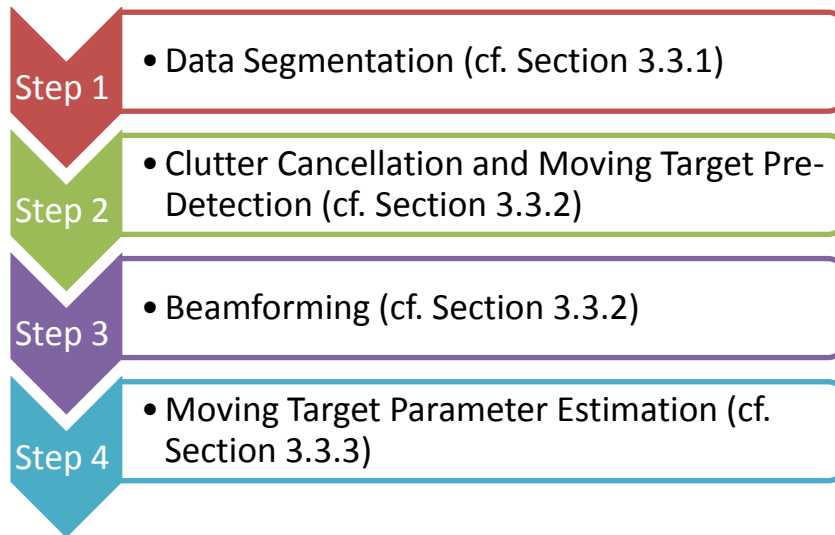


Figure 3.2. Main steps of the PD STAP core.

3.3.1 Data Segmentation

The PD STAP operates on the radar data cube shown in **Figure 3.3a**, which is very convenient for visualizing subsequent space-time processing [82]. Each radar data cube corresponds to one CPI containing $N_{a,CPI}$ azimuth (temporal) samples or pulses, K range samples and M receiving antennas or channels, so that $N_{a,CPI} \cdot K \cdot M$ complex baseband samples are obtained in total. The radar data cube is processed in data pages also known as “snapshots”, where one data page is obtained for each range gate k .

Before applying the PD STAP, the data page is transformed to Doppler domain by carrying out a fast Fourier transform (FFT) over azimuth, as shown in **Figure 3.3b**. The PD STAP technique processes one CPI at a time in range-Doppler domain (i.e., a coherent summation is carried out), exploring the concept that the azimuth phase can be considered linear for sufficient small CPIs (e.g., 128 azimuth samples for the F-SAR system with typical acquisition parameters). Due to the small CPI, the PD STAP technique can be applied not only to stripmap data but also to circular SAR data [87]. This process is denominated *Data Segmentation* (cf. **Figure 3.2**) and is depicted in **Figure 3.4**. In this figure, the multi-channel radar data are segmented in the azimuth or slow time domain, so that N CPIs are obtained to be processed by the PD STAP core.

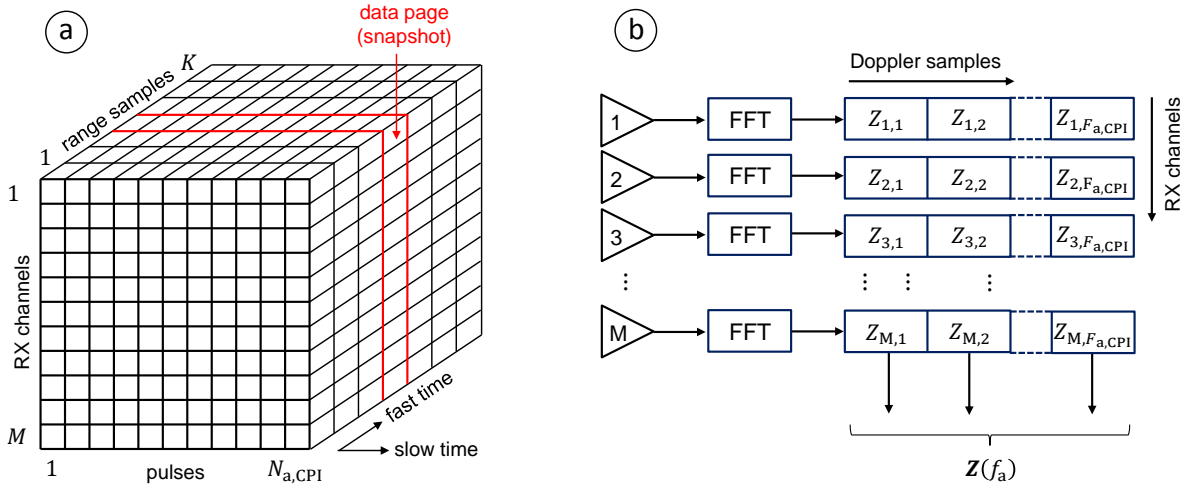


Figure 3.3. (a) Radar data cube corresponding to one CPI and (b) the data page (on the left side in red) in Doppler domain. The data vector $\mathbf{Z}(f_a)$ is processed by PD STAP.

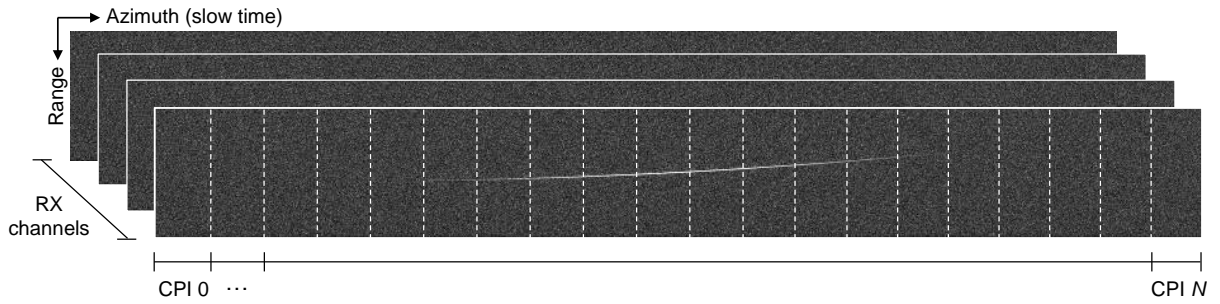


Figure 3.4. Data segmentation carried out in the azimuth or slow time domain.

The measured data page (or snapshot) corresponding to the k -th range gate can be expressed in time domain by [82]

$$\mathbf{z} = \begin{pmatrix} Z_{1,1} & Z_{1,2} & \cdots & Z_{1,N_{a,CPI}} \\ Z_{2,1} & Z_{2,2} & \cdots & Z_{2,N_{a,CPI}} \\ \vdots & \vdots & \cdots & \vdots \\ Z_{M,1} & Z_{M,2} & \cdots & Z_{M,N_{a,CPI}} \end{pmatrix}, \mathbf{z} \in \mathbb{C}^{M \times N_{a,CPI}}, \quad (3.1)$$

The data page is generally composed of

$$\mathbf{z} = \mathbf{s} + \mathbf{c} + \mathbf{n}, \quad (3.2)$$

where \mathbf{s} denotes the multi-channel moving target signal, \mathbf{c} denotes the ground clutter or interferences, and \mathbf{n} denotes the uncorrelated background white noise caused by the

radar receiver circuitry. Indeed, the desired moving target signal power is generally a very small fraction of the overall interference power [88].

3.3.2 Signal Model and Test Statistics

The multi-channel signal model can be expressed by [89]

$$\mathbf{s}(t) = a_s e^{-j\frac{4\pi}{\lambda}R(t)} D_{\text{tx}}(u_{\text{array}}(t)) \begin{bmatrix} D_{\text{rx},1}(u_{\text{array}}(t)) e^{j\frac{2\pi}{\lambda}u_{\text{array}}(t)x_1} \\ D_{\text{rx},2}(u_{\text{array}}(t)) e^{j\frac{2\pi}{\lambda}u_{\text{array}}(t)x_2} \\ \vdots \\ D_{\text{rx},M}(u_{\text{array}}(t)) e^{j\frac{2\pi}{\lambda}u_{\text{array}}(t)x_M} \end{bmatrix} \quad (3.3)$$

$$\mathbf{s}(t) = a_s e^{-j\frac{4\pi}{\lambda}R(t)} \mathbf{d}(u_{\text{array}}(t)) \in \mathbb{C}^{M \times 1},$$

where a_s denotes a complex value that accounts for the reflectivity of the scatterer, $D_{\text{tx}}(u_{\text{array}}(t))$ and $D_{\text{rx},m}(u_{\text{array}}(t))$ are the complex transmitting (TX) and receiving (RX) antenna characteristics of the m -th channel, x_m is the position of the antenna center in the azimuth direction with respect to the antenna array origin (cf. **Figure 3.5**), $\mathbf{d}(u_{\text{array}}(t))$ is the beamforming or DOA vector, $u_{\text{array}} = \cos(\Psi_{\text{DOA,array}})$ is the directional cosine and $\Psi_{\text{DOA,array}}$ denotes the DOA angle of the target measured with respect to the antenna array axis.

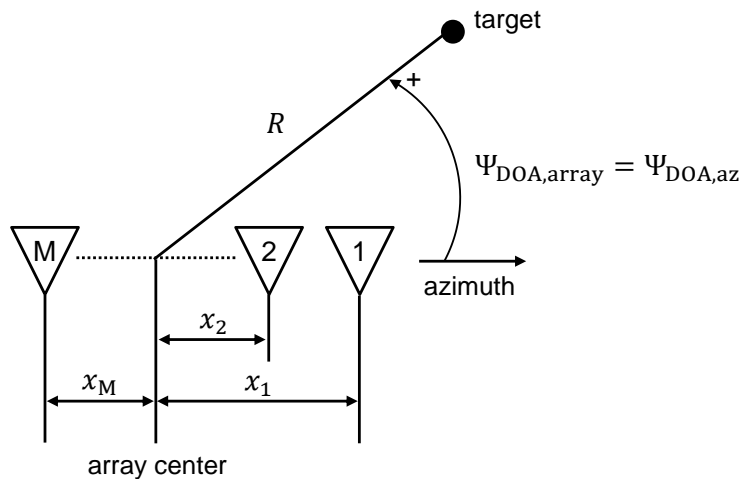


Figure 3.5. Acquisition geometry with a multi-channel antenna and zero squint angle.

Figure 3.5 shows an acquisition geometry using a multi-channel antenna, where the antenna array center origin is freely chosen at the center of the array, so that $\sum_m x_m = 0$. In this figure, the antenna array and the azimuth (or flight direction) axes coincide because the squint angle is zero. The DOA angle of the target measured with respect to the azimuth or flight direction is denoted by $\Psi_{\text{DOA,az}}$.

The moving target detection is carried out based on the well-known Adaptive Matched Filter (AMF) test [90]:

$$\bar{T}(r_k, f_a) = \frac{|\mathbf{d}^H(u_{\text{array}}, f_a) \hat{\mathbf{R}}_W^{-1}(f_a) \mathbf{z}(r_k, f_a)|^2}{\mathbf{d}^H(u_{\text{array}}, f_a) \hat{\mathbf{R}}_W^{-1}(f_a) \mathbf{d}(u_{\text{array}}, f_a)} \leq \eta, \quad (3.4)$$

where $\hat{\mathbf{R}}_W$ denotes the CCM, $[\cdot]^H$ denotes the Hermitian operator (complex conjugate transposition) and η denotes the desired CFAR threshold, whose computation is presented in Section 3.4 for homogeneous and heterogeneous ground clutter. The normalization in Equation (3.4) is necessary for providing the desired CFAR behavior [90].

The CCM can be estimated empirically from the data by applying the Sample Matrix Inverse (SMI) method [91], which is the basis for most modern STAP algorithms (notice that other CCM estimation strategies are also possible [92]):

$$\hat{\mathbf{R}}_W(f_a) = \frac{1}{K} \sum_{k=1}^K \mathbf{z}(r_k, f_a) \mathbf{z}^H(r_k, f_a), \quad \hat{\mathbf{R}}_W(f_a) \in \mathbb{C}^{M \times M}, \quad (3.5)$$

where K denotes the total number of range bins used for averaging.

For the CCM estimation, it is crucial that the multi-channel vectors \mathbf{z} are free of strong discrete scatterers and moving target signals. This condition needs to be ensured by a proper training data selection algorithm (cf. Chapter 7), otherwise the clutter suppression performance degrades and the target signals are attenuated or cancelled. This effect is known in the literature as target “self-whitening”.

3.3.3 Clutter Cancellation and Moving Target Pre-Detection

For moving target pre-detection (cf. **Figure 3.2**), it is normally enough to compute the test statistics \bar{T} for the broadside direction of the antenna array $u_0 = u_{\text{array}} = 0$ (i.e., assuming zero Doppler centroid) [93]

$$\bar{T}(r_k, f_a) = \frac{|\mathbf{d}^H(u_0, f_a) \hat{\mathbf{R}}_W^{-1}(f_a) \mathbf{z}(r_k, f_a)|^2}{\mathbf{d}^H(u_0, f_a) \hat{\mathbf{R}}_W^{-1}(f_a) \mathbf{d}(u_0, f_a)} \leq \eta . \quad (3.6)$$

The pre-detection saves processing time since not all possible u need to be applied for matched filtering. The drawback in this case is that very weak target signals may not be detected. Equation (3.6) is very important and allows pointing out that [13]:

1. The sum of the RX channels before clutter cancellation is given by

$$z_{\text{BCC}}(r_k, f_a) = |\mathbf{d}^H(u_0, f_a) \mathbf{z}(r_k, f_a)|^2 . \quad (3.7)$$

2. The clutter cancellation is carried out by multiplying each Doppler frequency bin f_a of the signal vector $\mathbf{z}(r_k, f_a)$ with the inverse of the CCM, i.e., $\hat{\mathbf{R}}_W^{-1}(f_a)$. The target matched filtering (e.g., for the broadside direction of the antenna array) is done by multiplying the intermediate result from Equation (3.7) with the Hermitian of the DOA vector $\mathbf{d}^H(u_0, f_a)$ (i.e., the expected moving target signal). The sum of the RX channels after clutter suppression is then given by

$$z_{\text{ACC}}(r_k, f_a) = |\mathbf{d}^H(u_0, f_a) \hat{\mathbf{R}}_W^{-1}(f_a) \mathbf{z}(r_k, f_a)|^2 . \quad (3.8)$$

Figure 3.6 shows the sum of the RX channels before and after clutter cancellation by applying Equation (3.7) and Equation (3.8), respectively. In this example, one CPI containing 2048 x 128 range-Doppler samples is processed from data take 4 (cf. Appendix A) including homogeneous ground clutter and the beamforming vector \mathbf{d} is steered to u_0 . Besides, the measured data are centered at zero Doppler by taking into account the variation of the Doppler centroid over slant range (cf. Chapter 6), which is known in the literature as “J-Hook” [94]. This Doppler centroid correction is very important since the CCM is estimated for each Doppler frequency bin by performing an averaging over range, as it can be seen in Equation (3.5).

After the pre-detection process, the beamforming operation (cf. **Figure 3.2**) is applied in order to estimate the directional cosine (or the DOA angle) of the moving target with respect to the antenna array axis $u_{\text{array}} = \cos(\Psi_{\text{DOA,array}})$, according to [95]

$$\hat{u}_{\text{array}} = \operatorname{argmax}_{u_{\text{array}}} \left\{ \frac{|d^H(u_{\text{array}}, f_a) \hat{R}_W^{-1}(f_a) z(r_k, f_a)|^2}{d^H(u_{\text{array}}, f_a) \hat{R}_W^{-1}(f_a) d(u_{\text{array}}, f_a)} \right\}, \quad (3.9)$$

where the maximum is obtained by selecting the DOA yielding the maximum value of this function from a discrete set of possible DOAs. Also, notice that the beamformer d includes the estimated amplitudes of the antenna patterns in the direction of the moving target and the phase differences between them, as expressed in Equation (3.3).

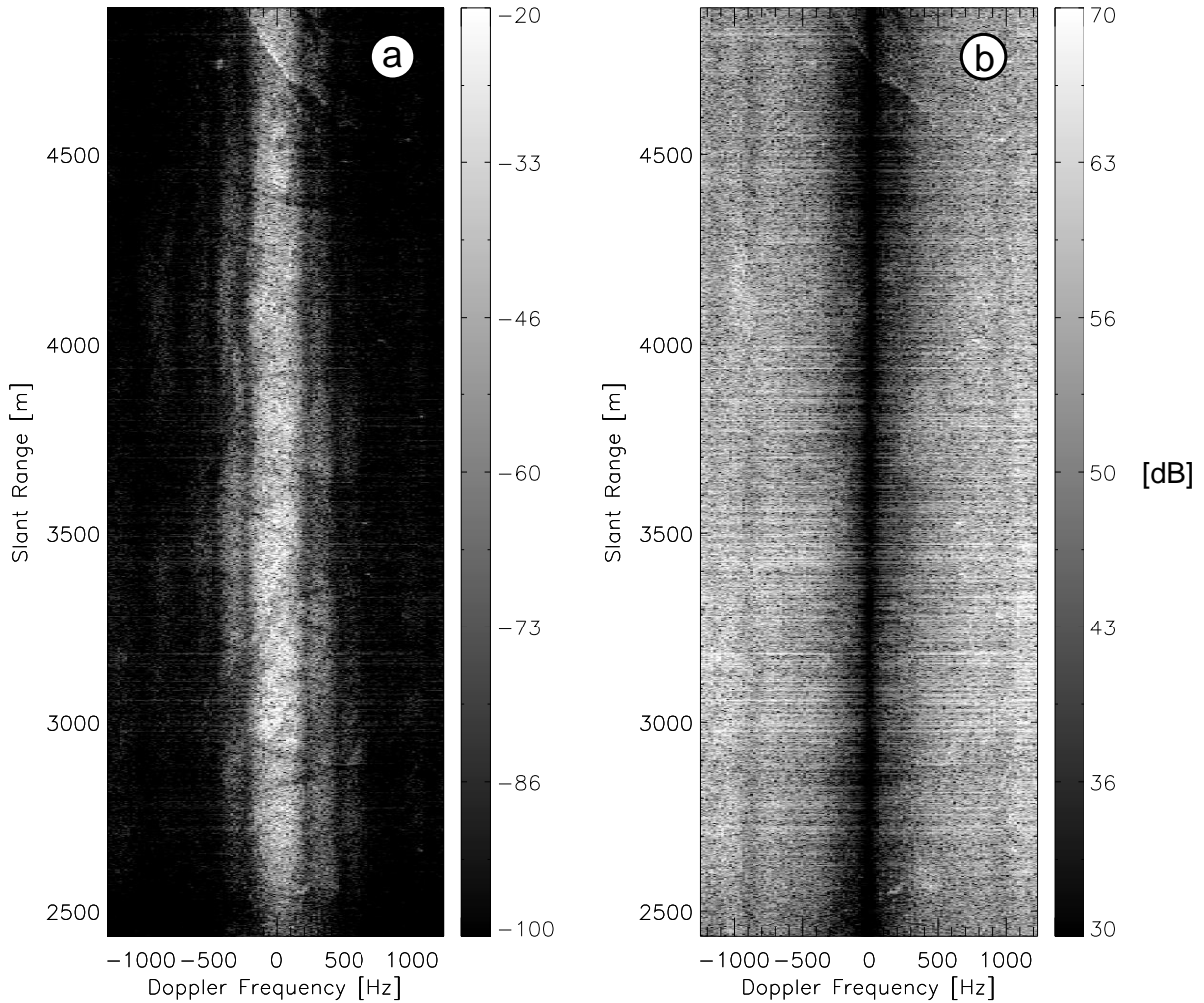


Figure 3.6. Sum of the RX channels for one CPI containing 2048 x 128 range-Doppler samples: (a) before (z_{BCC}) and (b) after clutter cancellation (z_{ACC}) for u_0 . Note the different dB scale of both images. The data are centered at zero Doppler centroid.

This scenario is illustrated in **Figure 3.7**, where the antenna array is tilted by a certain tilt angle Ψ_{tilt} measured in the xy -plane (i.e., the pitch angle is omitted in this case for simplification). In this figure, the angles in the slant range direction are shown in blue and can be related as

$$\Psi_{\text{DOA,az}} = \Psi_{\text{tilt}} + \Psi_{\text{DOA,array}}, \quad (3.10)$$

$$\Psi_{\text{tilt}} = -\Psi_{\text{sq}}, \quad (3.11)$$

where $\Psi_{\text{DOA,az}}$ is the DOA angle of the target with respect to the azimuth axis and Ψ_{sq} is the squint angle with respect to the broadside direction of the array u_0 . Note that the array and the azimuth axes would coincide only if the squint (or the tilt) angle is zero. As formerly mentioned, the PD STAP processor estimates $u_{\text{array}} = \cos(\Psi_{\text{DOA,array}})$ according to Equation (3.9) and obtains $\Psi_{\text{DOA,az}}$ according to Equation (3.10). The relationship between $\Psi_{\text{DOA,az}}$ and its projection on ground can be readily obtained from the acquisition geometry shown in **Figure 3.7** as

$$\Psi_{\text{DOA,az,g}} = \cos^{-1} \left[\frac{R}{R_g} \cos(\Psi_{\text{DOA,az}}) \right], \quad (3.12)$$

where $R_g = \sqrt{R^2 - h^2}$ is the projection on ground of the moving target's slant range and $h = z_p - z_t$ is the flight altitude of the platform above the ground. An accurate DEM is needed for obtaining the height of the scene z_t , which is especially important in case of a strong topography [96]. Equation (3.12) is important since $\Psi_{\text{DOA,az}}$ can be used for estimating the moving target's position, as described in the following section.

3.3.4.1 Moving Target Position

The coordinates of the moving target in azimuth and in ground range can be expressed respectively as

$$x_t = x_p + \Delta x = x_p + R_g \cdot \cos(\Psi_{\text{DOA,az,g}}), \quad (3.13)$$

$$y_t = y_p + R_{0,g} = y_p + R_g \cdot \sin(\Psi_{\text{DOA,az,g}}), \quad (3.14)$$

where Δx is the azimuth distance between the radar and the moving target, and $R_{0,g}$ is the projection on ground of R_0 (cf. **Figure 3.7**). The altitude of the moving target z_t can be obtained for instance from a DEM.

The position of the moving target can also be obtained in the Universal Transverse Mercator (UTM) [97] Cartesian coordinate system: $\mathbf{x}_{t,UTM} = [x_{t,UTM}, y_{t,UTM}, z_{t,UTM}]^T$. **Figure 3.8** shows the top view acquisition geometry from where the coordinates of the moving target in UTM Easting and Northing can be readily computed respectively as

$$x_{t,UTM} = x_{p,UTM} + \Delta x_{UTM} = x_{p,UTM} + R_g \cdot \cos(\alpha_p + \Psi_{DOA,az,g}), \quad (3.15)$$

$$y_{t,UTM} = y_{p,UTM} + \Delta y_{UTM} = y_{p,UTM} + R_g \cdot \sin(\alpha_p + \Psi_{DOA,az,g}), \quad (3.16)$$

where Δx_{UTM} and Δy_{UTM} are the distances between the radar and the moving target in the UTM Easting and Northing axes, respectively, α_p is the platform heading angle with respect to the UTM Easting axis and $\mathbf{p}_{UTM} = [x_{p,UTM}, y_{p,UTM}, z_{p,UTM}]^T$ are the UTM coordinates of the platform. It is assumed $z_{t,UTM} = z_t$ without loss of generality.

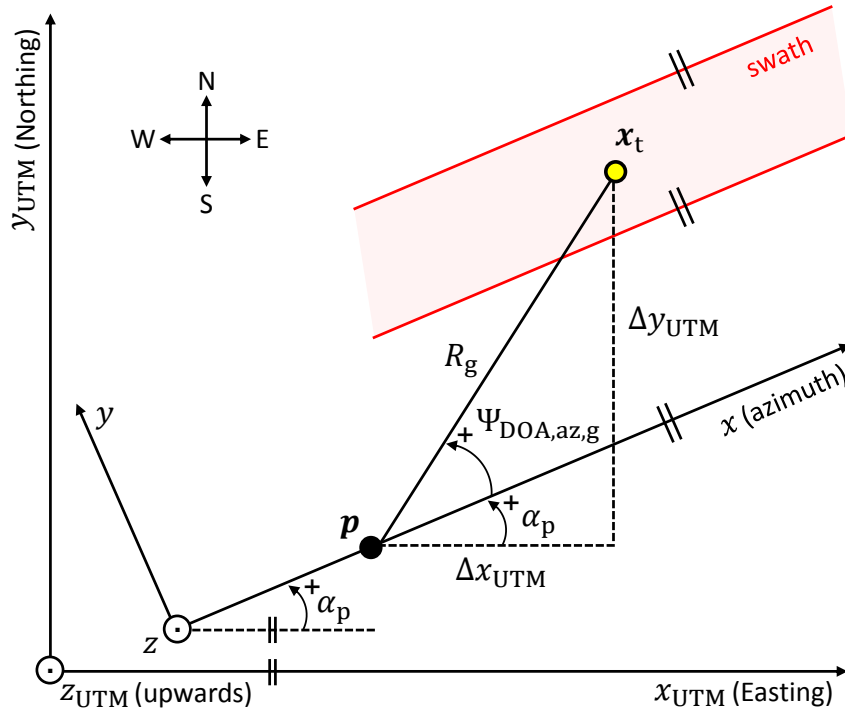


Figure 3.8. Simplified acquisition geometry used for obtaining the position of the moving target in the UTM Cartesian coordinate system.

3.3.4.2 Moving Target Velocity and Moving Direction

Assuming that the platform velocity v_p is only along the x -axis, the squint (or the tilt) angle measured in the xy -plane (cf. **Figure 3.7**) can be related to the Doppler centroid according to

$$f_{\text{DC}} = \frac{2 \cdot v_p}{\lambda} \cdot \sin \Psi_{\text{sq}} = -\frac{2 \cdot v_p}{\lambda} \cdot \sin \Psi_{\text{tilt}} . \quad (3.17)$$

In reality, the squint angle (and therefore the Doppler centroid) changes not only over slant range, but also over time due to the motion of the aircraft caused by external influences (e.g., cross-winds). This variation needs to be corrected by the PD STAP processor in the data calibration step (cf. Section 6.6), so that the data processing can be carried out at zero Doppler.

The line-of-sight velocity of the target v_r is estimated according to [82]

$$v_r = u_{\text{array}} \cdot v_p - \frac{\lambda}{2} \cdot (f_a - f_{\text{DC}}) . \quad (3.18)$$

The proposed PD STAP processor does not need to estimate the azimuth velocity of the target. Indeed, the OSM provides the geographical positions of the road points from where it is possible to compute the corresponding road point angles α_r with respect to the UTM Easting axis, as shown in **Figure 3.9** (tangent on road). Therefore, the road point angle with respect to the azimuth direction $\alpha_{r,\text{az}} = \alpha_r - \alpha_p$ allows the computation of the absolute velocity of the target on the road by using only the line-of-sight velocity and the incidence angle $\theta_i = \cos^{-1}(h/R)$ of the target [36], [63]

$$v_{\text{road}} = \left| \frac{v_r}{\sin(\theta_i) \cdot \sin(\alpha_{r,\text{az}})} \right| = |v_{\text{abs}}| . \quad (3.19)$$

Finally, the moving direction of the target is given by [36], [63]

$$\alpha_t = \begin{cases} \alpha_r , & \text{sgn}(v_{\text{abs}}) = +1 \\ \alpha_r - 180^\circ , & \text{sgn}(v_{\text{abs}}) = -1 \end{cases} , \quad (3.20)$$

where $\text{sgn}[\cdot]$ denotes the sign function.

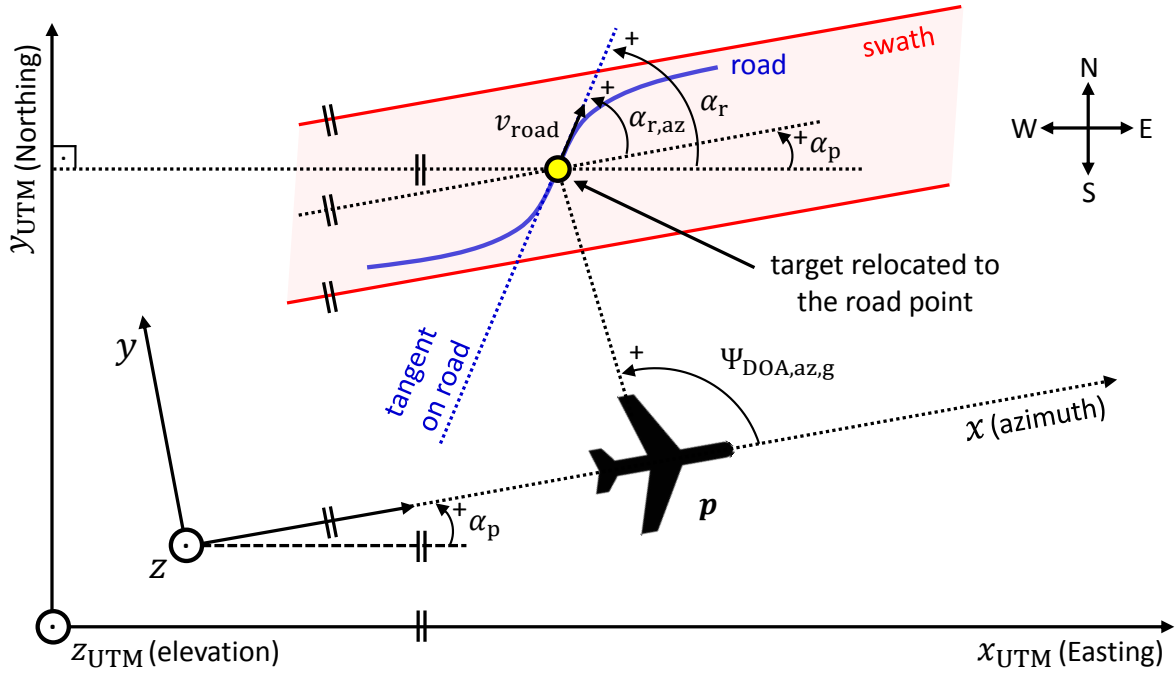


Figure 3.9. Simplified acquisition geometry illustrating the road point angle α_r provided by the OSM database, which is measured in the counterclockwise direction. This angle is necessary for estimating the absolute velocity of the target on the road.

3.4 Clutter Model

An appropriate and accurate clutter model needs to be fit to the test statistics \bar{T} in order to estimate a reliable CFAR detection threshold. Normally, this fit is done for the broadside direction of the antenna array u_0 . For estimating the CFAR threshold, it is important that the test statistics \bar{T} use training data free of moving target signals and strong discrete scatterers, which may be present due to imperfect clutter cancellation. Strategies for selecting proper training data for the CCM estimation are presented and discussed in Chapter 7.

Two clutter models are discussed in this section: one for homogeneous terrain and one for heterogeneous terrain. In both cases, the framework introduced in [98] and further investigated in [31], [93] is used. The advantage of the heterogeneous model is that it covers different types of heterogeneity, including completely homogeneous ground clutter. Therefore, it is very flexible for ground moving target indication over land with changing clutter characteristics.

3.4.1 Homogeneous Terrain

In this model, the probability density function (PDF) of the test statistics \bar{T} can be expressed by [31], [93], [98]

$$f_{\bar{T}}(\bar{t}) = \frac{\bar{t}^{n-1} \cdot e^{-\bar{t}}}{\Gamma(n)}, \quad (3.21)$$

where $\Gamma[\cdot]$ denotes the gamma function and $n = E\{\bar{T}\}$ the effective number of looks.

The test statistics can be normalized by its expectation (i.e., $T = \bar{T}/E\{\bar{T}\} = \bar{T}/n$), yielding the PDF [31], [93], [98]

$$f_T(t) = \frac{n^n}{\Gamma(n)} \cdot t^{n-1} \cdot e^{-n \cdot t}, \quad (3.22)$$

which follows a Chi-squared (χ^2) density function.

The cumulative distribution function (CDF) of the normalized test statistics T can be expressed by

$$\begin{aligned} F_T(t) &= \int_0^t f_T(x) dx = \int_0^t \frac{n^n}{\Gamma(n)} \cdot x^{n-1} \cdot e^{-n \cdot x} dx \\ F_T(t) &= \frac{n^n}{\Gamma(n)} \int_0^t x^{n-1} \cdot e^{-n \cdot x} dx. \end{aligned} \quad (3.23)$$

The integral on the right-hand side of Equation (3.23) can be solved by using the result 3.381-1 in [99], yielding the CDF

$$\begin{aligned} F_T(t) &= \frac{n^n}{\Gamma(n)} \cdot [n^{-n} \cdot \gamma(n, n \cdot t)] \\ F_T(t) &= \frac{\gamma(n, n \cdot t)}{\Gamma(n)}, \end{aligned} \quad (3.24)$$

where $\gamma[\cdot]$ denotes the incomplete gamma function.

Finally, the desired CFAR threshold η_{homo} for homogeneous terrain can be estimated according to

$$\eta_{\text{homo}} = \frac{t_0}{2 \cdot n}, \quad (3.25)$$

where t_0 denotes the abscissa value of the CDF given in Equation (3.24) at ordinate $(1 - P_{\text{fa}})$, and P_{fa} denotes the desired probability of false alarm.

Figure 3.10 shows the PDF and the CDF obtained for different effective number of looks n by using Equation (3.22) and Equation (3.24), respectively. Note that the PDF shown in **Figure 3.10a** tends to be exponentially distributed for $n = 1$ (i.e., no multilooking is considered).

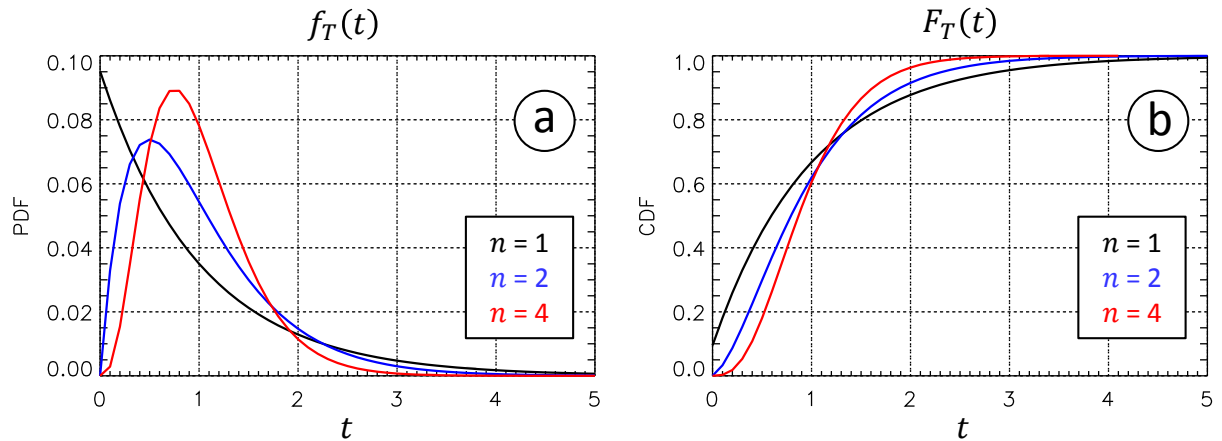


Figure 3.10. (a) PDF and (b) CDF of the homogeneous model for different effective number of looks.

3.4.2 Heterogeneous Terrain

In reality, the homogeneous clutter model presents limitations when the background reflectivity of the scene changes. For instance, a single scene may contain grassy and urban areas, together with cropping fields and regions of forests. Thus, it is important to introduce a texture parameter in the clutter model in order to describe the degree of heterogeneity of the terrain.

In the heterogeneous clutter model presented in [31], [93], [98], the effective number of looks n and a texture parameter ν need to be estimated from the training data. This texture parameter describes the degree of heterogeneity of the underlying terrain, i.e., the larger the texture parameter ν , the more homogeneous is the clutter (therefore, low values indicate strong heterogeneity).

The PDF of the adopted heterogeneous model follows a scaled F -distribution with $2n$, 2ν degrees of freedom (DoF) that is given by [31], [93], [98]

$$f_X(x) = \frac{\Gamma(n+\nu)}{\Gamma(n)\Gamma(\nu)} \cdot \left(\frac{n}{\nu-1}\right)^n \cdot \frac{x^{n-1}}{\left(1+\frac{n}{\nu-1}x\right)^{n+\nu}}. \quad (3.26)$$

The texture parameter ν can be estimated according to

$$\nu = \frac{2 \cdot n \cdot m_2 - (n+1)}{n \cdot m_2 - (n+1)}, \quad (3.27)$$

where $m_2 = \sum_i |x_i|^2$ is the estimated quadratic mean over all available samples.

It is pointed out that for $\nu > 20$, the F -distributed heterogeneous model expressed in Equation (3.26) converges to the χ^2 -distributed homogeneous model expressed in Equation (3.22).

The CDF can be expressed by

$$F_X(x) = \int_0^x f_X(y) dy = \int_0^x \frac{\Gamma(n+\nu)}{\Gamma(n)\Gamma(\nu)} \cdot \left(\frac{n}{\nu-1}\right)^n \cdot \frac{y^{n-1}}{\left(1+\frac{n}{\nu-1}y\right)^{n+\nu}} dy. \quad (3.28)$$

The integral on the right-hand side of Equation (3.28) can be solved by using the result 3.194-1 in [99], yielding the CDF [31], [93], [98]

$$F_X(x) = \frac{\Gamma(n+\nu)}{n \cdot \Gamma(n)\Gamma(\nu)} \cdot \left(\frac{x}{\nu-1}\right)^n \cdot {}_2F_1\left(n+\nu, n; n+1; -\frac{x}{\nu-1}\right), \quad (3.29)$$

where ${}_2F_1[\cdot]$ denotes the Gaussian hypergeometric function.

Finally, the desired CFAR threshold η_{hete} for heterogeneous terrain can be estimated according to

$$\eta_{\text{hete}} = \frac{x_0 \cdot (v-1)}{v}, \quad (3.30)$$

where x_0 denotes the abscissa value of the CDF given in Equation (3.29) at ordinate $(1 - P_{\text{fa}})$.

Figure 3.11 shows the data histogram of one CPI (2048 x 128 range-Doppler samples) processed from data take 4 (cf. Appendix A) along with the PDFs of the homogeneous and heterogeneous clutter models, computed by using (3.22) and (3.26), respectively. As it can be seen in this example, the heterogeneous model fits better to the measured data due to the use of a texture parameter [93], [31]. Besides, the estimated parameters are $n = 1.00$ (i.e., no multilooking was considered) and $v = 3.08$, which suggests a moderately heterogeneous terrain.

In reality, the texture parameter v changes over slant range and azimuth time. Some of the main real-world effects on the DLR's F-SAR data acquisition are shown in Chapter 7, including the clutter statistics change according to the texture parameter v .

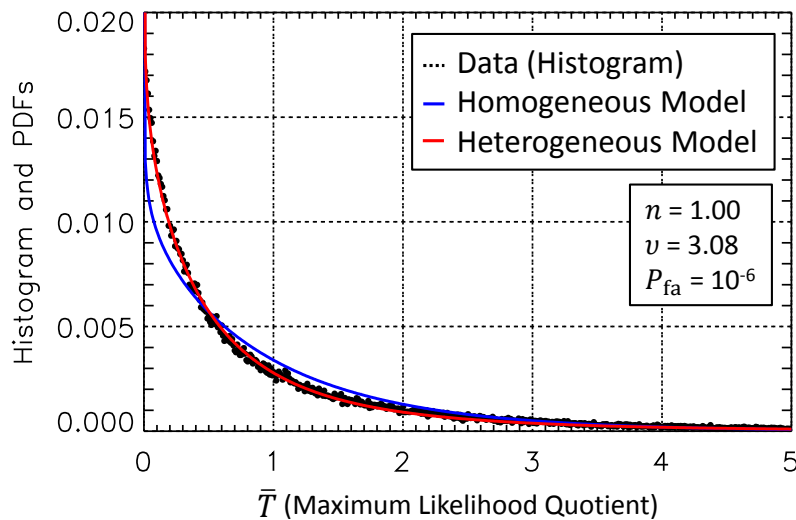


Figure 3.11. Data histogram of one CPI (2048 x 128 range-Doppler samples) along with the PDFs of the clutter models for homogeneous and heterogeneous terrains. The PDF of the heterogeneous model fits very well to the measured data, showing that this clutter model is indeed appropriate and accurate.

3.5 Performance Model

This section presents theoretical performance predictions of the PD STAP processor, such as: detection performance, achievable position and velocity estimation accuracy. This performance model is based on the framework presented in [89]. Part of the results presented in this section was already published in [59].

The performance investigations are carried out according to the parameters shown in **Table 3.1** [38], which is based on the DLR's F-SAR system (cf. Appendix A). In this table, it is assumed that the radar cross section (RCS) of the target is $\sigma_t = -5 \text{ dBm}^2$. It is shown in [100] that the σ_t of a common passenger car depends strongly on the incidence angle θ_i and on the asphalt's condition. For instance, the RCS of a Golf V vehicle can vary from -10 dBm^2 to 25 dBm^2 under wet asphalt ($\approx 0.5 \text{ mm}$ of water).

TABLE 3.1
F-SAR'S SYSTEM PARAMETERS USED FOR THE PERFORMANCE INVESTIGATIONS [38]

Parameter	Symbol	Value
Effective PRF (in AS mode)	PRF	2500 Hz
Platform velocity	v_p	90 m/s
Incidence angle	θ_i	45°
Range sampling frequency	f_r	100 MHz
Number of Channels	M	4
Transmit antenna length	L_a	0.3 m
Effective along-track baseline	d_a	0.1 m
Peak transmit power	P_t	63.2 dBm (= 2089 W)
TX antenna gain (measured)	G_{TX}	19.80 dBi
RX antenna gain (measured)	G_{RX}	16.00 dBi
Radar wavelength	λ	0.03122 m
TX pulse duration	τ_p	5 μ s
RCS	σ_t	-5 dBm ²
Clutter reflectivity	σ_0	-10 dB
Slant range of the target	R	3111 m
RX system noise temperature	T_0	293 K
System noise figure	F	5.66 dB
Losses (assumed for AS configuration)	L	2.5 dB
Boltzmann constant	k_B	$1.38064852 \times 10^{-23} \text{ J/K}$
Number of azimuth samples per CPI	$n_{a,CPI}$	128

3.5.1 SNR and CNR

The SNR and the clutter-to-noise ratio (CNR) are important input parameters of the performance model and can be estimated according to the radar equation [6]. In this sense, the single-channel SNR can be expressed by the approximation

$$SNR \cong \frac{P_t \cdot G_{TX} \cdot G_{RX} \cdot \lambda^2 \cdot \tau_p \cdot \sigma_t}{(4\pi)^3 \cdot R^4 \cdot k_B \cdot T_0 \cdot F \cdot L} \cdot n_{a,CPI} , \quad (3.31)$$

where P_t denotes the peak transmit power, G_{TX} and G_{RX} denote the gains of the TX and the single RX antenna, respectively, k_B denotes the Boltzmann constant, T_0 denotes the noise reference temperature, F denotes the system noise figure, L denotes the losses and $n_{a,CPI}$ denotes the number of azimuth temporal samples or pulses used for coherent integration (cf. Section 3.7).

The single-channel CNR can be expressed by the approximation

$$CNR \cong \frac{P_t \cdot G_{TX} \cdot G_{RX} \cdot \lambda^2 \cdot \tau_p \cdot \sigma_0 \cdot A_{res}}{(4\pi)^3 \cdot R^4 \cdot k_B \cdot T_0 \cdot F \cdot L} \cdot n_{a,CPI} , \quad (3.32)$$

where σ_0 denotes the normalized clutter reflectivity and A_{res} denotes the ground resolution cell size, which can be expressed by the approximation [38]

$$A_{res} \cong \frac{c_0}{\underbrace{2 \cdot B_r \cdot \sin \theta_i}_{\text{ground range resolution}}} \cdot \frac{\lambda \cdot R \cdot PRF}{\underbrace{2 \cdot v_p \cdot n_{a,CPI}}_{\text{azimuth resolution}}} . \quad (3.33)$$

By applying the parameters from **Table 3.1** in Equation (3.31) and in Equation (3.32), it is obtained $SNR = 25.02$ dB and $CNR = 33.51$ dB.

3.5.2 Detection Performance

The theoretical covariance matrix under the assumption of homogeneous (Gaussian) clutter can be expressed by [89]

$$\mathbf{R}_W(u_{\text{array}}, f_a) = \sigma_n^2 \cdot \mathbf{I}_M + \sum_{\kappa} \sigma_{\kappa}^2 \cdot \mathbf{d}(u_{\kappa}, f_a) \cdot \mathbf{d}(u_{\kappa}, f_a)^H, \quad (3.34)$$

where σ_n^2 denotes the additive thermal noise power assumed statistically white, \mathbf{I}_M denotes the identity matrix with dimensions $M \times M$ and σ_{κ}^2 denotes the clutter power contributions coming from the directions

$$u_{\kappa} = \frac{\lambda \cdot f_a}{2 \cdot v_p} + \frac{\lambda \cdot \text{PRF} \cdot \kappa}{2 \cdot v_p}, \quad (3.35)$$

where κ is an integer number. The sum over κ comprises the clutter ambiguities that may cause severe impacts in case of a low PRF [101].

The signal-to-clutter plus noise ratio (SCNR) of the optimum filter can be expressed by [89]

$$\text{SCNR}(u_{\text{array}}, f_a) = |a_s|^2 \cdot \mathbf{d}(u_{\text{array}}, f_a) \cdot \mathbf{R}_W^{-1}(u_{\text{array}}, f_a) \cdot \mathbf{d}(u_{\text{array}}, f_a)^H. \quad (3.36)$$

The SCNR is directly related to the detection performance. Therefore, if the SCNR is known, the probability of detection P_d can be computed for a desired probability of false alarm rate P_{fa} . In this case, assuming homogeneous Gaussian clutter and non-fluctuating target RCS (Swerling case 0), the probability of detection as a function of the SCNR can be expressed by [102], [82]

$$\begin{aligned} P_d(u_{\text{array}}, f_a) &= \int_{\beta_T}^{\infty} x \cdot \exp\left[-\frac{(x^2 + \alpha(u_{\text{array}}, f_a)^2)}{2}\right] \cdot I_0[\alpha(u_{\text{array}}, f_a) \cdot x] dx \\ &= 1 - \int_0^{\beta_T} x \cdot \exp\left[-\frac{(x^2 + \alpha(u_{\text{array}}, f_a)^2)}{2}\right] \cdot I_0[\alpha(u_{\text{array}}, f_a) \cdot x] dx, \end{aligned} \quad (3.37)$$

where $I_0[\cdot]$ denotes the modified zero-order Bessel function of the first kind with

$$\alpha(u_{\text{array}}, f_a)^2 = 2 \cdot \text{SCNR}(u_{\text{array}}, f_a). \quad (3.38)$$

Finally, the normalized detection threshold can be estimated by

$$\beta_T = \sqrt{-2 \cdot \ln P_{\text{fa}}}. \quad (3.39)$$

Analytical descriptions for computing the probability of detection for different clutter PDF's and Swerling cases are available in [103].

3.5.3 Position and Velocity Estimation Accuracy

The standard deviation of the azimuth position can be obtained from the Cramér-Rao bound (CRB), which is computed by using the Fisher information matrix [89]

$$\sigma_x(u_{\text{array}}, v_{r0}) = \sigma_u(u_{\text{array}}, v_{r0}) \cdot R = \sqrt{\frac{1}{|a_s|^2} \cdot \frac{\mathbf{d}^H \mathbf{R}_W^{-1} \mathbf{d}}{\mathbf{d}^H \mathbf{R}_W^{-1} \mathbf{d} \mathbf{d}_u^H \mathbf{R}_W^{-1} \mathbf{d}_u - |\mathbf{d}_u^H \mathbf{R}_W^{-1} \mathbf{d}|^2}} \cdot R, \quad (3.40)$$

where \mathbf{d}_u is the first derivative of the beamforming vector \mathbf{d} with respect to u and σ_u is the standard deviation of the directional cosine obtained from the CRB, which is important for the target's positioning error model (cf. Section 5.2).

In the clutter free case (where only noise remains), the minimum azimuth positioning error obtained from the CRB can be expressed by [101]

$$\sigma_{x,\text{min}}(u_{\text{array}}, v_{r0}) = \sqrt{\frac{1}{8\pi^2 \cdot \text{SNR} \cdot \sum_m x_m^2}} \cdot R \cdot \lambda, \quad (3.41)$$

where the single-channel SNR after coherent integration is considered.

Finally, the standard deviation of the line-of-sight velocity can be expressed by

$$\sigma_{vr}(u_{\text{array}}, v_{r0}) = \left| -\frac{v_p}{R} \right| \cdot \sigma_x(u_{\text{array}}, v_{r0}). \quad (3.42)$$

3.5.4 Simulation Results

The results shown in this section were obtained using the parameters from Table 3.1. **Figure 3.12a** shows the expected output SCNR of the optimum PD STAP processor, considering four RX channels, zero squint angle and $\sigma_n^2 = 0$ dB. **Figure 3.12b** shows a cut over the platform's broadside direction ($\Psi_{\text{DOA},\text{az}} = \Psi_{\text{DOA},\text{array}} = 90^\circ$), where the notches obtained around ± 39 m/s indicate the blind line-of-sight velocities (cf. Section 3.6.2). Targets moving at such velocities are suppressed like clutter and thus generally cannot be detected. A higher PRF would be required for avoiding such blind velocities, whereas $PRF = 2500$ Hz is currently the maximum in the four-channel AS mode of the F-SAR. In the dual-channel mode, $PRF = 5000$ Hz is possible [38].

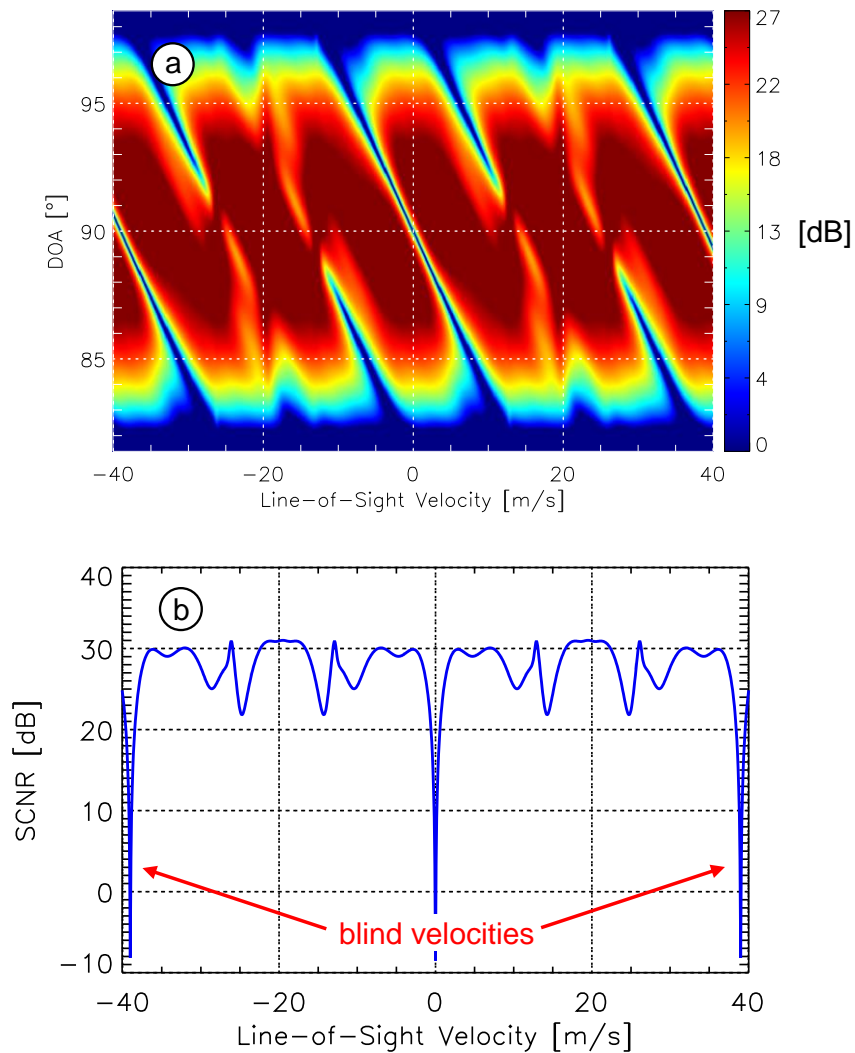


Figure 3.12. (a) SCNR and (b) a cut over the broadside direction of the antenna array ($\Psi_{\text{DOA},\text{array}} = 90^\circ$) showing the blind velocities obtained in slant range (cf. Section 3.6.2).

Figure 3.13a shows the probability of detection P_d over SCNR, considering four RX channels and $P_{fa} = 10^{-6}$. **Figure 3.13b** shows a cut over the platform's broadside direction, where the minimum detectable velocity (MDV) is in the order of 0.28 m/s for achieving a probability of detection of $P_d = 0.9$. It is shown in [38] that the MDV obtained for the dual-channel F-SAR configuration is in the order of 0.7 m/s, which would be sufficient for detecting slow moving cars.

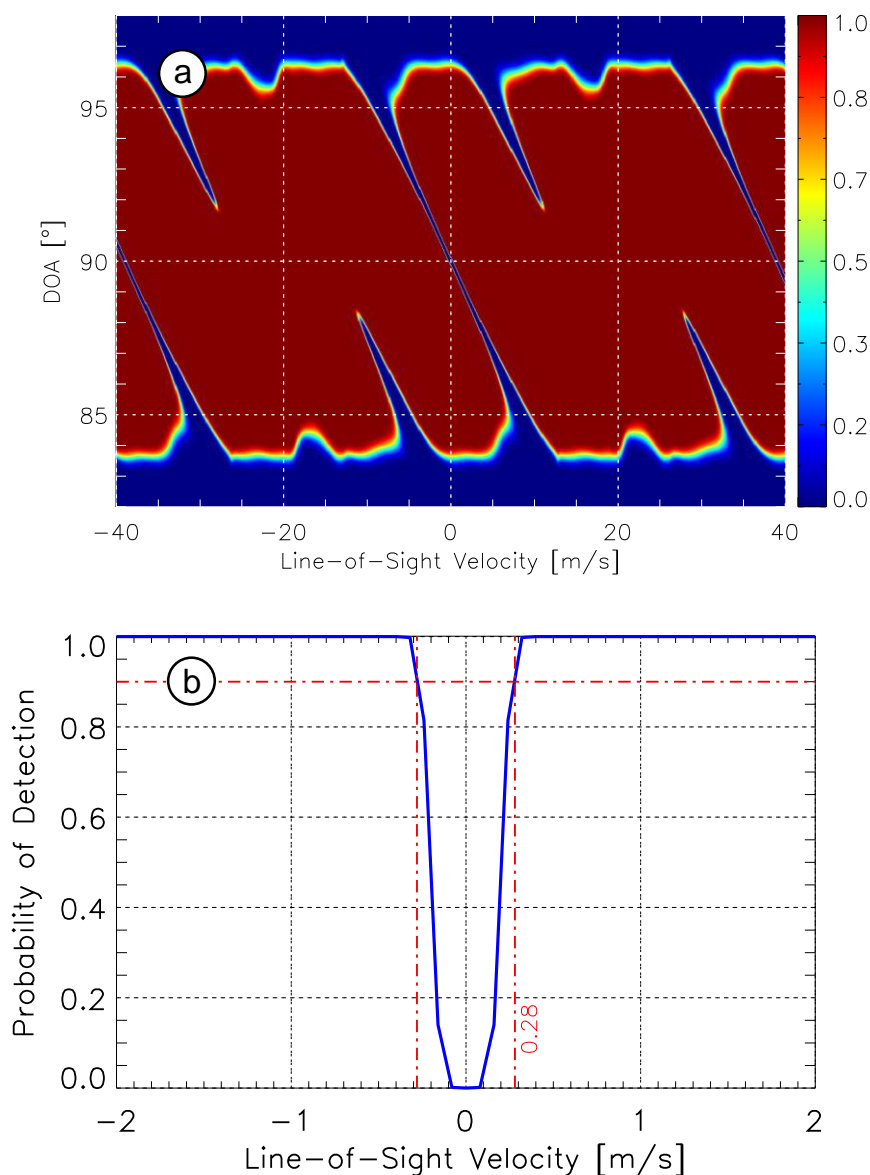


Figure 3.13. (a) Probability of detection over SCNR considering four RX channels and $P_{fa} = 10^{-6}$; (b) cut over the broadside direction showing the minimum detectable velocity obtained in the order of 0.28 m/s for $P_d = 0.9$.

Figure 3.14a shows the standard deviation of the azimuth position σ_x , considering four RX channels. **Figure 3.14b** shows a cut over the platform's broadside direction, where the minimum azimuth positioning error is $\sigma_{x,\min} = 1.37$ m and the maximum azimuth positioning error is in the order of 15 m. In this case, it is shown in [38] that a dramatic performance improvement is obtained if more than two RX channels are used. For instance, it is shown in [38] that the maximum azimuth positioning error obtained for the dual-channel F-SAR configuration is in the order of 145 m (i.e., a factor of approximately 9.5 worse compared to the four-channel case).

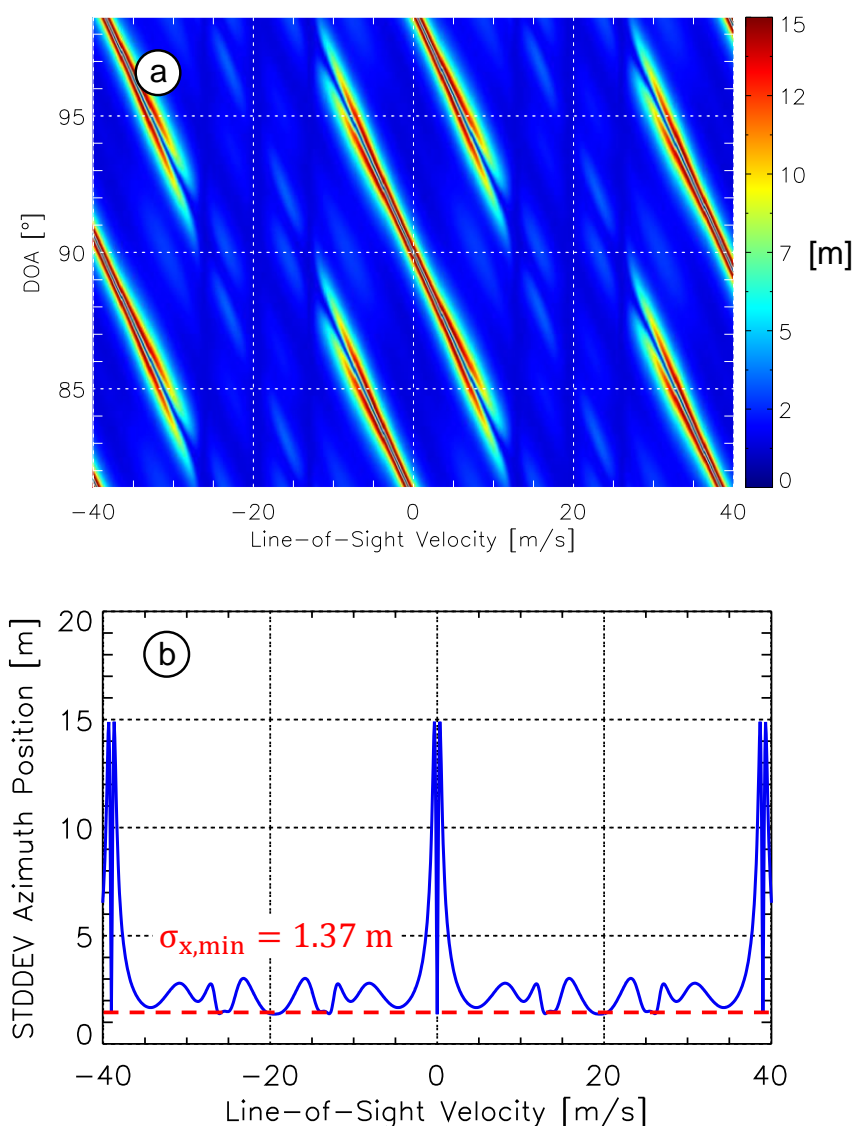


Figure 3.14. (a) Standard deviation of the azimuth position considering four RX channels; (b) cut over the broadside direction showing the minimum azimuth positioning error obtained in the order of 1.37 m.

Figure 3.15a shows the standard deviation of the line-of-sight velocity σ_{vr} , considering four RX channels. Indeed, it can be noticed that the obtained result is a scaled version of the standard deviation of the azimuth position σ_x . **Figure 3.15b** shows a cut over the platform's broadside direction, where the maximum line-of-sight velocity error is in the order of 0.45 m/s (or 1.62 km/h).

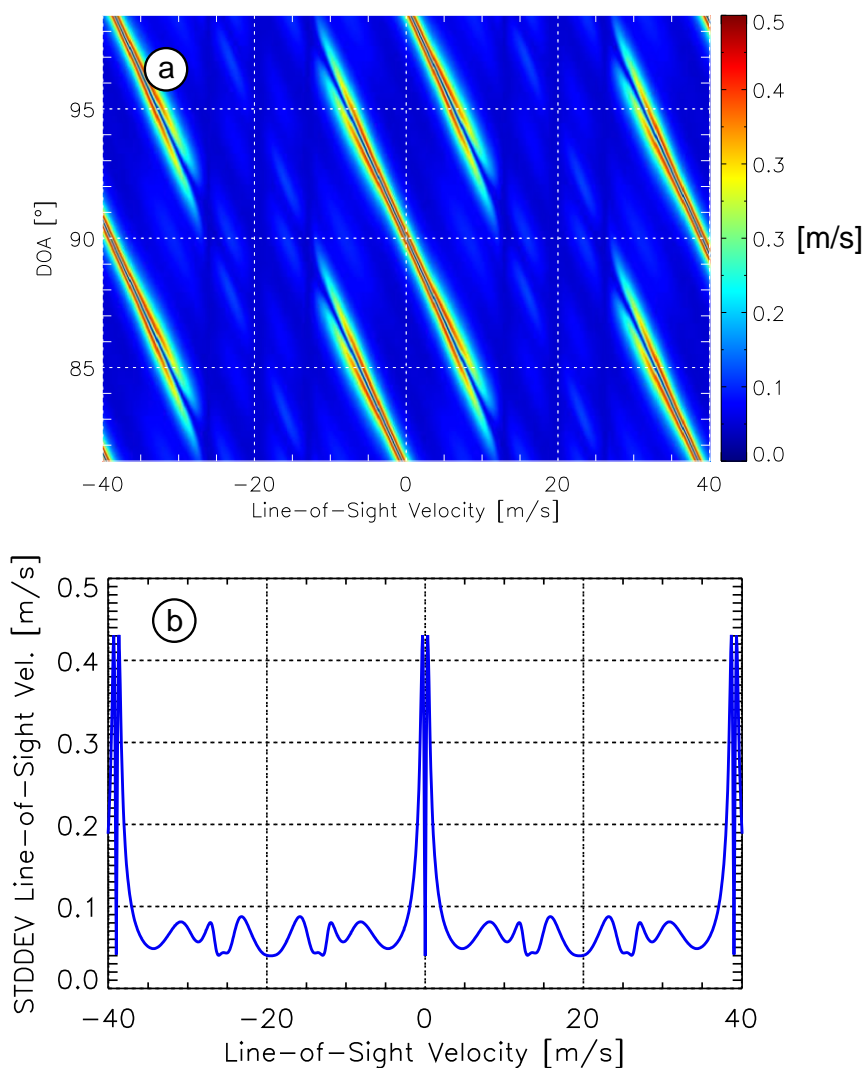


Figure 3.15. (a) Standard deviation of the line-of-sight velocity considering four RX channels; (b) cut over the broadside direction showing the maximum error obtained of 0.45 m/s (\cong 1.62 km/h).

The performance model provides the expected errors in an optimal case, whereas additional error sources still need to be taken into account (e.g., the antenna's pointing direction, the road axes uncertainties, the DEM's accuracy, among others). Such error sources are included in the positioning error models that are presented in Chapter 5.

3.6 Main Limitations

3.6.1 DOA Angle Ambiguities

Figure 3.16 shows the acquisition geometry of a tilted array with three RX channels, where the reference channel RX2 is located at the origin of the antenna array and the physical separation between two adjacent RX antenna centers are given by

$$b_a = 2 \cdot d_a , \quad (3.43)$$

where d_a denotes the effective along-track baseline.

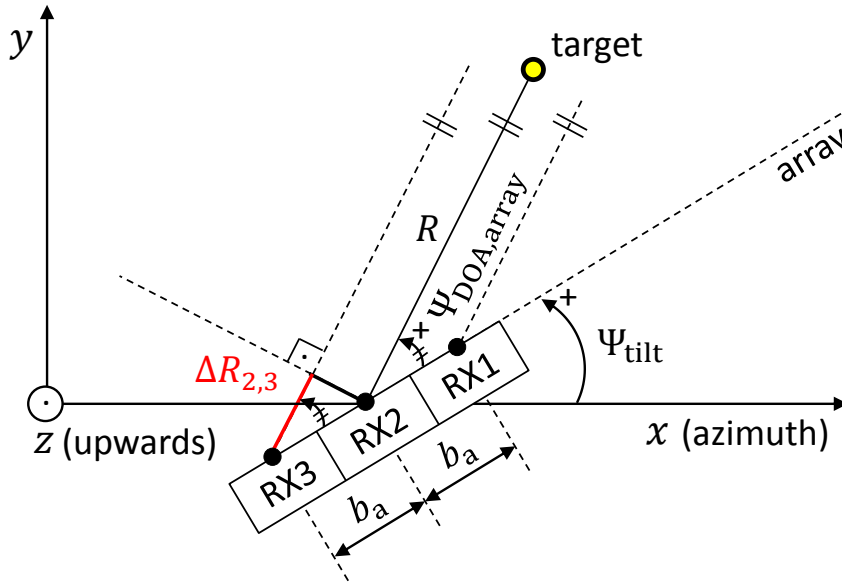


Figure 3.16. Simplified top-view geometry of a tilted array with three RX channels. For instance, the range difference $\Delta R_{2,3}$ (i.e., between RX2 and RX3) is highlighted in red.

In this example, the range difference between RX2 and RX3 is given by

$$\Delta R_{2,3} = b_a \cdot \cos \Psi_{\text{DOA,array}} , \quad (3.44)$$

with respective interferometric phase

$$\phi_{2,3} = -\frac{2 \cdot \pi}{\lambda} \cdot \Delta R_{2,3} . \quad (3.45)$$

Therefore,

$$\phi_{2,3} = -\frac{2\cdot\pi}{\lambda} \cdot b_a \cdot \cos \Psi_{\text{DOA,array}} = -\frac{2\cdot\pi}{\lambda} \cdot b_a \cdot u_{\text{array}} . \quad (3.46)$$

The directional cosine ambiguities are obtained at every 2π change in the interferometric phase (i.e., $\phi_{2,3} = 2\pi \cdot i$, $i \in \mathbb{Z}$), so that

$$u_{\text{array,amb}} = -\frac{\lambda}{b_a} \cdot i , i \in \mathbb{Z} . \quad (3.47)$$

Thus, the DOA angle ambiguities can be expressed by

$$\Psi_{\text{DOA,array,amb}} = \cos^{-1}(u_{\text{array,amb}}) = \cos^{-1}\left(-\frac{\lambda}{b_a} \cdot i\right), i \in \mathbb{Z} . \quad (3.48)$$

These DOA angle ambiguities can be verified on the simulated data results shown in **Figure 3.17**. In this case, the parameters from **Table 3.1** are used and it is considered a moving target with line-of-sight velocity $v_r = 10$ m/s, $\sigma_t = 10$ dBm², $b_a = 0.2$ m, zero squint angle and homogeneous ground clutter.

Figure 3.17a shows the output of the test statistics \bar{T} obtained according to Equation (3.6), where it can be noticed how the signal power of the moving target (located at the broadside direction $\Psi_{\text{DOA,array}} = 90^\circ$) changes according to a wide DOA angle span. In this case, the estimated CFAR detection threshold is $\eta_{\text{hete}} = 8.39$ and the target's Doppler frequency is

$$f_a = -\frac{2}{\lambda} \cdot v_r = -\frac{2}{0.03125} \cdot 10.00 = -640.00 \text{ Hz} . \quad (3.49)$$

Figure 3.17b shows a cut at the moving target's Doppler frequency, from where the first DOA angle ambiguities can be observed

$$\Psi_{\text{DOA,array,amb}}^{i=1} = \cos^{-1}\left(-\frac{0.03125}{0.2}\right) \cong 99^\circ , \quad (3.50)$$

$$\Psi_{\text{DOA,array,amb}}^{i=-1} = \cos^{-1}\left(\frac{0.03125}{0.2}\right) \cong 81^\circ . \quad (3.51)$$

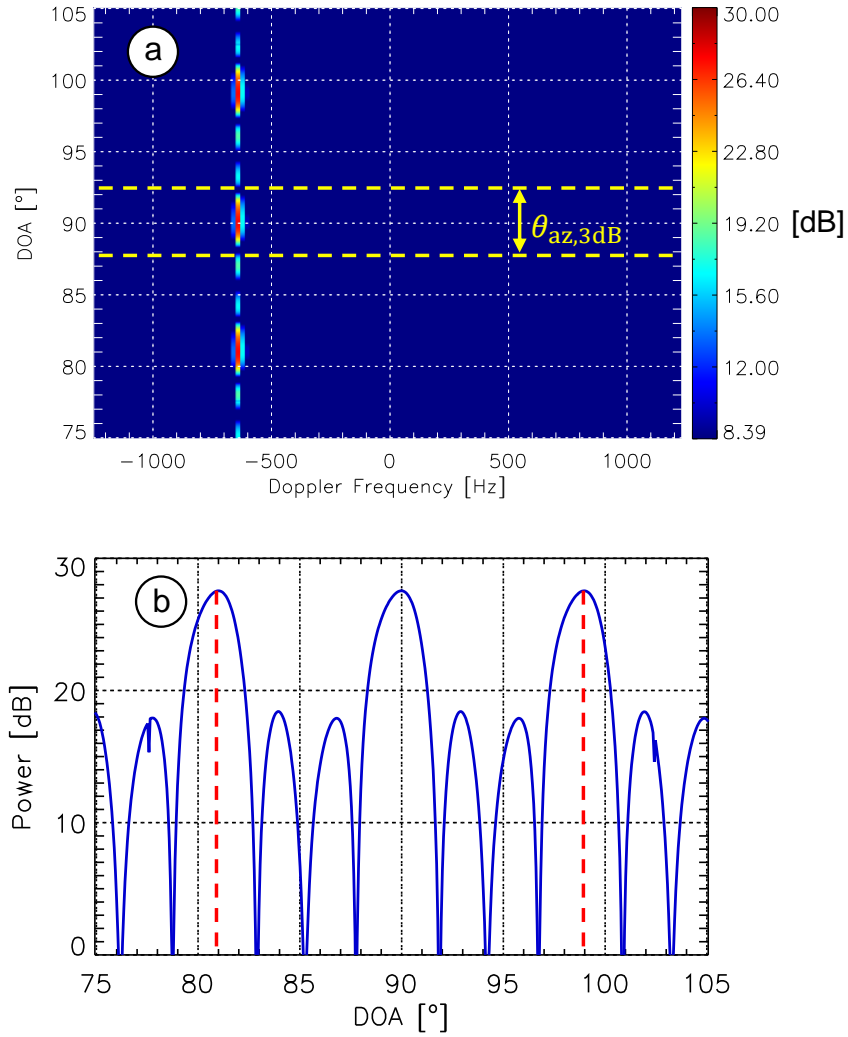


Figure 3.17. DOA angle ambiguities obtained from simulated data: (a) test statistics \bar{T} (color bar limited to the estimated CFAR threshold $\eta_{\text{hete}} = 8.39$) and (b) a cut at the moving target's Doppler frequency ($f_a = -640$ Hz), where the red lines show the peaks of the DOA ambiguities.

An effective approach to deal with the DOA angle ambiguities consists in limiting the beamforming operation given in Equation (3.9) to the DOA angles defined within the 3 dB beamwidth in azimuth $\theta_{\text{az},3\text{dB}} = 5.25^\circ$, as shown in **Figure 3.17a** (yellow lines).

3.6.2 Blind Velocities

The PD STAP is affected by a comb of blind line-of-sight velocities that are given by [104]

$$v_{r,\text{blind}} = \frac{\lambda \cdot \text{PRF}}{2} \cdot i, i \in \mathbb{N}. \quad (3.52)$$

Targets moving at such blind velocities are suppressed like clutter and therefore they may not be detected. As it can be seen in Equation (3.52), such blind velocities can be changed by adjusting either the PRF or the radar wavelength λ . As an example, the blind velocities observed in **Figure 3.12b** (using the parameters from **Table 3.1**) are

$$v_{r,\text{blind}}^{i=1} = \frac{(0.03125) \cdot (2500)}{2} \cong 39 \text{ m/s} , \quad (3.53)$$

$$v_{r,\text{blind}}^{i=-1} = -\frac{(0.03125) \cdot (2500)}{2} \cong -39 \text{ m/s} . \quad (3.54)$$

3.7 Coherent Processing Interval Length

This section sheds light on the number of temporal azimuth samples that can be used for the CPIs processed by the PD STAP processor (without the need for performing RCMC). The mathematical derivations contained in this section are based on the framework presented in [36]. **Figure 3.18** shows the slant range history $R(t)$ as well as the Doppler frequency history $f_a(t)$ for the particular case of a stationary point-like target (i.e., zero Doppler centroid).

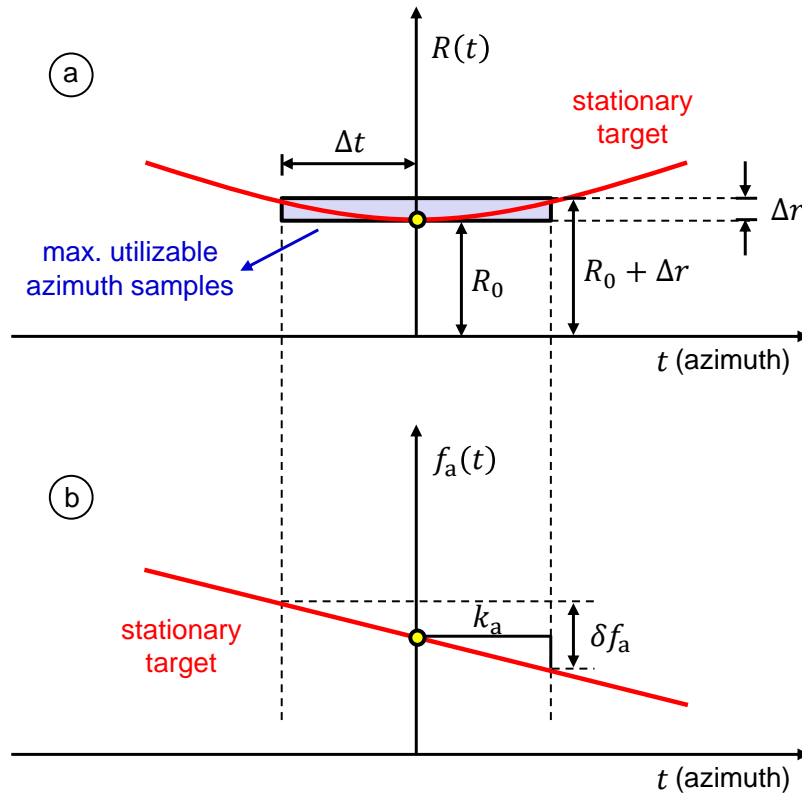


Figure 3.18. (a) Range and (b) Doppler frequency history of a stationary point-like target.

In **Figure 3.18a**, it is depicted in blue the maximum number of azimuth temporal samples where the target signal remains within one pixel spacing in slant range Δr . The maximum number of azimuth samples corresponds to the maximum CPI length.

The pixel spacing in slant range Δr is given by

$$\Delta r = \frac{c}{2 \cdot f_r}, \quad (3.55)$$

where f_r denotes the range sampling frequency. The maximum number of utilizable azimuth samples that contain information about the target is given by

$$n_{a,CPI,max} = 2 \cdot PRF \cdot |\Delta t|, \quad (3.56)$$

where Δt is the time interval where the range migration is contained in one pixel spacing in range Δr . For the particular case of a stationary point-like target (i.e., zero Doppler centroid), Δt can be approximated as [36]

$$\Delta t \cong \sqrt{\frac{R_0 \cdot c}{v_p^2 \cdot f_r}}. \quad (3.57)$$

By using the F-SAR parameters from **Table 3.1** and $R_0 = 3111$ m, it is obtained $n_{a,CPI,max} \cong 5366$ samples. In this particular case, several azimuth samples contain information about the stationary point-like target since the RCM is less pronounced. However, in reality the target's range history $R(t)$ is velocity dependent and therefore $n_{a,CPI,max}$ varies according to the target's velocity and heading angle [36].

The CPI containing the desired number of azimuth samples $n_{a,CPI} \leq n_{a,CPI,max}$ can be expressed as [35]

$$T_{CPI} = \frac{n_{a,CPI}}{PRF} = \frac{1}{\Delta f_a}, \quad (3.58)$$

where $\Delta f_a = PRF/n_{a,CPI}$ is the Doppler frequency resolution, which needs to be fine enough for ensuring accurate estimation of the moving target parameters. The impact of the Doppler frequency resolution on the accuracy of the moving target's line-of-sight velocity v_r is presented in Section 3.8.

In **Figure 3.18b**, the linear approximation of the Doppler frequency history can be expressed as [7]

$$f_a(t) \cong \left(-\frac{2 \cdot v_p^2}{\lambda \cdot R_0} \right) \cdot t = k_a \cdot t . \quad (3.59)$$

It is pointed out that the Doppler frequency history varies linearly along the azimuth time t with either a positive or a negative angular coefficient depending on the sign of the Doppler slope k_a .

Finally, the Doppler frequency spread (or Doppler bandwidth) can be expressed as a function of T_{CPI} according to the approximation

$$\delta f_a \cong |k_a| \cdot T_{CPI} = |k_a| \cdot \frac{n_{a,CPI}}{PRF} , \quad (3.60)$$

where $\delta f_a \leq \Delta f_a$. It is pointed out that this approximation only leads to small errors if $|k_a| \gg 0$ [36], which is generally true.

It is assumed in this doctoral thesis that $n_{a,CPI} = 128$ samples. Therefore, by using the parameters shown in **Table 3.1.**, it is obtained

$$\Delta f_a = \frac{PRF}{n_{a,CPI}} = \frac{2500}{128} \cong 19.53 \text{ Hz} , \quad (3.61)$$

$$\delta f_a = |k_a| \cdot \frac{n_{a,CPI}}{PRF} = \left| -\frac{2 \cdot v_p^2}{\lambda \cdot R_0} \right| \cdot \frac{n_{a,CPI}}{PRF} = \left| -\frac{2 \cdot 90^2}{0.03122 \cdot 3111} \right| \cdot \frac{128}{2500} \cong 8.53 \text{ Hz} , \quad (3.62)$$

which satisfy the condition $\delta f_a \leq \Delta f_a$.

3.8 Position and Velocity Errors

The coordinates of the moving target in azimuth can be expressed as (cf. **Figure 3.5**)

$$\begin{aligned} x_t &= x_p + R \cdot \cos(\Psi_{\text{DOA,az}}) = x_p + R \cdot \cos(\Psi_{\text{DOA,array}}) \\ x_t &= x_p + R \cdot u_{\text{array}}, \end{aligned} \quad (3.63)$$

where zero squint angle is considered for simplicity (i.e., $\Psi_{\text{DOA,array}} = \Psi_{\text{DOA,az}}$).

The maximum error of the target's position in azimuth due to the directional cosine resolution Δu_{array} can be obtained according to the error propagation model

$$\Delta x_t = \left| \frac{\partial x_t}{\partial u_{\text{array}}} \right| \cdot \Delta u_{\text{array}}, \quad (3.64)$$

which results in

$$\Delta x_t = R \cdot \Delta u_{\text{array}}. \quad (3.65)$$

By assuming that $\Delta u_{\text{array}} = 0.001$ and $R = 3111$ m, it is obtained

$$\Delta x_t = 3.11 \text{ m}. \quad (3.66)$$

Therefore, it can be seen that the choice of the directional cosine resolution Δu_{array} (applied in the beamforming operation expressed in Equation (3.9)) plays an important role in the accuracy of the target's position in azimuth.

The line-of-sight velocity v_r of the target can be estimated according to Equation (3.18), which is repeated below for convenience [82]

$$v_r = u_{\text{array}} \cdot v_p - \frac{\lambda}{2} \cdot (f_a - f_{\text{DC}}). \quad (3.67)$$

The maximum error of the target's line-of-sight velocity Δv_r due to the Doppler frequency resolution Δf_a and the directional cosine resolution Δu_{array} can be obtained according to the error propagation model

$$\Delta v_r = \left| \frac{\partial v_r}{\partial u_{\text{array}}} \right| \cdot \Delta u_{\text{array}} + \left| \frac{\partial v_r}{\partial f_a} \right| \cdot \Delta f_a , \quad (3.68)$$

which results in

$$\Delta v_r = |v_p| \cdot \Delta u_{\text{array}} + \left| \frac{\lambda}{2} \right| \cdot \Delta f_a . \quad (3.69)$$

By assuming that $\Delta u_{\text{array}} = 0.001$, $\Delta f_a = 19.53$ Hz (obtained from Equation (3.61)), $v_p = 90$ m/s and $\lambda = 0.03122$ m, it is obtained

$$\Delta v_r = (90 \cdot 0.001) + \left(\left[\frac{0.03122}{2} \right] \cdot 19.53 \right) \cong 0.39 \text{ m/s} \cong 1.40 \text{ km/h} . \quad (3.70)$$

The absolute velocity of the target on the road v_{road} can be obtained by applying Equation (3.67) into Equation (3.19) [36], [63]

$$v_{\text{road}} = \left| \frac{v_r}{\sin(\theta_i) \cdot \sin(\alpha_{r,az})} \right| = \left| \frac{2 \cdot u_{\text{array}} \cdot v_p - \lambda \cdot (f_a - f_{\text{DC}})}{2 \cdot \sin(\theta_i) \cdot \sin(\alpha_{r,az})} \right| . \quad (3.71)$$

The maximum error of the target's absolute velocity on the road Δv_{road} due to the Doppler frequency resolution Δf_a and the directional cosine resolution Δu_{array} can be obtained according to the error propagation model

$$\Delta v_{\text{road}} = \left| \frac{\partial v_{\text{road}}}{\partial f_a} \right| \cdot \Delta f_a + \left| \frac{\partial v_{\text{road}}}{\partial u_{\text{array}}} \right| \cdot \Delta u_{\text{array}} , \quad (3.72)$$

which results in

$$\Delta v_{\text{road}} = \left| \frac{-\lambda}{2 \cdot \sin(\theta_i) \cdot \sin(\alpha_{r,az})} \right| \cdot \Delta f_a + \left| \frac{v_p}{\sin(\theta_i) \cdot \sin(\alpha_{r,az})} \right| \cdot \Delta u_{\text{array}} . \quad (3.73)$$

Figure 3.19 shows the simulation results obtained from Equation (3.73) for near range and far range (i.e., $\theta_i = 20^\circ$ and $\theta_i = 63^\circ$, respectively, cf. Table A.2 in Appendix A). In this simulation, the same parameters from Equation (3.70) were assumed and the vehicle heading span was $\alpha_{r,az} = [0^\circ, 180^\circ]$. As it can be seen, the velocity resolution Δv_{road} degrades as the vehicle tends to move parallel ($\alpha_{r,az} \rightarrow 0^\circ$) or anti-parallel ($\alpha_{r,az} \rightarrow 180^\circ$) with respect to the azimuth or flight direction. Indeed, vehicles moving at such directions can even hardly be detected since their line-of-sight velocities are normally lower than the MDV and therefore they are suppressed like the clutter.

In addition, it can be seen from **Figure 3.19** that in far range ($\theta_i = 63^\circ$) the achievable velocity resolution for a vehicle heading from 9° to 171° is better than 10 km/h. Notice that the velocity resolution degrades for steeper incidence angles. In the near range ($\theta_i = 20^\circ$), the achievable velocity resolution is better than 10 km/h only in the vehicle heading range from 24° to 155° . Thus, if the velocity resolution of 10 km/h is sufficient for fulfilling the requirements of the traffic monitoring application, the results shown in this section are very promising.

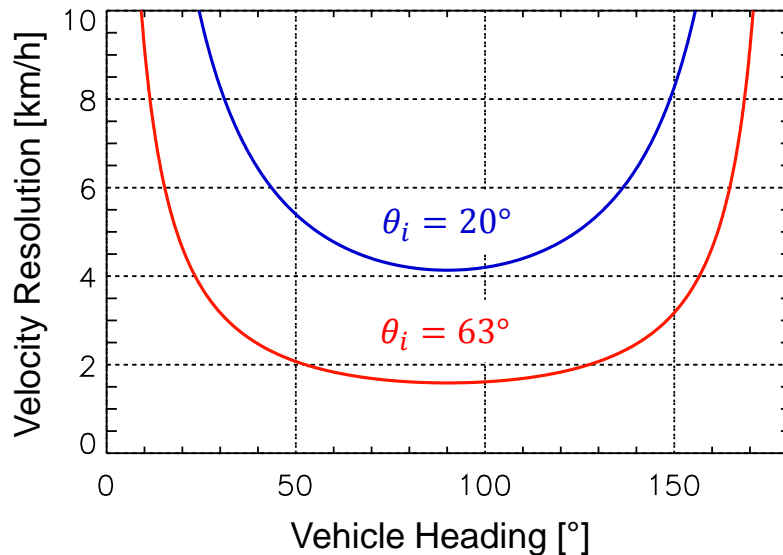


Figure 3.19. Maximum error of the target's absolute velocity on the road Δv_{road} for different heading angles $\alpha_{r,az}$, considering the near range (in blue) and far range (in red) of the F-SAR data acquisition (cf. Appendix A). The Doppler frequency resolution $\Delta f_a = 19.53$ Hz was obtained by considering $PRF = 2500$ Hz and $n_{a,CPI} = 128$ samples.

3.9 Chapter Summary

The PD STAP technique processes one CPI at a time in range-Doppler domain. The ground clutter cancellation is performed by using a CCM that is estimated from measured training data (ideally) free of strong discrete scatterers and moving target signals. The moving target detection is carried out based on a CFAR threshold that is estimated according to a heterogeneous ground clutter model. The PD STAP basically estimates the moving target's line-of-sight velocity, Doppler frequency and DOA angle, which are all related in Equation (3.18). The moving target's position can be obtained from the DOA angle. The moving target's absolute velocity on the road and moving direction can be obtained by combining the PD STAP with an a priori known road database (e.g., the OSM) so that the angles of the roads of interest are known. The performance model allows obtaining important theoretical predictions of the PD STAP processor, such as blind velocities, MDV, azimuth positioning error, among others. The PD STAP technique is affected by DOA and Doppler ambiguities depending on the system parameters (e.g., PRF, radar wavelength and the along-track baselines).

4 PD STAP Processor with Different Modes

4.1 Chapter Overview

This chapter presents three operational modes that are possible with the novel PD STAP processor. The basic ideas of all operational modes are depicted in **Figure 4.1**. The first operational mode (cf. **Figure 4.1a**) comprises the conventional PD STAP processor without a priori knowledge information, where the targets are detected but not relocated to the roads of interest. The second operational mode (cf. **Figure 4.1b**) uses a priori knowledge information for assigning the moving vehicles to their correct positions on the roads and for discarding the detections that lie far from the roads, considered as false detections. The third operational mode (cf. **Figure 4.1c**) is a faster processing version of the second mode, where only the relevant data around the roads are selected to be processed by the PD STAP core. In this case, a reduced number of detections can be expected since only a part of the available SAR data is processed. One possible solution for increasing the number of detections consists in processing the selected data using multiple DOA angles (cf. Section 4.4), whereas at the expense of an increased computational time. All operational modes are presented in terms of structure and main applications.

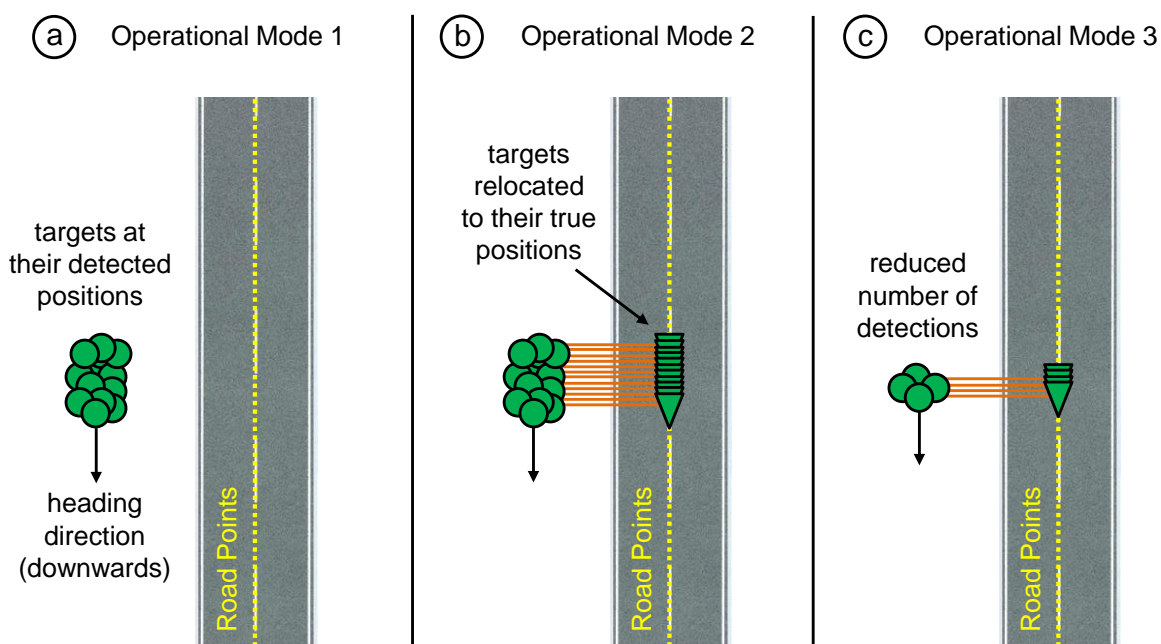


Figure 4.1. Basic ideas of all operational modes of the novel PD STAP processor.

4.2 Mode 1: Conventional PD STAP

The first operational mode comprises the conventional PD STAP (i.e., without a priori knowledge information), which is able to detect and to estimate the positions and line-of-sight velocities of the moving targets. The simplified flowchart of this processor is shown in **Figure 4.2**. It is pointed out that this structure is the basis of the operational modes 2 and 3 (cf. Section 4.3 and Section 4.4).

The PD STAP works directly on multi-channel RC data (i.e., after pulse compression). The first step consists in obtaining the navigation data of the aircraft from the IMU system (e.g., position, velocity, heading and attitude angles: yaw, pitch and roll) as well as the radar system parameters, which are required in the whole processing chain.

The *Data Calibration* block corrects not only the offsets due to residual ATI phases and magnitudes of the RX channels, but also the Doppler centroid over slant range and time by using the attitude angles of the antenna array. The calibration algorithm is essential for detecting the moving targets and for estimating their positions and velocities accurately. It is presented in detail in Chapter 6.

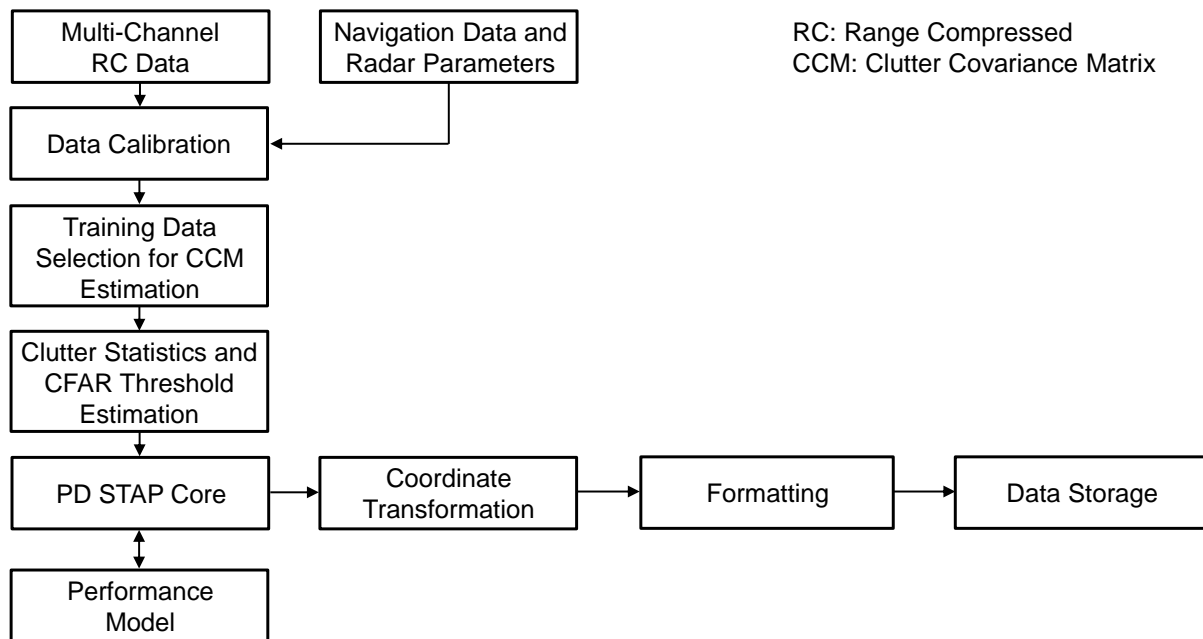


Figure 4.2. Simplified flowchart of the first operational mode of the PD STAP processor.

The *Training Data Selection and CCM Estimation* block collects training data free of moving targets and strong discrete signals for the CCM estimation. The quality of the training data impacts directly on the PD STAP performance since the CCM is used for clutter cancellation, so that this operation is of great importance. Some strategies for training data selection and update are presented and discussed in detail in Chapter 7.

The *PD STAP Core* is the hearth of the processing chain and has to accomplish three main tasks: 1) the clutter cancellation using the previously estimated CCM (i.e., $\hat{\mathbf{R}}_W$); 2) the moving target detection using the previously estimated clutter statistics \bar{T} and CFAR threshold η_{hete} (cf. Section 3.4); and 3) the estimation of the moving target's position and line-of-sight velocity. The mathematical framework for carrying out these main tasks is presented in detail in Chapter 3.

The *Performance Model* block provides the GMTI performance of the optimum PD STAP processor, including theoretical predictions of the detection performance, blind velocities, MDV, azimuth positioning error, among others. Some of the performance results were already presented in [59] based on the framework presented in [89]. The performance model is presented in detail in Section 3.5.

In the *Coordinate Transformation* block, the positions of the moving targets are obtained in both spherical and UTM Cartesian coordinate systems with respect to the World Geodetic System 1984 (WGS84) reference ellipsoid (i.e., latitude, longitude and elevation).

In the *Formatting* block, Keyhole Markup Language (KML) files [105] are generated containing several parameters of the moving targets that can be visualized in Google Earth [106], [107], such as: spherical and UTM coordinates, velocities, heading directions, SCNRs, Doppler frequencies, among others. Finally, the traffic data are stored in the mass memory and can be distributed to a traffic management center via data link [16].

The conventional PD STAP processor is especially suitable for military applications and for areas where road information is unavailable because it detects also vehicles

moving off-road (note that such off-road vehicles are discarded as false detections in the operational modes 2 and 3). It is pointed out that the current implementation has no real-time capability because the complete radar data need to be processed by the PD STAP processor.

Theoretically, it has limited performance for detecting vehicles moving on roads that are parallel or nearly parallel to the flight direction. Indeed, the line-of-sight velocities of such vehicles are generally lower than the MDV (cf. Section 3.5) and therefore they are suppressed like the stationary ground clutter. This limitation exists for all operational modes described in this chapter, as well as for MTI algorithms with clutter suppression based on STAP or DPCA.

4.3 Mode 2: A Priori Knowledge-Based PD STAP

There are different approaches for combining the PD STAP with a priori knowledge information [63]. In the operational mode presented in this section, a priori knowledge information is used in a post-detection step for assigning the moving vehicles to their correct roads as well as for discarding the detections that lie far from the roads of interest, which are considered in this case as false detections [59].

The simplified flowchart of this processor is shown in **Figure 4.3**. The novelty lies in the addition of a *Post-Detection* module (in red) that combines two freely available databases: the road map from the OSM [37] and the DEM from the SRTM [55], [56]. The DEM is necessary because the OSM does not provide geographical height information. DEMs with better accuracy can also be employed in the future, such as the DEM obtained from the German TanDEM-X mission [108], [109].

The *Roads Selection and Interpolation* block selects the roads of interest contained in the SAR data and performs an interpolation in order to fill possible gaps between the OSM road points [36]. For instance, the proposed processor sets the interpolation distance to the pixel spacing in the slant range direction so that one road point is obtained for each pixel in slant range.

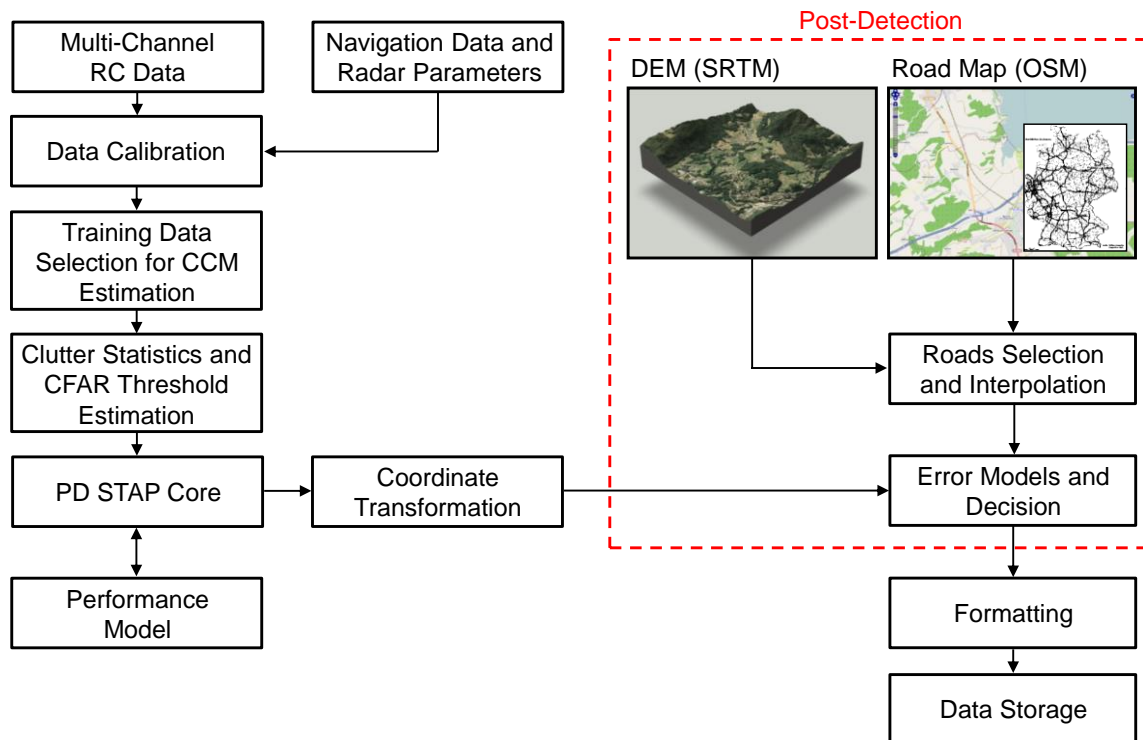


Figure 4.3. Simplified flowchart of the second operational mode of the PD STAP processor, where the *Post-Detection* module (in red) fuses the road map from the OSM with the DEM from the SRTM.

A decision has to be made for each PD STAP detection in order to verify whether the detection is actually a vehicle moving with high probability on the road or not (cf. Section 5.4.5). This decision is carried out by the *Error Models and Decision* block, which combines two positioning error models: one for the moving targets and one for the OSM road points. If the detection is true, then the target is assigned to its closest OSM road point and its absolute velocity on the road and moving direction are estimated (cf. Section 3.3.4.2). If the detection lies far from the roads of interest (e.g., vehicles moving off-road), then it is discarded as a false detection. The positioning error models and the decision step are presented in detail in Chapter 5.

The a priori knowledge-based PD STAP processor is especially suitable for civilian traffic monitoring, where it is strictly assumed that the vehicles move on known roads. However, it is still challenging to achieve real-time capability with this mode since the complete radar data need to be processed by the PD STAP core (similarly to mode 1).

Finally, note that the detections obtained from vehicles moving off-road are assumed as false detections and therefore they are discarded in the *Post-Detection* module.

4.4 Mode 3: Fast A Priori Knowledge-Based PD STAP

An alternative way for combining PD STAP with a priori knowledge information is to use the road database for mapping the roads of interest into the multi-channel RC data array, so that only the relevant azimuth samples around the road points are selected for processing [61]. The main goal is to reduce the amount of SAR data to be processed by the computationally expensive PD STAP core. Thus, the processing time can be decreased considerably, which paves the way for real-time traffic monitoring.

This approach was originally presented for a fast dual-channel DPCA-based processor with real-time traffic monitoring capability [36], where the data selected along the roads were processed using only one aspect angle or DOA angle. This section introduces a follow-up version of the processor presented in [36], where the data selected along the roads can be optionally processed using multiple DOA angles. The objective of this operation is to increase the number of detections since the RCS of the moving target depends strongly on the aspect angle [100].

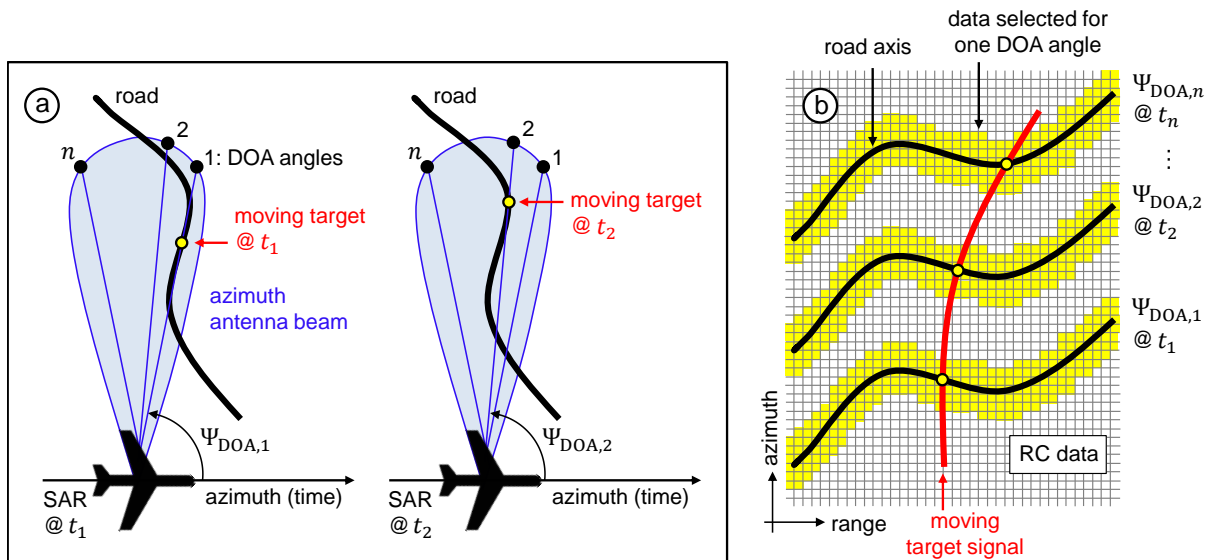


Figure 4.4. Principle of the fast a priori knowledge-based PD STAP processor: (a) acquisition geometry with an airborne SAR illuminating a target moving on the road at different azimuth times t_i , where each time generally corresponds to a different DOA angle $\Psi_{DOA,i}$; and (b) the road points mapped into the RC data array for the multiple DOA angles (for visualization purpose).

The principle of the fast a priori knowledge-based PD STAP processor is depicted in **Figure 4.4a**, where an airborne SAR illuminates a vehicle moving on a road of interest using multiple DOA angles ($\Psi_{\text{DOA},1}, \dots, \Psi_{\text{DOA},n}$) defined within the antenna beam in azimuth (in blue). As the aircraft flies, notice that the moving target presents different DOA angles for different instants of time t . **Figure 4.4b** shows the road points mapped into the RC data array for the multiple DOA angles, where the relevant data selected along the road of interest are depicted by the yellow pixels for each DOA angle. In addition, notice that each DOA angle allows obtaining a different portion of the moving target signal (in red) at different instants of time.

The simplified flowchart of this processor is shown in **Figure 4.5**. The main novelty lies in the addition of the *Data Selection for Processing* block (in green), which uses the OSM database for selecting only the relevant SAR data around the roads of interest to be processed by the PD STAP core. Each CPI contains the data selected around one road of interest. Notice that since this operation is carried out at the beginning of the processing chain, this processor can recognize if no roads are contained in the SAR data so that no further data processing needs to be carried out.

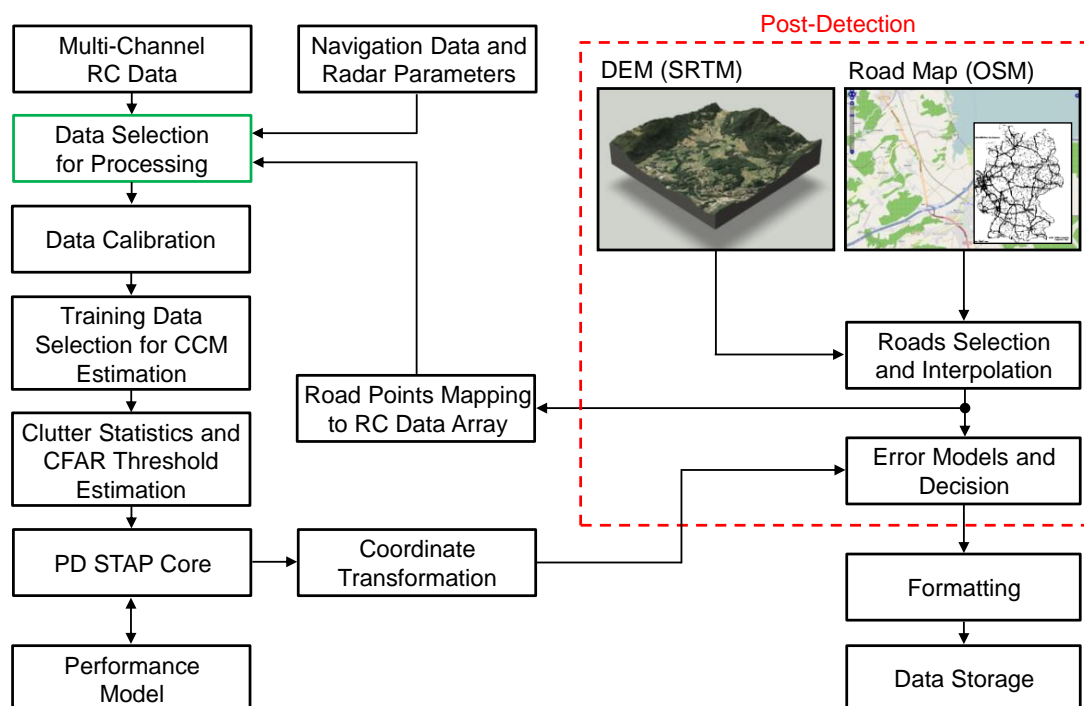


Figure 4.5. Simplified flowchart of the fast a priori knowledge-based traffic processor. The *Data Selection for Processing* block (in green) collects only the relevant data around the roads of interest.

Some of the main features of the fast PD STAP processor are:

1. It is suitable for civilian traffic monitoring, where it is strictly assumed that the vehicles move on known roads;
2. It processes only the relevant azimuth samples selected along the roads instead of the complete SAR data. Thus, the processing time can be considerably decreased, which paves the way for real-time traffic monitoring applications;
3. It is not suitable for areas without road information since the detections obtained from vehicles moving off-road are discarded in the *Post-Detection* module, similarly to operational mode 2;
4. Theoretically, it has limited performance for vehicles moving on roads that are parallel or nearly parallel to the flight direction, as pointed out in Section 4.2. Modern algorithms could be applied for estimating azimuth velocities in such conditions [78] [110], whereas it is out of the scope of this doctoral thesis.

4.5 Chapter Summary

This chapter regards the operational modes of the proposed PD STAP processor. The first mode comprises the conventional PD STAP processor that is able to detect also vehicles moving off-road. Therefore, it is suitable especially for military applications and for areas where road information is unavailable. The second mode uses a priori knowledge information (i.e., a road map from the OSM and a DEM from the SRTM) for assigning the true vehicles to their correct road axes and for rejecting detections that lie far from roads, which includes vehicles moving off-road. Thus, it is suitable especially for non-real-time traffic monitoring since the complete SAR data need to be processed by the PD STAP core. The third mode is a faster processing version of the second mode, where the PD STAP core is applied only on the relevant data selected around the OSM road axes. This approach reduces the amount of processed data and speeds up the overall processing time significantly, which paves the way for real-time traffic monitoring. Experimental GMTI results obtained with all operational modes are presented in Chapter 7, where four data takes are considered including controlled vehicles as well as several vehicles of opportunity in a real traffic scenario.

5 Positioning Error Models and Decision

5.1 Chapter Overview

This chapter presents two positioning error models: one for the targets (i.e., PD STAP detections) and one for the OSM road points. These models are combined in order to recognize and to reject false detections that lie far from the roads of interest. Basically, one positioning error ellipse is obtained for each model, as depicted in **Figure 5.1**. If both ellipses overlap, then the target is considered true and is assigned to its closest OSM road point. Otherwise, the target is discarded as a false detection. The complete procedure for decision is presented step by step.

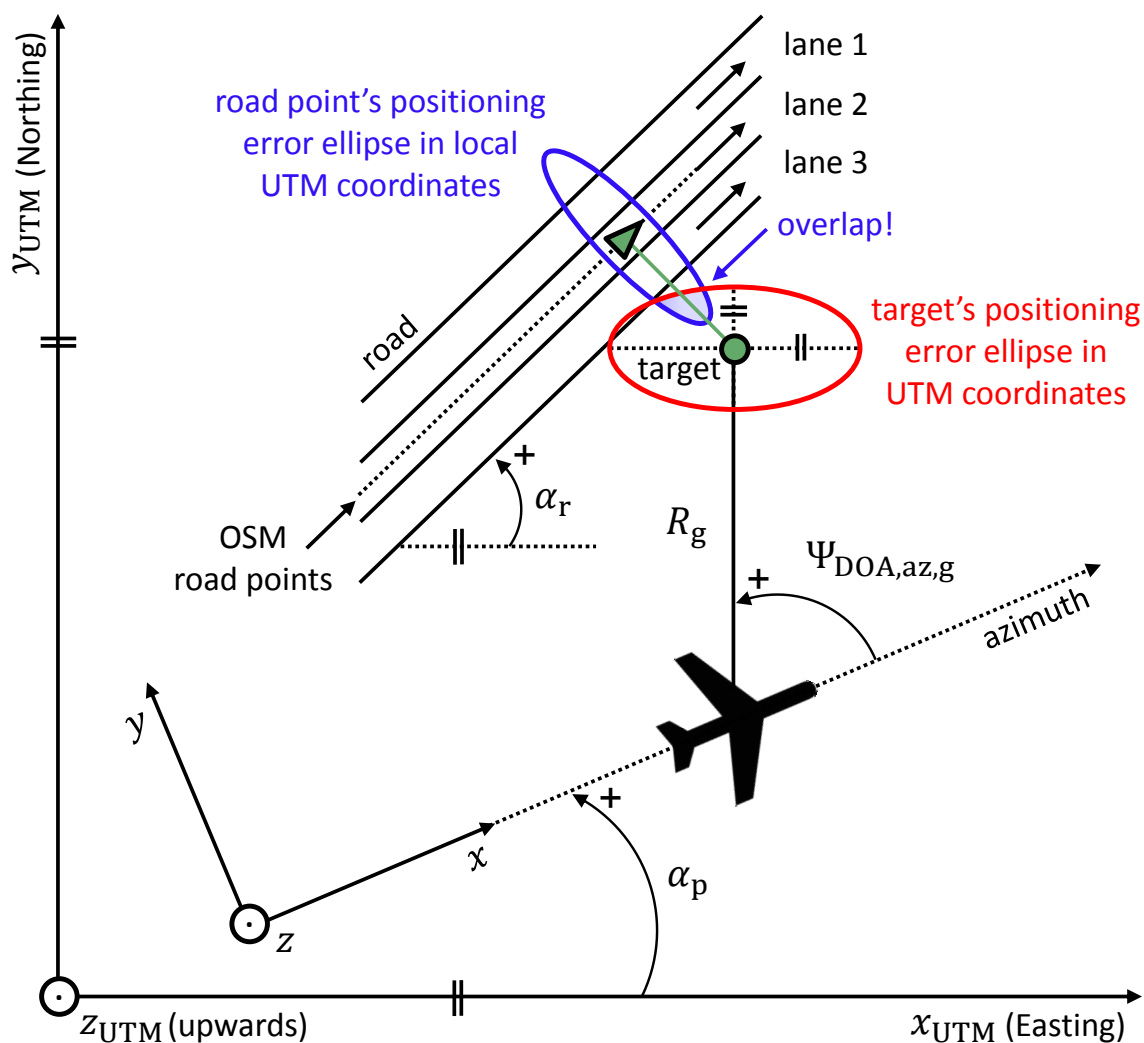


Figure 5.1. Simplified top-view geometry to illustrate the positioning error ellipses obtained for the target (circle) as well as for its closest OSM road point (triangle). In this example an overlap exists between both ellipses, so that the target is considered true and is relocated onto the road of interest.

The positioning error models contain several error sources that need to be assumed reasonably. For instance, this chapter evaluates the target's positioning error caused by each individual error source, so that the major contributions can be verified. Lastly, experimental results stress the importance and the robustness of the positioning error models. A part of the results presented in this chapter was already published in [58].

5.2 Positioning Error Model for Targets

The positioning error model for the targets (i.e., PD STAP detections) is described in this section based on the framework presented in [35]. However, instead of computing maximum errors (as carried out in [35]), in this doctoral thesis the error sources are considered as random variables and thus the standard deviation of the target's position can be estimated by considering the laws of error propagation, expressed generally as

$$\sigma_y = \sqrt{\sum_{n=1}^N \left(\frac{\partial y}{\partial x_n} \right)^2 \cdot \sigma_{x_n}^2}, \quad y = f(x_1, \dots, x_N), \quad (5.1)$$

where σ is the standard deviation and (x_1, \dots, x_N) are independent random variables.

The coordinates of a moving target in UTM Easting and Northing (cf. Section 3.3.4.1) can be expressed respectively by

$$x_{t,UTM} = x_{p,UTM} + \sqrt{R^2 - (z_p - z_t)^2} \cdot \cos(\alpha_p + \Psi_{DOA,az,g}), \quad (5.2)$$

$$y_{t,UTM} = y_{p,UTM} + \sqrt{R^2 - (z_p - z_t)^2} \cdot \sin(\alpha_p + \Psi_{DOA,az,g}), \quad (5.3)$$

where it is assumed that $z_p = z_{p,UTM}$ and $z_t = z_{t,UTM}$ (cf. Chapter 3). Comparing with the framework presented in [35], notice that Equation (5.2) and Equation (5.3) do not consider the so called “wind correction angle” nor the synchronization shift that exists between the GPS or differential GPS (DGPS) data take and the radar data take.

The standard deviation of the target's coordinates can be calculated by applying the error propagation model (adapted from [35]):

$$\sigma_{x_t,UTM} = \left[\left(\frac{\partial x_{t,UTM}}{\partial x_{p,UTM}} \right)^2 \cdot \sigma_{x_{p,UTM}}^2 + \left(\frac{\partial x_{t,UTM}}{\partial \alpha_p} \right)^2 \cdot \sigma_{\alpha_p}^2 + \left(\frac{\partial x_{t,UTM}}{\partial z_t} \right)^2 \cdot \sigma_{z_t}^2 + \left(\frac{\partial x_{t,UTM}}{\partial z_p} \right)^2 \cdot \sigma_{z_p}^2 + \left(\frac{\partial x_{t,UTM}}{\partial R} \right)^2 \cdot \sigma_R^2 + \left(\frac{\partial x_{t,UTM}}{\partial \Psi_{DOA,az,g}} \right)^2 \cdot \sigma_{\Psi_{DOA,az,g}}^2 \right]^{1/2}, \quad (5.4)$$

$$\sigma_{y_t,UTM} = \left[\left(\frac{\partial y_{t,UTM}}{\partial y_{p,UTM}} \right)^2 \cdot \sigma_{y_{p,UTM}}^2 + \left(\frac{\partial y_{t,UTM}}{\partial \alpha_p} \right)^2 \cdot \sigma_{\alpha_p}^2 + \left(\frac{\partial y_{t,UTM}}{\partial z_t} \right)^2 \cdot \sigma_{z_t}^2 + \left(\frac{\partial y_{t,UTM}}{\partial z_p} \right)^2 \cdot \sigma_{z_p}^2 + \left(\frac{\partial y_{t,UTM}}{\partial R} \right)^2 \cdot \sigma_R^2 + \left(\frac{\partial y_{t,UTM}}{\partial \Psi_{DOA,az,g}} \right)^2 \cdot \sigma_{\Psi_{DOA,az,g}}^2 \right]^{1/2}. \quad (5.5)$$

By assuming independent random variables, the calculation of the derivatives in Equation (5.4) and Equation (5.5) results in

$$\sigma_{x_t,UTM} = \left[\sigma_{x_{p,UTM}}^2 + \sin^2(\alpha_p + \Psi_{DOA,az,g}) \left[R^2 - (z_p - z_t)^2 \right] \left(\sigma_{\alpha_p}^2 + \sigma_{\Psi_{DOA,az,g}}^2 \right) + \frac{\cos^2(\alpha_p + \Psi_{DOA,az,g})}{R^2 - (z_p - z_t)^2} \cdot \left[R^2 \sigma_R^2 + (z_p - z_t)^2 \cdot \left(\sigma_{z_p}^2 + \sigma_{z_t}^2 \right) \right] \right]^{1/2}, \quad (5.6)$$

$$\sigma_{y_t,UTM} = \left[\sigma_{y_{p,UTM}}^2 + \cos^2(\alpha_p + \Psi_{DOA,az,g}) \left[R^2 - (z_p - z_t)^2 \right] \left(\sigma_{\alpha_p}^2 + \sigma_{\Psi_{DOA,az,g}}^2 \right) + \frac{\sin^2(\alpha_p + \Psi_{DOA,az,g})}{R^2 - (z_p - z_t)^2} \cdot \left[R^2 \sigma_R^2 + (z_p - z_t)^2 \cdot \left(\sigma_{z_p}^2 + \sigma_{z_t}^2 \right) \right] \right]^{1/2}. \quad (5.7)$$

As it can be seen, the standard deviations given in Equation (5.6) and Equation (5.7) contain several error sources (i.e., $\sigma_{x_{p,UTM}}^2$, $\sigma_{y_{p,UTM}}^2$, $\sigma_{\alpha_p}^2$, $\sigma_{z_t}^2$, $\sigma_{z_p}^2$, σ_R^2 and $\sigma_{\Psi_{DOA,az,g}}^2$) that need to be assumed reasonably. In this sense, **Table 5.1** shows the assumptions made for the target's positioning error model, where it is pointed out that:

1. The standard deviation of the platform's coordinates (i.e., σ_{x_p} , σ_{y_p} and σ_{z_p}) are assumed based on the accuracy of the F-SAR's navigation unit;
2. The standard deviation of the DEM (i.e., σ_{z_t}) is assumed based on the SRTM's absolute vertical accuracy in the worst case scenario [55],[56];
3. The standard deviation of the target's slant range (i.e., σ_R) is assumed based on the slant range resolution (cf. Appendix A);
4. The standard deviation of the flight course (i.e., σ_{α_p}) is assumed by taking into account that a first order motion compensation [76] is carried out;
5. The standard deviation of the target's DOA angle $\sigma_{\Psi_{\text{DOA},az,g}}$ (cf. **Figure 5.1**) can be obtained by applying the error propagation model on the target's directional cosine $u_{az} = \cos(\Psi_{\text{DOA},az})$, i.e.,

$$\sigma_{u,az}^2 = \left(\frac{\partial u_{az}}{\partial \Psi_{\text{DOA},az}} \right)^2 \cdot \sigma_{\Psi_{\text{DOA},az}}^2, \quad (5.8)$$

which results in

$$\sigma_{\Psi_{\text{DOA},az}} = \frac{\sigma_{u,az}}{|\sin(\Psi_{\text{DOA},az})|}. \quad (5.9)$$

In the X-band configuration of the DLR's F-SAR system (cf. Appendix A), the beamforming operation practically limits the DOA angles defined within the 3 dB beamwidth in azimuth $\theta_{az,3dB} = 5.25^\circ$ (cf. Section 3.6.1). Hence, one can assume that $|\sin(\Psi_{\text{DOA},az})| \rightarrow 1$, which yields the approximation

$$\sigma_{\Psi_{\text{DOA},az}} \approx \sigma_{u,az}. \quad (5.10)$$

Finally, by assuming that $\sigma_{\Psi_{\text{DOA},az}} \approx \sigma_{\Psi_{\text{DOA},az,g}}$ and $\sigma_{u,az} \approx \sigma_u$, it is obtained the approximation (cf. Equation (3.40))

$$\sigma_{\Psi_{\text{DOA},az,g}} \approx \sigma_u = \sqrt{\frac{1}{|a_s|^2} \cdot \frac{d^H R_W^{-1} d}{d^H R_W^{-1} d d_u^H R_W^{-1} d_u - |d_u^H R_W^{-1} d|^2}}. \quad (5.11)$$

TABLE 5.1
ASSUMPTIONS FOR THE TARGET'S POSITIONING ERROR MODEL

Parameter	Symbol	Value
Standard deviation of the platform's coordinates (GPS/DGPS)	$\sigma_{x_p,UTM}$	0.29 m
	$\sigma_{y_p,UTM}$	0.29 m
	$\sigma_{z_p,UTM} = \sigma_{z_p}$	0.29 m
Standard deviation of the DEM (e.g., SRTM)	σ_{z_t}	9.00 m
Standard deviation of the target's slant range	σ_R	1.20 m
Standard deviation of the flight course	σ_{α_p}	0.03°

5.3 Positioning Error Model for Road Points

The positioning error model for the OSM road points is introduced in **Figure 5.3**, where the top view geometry of a generic road is depicted in local UTM coordinates.

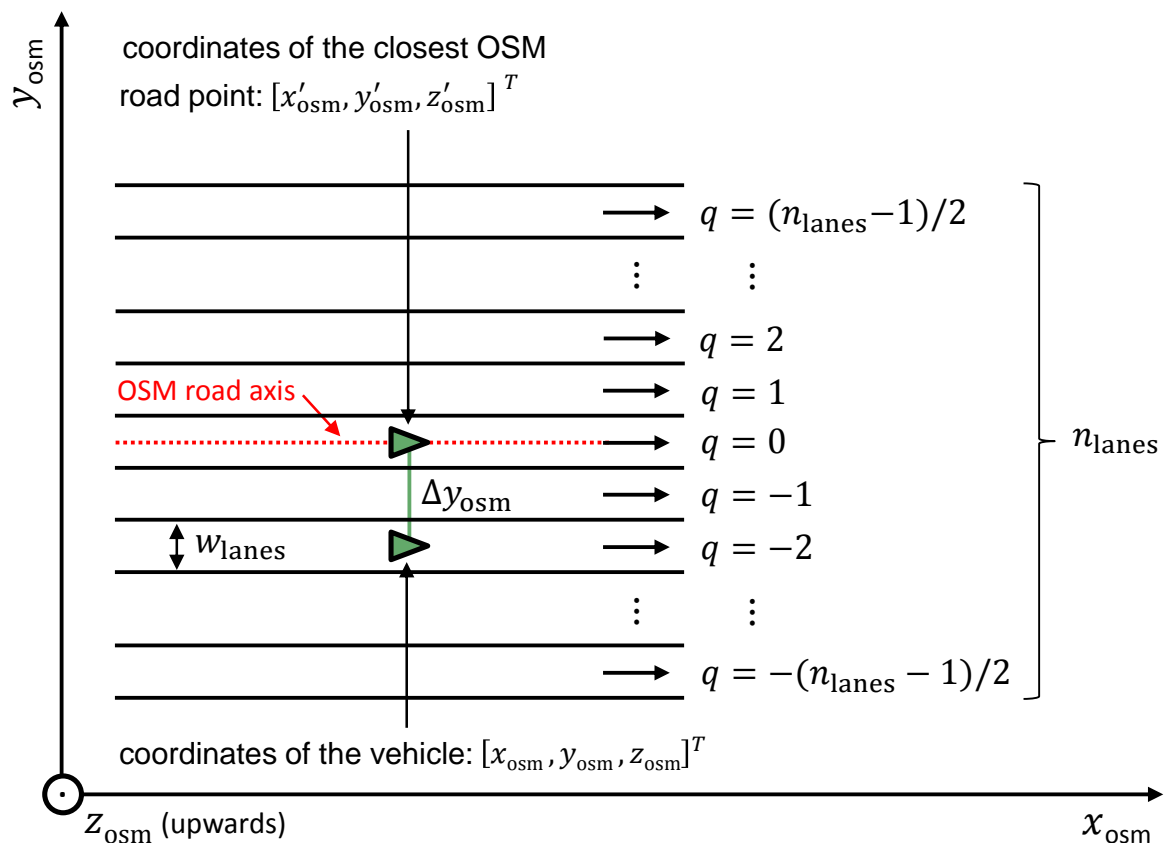


Figure 5.2. Simplified top view geometry illustrating a generic OSM road with a certain number of road lanes (n_{lanes}) in local UTM coordinates. A positioning error Δy_{osm} is observed along the y-axis due to the distance between the OSM road axis and the road lane where the vehicle moves.

It is pointed out that only one road axis is obtained from the OSM database, generally at the center of the road (cf. the red dotted line at the road lane index $q = 0$). Besides, $[x'_{osm}, y'_{osm}, z'_{osm}]^T$ are the coordinates of the road points, $[x_{osm}, y_{osm}, z_{osm}]^T$ are the coordinates of the vehicle (green triangle) moving on a particular lane (e.g., $q = -2$), n_{lanes} is the number of road lanes and w_{lanes} is the width of the road lanes in meters. In reality, the road lane where the vehicle moves is not known a priori by the proposed PD STAP processor. Thus, a positioning error along the y -axis exists and is given by:

$$\Delta y_{osm} = q \cdot w_{lanes} . \quad (5.12)$$

By assuming that: 1) the interpolation distance between the adjacent OSM road points is sufficiently small and 2) the vehicle moves at the center of its lane, it is obtained

$$x_{osm} \cong x'_{osm} , \quad (5.13)$$

$$y_{osm} = y'_{osm} + \Delta y_{osm} = y'_{osm} + q \cdot w_{lanes} . \quad (5.14)$$

The standard deviations of the OSM road point's coordinates can be calculated by applying the error propagation model:

$$\sigma_{x_{osm}} = \sqrt{\left(\frac{\delta x_{osm}}{\delta x'_{osm}}\right)^2 \cdot \sigma_{x'_{osm}}^2} , \quad (5.15)$$

$$\sigma_{y_{osm}} = \sqrt{\left(\frac{\delta y_{osm}}{\delta y'_{osm}}\right)^2 \cdot \sigma_{y'_{osm}}^2 + \left(\frac{\delta y_{osm}}{\delta q}\right)^2 \cdot \sigma_q^2 + \left(\frac{\delta y_{osm}}{\delta w_{lanes}}\right)^2 \cdot \sigma_{w_{lanes}}^2} . \quad (5.16)$$

By assuming independent random variables, the calculation of the derivatives in Equation (5.15) and Equation (5.16) results in

$$\sigma_{x_{osm}} = \sigma_{x'_{osm}} , \quad (5.17)$$

$$\sigma_{y_{osm}} = \sqrt{\sigma_{y'_{osm}}^2 + \bar{w}_{lanes}^2 \cdot \sigma_q^2 + q^2 \cdot \sigma_{w_{lanes}}^2} . \quad (5.18)$$

Indeed, the standard deviations given in Equation (5.17) and Equation (5.18) contain error sources (i.e., $\sigma_{x'_{osm}}^2$, $\sigma_{y'_{osm}}^2$, σ_q^2 and $\sigma_{w_{lanes}}^2$) that need to be assumed reasonably.

Table 5.2 shows the assumptions made for the OSM road point's positioning error model, where it is pointed out that:

1. The number and the width of the road lanes are generally not available in the OSM database. Therefore, the parameters \bar{n}_{lanes} , \bar{w}_{lanes} , $\sigma_{n_{lanes}}$ and $\sigma_{w_{lanes}}$ were estimated empirically considering 16 roads from different types (urban and rural), which were selected from all states of Germany. The log of roads and the estimates of the aforementioned parameters are shown in Appendix B;
2. The standard deviation of the road lane index σ_q is assumed to be the same as the standard deviation of the number of road lanes (i.e., $\sigma_q = \sigma_{n_{lanes}}$), since the road lane index q (and therefore its standard deviation σ_q) are not known a priori by the proposed PD STAP processor. In this sense, it is also assumed that

$$q = \frac{\bar{n}_{lanes} - 1}{2}, \quad (5.19)$$

which takes into account the worst case scenario where the vehicles move on the most distant lanes with respect to the center of the road (i.e., where the OSM road axis is located).

3. The standard deviation of the OSM road point's coordinates (i.e., $\sigma_{x'_{osm}}$ and $\sigma_{y'_{osm}}$) are assumed based on the accuracy of an ordinary GPS receiver.

By applying the parameters from **Table 5.2** in Equation (5.17) and in Equation (5.18), the standard deviations of the OSM road point's positioning error ellipse are obtained:

$$\sigma_{x_{osm}} = \sigma_{x'_{osm}} = 3.0 \text{ m}, \quad (5.20)$$

$$\sigma_{y_{osm}} = \sqrt{\sigma_{y'_{osm}}^2 + \bar{w}_{lanes}^2 \cdot \sigma_q^2 + q^2 \cdot \sigma_{w_{lanes}}^2} \quad (5.21)$$

$$\sigma_{y_{osm}} = \sqrt{(3.0)^2 + (3.2)^2 \cdot (0.9)^2 + \left(\frac{2.5-1}{2}\right)^2 \cdot (0.5)^2} \cong 4.2 \text{ m}.$$

Equation (5.21) is mostly affected by the mean width of the road lanes $\bar{w}_{lanes} = 3.2 \text{ m}$. This estimation is realistic and agrees with the standard guidelines for the construction of city roads and highways in Germany [111], [112] (cf. Appendix B).

TABLE 5.2
ASSUMPTIONS FOR THE OSM ROAD POINT'S POSITIONING ERROR MODEL

Parameter	Symbol	Value
Standard deviation of the number of road lanes	$\sigma_{n_{lanes}} = \sigma_q$	0.9
Standard deviation of the width of the road lanes	$\sigma_{w_{lanes}}$	0.5
Mean number of road lanes	\bar{n}_{lanes}	2.5
Mean width of the road lanes	\bar{w}_{lanes}	3.2 m
Standard deviation of the OSM road point's coordinates	$\sigma_{x'_{osm}}$	3.0 m
	$\sigma_{y'_{osm}}$	3.0 m

5.4 Decision

This section introduces the mathematical background necessary for obtaining the positioning error ellipses as well as for checking their intersection (overlapping test). In addition, the complete procedure for decision is described step by step.

5.4.1 General Form of an Ellipse

An ellipse can be expressed in its general form as:

$$\left[\frac{(X_{el} + X_0) \cdot \cos \beta + (Y_{el} + Y_0) \cdot \sin \beta}{a} \right]^2 + \left[\frac{(X_{el} + X_0) \cdot \sin \beta - (Y_{el} + Y_0) \cdot \cos \beta}{b} \right]^2 = 1, \quad (5.22)$$

where (X_{el}, Y_{el}) are the coordinates of the ellipse (in green) centered at (X_0, Y_0) , β is the rotation angle and (a, b) are the semi-axes, as depicted in **Figure 5.5**.

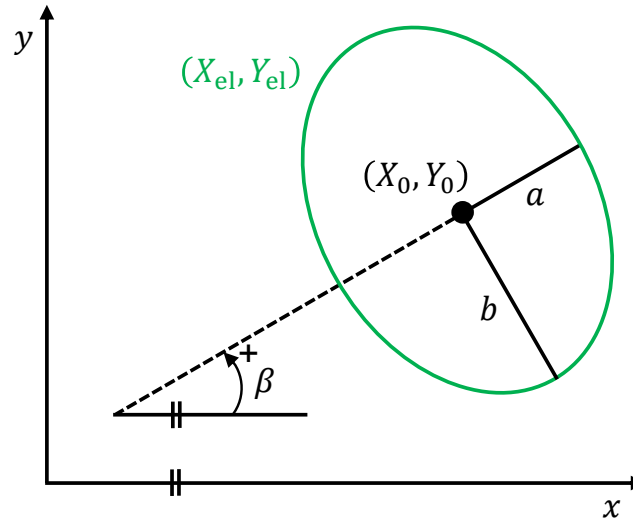


Figure 5.3. General form of an ellipse rotated by β and centered at (X_0, Y_0) .

The coordinates of the ellipse (X_{el}, Y_{el}) can also be expressed in the general parametric form as

$$X_{el} = X_0 + a \cdot \cos g \cdot \cos \beta - b \cdot \sin g \cdot \sin \beta , \quad (5.23)$$

$$Y_{el} = Y_0 + a \cdot \cos g \cdot \sin \beta + b \cdot \sin g \cdot \cos \beta , \quad (5.24)$$

where g ranges from $(0, 2\pi)$ and defines the number of points of the ellipse.

Finally, the area of the ellipse can be expressed by:

$$A_{el} = \pi \cdot a \cdot b . \quad (5.25)$$

5.4.2 Target's Positioning Error Ellipse

The positioning error ellipse of the target can be expressed by

$$\left[\frac{(X_{t,el} + x_{t,UTM})}{(\zeta \cdot \sigma_{x_{t,UTM}})} \right]^2 + \left[\frac{(Y_{t,el} + y_{t,UTM})}{(\zeta \cdot \sigma_{y_{t,UTM}})} \right]^2 = 1 , \quad (5.26)$$

where $(x_{t,UTM}, y_{t,UTM})$ are the coordinates of the detected target located at the origin of the ellipse and $(X_{t,el}, Y_{t,el})$ are the coordinates of its positioning error ellipse

(depicted in red in **Figure 5.4**). The parameter ζ is known in the literature as “z-score” and defines the confidence level for a Normal distribution. Typical values for the confidence level are: 68.2% ($\zeta = 1$), 95.4% ($\zeta = 2$) and 99.7% ($\zeta = 3$) [113], [114].

The parametric form of the target’s positioning error ellipse can be expressed by

$$X_{t,el} = x_{t,UTM} + (\zeta \cdot \sigma_{x_t}) \cdot \cos g , \quad (5.27)$$

$$Y_{t,el} = y_{t,UTM} + (\zeta \cdot \sigma_{y_t}) \cdot \sin g . \quad (5.28)$$

The area of the target’s positioning error ellipse can be expressed by:

$$A_{t,el} = \pi \cdot (\zeta \cdot \sigma_{x_{t,UTM}}) \cdot (\zeta \cdot \sigma_{y_{t,UTM}}) . \quad (5.29)$$

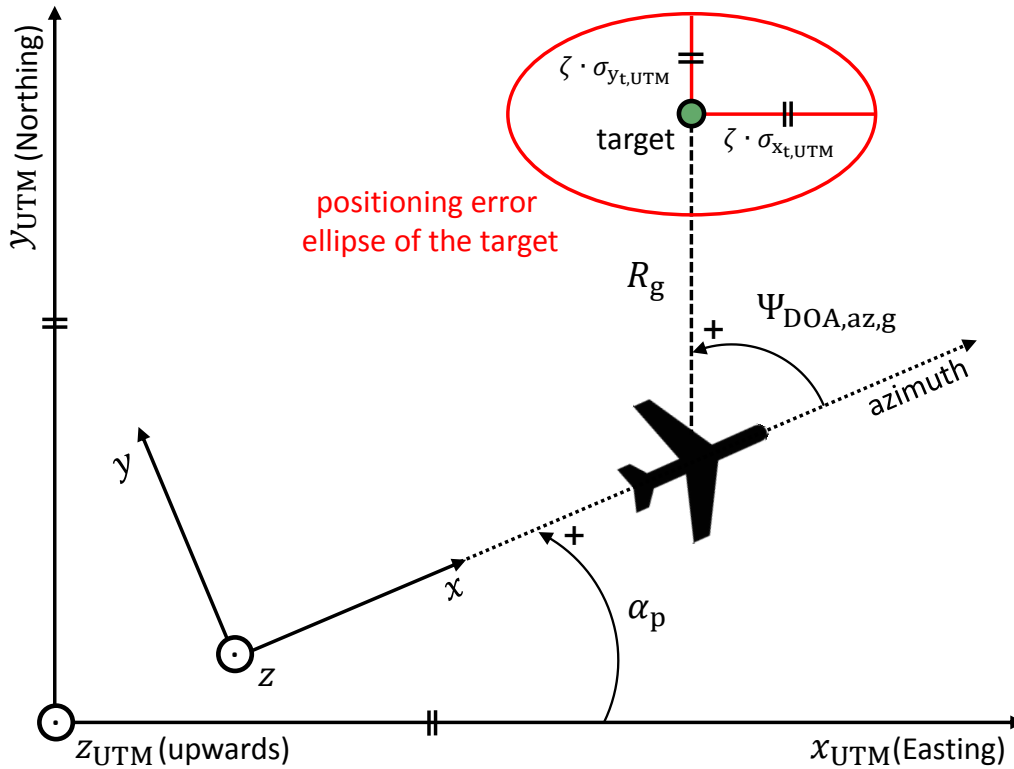


Figure 5.4. Simplified top view geometry illustrating the target’s positioning error ellipse, where the semi-axes are parallel to the UTM coordinate system.

Figure 5.4 shows the target’s positioning error ellipse, where the semi-axes are given by Equation (5.6) and Equation (5.7). It is pointed out that $\zeta = 2$ is assumed for the

proposed PD STAP processor. Indeed, notice that the confidence level influences directly on the sizes of the positioning error ellipses and therefore on the number of detections obtained in the final image.

5.4.3 Road Point's Positioning Error Ellipse

The positioning error ellipse of the OSM road point can be expressed by

$$\left[\frac{(X_{\text{osm,el}} + x_{\text{osm}}) \cdot \cos \alpha_r + (Y_{\text{osm,el}} + y_{\text{osm}}) \cdot \sin \alpha_r}{(\zeta \cdot \sigma_{x_{\text{osm}}})^2} \right]^2 + \left[\frac{(X_{\text{osm,el}} + x_{\text{osm}}) \cdot \sin \alpha_r - (Y_{\text{osm,el}} + y_{\text{osm}}) \cdot \cos \alpha_r}{(\zeta \cdot \sigma_{y_{\text{osm}}})^2} \right]^2 = 1, \quad (5.30)$$

where $(x_{\text{osm}}, y_{\text{osm}})$ are the coordinates of the road point located at the origin of the ellipse and $(X_{\text{osm,el}}, Y_{\text{osm,el}})$ are the coordinates of its positioning ellipse (depicted in blue in **Figure 5.5**). Notice that the ellipse is rotated by the road angle α_r measured with respect to the UTM Easting axis.

The parametric form of the road point's positioning error ellipse can be expressed by:

$$X_{\text{osm,el}} = x_{\text{osm}} + (\zeta \cdot \sigma_{x_{\text{osm}}}) \cdot \cos g \cdot \cos \alpha_r - (\zeta \cdot \sigma_{y_{\text{osm}}}) \cdot \sin g \cdot \sin \alpha_r, \quad (5.31)$$

$$Y_{\text{osm,el}} = y_{\text{osm}} + (\zeta \cdot \sigma_{x_{\text{osm}}}) \cdot \cos g \cdot \sin \alpha_r + (\zeta \cdot \sigma_{y_{\text{osm}}}) \cdot \sin g \cdot \cos \alpha_r. \quad (5.32)$$

The area of the road point's positioning error ellipse can be expressed by:

$$A_{\text{osm,el}} = \pi \cdot (\zeta \cdot \sigma_{x_{\text{osm}}}) \cdot (\zeta \cdot \sigma_{y_{\text{osm}}}). \quad (5.33)$$

The OSM road point's positioning error ellipse is depicted in **Figure 5.5**, where the semi-axes are given by the standard deviations computed with Equation (5.17) and Equation (5.18) as well as by the “z-score” parameter ζ . Notice that the error ellipse is obtained in local UTM coordinates $[x_{\text{osm}}, y_{\text{osm}}, z_{\text{osm}}]^T$ and is rotated according to the road point angle α_r measured with respect to the UTM Easting axis and obtained from

the OSM database. The positioning error along the y -axis is larger than in x -axis since the road may contain several lanes (the number of road lanes is not known a priori and for this reason a mean number of road lanes $\bar{n}_{\text{lanes}} = 2.53$ is assumed, cf. **Table 5.2**).

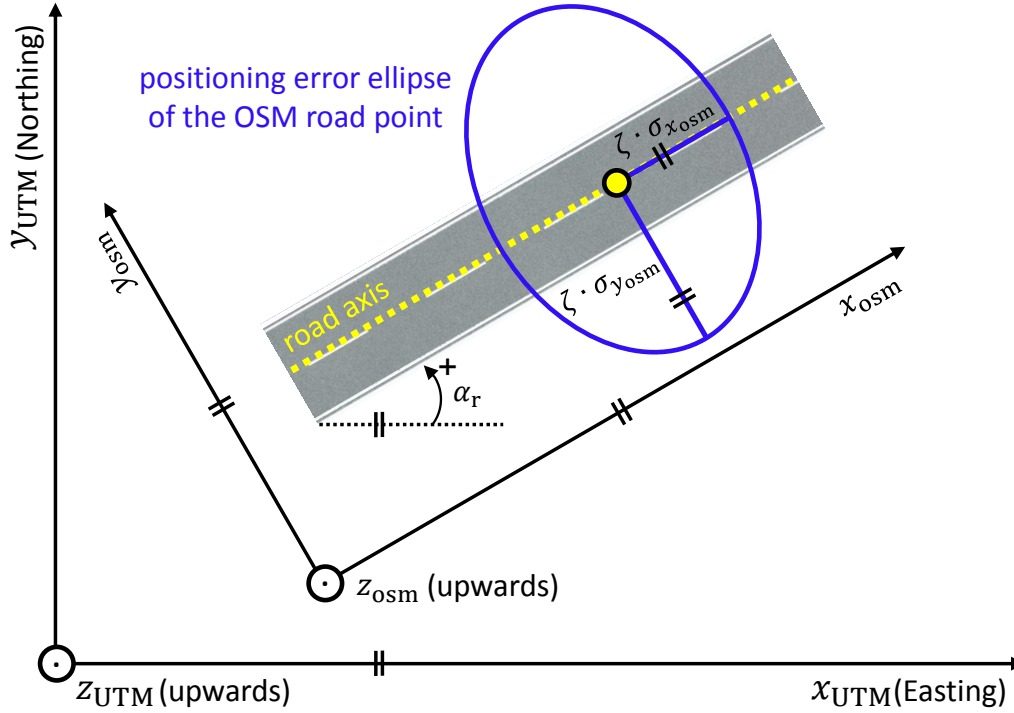


Figure 5.5. Simplified top view geometry illustrating the OSM road point's positioning error ellipse.

5.4.4 Intersection of Positioning Error Ellipses

All possible cases regarding the intersection of the positioning error ellipses are shown in **Figure 5.6**. As it can be seen, the target is considered true if at least a single point of one ellipse intersects or lies inside the other ellipse. Naturally, the target is also true if both ellipses are equal or if one ellipse is completely inside the other. The target is considered false only if the ellipses are completely separated.

The proposed PD STAP processor does not require the coordinates of the intersection points and therefore it is not necessary to test all the cases shown in **Figure 5.6**. A fast intersection test is carried out according to one of the following three cases, depending on the areas of the positioning error ellipse obtained from Equation (5.29) and from Equation (5.33).

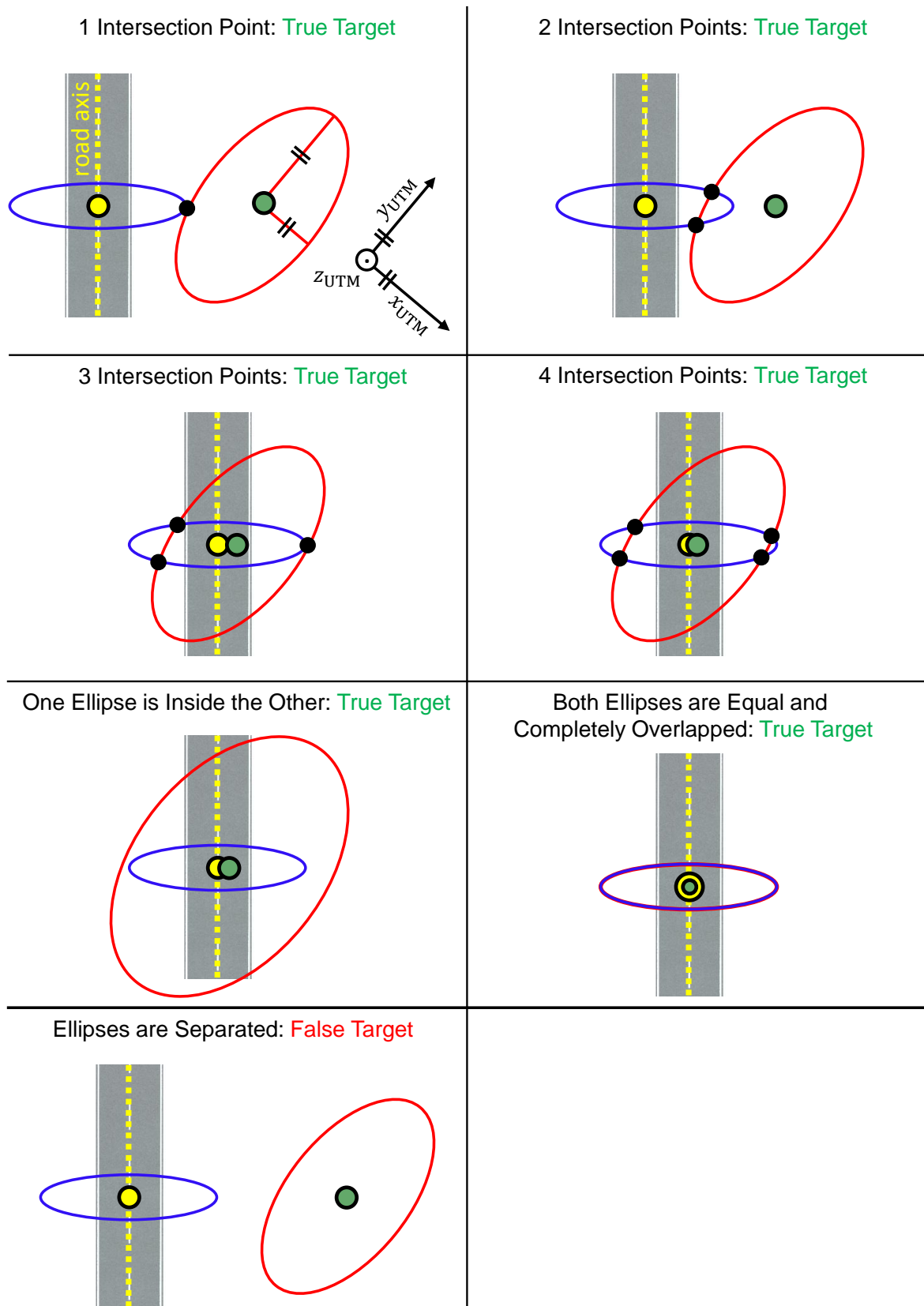


Figure 5.6. All possible cases regarding the positioning error ellipses of the target (in red) and the OSM road point (in blue). The intersection points are shown in black. Notice that the axes of the target's positioning error ellipse are parallel to the UTM coordinates system (cf. Section 5.5.2).

Case 1: $A_{t,el} > A_{osm,el}$.

The coordinates $(X_{osm,el}, Y_{osm,el})$ of the OSM road point's positioning error ellipse (i.e., the smaller ellipse) are applied into the target's positioning error ellipse (i.e., the larger ellipse) obtained from Equation (5.26) and the following inequality is tested:

$$\left[\frac{(X_{osm,el} + x_{t,UTM})}{(\zeta \cdot \sigma_{x_{t,UTM}})^2} \right]^2 + \left[\frac{(Y_{osm,el} + y_{t,UTM})}{(\zeta \cdot \sigma_{y_{t,UTM}})^2} \right]^2 \leq 1. \quad (5.34)$$

An overlap between both ellipses exists if this inequality holds for at least one point. Naturally, this inequality also holds if the smaller ellipse is located completely inside the larger ellipse since the larger ellipse is considered as a boundary for the inequality test. For this reason the areas of both ellipses need to be calculated beforehand.

Case 2: $A_{t,el} < A_{osm,el}$.

The coordinates $(X_{t,el}, Y_{t,el})$ of the target's positioning error ellipse (i.e., the smaller ellipse) are applied into the OSM road point's positioning error ellipse (i.e., the larger ellipse) obtained from Equation (5.30) and the following inequality is tested:

$$\left[\frac{(X_{t,el} + x_{osm}) \cdot \cos \alpha_r + (Y_{t,el} + y_{osm}) \cdot \sin \alpha_r}{(\zeta \cdot \sigma_{x_{osm}})^2} \right]^2 + \left[\frac{(X_{t,el} + x_{osm}) \cdot \sin \alpha_r - (Y_{t,el} + y_{osm}) \cdot \cos \alpha_r}{(\zeta \cdot \sigma_{y_{osm}})^2} \right]^2 \leq 1. \quad (5.35)$$

Similarly to the first case, an overlap between both ellipses exists if this inequality holds for at least one point. This inequality also holds if the smaller ellipse is located completely inside the larger ellipse.

Case 3: $A_{t,el} = A_{osm,el}$.

If both ellipses have exactly the same area, they can completely overlap (as depicted in **Figure 5.6**), but one ellipse would never be completely inside the other. Therefore, in this particular case it is possible to proceed according to Case 1 or Case 2.

5.4.5 Procedure for Decision

The decision stage requires at least the following main steps:

1. Obtain one detection from the PD STAP processor;
2. Obtain the closest road of interest that matches the heading direction of the target (cf. **Figure 5.7a**). This road matching is possible since the OSM database provides information about the traffic direction, as well as if the roads are one- or two-way. The PD STAP processor assumes that the vehicles do not move in the wrong way;
3. Obtain the road points of the road of interest. An interpolation is carried out for shortening the distance between adjacent road points (cf. **Figure 5.7b**). As previously pointed out in Section 4.3, the proposed PD STAP processor sets the interpolation distance to the pixel spacing in the slant range direction so that one road point can be obtained for each pixel in slant range;
4. Obtain the closest road point with respect to the target's position (cf. **Figure 5.7c**). For instance, in [59] the distance Δd is compared to an empirical threshold η_{dist} (e.g., $\eta_{\text{dist}} = 20$ m) in order to decide whether the detections are true or not. This approach is based simply on the distance Δd and neglects the several error sources pointed out in Sections 5.2 and 5.3;
5. Compute the positioning error ellipses for the target and for the closest road point by using Equation (5.26) and Equation (5.30), respectively (cf. **Figure 5.7d**);
6. Test if an overlap exists between the positioning error ellipses by using Equation (5.34) or Equation (5.35), depending on the areas of the ellipses. If both ellipses overlap, then the target is considered true and is assigned to its closest road point position (cf. **Figure 5.7e**). Otherwise, the target is discarded as a false detection;
7. Repeat from Step 1 for the next detected target.

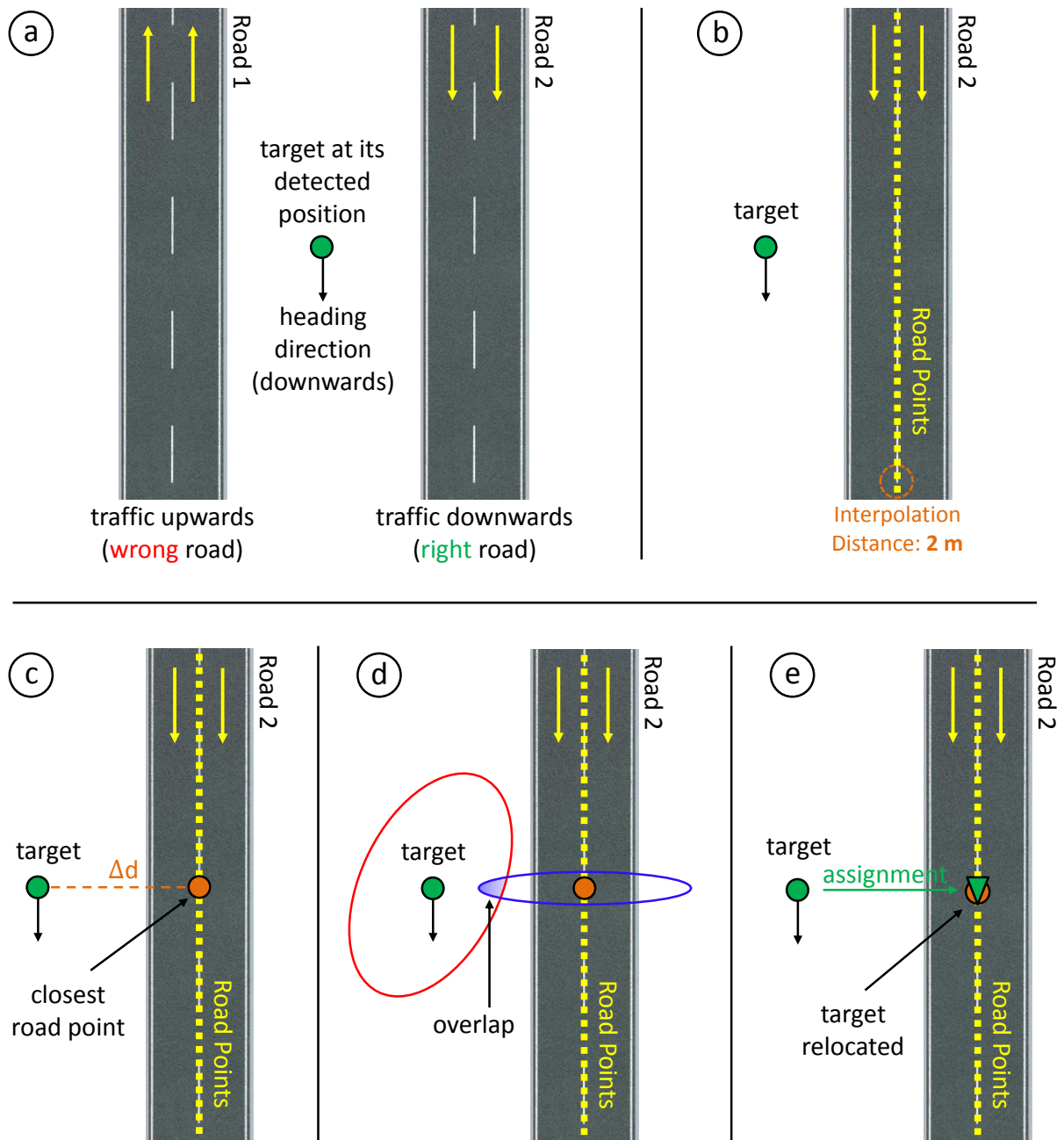


Figure 5.7. Simplified procedure for illustrating the decision step: (a) the target and the closest road that matches the target's heading direction are obtained; (b) the interpolated road points are obtained; (c) the closest road point with respect to the target's position is obtained; (d) the positioning error ellipses are obtained and an overlapping test is carried out; (e) if the ellipses overlap, then the target is assigned to the road (the triangle points to the target's heading direction).

5.5 Target's Positioning Error Contributions

This section evaluates the main contributions to the target's positioning errors given in Equation (5.6) and Equation (5.7). The simulation results were obtained according to the assumptions from **Table 5.1** as well as the following parameters: $\alpha_p = 300^\circ$, $z_p = 2838$ m, $z_t = 626$ m, $\Psi_{\text{DOA,az,g}} = 90^\circ$ and $R = 2942$ m (cf. also **Figure 5.1**).

5.5.1 Impact of Error Sources

The target's positioning errors due to each error source from **Table 5.1** are expressed below:

- Target's positioning error due to $\sigma_{\Psi_{\text{DOA,az,g}}}$:

$$\sigma_{x_t, \text{UTM}}(\sigma_{\Psi_{\text{DOA,az,g}}}) = \sqrt{\sin^2(\alpha_p + \Psi_{\text{DOA,az,g}}) \cdot [R^2 - (z_p - z_t)^2] \cdot \sigma_{\Psi_{\text{DOA,az,g}}}^2}, \quad (5.36)$$

$$\sigma_{y_t, \text{UTM}}(\sigma_{\Psi_{\text{DOA,az,g}}}) = \sqrt{\cos^2(\alpha_p + \Psi_{\text{DOA,az,g}}) \cdot [R^2 - (z_p - z_t)^2] \cdot \sigma_{\Psi_{\text{DOA,az,g}}}^2}. \quad (5.37)$$

- Target's positioning error due to σ_{z_t} :

$$\sigma_{x_t, \text{UTM}}(\sigma_{z_t, \text{UTM}}) = \sqrt{\frac{\cos^2(\alpha_p + \Psi_{\text{DOA,az,g}})}{R^2 - (z_p - z_t)^2} \cdot [(z_p - z_t)^2 \cdot \sigma_{z_t, \text{UTM}}^2]}, \quad (5.38)$$

$$\sigma_{y_t, \text{UTM}}(\sigma_{z_t, \text{UTM}}) = \sqrt{\frac{\sin^2(\alpha_p + \Psi_{\text{DOA,az,g}})}{R^2 - (z_p - z_t)^2} \cdot [(z_p - z_t)^2 \cdot \sigma_{z_t}^2]}. \quad (5.39)$$

- Target's positioning error due to σ_R :

$$\sigma_{x_t, \text{UTM}}(\sigma_R) = \sqrt{\frac{\cos^2(\alpha_p + \Psi_{\text{DOA,az,g}})}{R^2 - (z_p - z_t)^2} \cdot R^2 \cdot \sigma_R^2}, \quad (5.40)$$

$$\sigma_{y_t, \text{UTM}}(\sigma_R) = \sqrt{\frac{\sin^2(\alpha_p + \Psi_{\text{DOA,az,g}})}{R^2 - (z_p - z_t)^2} \cdot R^2 \cdot \sigma_R^2}. \quad (5.41)$$

- Target's positioning error due to σ_{α_p} :

$$\sigma_{x_t,UTM}(\sigma_{\alpha_p}) = \sqrt{\sin^2(\alpha_p + \Psi_{DOA,az,g}) \cdot [R^2 - (z_p - z_t)^2] \cdot \sigma_{\alpha_p}^2}, \quad (5.42)$$

$$\sigma_{y_t,UTM}(\sigma_{\alpha_p}) = \sqrt{\cos^2(\alpha_p + \Psi_{DOA,az,g}) \cdot [R^2 - (z_p - z_t)^2] \cdot \sigma_{\alpha_p}^2}. \quad (5.43)$$

- Target's positioning error due to $\sigma_{x_p,UTM}$:

$$\sigma_{x_t,UTM}(\sigma_{x_p,UTM}) = \sqrt{\sigma_{x_p,UTM}^2} = \sigma_{x_p,UTM}, \quad (5.44)$$

$$\sigma_{y_t,UTM}(\sigma_{x_p,UTM}) = 0. \quad (5.45)$$

- Target's positioning error due to $\sigma_{y_p,UTM}$:

$$\sigma_{x_t,UTM}(\sigma_{y_p,UTM}) = 0, \quad (5.46)$$

$$\sigma_{y_t,UTM}(\sigma_{y_p,UTM}) = \sqrt{\sigma_{y_p,UTM}^2} = \sigma_{y_p,UTM}. \quad (5.47)$$

- Target's positioning error due to σ_{z_p} :

$$\sigma_{x_t,UTM}(\sigma_{z_p}) = \sqrt{\frac{\cos^2(\alpha_p + \Psi_{DOA,az,g})}{R^2 - (z_p - z_t)^2} \cdot [(z_p - z_t)^2 \cdot \sigma_{z_p}^2]}, \quad (5.48)$$

$$\sigma_{y_t,UTM}(\sigma_{z_p}) = \sqrt{\frac{\sin^2(\alpha_p + \Psi_{DOA,az,g})}{R^2 - (z_p - z_t)^2} \cdot [(z_p - z_t)^2 \cdot \sigma_{z_p}^2]}. \quad (5.49)$$

The target's positioning errors obtained due to each aforementioned error source are shown in **Figure 5.8**. In particular, **Figure 5.8a** shows that a major positioning error is caused due to $\sigma_{\Psi_{DOA,az,g}}$, which depends on the target's line-of-sight velocity and SCNR [59], [88]. Exemplarily, for $\sigma_{\Psi_{DOA,az,g}} = 0.65^\circ$ it is obtained $\sigma_{x_t,UTM} \cong 11$ m and $\sigma_{y_t,UTM} \cong 19$ m.

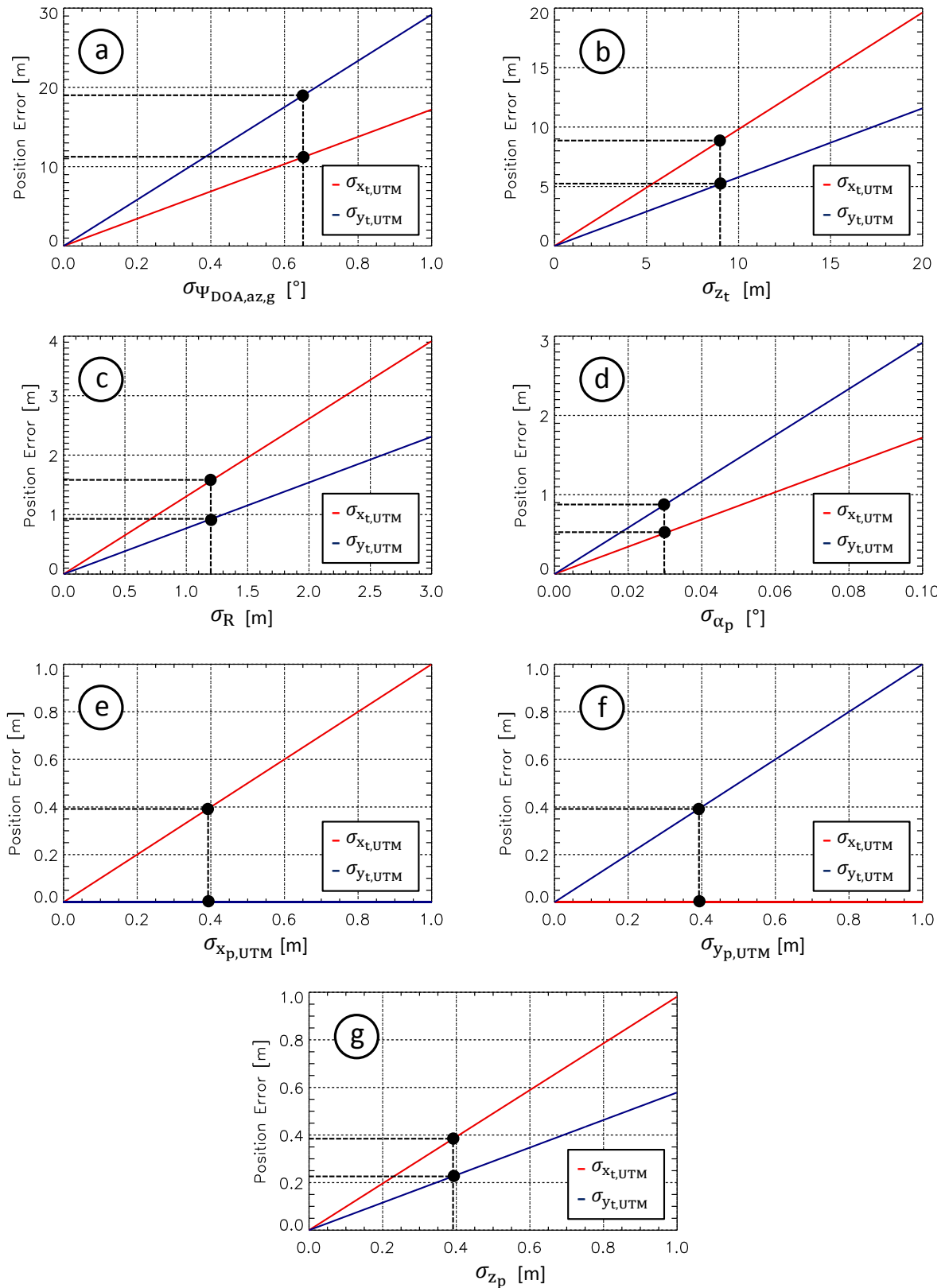


Figure 5.8. Target's positioning errors due to the standard deviation of: (a) the target's DOA angle, (b) the target's height (i.e., DEM's accuracy), (c) the target's slant range, (d) the platform's heading angle, (e) the platform's position in y-axis, (f) the platform's position in x-axis and (g) the platform's altitude. The black points show the positioning errors obtained with the assumptions from **Table 5.1**.

Another major positioning error is caused due to σ_{z_t} (i.e., the accuracy of the DEM), as shown in **Figure 5.8b**. For instance, a DEM's accuracy of $\sigma_{z_t} = 9$ m results in $\sigma_{x_{t,UTM}} \cong 9$ m and $\sigma_{y_{t,UTM}} \cong 5$ m. Notice that the target's positioning error would increase considerably if a DEM is not considered and the scene is not flat. Thus, a DEM needs to be incorporated in the PD STAP processing chain.

A minor positioning error is caused due to σ_R (cf. **Figure 5.8c**). For example, $\sigma_R = 1.2$ m is set based on the slant range resolution ($\delta_r = 1.2$ m), which results in $\sigma_{x_{t,UTM}} \cong 1.6$ m and $\sigma_{y_{t,UTM}} \cong 0.9$ m. The least impact on the target's positioning error is caused by σ_{α_p} , $\sigma_{x_{p,UTM}}$, $\sigma_{y_{p,UTM}}$ and σ_{z_p} (cf. **Figure 5.8d** to **Figure 5.8g**). It is assumed in such cases that: 1) a first order motion compensation [76] is carried out and 2) the platform's position is accurately known (e.g., measured by DGPS).

5.5.2 Impact of Platform's Heading Angle

This section aims to clarify that the target's positioning errors ($\sigma_{x_{t,UTM}}$ and $\sigma_{y_{t,UTM}}$) are obtained in UTM coordinates (i.e., Easting and Northing) and in this case the heading angle of the platform α_p plays an important role. **Figure 5.9a** shows how the target's position errors change according to α_p considering a DEM's accuracy of $\sigma_{z_t} = 9$ m (cf. **Table 5.1**). In this case, the maximum and the minimum positioning errors were $\sigma_{x_{t,UTM,max}} = \sigma_{y_{t,UTM,max}} = 22.04$ m and $\sigma_{x_{t,UTM,min}} = \sigma_{y_{t,UTM,min}} = 10.42$ m.

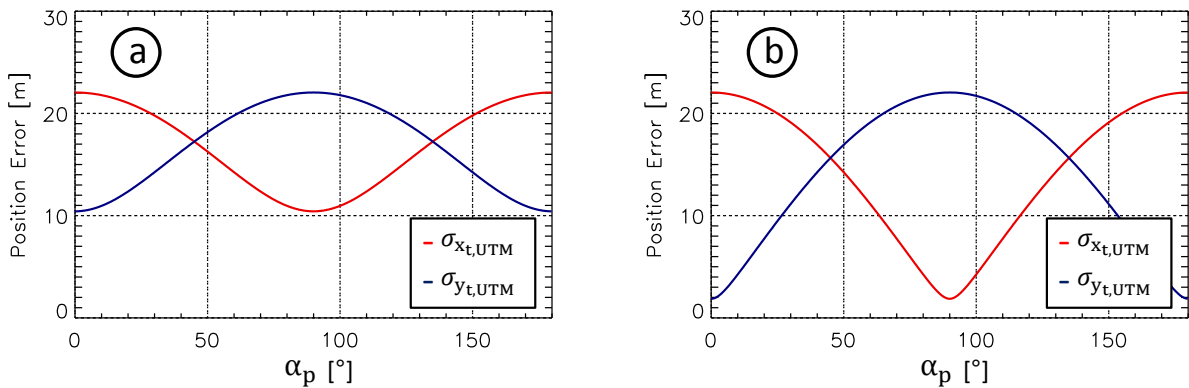


Figure 5.9. Target's positioning errors obtained as a function of the platform's heading angle α_p assuming a DEM's accuracy of: (a) $\sigma_{z_t} = 9$ m and (b) $\sigma_{z_t} = 0$ m.

The minimum positioning error can be significantly improved by considering a DEM with better accuracy. For instance, **Figure 5.9b** shows the ideal case where the height of the scene is exactly known so that the DEM's accuracy is $\sigma_{z_t} = 0$ m. In this ideal case, the minimum positioning error is reduced to $\sigma_{x_{t,UTM,min}} = \sigma_{y_{t,UTM,min}} = 1.87$ m. Therefore, as pointed out previously in Section 5.5.1, the proposed PD STAP processor requires an accurate DEM incorporated into the processing chain.

The physical interpretation of **Figure 5.9** is depicted in **Figure 5.10**, where an aircraft flies with three specific heading angles and a target is always detected at the broadside direction of the antenna array (i.e., $\Psi_{DOA,az,g} = 90^\circ$). The first case is shown in **Figure 5.10a**, where the aircraft flies parallel to the UTM Easting axis (i.e., $\alpha_p = 0^\circ$) and the target's positioning error ellipse is obtained with semi-axes $\sigma_{y_{t,UTM,min}}$ and $\sigma_{x_{t,UTM,max}}$. In other words, in this case the target's positioning error along the y -axis reaches its minimum and in x -axis it reaches its maximum (cf. also **Figure 5.9**). Notice that in this particular case $\sigma_{y_{t,UTM,min}}$ corresponds to the target's positioning error along range and $\sigma_{x_{t,UTM,max}}$ corresponds to the target's positioning error along azimuth.

The second case is shown in **Figure 5.10b**, where the aircraft flies parallel to the UTM Northing axis (i.e., $\alpha_p = 90^\circ$) and the target's positioning error ellipse is obtained with semi-axes $\sigma_{y_{t,UTM,max}}$ and $\sigma_{x_{t,UTM,min}}$. In this case the target's positioning error along the y -axis reaches its maximum and in x -axis it reaches its minimum (cf. also **Figure 5.9**). Notice that in this particular case $\sigma_{x_{t,UTM,min}}$ corresponds to the target's positioning error along range and $\sigma_{y_{t,UTM,max}}$ corresponds to the target's positioning error along azimuth.

The third case is shown in **Figure 5.10c**, where the aircraft's heading angle is $\alpha_p = 45^\circ$ and the target's positioning errors $\sigma_{y_{t,UTM}}$ and $\sigma_{x_{t,UTM}}$ are equal (cf. also **Figure 5.9**). In this particular case, a positioning error "circle" is obtained and the target's positioning errors along range and azimuth (green ellipse) are projections of $\sigma_{x_{t,UTM}}$ and $\sigma_{y_{t,UTM}}$.

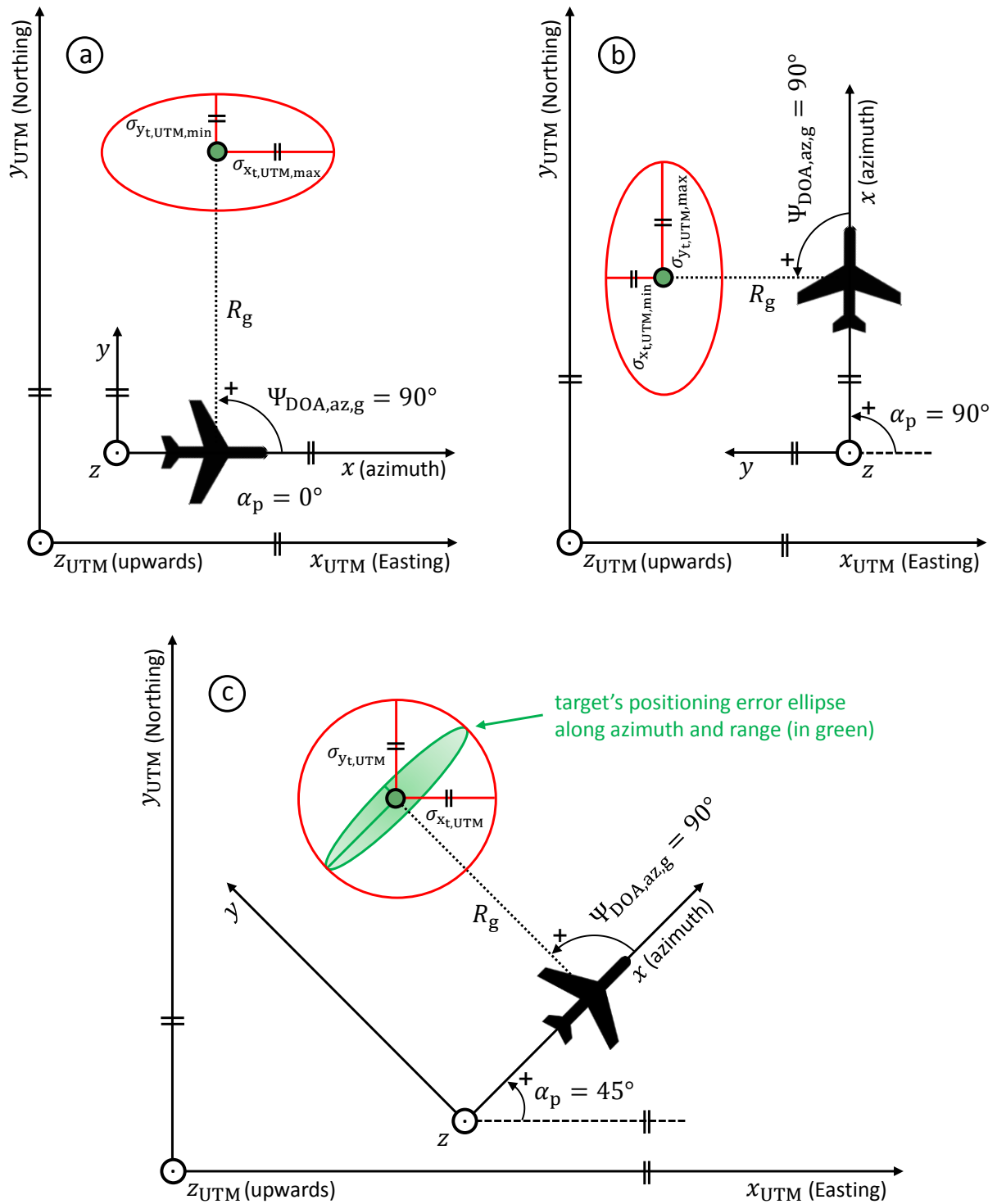


Figure 5.10. Top-view geometry illustrating the target's positioning error ellipses (in red) in UTM coordinates obtained for three platform's heading angles (assuming $\zeta = 1$): (a) $\alpha_p = 0^\circ$, (b) $\alpha_p = 90^\circ$ and (c) $\alpha_p = 45^\circ$. Notice that the red ellipses are strongly influenced by the platform's heading angle, which affects the length of the ellipse's semi-axes.

5.6 Experimental Results

The positioning error models were tested according to data take 3 (cf. Appendix A), where a convoy of five cars moved with controlled speed on the airport's runway. The radar parameters are given in Appendix A. The data take 3 contains 1024×32768 range-azimuth samples and the probability of false alarm rate was set to $P_{fa} = 10^{-7}$.

The GMTI results are shown in **Figure 5.11a**, where the PD STAP detections are shown before (circles) and after (triangles) the relocation to the runway (i.e., using the operational modes 1 and 2, cf. Chapter 4). The triangles point to the moving direction of the cars and the colors indicate their absolute velocity on the airport's runway. The center of the runway was considered as the OSM road axis (in white).

In **Figure 5.11a**, the information table shows examples of important parameters that were estimated for one particular target that was relocated onto the airport's runway. The platform's heading angle was $\alpha_p = 182.47^\circ$ (i.e., the aircraft flew nearly parallel to the UTM Easting axis toward West) and the semi-axes of the target's positioning error ellipse were $\sigma_{x_t,UTM} = 23.58$ m and $\sigma_{y_t,UTM} = 10.71$ m. Notice that such target's positioning errors are comparable to the results shown in **Figure 5.9a** for $\alpha_p = 180^\circ$.

Figure 5.11b shows in detail a part of the runway where the conventional passenger cars 1 to 5 moved in a convoy. The red ellipses show the positioning error of the targets (i.e., PD STAP detections) and the blue ellipses show the positioning error of their closest road points in the road axis, where $\zeta = 1$ was assumed (cf. Section 5.4.2 and Section 5.4.3). It can be seen that the cars were detected several times in five groups of detections (also known as "clusters"). It can be noticed that the positioning error ellipse of the detection obtained at the center of each cluster contains most of the adjacent detections, which indicates that the parameter $\zeta = 1$ was indeed properly chosen for data take 3 (cf. Appendix A).

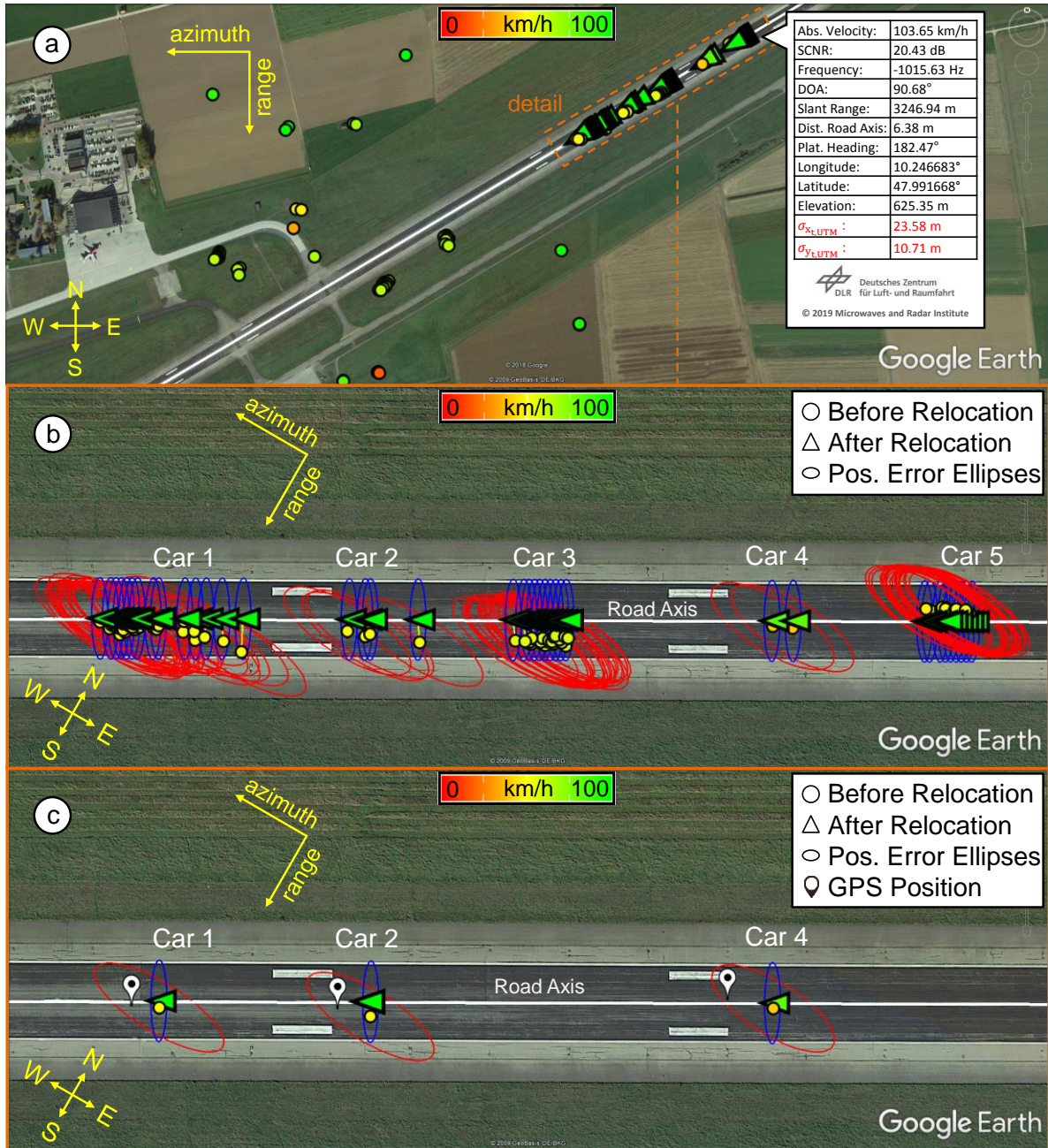


Figure 5.11. (a) Google Earth images overlaid with radar detections obtained from data take 3 (cf. Appendix A) before and after the relocation to the runway; (b) detections from cars 1 to 5, where the positioning error ellipses are shown for the targets (red) and for their closest OSM road points (blue); (c) detections obtained from cars 1, 2 and 4 at the center of their clusters and their respective GPS positions (white pins). Notice that the semi-axes of the target's positioning error ellipses (red) are parallel to the UTM coordinate system.

The cars 1, 2 and 4 were equipped with conventional handheld GPS receivers in order to retrieve reliable geographical reference positions and velocities. **Figure 5.11c** shows the GPS positions (white pins) of these cars and the radar detections obtained at the center of their clusters. It is pointed out that the GPS positions were obtained at the same time UTC (Coordinated Universal Time) as their respective radar detections. As it can be noticed, the GPS positions of the cars were contained in the positioning error ellipses of their detections (cf. red ellipses in **Figure 5.11c**), which reinforces that the parameter $\zeta = 1$ was properly chosen for this experiment.

Table 5.3 shows the target's velocity and geographical position estimation accuracies, where $v_{\text{road,GPS}}$ denotes the velocity of the car obtained from the GPS receiver and v_{road} denotes the absolute velocity of the car on the road computed according to Equation 3.19. It can be seen in **Table 5.3** that the PD STAP processor detected the cars 1, 2 and 4 with an absolute positioning error better than 17 m. It can also be seen in this table that the absolute velocity estimation error $|\Delta v_{\text{road}}|$ was better than 10 km/h, which is sufficient for many traffic monitoring applications.

TABLE 5.3

TARGET'S VELOCITY AND GEOGRAPHICAL POSITION ESTIMATION ACCURACIES (DATA TAKE 3)

	$v_{\text{road,GPS}}$ [km/h]	v_{road} [km/h]	$ \Delta v_{\text{road}} $ [km/h]	Absolute Positioning Error [m]
Car 1:	94.9	104.1	9.2	10.5
Car 2:	106.3	104.9	1.4	13.1
Car 4:	91.5	82.7	8.8	16.9

Figure 5.12 shows the histogram of absolute velocities on the road of cars 1 to 5 after rejecting all false detections. As it can be seen, cars 1, 2 and 5 moved with an average velocity of around 100 km/h, which agrees very well with the experiment description [115]. Cars 3 and 4 moved with average velocities of around 120 km/h and 80 km/h, respectively.

The parameters applied in the positioning error models are given in **Table 5.1** and in **Table 5.2**. However, the number and the width of the road lanes were known a priori

in this experiment ($w_{\text{lanes}} = 15$ m, $n_{\text{lanes}} = 2$, $\sigma_{w_{\text{lanes}}} = 0$, $\sigma_{n_{\text{lanes}}} = 0$ and $\sigma_n = 1$). Indeed, data takes 1 to 3 (cf. Appendix A) are unusual cases because the lane's width of the airport's runway is much larger than the average lane's width of regular roads ($\bar{w}_{\text{lanes}} = 3.2$ m, cf. Appendix B).

Finally, it is pointed out that the false detections obtained far from the runway were not assigned to the road axis and therefore they were discarded in the final image.

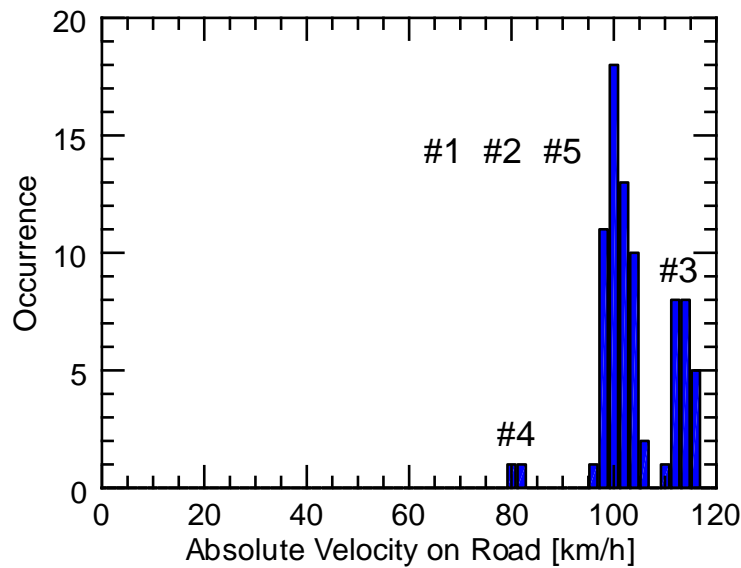


Figure 5.12. Histogram of absolute velocities on the road of cars 1 to 5 considering the data take 3 (cf. Appendix A).

5.7 Chapter Summary

This chapter regards the positioning error models for the targets (PD STAP detections) and for the OSM road points (cf. the empirical assumptions presented in Appendix B). These models are combined in order to recognize and to discard false detections that lie far from the roads of interest. The decision whether a target is true or not is carried out based on an overlapping test between the positioning error ellipses obtained for each model. If the ellipses overlap, the target is considered true and is assigned to its closest road of interest. Otherwise, it is discarded as a false detection. The positioning error models contain several error sources. For instance, this chapter evaluates the contributions of each individual error source to the target's positioning error. It is

shown in this evaluation that the most prominent positioning errors are obtained due to the standard deviations of 1) the target's DOA angle (which depends on the target's SCNR and line-of-sight velocity) and 2) the height of the terrain (which can be significantly reduced by incorporating a DEM into the PD STAP processing chain). It is also shown that the target's positioning errors are obtained in UTM coordinates (i.e., Easting and Northing) and therefore they are strongly influenced by the heading angle of the platform.

6 Data Calibration

6.1 Chapter Overview

Data calibration is essential for detecting the moving targets and for estimating their positions and velocities accurately. This chapter presents the data calibration algorithm of the proposed PD STAP processor that corrects not only the residual ATI phase and the magnitude offsets of the RX channels, but also the Doppler centroid variation over slant range and time. The main steps of the calibration algorithm are presented in terms of mathematical framework and experimental results obtained from real data acquired with DLR's system F-SAR. The effects caused by the lack of data calibration are also shown and discussed based on GMTI results. A part of the content presented in this chapter was already published in [60].

6.2 Introduction

In reality, it is not possible to build absolutely identical antennas and RX channels with the same electrical characteristics and time delays. Thus, the transfer functions and the antenna gain patterns of the RX channels differ from each other and need to be characterized or equalized [116].

For instance, the different TX and RX antenna characteristics (D_{tx} and $D_{rx,m}$) can be measured or estimated, and incorporated directly into the DOA vector \mathbf{d} expressed in Equation (3.3). Generally, external calibration is required for compensating different time delays between the RX channels (e.g., the use of reference targets or special calibration loops in the radar hardware design). Then, remaining ATI phase offsets can be estimated from the SAR data. Moreover, the precise knowledge of the along-track baselines among the multiple RX channels is important for estimating the DOA angles accurately, which affects the position and the velocity estimation of the targets.

An elegant and robust method for digital channel balancing (DCB) was introduced in [48] and discussed in detail in [116]. In this method, the RX channels are balanced with respect to a reference RX channel by performing an iterative approach in the 2-D

frequency domain, so that residual ATI phase and magnitude offsets are compensated. In addition, it is shown in [116] how the along-track baselines between individual RX channels can be estimated accurately in the range-Doppler domain.

More recently, an interesting review about data calibration techniques was presented in [117], where simple algorithms (e.g., based on 1-D and 2-D coregistrations) and more sophisticated algorithms (e.g., the DCB) were evaluated in detail for ATI, DPCA and STAP. As expected, the DCB was able to achieve better performance especially in terms of clutter cancellation, although at the expense of a high computational effort.

This chapter presents a fast and efficient data calibration algorithm that removes the channel imbalances on residual ATI phases and evens out the differences in channel magnitudes. Besides, the algorithm corrects the Doppler centroid over slant range and time according to the attitude angles of the antenna array.

6.3 Structure of the Algorithm

The simplified flowchart containing the main steps of the data calibration algorithm is shown in **Figure 6.1**. As it can be seen, after obtaining the aircraft's navigation data (e.g., position, velocity, heading and attitude angles) and the radar parameters, the first step is to compensate the time delay introduced by the antenna aperture switching (AS), as described in Section 6.4.

In the *Parameters Estimation* block, homogeneous data are collected in order to estimate the azimuth antenna patterns, the along-track baselines, the magnitude offsets and the attitude angle offsets (yaw, pitch and roll, cf. Section 6.6.3). It is pointed out that these parameters can optionally be estimated only once and stored in the memory for speeding up the processing time.

In the *Doppler Centroid Correction* block, all range bins of the measured data are shifted to Doppler zero by taking into account the range dependent Doppler centroid (known in the literature as “J-Hook” [94]) as well as the Doppler centroid variation over time caused by the aircraft's motion (cf. Section 6.6). Indeed, notice in Equation

(3.5) that the CCM $\widehat{\mathbf{R}}_W$ is estimated for each Doppler frequency bin f_a by performing an averaging along slant range. Therefore, the Doppler centroid correction is essential for removing the “J-Hook” that impacts directly on the CCM estimation.

In the *ATI Phase Correction* block, residual ATI phase offsets are estimated based on the phase differences or interferograms obtained between pairs of RX channels (for instance, assuming the channel RX1 as reference). After the phase offset correction, the phase distributions of the interferograms are centered at zero (cf. **Figure 6.9**). The benefits of the data calibration algorithm are shown and discussed in Section 6.8.

Finally, the differences in the RX channel magnitudes are corrected in the *Magnitude Correction* block by applying the estimated magnitude offsets (cf. Section 6.5.2).

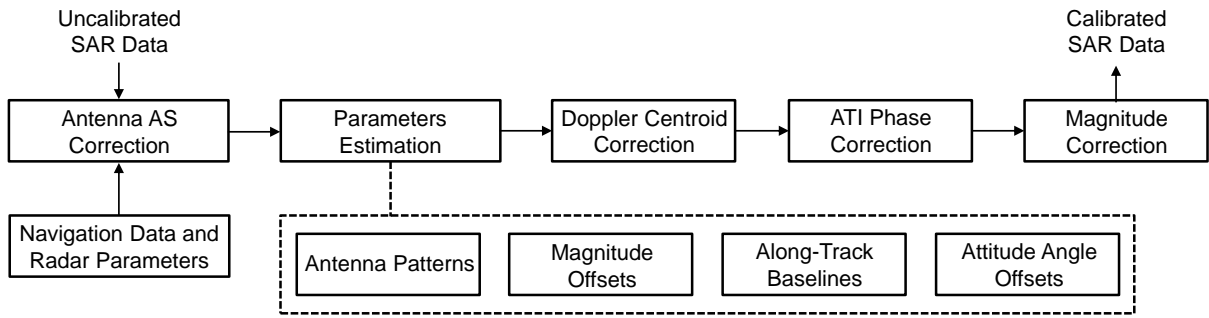


Figure 6.1. Simplified flowchart of the data calibration algorithm. The *Parameters Estimation* block can optionally be carried out only once for speeding up the overall processing time.

6.4 Antenna Aperture Switching Correction

The antenna aperture switching (AS) can improve the GMTI performance of radar systems by creating additional phase centers and longer ATI baselines, whereas this operation introduces a time delay that needs to be corrected [93]. This correction can be carried out in Doppler frequency domain by applying the following phase ramp to the radar data

$$\varphi_{AS}(f_a) = \exp\{-2 \cdot \pi \cdot f_a \cdot \Delta t_{AS}\}, \quad (6.1)$$

where $\Delta t_{AS} = 1/(2 \cdot PRF)$ denotes the time lag due to the antenna AS that contributes to the effective along-track baseline.

6.5 Parameters Estimation

The data calibration algorithm requires the estimation of important parameters that are described in this section. It is pointed out that the estimation of the attitude angle offsets (yaw, pitch and roll) is presented in Section 6.6.3.

6.5.1 Antenna Patterns

The two-way diagram of the azimuth antenna pattern can be estimated from the SAR data by averaging all available range bins K for each Doppler frequency bin f_a [35]

$$A(f_a, m) = \sqrt{\frac{1}{K} \sum_{k=1}^K |\mathbf{z}(r_k, f_a, m)|^2}, \quad m = 1, \dots, M, \quad (6.2)$$

where m denotes the index of the RX antenna or channel.

6.5.2 Magnitude Offsets

The magnitude (or gain) offsets can be obtained from the azimuth antenna pattern peaks according to:

$$\rho_{1,m} = \frac{\max(D_t D_{r,1})}{\max(D_t D_{r,m})}, \quad m = 2, \dots, M, \quad (6.3)$$

where the channel RX1 is assumed as reference.

Thus, the magnitude offset correction (with respect to RX1) can be carried out in time domain according to:

$$\mathbf{z}_{\text{mag,corr}}(r_k, f_a, m) = \mathbf{z}(r_k, f_a, m) \cdot \rho_{1,m}, \quad m = 2, \dots, M, \quad (6.4)$$

where $\mathbf{z}_{\text{mag,corr}}$ denotes the measured data after the magnitude correction.

Exemplarily, **Figure 6.2** shows the azimuth antenna patterns in Doppler frequency domain estimated according to Equation (6.2) before and after the correction of the magnitude imbalances. In this example, an homogeneous data patch containing 2048 x 16384 range-azimuth samples was obtained from data take 4 (cf. Appendix A) and the following magnitude offsets were estimated according to Equation (6.3): $\rho_{1,2} = 1.08$, $\rho_{1,3} = 1.01$ and $\rho_{1,4} = 1.05$. Notice that the azimuth antenna patterns are centered at the Doppler centroid $f_{DC} = -90.18$ Hz. The correction of the magnitude imbalances is essential for PD STAP since the magnitude of the azimuth antenna patterns (D_{tx} and $D_{rx,m}$) are contained in the DOA vector \mathbf{d} , as it can be seen in Equation (3.3).

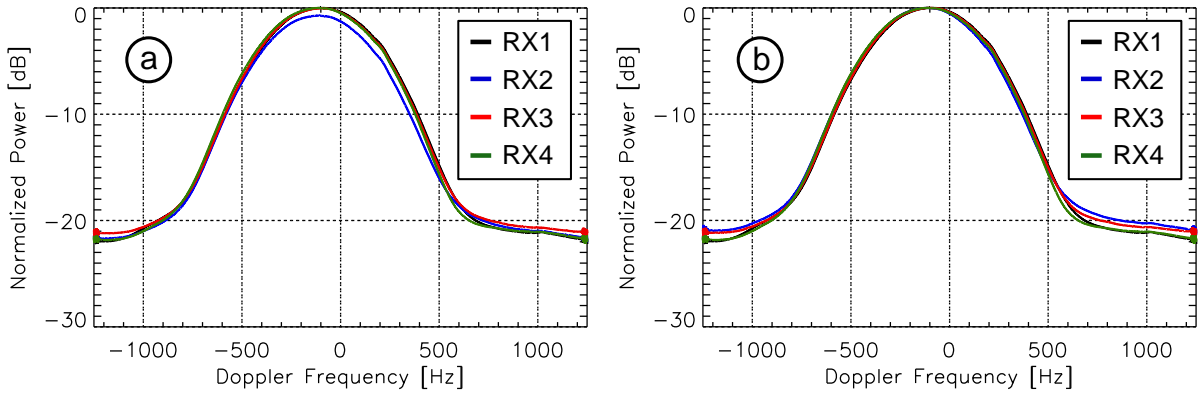


Figure 6.2. Azimuth antenna patterns estimated from an homogeneous data patch from data take 4: (a) before and (b) after the correction of the magnitude imbalances among the RX channels ($\rho_{1,2} = 1.08$, $\rho_{1,3} = 1.01$ and $\rho_{1,4} = 1.05$).

6.5.3 Along-Track Baselines

The F-SAR X-band configuration contains four RX antennas aligned in the azimuth or flight direction (cf. Appendix A). The effective along-track baselines among the RX channels assuming channel RX1 as reference are: $|d_{a1,2}| = 0.1$ m, $|d_{a1,3}| = 0.2$ m and $|d_{a1,4}| = 0.3$ m, as depicted in **Figure 6.3**. Notice that due to the bi-static operation, the effective along-track baselines are generally half as large as the physical antenna center separation. These effective baselines can be estimated from the measured data by using the slopes of the ATI phases along the Doppler frequency [116].

Exemplarily, **Figure 6.4** shows the effective along-track baselines estimated from data take 4 containing 2048×16384 range-azimuth samples. The means and standard deviations of $d_{a1,2}$, $d_{a1,3}$ and $d_{a1,4}$ were respectively: $[-0.098, 0.001]$ m, $[-0.199, 0.001]$ m and $[-0.296, 0.002]$ m. In this example, a moving window containing 2048×1024 range-azimuth samples was applied with a moving window step size of 3.6 m in azimuth and all available range bins K were used. Since the obtained standard deviations were in the order of just a few millimeters, the effective along-track baselines can optionally be estimated only once and stored in the memory in order to speed up the processing time. An accurate estimation of the effective along-track baselines is essential for the PD STAP operation since it affects the DOA vector \mathbf{d} , as it can be seen in Equation (3.3).

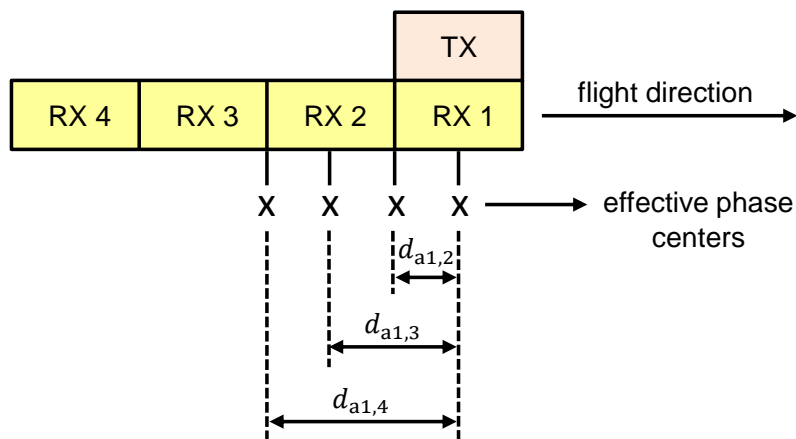


Figure 6.3. Effective along-track baselines among the receive channels assuming RX1 as reference.

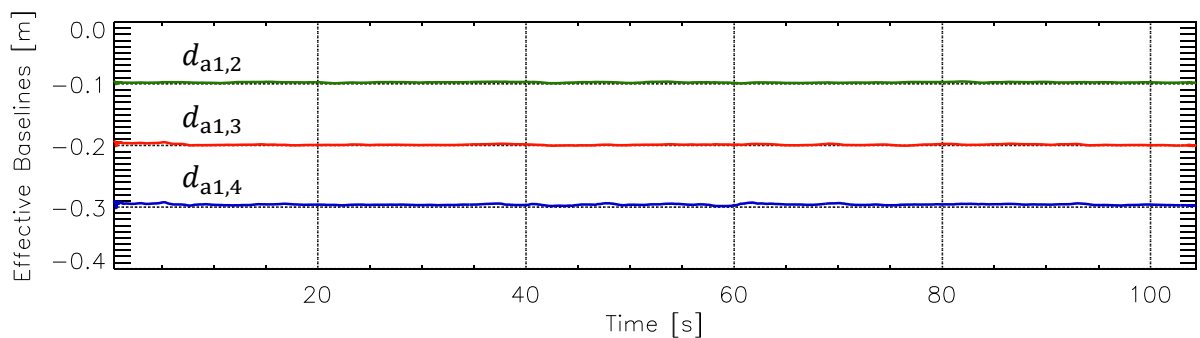


Figure 6.4. Effective along-track baselines $d_{a1,i}$ estimated from the complete data take 4.

6.6 Doppler Centroid

This section presents the mathematical framework for estimating the Doppler centroid according to the attitude angles of the antenna array and the main steps for estimating the attitude angle offsets. The theory presented in this section is verified based on experimental results obtained from measured data acquired by DLR's system F-SAR.

6.6.1 Aircraft's Motion

In reality, the aircraft is not able to follow a straight flight path due to atmospheric turbulences and therefore its attitude angles (yaw, pitch and roll) change over time. The aircraft's motion plays an important role especially if the platform is equipped with a flat antenna array which does not allow zero-Doppler beam steering, as in the case of F-SAR. For instance, nominal pitch angles are often in the order of 1° or 2° , reaching up to 7° depending on the type of the aircraft and on the airspeed [118]. This section presents the impact of the aircraft's motion on the squint angle (and thus on the Doppler centroid), which affects the target's velocity and position estimations.

The axes of the aircraft's attitude angles are depicted in **Figure 6.5**. As it can be seen, the pitch angle is positive when the aircraft's nose points upwards and negative when it points downwards. The yaw angle is positive when the aircraft's nose points towards to the right and negative when it points towards to the left (with respect to the flight direction). The roll angle is positive when the right wing of the aircraft rolls downwards and negative when it rolls upwards.

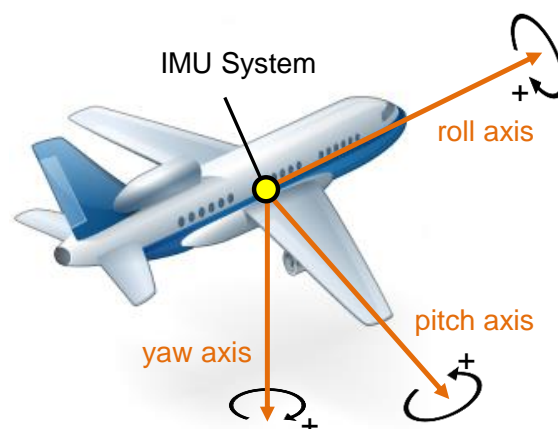


Figure 6.5. Axes of the aircraft's attitude angles: yaw, pitch and roll (for visualization purpose).

It is pointed out that the F-SAR's IMU provides the aircraft's pitch, roll and heading angles with respect to the true North. The aircraft's heading is used for obtaining the yaw angle according to (cf. **Figure 6.6**):

$$\theta_{\text{YAW,IMU}}(t) = \theta_{\text{HEADING,IMU}}(t) - \bar{\theta}_{\text{COURSE}} , \quad (6.5)$$

where $\bar{\theta}_{\text{COURSE}}$ denotes the aircraft's mean flight course with respect to the true North. This parameter is obtained through the aircraft's GPS coordinates and can be updated for each CPI (for instance).

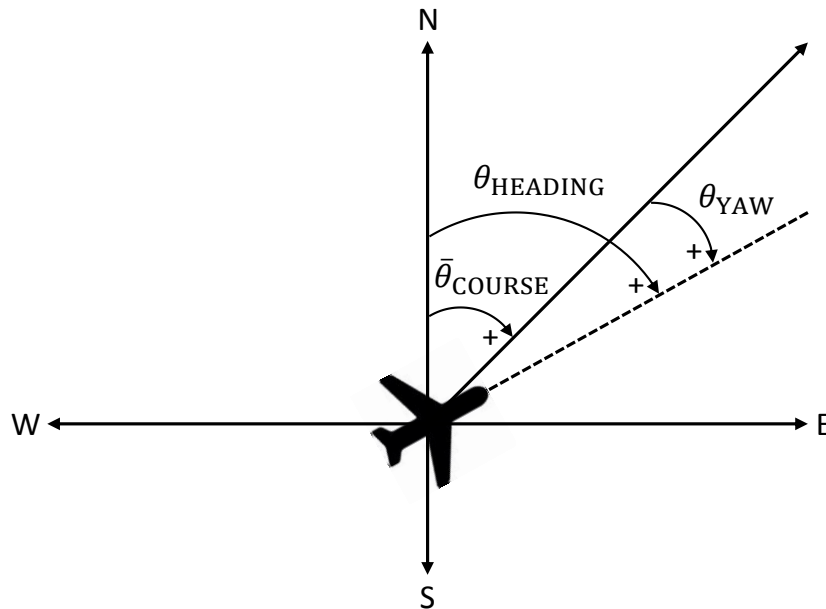


Figure 6.6. Top view geometry showing the aircraft's yaw, heading direction and flight course.

The sign relationship between the yaw angle and the Doppler centroid is depicted in **Figure 6.7**. Notice that for a left-looking antenna (LLA), a positive yaw angle causes a positive Doppler centroid because the antenna is steered forwards with respect to the flight course $\bar{\theta}_{\text{COURSE}}$.

On the other hand, for a right-looking antenna (RLA) a positive yaw angle causes a negative Doppler centroid and a negative yaw angle causes a positive Doppler centroid. Therefore, the PD STAP processor needs to know a priori if the antenna is left or right-looking.

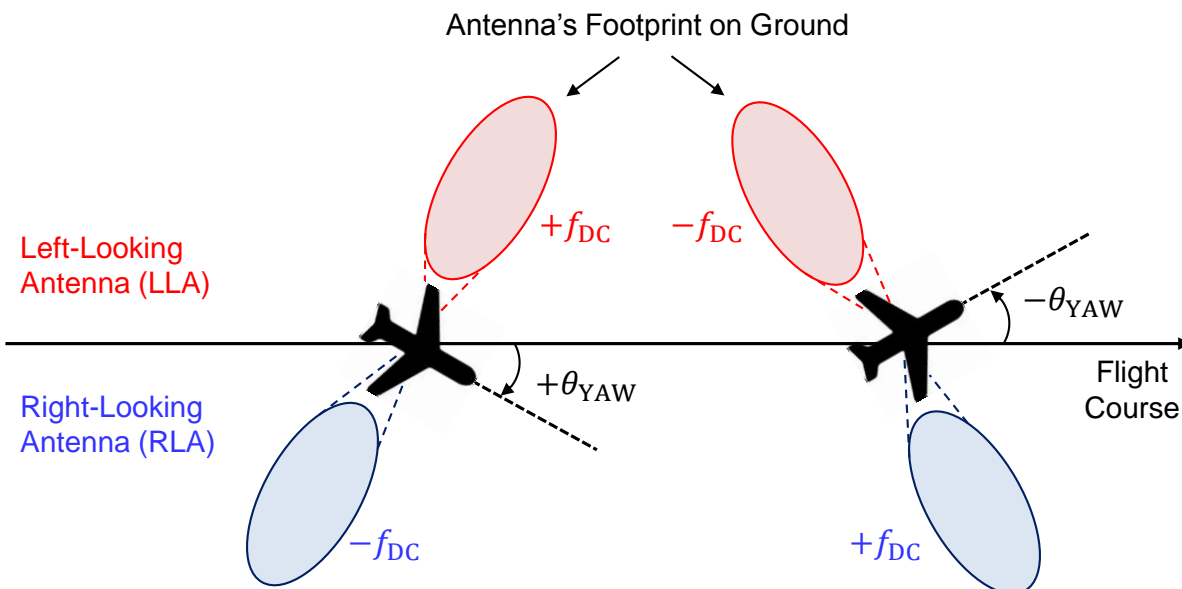


Figure 6.7. Signs of the yaw angle and Doppler centroid for a left and right-looking antenna.

6.6.2 Squint Angle and Doppler Centroid Estimation

This section presents the contributions of the antenna array's attitude angles to the Doppler centroid. The squint angle and the Doppler centroid are generally related as

$$f_{DC} = \frac{2 \cdot v_p}{\lambda} \sin(\Psi_{sq}). \quad (6.6)$$

The squint angle varies over slant range r_k due to the incidence angle change and over time t due to the variation of the antenna array's attitude angles. This squint variation can be expressed for a left-looking antenna (LLA) and for a right-looking antenna (RLA) respectively as (cf. **Figure 6.7**) [119]

$$\begin{aligned} \Psi_{sq,LLA}(r_k, t) \approx & \sin^{-1} \left[\cos(\theta_i(r_k) + \theta_{ROLL,ANT}(t)) \cdot \tan(\theta_{PITCH,ANT}(t)) \right. \\ & \left. + \sin(\theta_i(r_k) + \theta_{ROLL,ANT}(t)) \cdot \tan(\theta_{YAW,ANT}(t)) \right], \end{aligned} \quad (6.7)$$

$$\begin{aligned} \Psi_{sq,RLA}(r_k, t) \approx & \sin^{-1} \left[\cos(\theta_i(r_k) + \theta_{ROLL,ANT}(t)) \cdot \tan(\theta_{PITCH,ANT}(t)) \right. \\ & \left. - \sin(\theta_i(r_k) + \theta_{ROLL,ANT}(t)) \cdot \tan(\theta_{YAW,ANT}(t)) \right], \end{aligned} \quad (6.8)$$

where $\theta_{\text{YAW,ANT}}$, $\theta_{\text{PITCH,ANT}}$ and $\theta_{\text{ROLL,ANT}}$ denote the yaw, pitch and roll angles of the antenna array, respectively. These attitude angles can be expressed respectively as

$$\theta_{\text{YAW,ANT}}(t) = \theta_{\text{YAW,IMU}}(t) + \Delta\theta_{\text{YAW}}, \quad (6.9)$$

$$\theta_{\text{PITCH,ANT}}(t) = \theta_{\text{PITCH,IMU}}(t) + \Delta\theta_{\text{PITCH}}, \quad (6.10)$$

$$\theta_{\text{ROLL,ANT}}(t) = \theta_{\text{ROLL,IMU}}(t) + \Delta\theta_{\text{ROLL}}, \quad (6.11)$$

where $\theta_{\text{YAW,IMU}}$, $\theta_{\text{PITCH,IMU}}$ and $\theta_{\text{ROLL,IMU}}$ denote the yaw, pitch and roll angles of the aircraft obtained from the IMU system. The terms $\Delta\theta_{\text{YAW}}$, $\Delta\theta_{\text{PITCH}}$ and $\Delta\theta_{\text{ROLL}}$ denote the attitude angle offsets, which need to be estimated (e.g., by using the approach presented in Section 6.6.3) in case they are not known a priori. In reality, such offsets may arise due to an imperfect alignment of the antenna patches or elements, as well as due to the antenna pod's mounting on the aircraft's fuselage (i.e., non-parallel with respect to the aircraft's longitudinal axis).

The Doppler centroid variation over slant range r_k and over time t can be expressed for a LLA and for RLA respectively as (cf. **Figure 6.7**)

$$\begin{aligned} f_{\text{DC,ATT,LLA}}(r_k, t) \approx & \frac{2 \cdot v_p}{\lambda} \left[\cos(\theta_i(r_k) + \theta_{\text{ROLL,ANT}}(t)) \cdot \tan(\theta_{\text{PITCH,ANT}}(t)) \right. \\ & \left. + \sin(\theta_i(r_k) + \theta_{\text{ROLL,ANT}}(t)) \cdot \tan(\theta_{\text{YAW,ANT}}(t)) \right], \end{aligned} \quad (6.12)$$

$$\begin{aligned} f_{\text{DC,ATT,RLA}}(r_k, t) \approx & \frac{2 \cdot v_p}{\lambda} \left[\cos(\theta_i(r_k) + \theta_{\text{ROLL,ANT}}(t)) \cdot \tan(\theta_{\text{PITCH,ANT}}(t)) \right. \\ & \left. - \sin(\theta_i(r_k) + \theta_{\text{ROLL,ANT}}(t)) \cdot \tan(\theta_{\text{YAW,ANT}}(t)) \right]. \end{aligned} \quad (6.13)$$

The squint angle causes a range dependent Doppler centroid shift. Especially for large squint angles, this range dependency can be clearly recognized in the range-Doppler domain as a J-shaped structure known as ‘‘J-Hook’’ [94] (cf. **Figure 6.8e**).

In reality, also the platform's velocity v_p may change slightly over time t . Therefore, the platform's velocity estimation needs to be updated regularly during the successive CPIs in case no computationally time consuming first-order motion compensation [76] is carried out beforehand.

6.6.3 Attitude Angle Offsets

The results presented in this section were obtained from data take 4 (cf. Appendix A), where the measured data were acquired using a left-looking antenna (LLA). The SAR image containing 2048 x 262144 range-azimuth samples is shown in **Figure 6.8a**.

The estimation of the attitude angle offsets requires two main steps:

1. The reference Doppler centroid of the scene $f_{DC,REF}(r_k, t)$ is estimated from the reference channel RX1 (e.g., by using the energy balancing method proposed in [120]). The result is shown in **Figure 6.8b**, where it was applied a moving window containing 512 x 2048 range-azimuth samples with step sizes of 1.2 m and 3.6 m in slant range and azimuth, respectively;
2. The attitude angle offsets are obtained by the multidimensional minimization (e.g., using the well-known downhill simplex [121] or Powell's methods [122])

$$\operatorname{argmin}_{\Delta\theta_{YAW}, \Delta\theta_{PITCH}, \Delta\theta_{ROLL}} \left\{ \max(\|f_{DC,REF}(r_k, t) - f_{DC,ATT}(r_k, t)\|) \right\}, \quad (6.14)$$

where $f_{DC,ATT}(r_k, t)$ can be obtained from Equation (6.12) or Equation (6.13).

In this experiment, it was obtained from Equation (6.14): $\Delta\theta_{YAW} = 0.86^\circ$, $\Delta\theta_{PITCH} = 0.54^\circ$ and $\Delta\theta_{ROLL} = -0.95^\circ$, which are plausible results in reality. **Figure 6.8c** shows the Doppler centroid of the scene computed by using Equation (6.12) and applying the previously estimated attitude angle offsets.

It is pointed out that similar attitude angle offsets were obtained for data take 1. Thus, the aforementioned procedure can optionally be estimated only once during the flight campaign if the antenna pod remains untouched, which saves processing time.

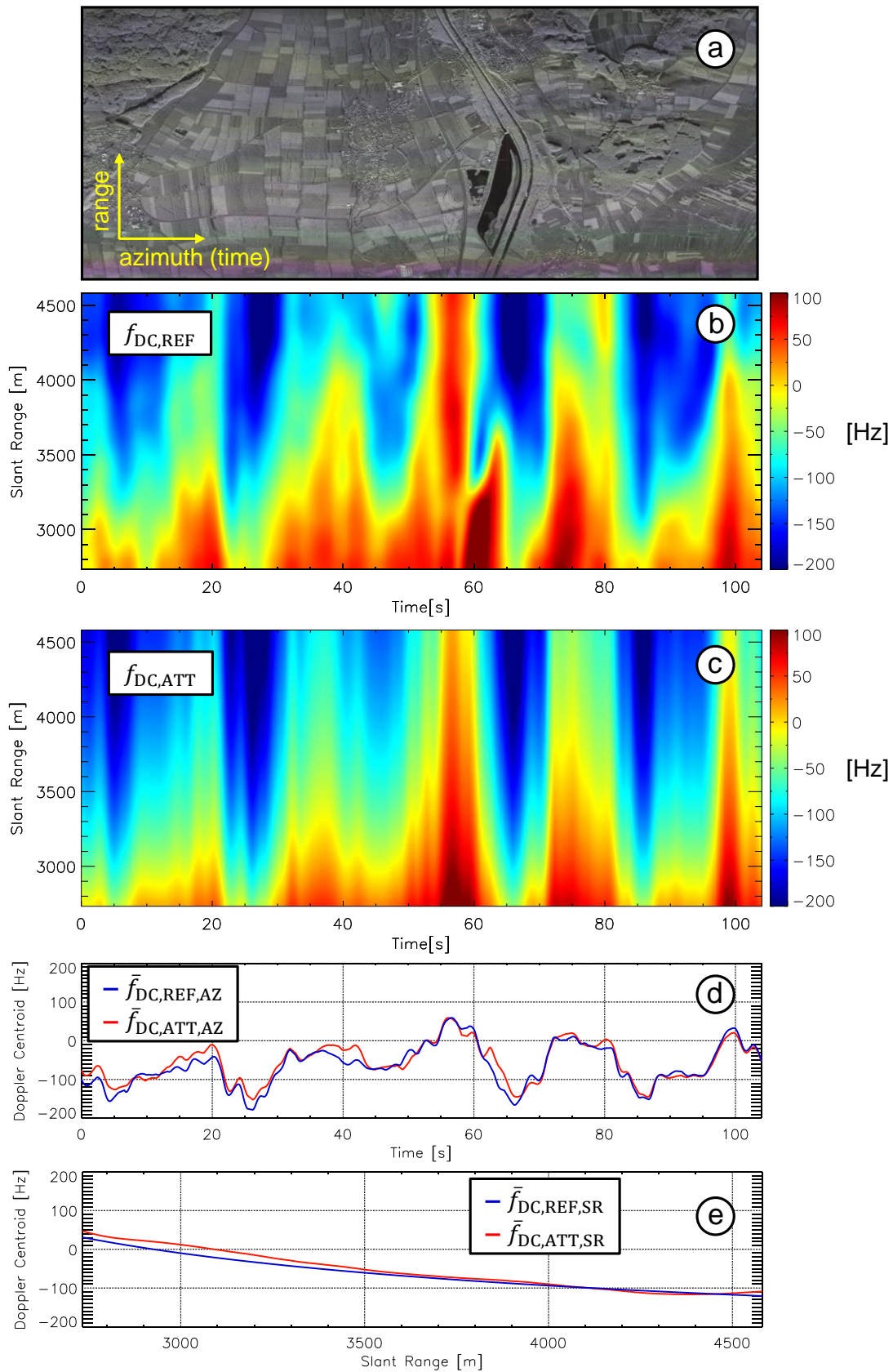


Figure 6.8. (a) SAR image (data take 4); (b) Doppler centroid estimated from the radar data (RX 1); (c) Doppler centroid estimated by using the antenna array's attitude angles; (d) Doppler centroid profiles over azimuth time t and (e) over slant range r_k , where the "J-Hook" shape can be noticed.

The Doppler centroid estimated from the radar data (cf. **Figure 6.8b**) and the Doppler centroid obtained from Equation (6.12) (cf. **Figure 6.8c**) are visually comparable. The visual differences between both images can be explained by three main factors:

1. The measured data contained moving vehicles that were not removed before estimating $f_{DC,REF}(r_k, t)$. Hence, in **Figure 6.8b** a bias was expected especially along the road axes due to the Doppler shift caused by these moving vehicles;
2. A bias was also expected in **Figure 6.8b** in the region of the lake due to its low reflectivity. Note that the highest Doppler values were obtained in this region;
3. A possible misalignment of the antenna phase center (located at the array axis) with respect to the aircraft's longitudinal axis obtained from the IMU system.

The average azimuth profiles of the Doppler centroid shown in **Figure 6.8b** and **Figure 6.8c** can be obtained respectively by

$$\bar{f}_{DC,REF,AZ}(t) = \frac{1}{K} \sum_{k=0}^{K-1} f_{DC,REF}(r_k, t) , \quad (6.15)$$

$$\bar{f}_{DC,ATT,AZ}(t) = \frac{1}{K} \sum_{k=0}^{K-1} f_{DC,ATT}(r_k, t) , \quad (6.16)$$

and the average slant range profiles can be obtained respectively by

$$\bar{f}_{DC,REF,SR}(r_k) = \frac{1}{N_a} \sum_{t=0}^{N_a-1} f_{DC,REF}(r_k, t) , \quad (6.17)$$

$$\bar{f}_{DC,ATT,SR}(r_k) = \frac{1}{N_a} \sum_{t=0}^{N_a-1} f_{DC,ATT}(r_k, t) . \quad (6.18)$$

The results obtained from Equation (6.15) and Equation (6.16) are shown in **Figure 6.8d**. Notice that the average azimuth profiles matched mainly in the regions of crop fields, where the clutter was more homogeneous. In contrast, mismatches are noticed mainly in the central part of the data take 4, where a highway with several moving vehicles was located along the slant range direction.

The results obtained from Equation (6.17) and Equation (6.18) are shown in **Figure 6.8e**, where it can be clearly noticed the J-Hook shape of the Doppler frequency along slant range. As it can be seen, the average slant range profiles of the Doppler centroids matched very well.

6.7 ATI Phase Correction

The ATI signal can be generally computed by multiplying the signal $s_1(t)$ received by the first antenna in the azimuth or flight direction (e.g., antenna “1” in **Figure 3.5**) with the complex conjugate and co-registered signal $s_{i,\text{reg}}^*(t)$ of a second antenna (e.g., antenna “2” up to antenna “M” in **Figure 3.5**) [22]

$$s_{\text{ATI}}(t) = s_1(t) \cdot s_{m,\text{reg}}^*(t), \quad m = 2, \dots, M, \quad (6.19)$$

$$s_{\text{ATI}}(t) = A_1(t) \cdot A_{m,\text{reg}}^*(t) \exp\{j[\varphi_1(t) - \varphi_{m,\text{reg}}(t)]\},$$

where $A_1(t)$ and $A_{m,\text{reg}}(t)$ are the complex coefficients, $\varphi_1(t)$ and $\varphi_{m,\text{reg}}(t)$ are the phases.

If the RCS of the target does not change between the observations in the individual RX channels, then it can be assumed that $A_1 = A_{m,\text{reg}}$. In this case, the ATI phase difference or interferogram can be expressed as

$$\Delta\varphi_{1,m}(t) = \arg\{s_{\text{ATI}}(t)\} = \varphi_1(t) - \varphi_{m,\text{reg}}(t), \quad m = 2, \dots, M. \quad (6.20)$$

Thus, the correction of the residual ATI phase offsets (with respect to RX1) can be carried out in azimuth time domain according to

$$\mathbf{z}_{\text{ATI,corr}}(r_k, t, m) = \mathbf{z}(r_k, t, m) \cdot \exp\{j\overline{\Delta\varphi_{1,m}}\}, \quad m = 2, \dots, M, \quad (6.21)$$

where $\mathbf{z}_{\text{ATI,corr}}$ denotes the measured data after the residual ATI phase correction and $\overline{\Delta\varphi_{1,m}}$ denotes the averages of the interferograms obtained with respect to RX1.

Exemplarily, **Figure 6.9** shows the interferograms obtained among the RX channels (assuming channel RX1 as reference) before and after the correction of the residual ATI phase offsets. In this case, a data patch obtained from data take 4 (cf. Appendix A) was processed containing 1024×16384 range-azimuth samples and the following residual ATI phase offsets were estimated: $\overline{\Delta\varphi}_{1,2} = -66.52^\circ$, $\overline{\Delta\varphi}_{1,3} = 155.62^\circ$ and $\overline{\Delta\varphi}_{1,4} = -72.21^\circ$. Indeed, after the correction of the residual ATI phase offsets the interferograms were centered at zero (i.e., at the green region of the color bar).

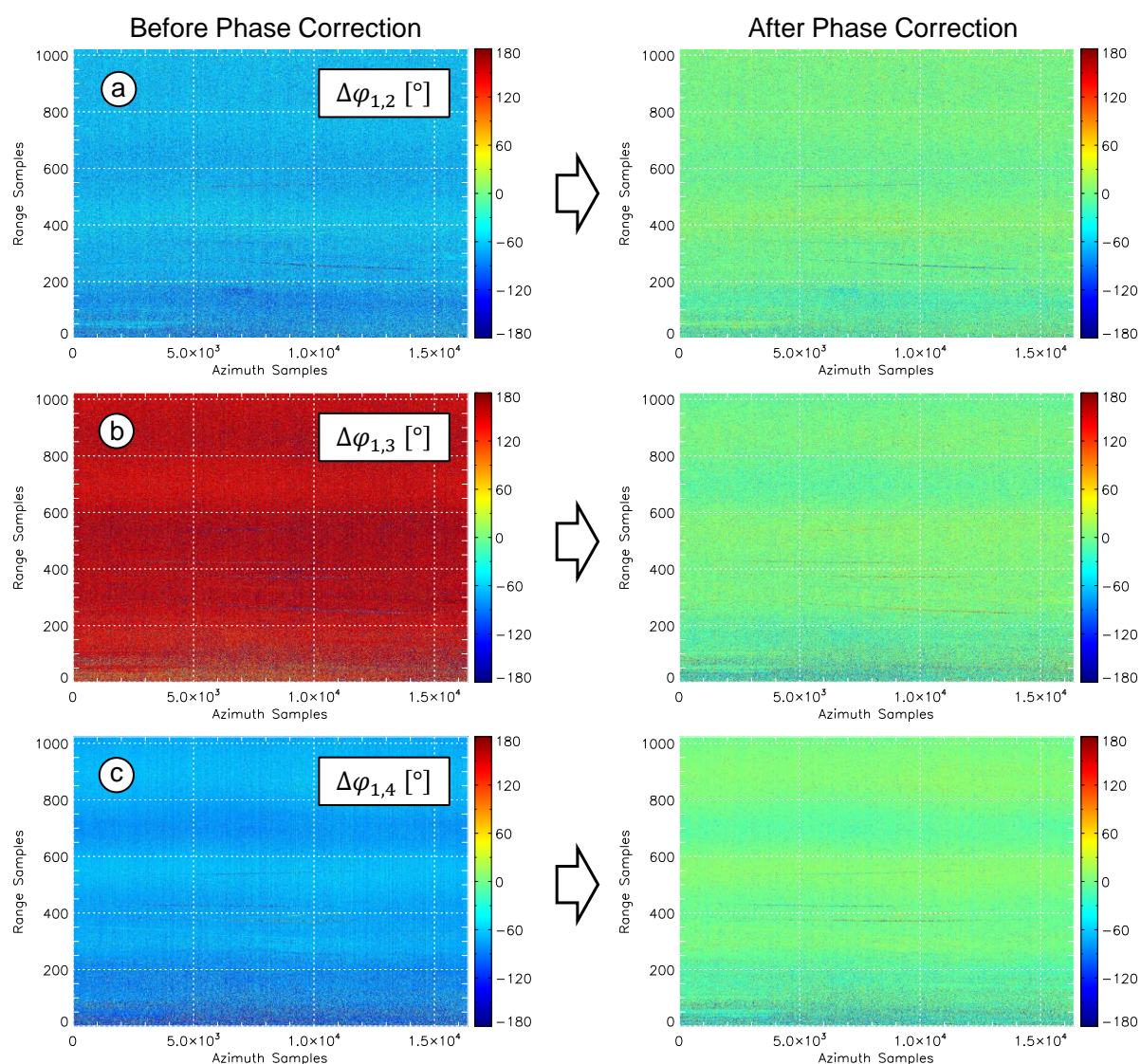


Figure 6.9. Interferograms obtained among the four RX channels for data take 1 ($\overline{\Delta\varphi}_{1,2} = -66.52^\circ$, $\overline{\Delta\varphi}_{1,3} = 155.62^\circ$ and $\overline{\Delta\varphi}_{1,4} = -72.21^\circ$).

6.8 GMTI Results from Data Take 1

In this section, the conventional PD STAP processor (i.e., operational mode 1, cf. Chapter 4) was applied on data take 1 (cf. Appendix A) containing 1024×16384 range-azimuth samples and the probability of false alarm rate was set to $P_{fa} = 10^{-6}$.

Figure 6.10 shows the GMTI results obtained with and without the data calibration algorithm presented in this chapter, where the colors of the PD STAP detections (circles) are related to their estimated ground range velocities. **Figure 6.10a** shows the clean GMTI results obtained with calibrated data, where all cars were detected several times and only a few false detections were obtained. In contrast, **Figure 6.10b** shows the GMTI results obtained with uncalibrated data, where the residual ATI phase and the magnitude offsets as well as the Doppler centroid were not corrected, resulting in systematic phase errors that extended along range and azimuth. Consequently, the cars could not be detected and several false detections as well as wrong position estimates were obtained.

Figure 6.11 shows the histograms of the interferograms obtained from channels RX1 and RX2 with and without calibrating the data (i.e., for the scenarios shown in **Figure 6.10a** and **Figure 6.10b**, respectively). Notice that the interferometric phase obtained without data calibration appears shifted and slightly skewed, which are typical effects of uncalibrated data [116]. In this case, it was expected that the calculation and the application of the CFAR detection thresholds based on the clutter models described in Section 3.4.2 would fail, which explains the several false detections shown in **Figure 6.10b**.

To conclude, the lack of data calibration affects not only the position and the velocity estimates of the moving targets, but it also prevents the estimation of accurate CFAR detection thresholds. Therefore, data calibration is indeed essential for a proper PD STAP operation.



Figure 6.10. Google Earth images overlaid with radar detections (circles) obtained from data take 1: (a) with and (b) without applying the data calibration algorithm presented in this chapter. Notice that without data calibration, the performance of PD STAP is not acceptable. The conventional PD STAP processor (i.e., operational mode 1, cf. Section 4.2) was used and algorithm 4 (cf. Section 7.4.4) was applied for selecting the training data for the CCM estimation.

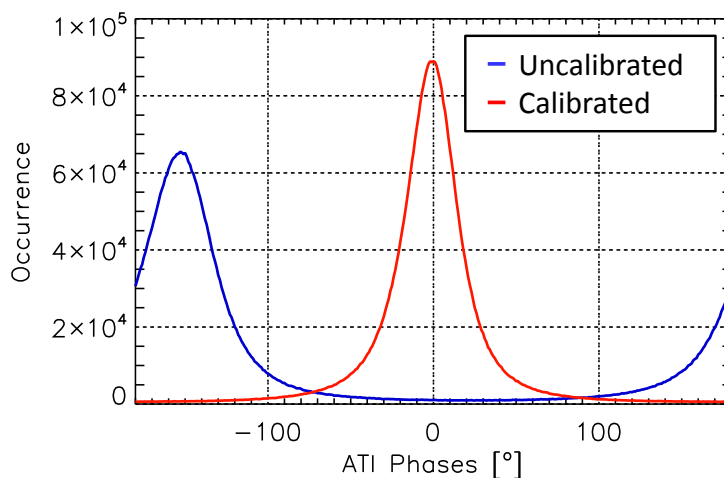


Figure 6.11. Histograms of the interferograms obtained between channels RX1 and RX2 when using calibrated (in red) and uncalibrated data (in blue) (cf. scenarios shown in **Figure 6.10**).

6.9 Chapter Summary

This chapter regards the data calibration algorithm applied on the proposed PD STAP processor for correcting the RX channel imbalances and imperfections. The algorithm corrects not only the residual interferometric phase and the magnitude offsets of the RX channels, but also the Doppler centroid by taking into account the “J-Hook” over slant range and the aircraft’s motion over time. Important parameters (e.g., azimuth antenna patterns, effective along-track baselines, magnitude and attitude angle offsets) can be optionally estimated from the radar data only once and stored in the memory in order to speed up the processing time. This data calibration algorithm is efficient and works very well for different data takes containing different number of roads and moving vehicles, as shown in the experimental results in Chapter 7.

7 Training Data Selection Strategies and Experimental Results

7.1 Chapter Overview

PD STAP is a powerful method for detecting ground moving targets, as well as for estimating their geographical positions and line-of-sight velocities. Essential steps for practical applications of PD STAP are: 1) the appropriate and automatic selection of the training data and 2) the periodic update of these training data in order to take into account the clutter statistics change over space and time. Improper training data and contamination by moving target signals may result in: a decreased clutter suppression performance, an incorrect CFAR threshold and a target cancellation by self-whitening. In this chapter, two conventional and two novel methods for training data selection are presented and compared using measured data acquired with DLR's system F-SAR. In addition, a module for rejecting potential moving target signals and strong scatterers from the training data is proposed and discussed. All methods are evaluated for the conventional and the a priori knowledge-based traffic processors (i.e., operational modes 1 and 2, cf. Chapter 4). A part of the content presented in this chapter was already published in [64] and accepted for a journal publication in [60].

7.2 Introduction

The clutter suppression in STAP algorithms is carried out by applying the inverse of the CCM, which generally has to be estimated from appropriate training data since the clutter spectral properties are rarely known a priori. The selected training data for CCM estimation impact not only on the achievable clutter suppression performance but also on the statistics of the clutter suppressed data, which is employed for fitting a clutter model and for deriving a CFAR detection threshold that achieves CFAR. In this sense, a training data contamination with strong discrete scatterers and interfering moving targets signals may lead to an improper CFAR threshold setting and may cause the "self-whitening" of the target. Therefore, the training data selection plays an important role for an effective application of STAP algorithms [26], [82], [85], [123].

An interesting literature review about training data selection methods is presented in [72]. However, several of the discussed algorithms are time-consuming (e.g., designed for joint-domain STAP, which demands higher sample support and processing time) or may require a massively complex series of decisions to be made in real-time, which is especially the case of knowledge-aided (KA) algorithms.

For instance, the KA parametric covariance estimation (KAPE) approach presented in [124] blends both a priori knowledge information and measured observations in order to mitigate the impact of heterogeneous clutter on space-time detection. Rather than estimating the whole CCM, the KAPE approach estimates the parameters of a CCM model for each individual range bin of interest. Although this approach is robust for STAP applications, it demands an extraordinary computational effort for carrying out the CCM reconstruction. Besides, it is pointed out that: 1) the accuracy of the modeled CCM determines the detection performance potential of KAPE, and 2) the knowledge of the array manifold is critical for the KAPE's clutter suppression capability. An advance of this framework is presented in [125] and denominated as "Enhanced KAPE" (E-KAPE). This new approach improves the KAPE's susceptibility to array errors by applying a new iterative calibration technique. Moreover, the computational burden of KAPE is also improved by circumventing the need for direct inversion of the data matrices for each range bin.

More recently, a KA algorithm showed that the Generalized Inner Product (GIP) test can be applied in the space-Doppler domain in order to remove non-homogeneous training data from the CCM estimation [126]. This method requires a terrain database for obtaining the statistical properties of the clutter for each region of interest (ROI).

Especially when real-time processing is desired, the use of KA algorithms (e.g., those presented in [124]–[126]) would further increase the complexity of STAP algorithms, which are already very demanding in terms of processing time.

This chapter presents an evaluation of four training data selection algorithms that can be combined with a module that rejects potential strong scatterers and moving target

signals. These algorithms are applied on two traffic processors: the conventional PD STAP and a particular PD STAP that uses a priori knowledge information [59] (cf. Chapter 4, operational modes 1 and 2). The main objective is to improve the clutter suppression capability and therefore to increase the number of true detections.

7.3 Real-World Effects

Training data selection and STAP are more challenging when the aircraft is equipped with a low-cost flat antenna array which does not allow electronic or gimbal-based zero-Doppler beam steering. In this case, the time-varying acquisition geometry has to be considered during processing in order to obtain accurate detection, position and velocity estimates.

This section shows some examples of real-world effects obtained on data take 4 (cf. Appendix A). The radar and the geometry parameters are given in [127], [128] as well as in Appendix A. The SAR image (area on ground $\cong 9.4 \times 1.8 \text{ km}^2$) is shown in **Figure 7.1a**. As it can be seen, this vast area contains forests, crop fields, villages and a lake, and therefore it is especially useful for evaluating the clutter statistics change.

As pointed out in Chapter 6, in reality the aircraft is not able to follow exactly a straight flight path due to atmospheric turbulences. **Figure 7.1b** shows the aircraft's attitude angles (yaw, pitch and roll) obtained from the IMU system of the F-SAR during the data acquisition. As it can be seen, the F-SAR collected the SAR data with a positive pitch of around 1.9° , which is typical for F-SAR. Note that the yaw and roll angles changed drastically mainly due to cross-winds. In particular, the yaw variation plays an important role on the Doppler centroid (cf. Section 6.6).

Figure 7.1c shows the Doppler centroid variation over slant range and azimuth (or slow time). The Doppler centroid was estimated from the measured data according to the energy balancing method proposed in [120]. In this example, a moving window containing 512×2048 range-azimuth samples with step size of 1.2 m and 3.6 m in slant range and azimuth, respectively, was applied. The result shown in this figure is discussed in detail in Section 6.6.3.

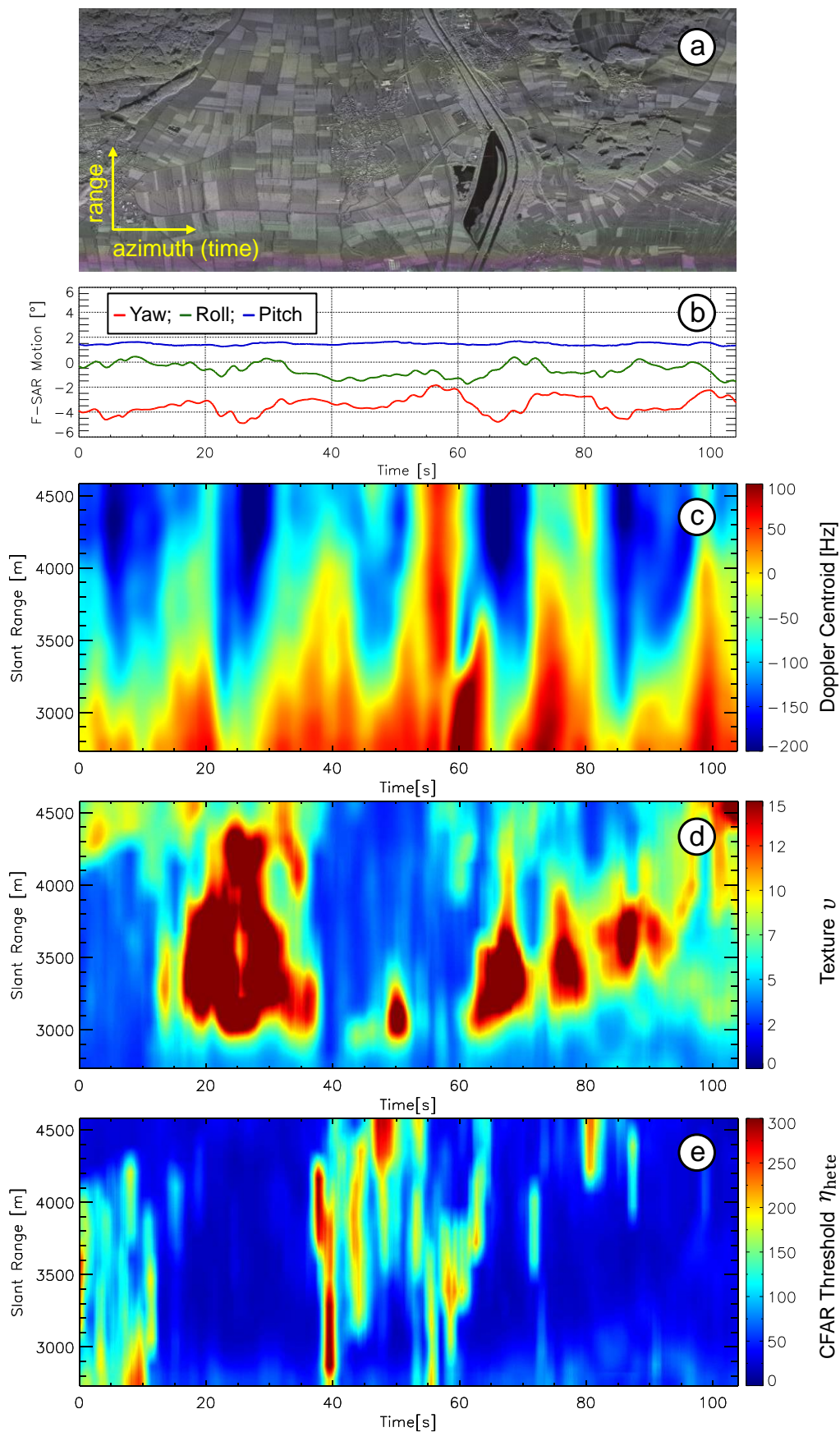


Figure 7.1. Examples of real-world effects on F-SAR data acquisition (data take 4): (a) SAR image, (b) attitude angles, (c) Doppler centroid estimated from the data, (d) texture and (e) CFAR threshold.

Figure 7.1d shows the clutter statistics change in terms of the texture parameter ν , estimated according to Equation (3.27). It can be seen that low texture values were obtained in regions of forests and villages (i.e., heterogeneous clutter patches). In contrast, high texture values were obtained in regions of crop fields as well as over the lake (i.e., homogeneous clutter patches).

Figure 7.1e shows the CFAR detection threshold η_{hete} obtained for $P_{\text{fa}} = 10^{-6}$, estimated according to Equation (3.30). It can be seen from **Figure 7.1d** and **Figure 7.1e** that regions with low texture values lead to high CFAR thresholds, while regions with high texture values lead to low CFAR thresholds, as verified in [31], [93], [98].

The results shown in **Figure 7.1d** and **Figure 7.1e** were obtained by applying a moving window containing 501×128 range-azimuth samples with a moving window step size of 1.2 m and 3.6 m in slant range and azimuth, respectively.

Figure 7.1c, **Figure 7.1d** and **Figure 7.1e** show that indeed the Doppler centroid and the clutter statistics change over slant range and azimuth. Consequently, additionally to the Doppler centroid correction, the training data must be updated periodically over slant range and azimuth. This is especially important for achieving a high performance with any STAP algorithm.

7.4 Algorithms for Training Data Selection and Update

This section presents four training data selection algorithms for the CCM estimation. The algorithms 1 and 2 are examples of conventional methods employed for STAP, while the algorithms 3 and 4 are novel methods [60], [64]. The last topic of this section presents a module for moving target signal rejection (MTSR) that can be applied independently to the four algorithms.

7.4.1 Algorithm 1 (Conventional)

In this algorithm, the CCM is estimated once per CPI using all available samples of the CPI as training data, as depicted in **Figure 7.2**.

In this case, the main steps for processing one CPI are listed below:

1. Obtain the CPI by partitioning the multi-channel data in time domain, in the azimuth direction (e.g., $n_{a,CPI} = 128$ azimuth samples). Use all the available range bins K ;
2. Obtain the training data by using the full content of the CPI. Next, transform the training data to range-Doppler domain via an azimuth FFT;
3. Estimate the CCM according to Equation (3.5), using $K = K_1$;
4. Apply the PD STAP processor on the CPI and estimate the CFAR detection threshold η_{hete} (cf. Section 3.4.2);
5. Detect the moving targets using the CFAR detection threshold η_{hete} . Finally, estimate their parameters (cf. Section 3.3.3);
6. Obtain the next CPI and go back to Step 1.

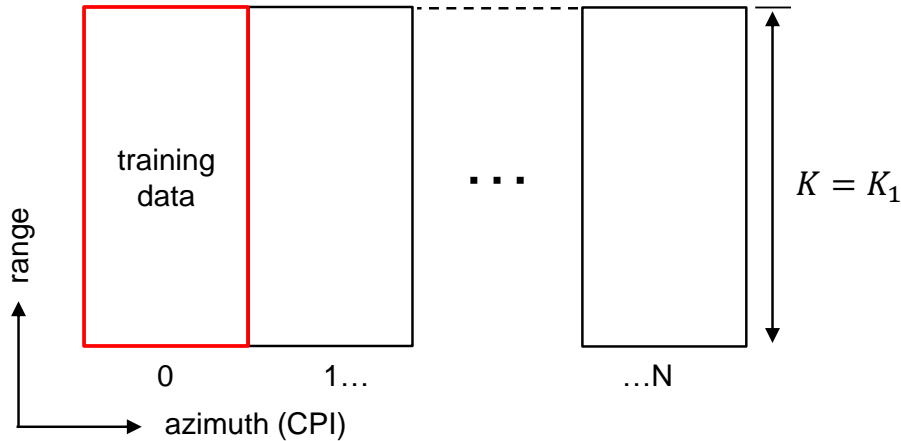


Figure 7.2. Principle of algorithm 1 (conventional). The training data (in red) are obtained by using all the available samples of the CPI. The CCM is estimated once per CPI.

7.4.2 Algorithm 2 (Conventional)

The principle of this algorithm is depicted in **Figure 7.3**. This algorithm applies a moving window along slant range for each CPI, so that the training data (in red) are updated for each cell under test (CUT). In this sense, for each CUT, K_{gz} range bins are used as guard zones and K_2 range bins are selected as training data (e.g., $K_{gz} = 2$ and $K_2 = 128$ range bins).

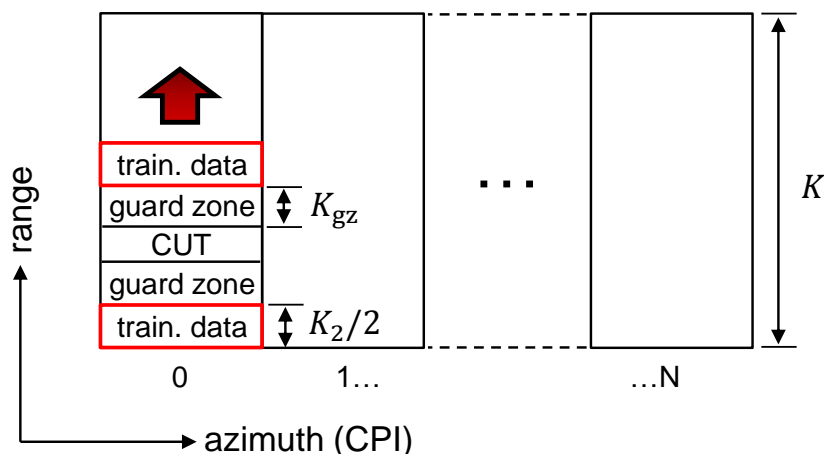


Figure 7.3. Principle of algorithm 2 (conventional). The training data (in red) are updated for each CUT as the moving window slides over slant range. The CCM is estimated K times for each CPI.

In this case, the main steps for processing one CUT are listed below:

1. Obtain the CUT by selecting one range bin of the CPI;
2. Obtain the training data by selecting K_2 range bins around the CUT and the guard zones. Next, transform the training data to range-Doppler domain via an azimuth FFT;
3. Estimate the CCM according to Equation (3.5), using $K = K_2$;
4. Apply the PD STAP processor on the training data for estimating the CFAR detection threshold η_{hete} ;
5. Apply the PD STAP processor on the CUT and detect the moving targets using the CFAR detection threshold η_{hete} . Finally, estimate the parameters of the moving targets;
6. Obtain the next CPI and go back to Step 1.

This algorithm takes into account the clutter change of the scene since the CCM (and therefore the CFAR threshold) is updated adaptively for each CUT as the window moves over slant range. It is pointed out that this algorithm requires a much higher computational effort than algorithm 1, where the CCM is estimated only once per CPI.

Furthermore, a trade-off is observed regarding the chosen number of range bins K_2 of the training data. Note that for large K_2 the algorithm loses robustness against the clutter change, while for small K_2 the training data may be not enough for estimating

reliable CFAR detection thresholds. Special attention has to be given if the MTSR module is applied on this algorithm, since it decreases even further the number of range bins of the training data.

An alternative to overcome this issue is presented by the proposed algorithms 3 and 4, where several CPIs are used as training data within the moving window.

7.4.3 Algorithm 3 (Novel)

The principle of this algorithm is shown in **Figure 7.4**. This algorithm applies a moving window in the azimuth direction, where the length $L = 2T + D$ of the window determines the number of CPIs used as training data (red box in **Figure 7.4**). The CPIs marked as D are those processed by the PD STAP and all L CPIs are used as training data. Besides, note that all the available range bins n_r are used by this algorithm.

The training data array is built by: 1) “stacking” the L CPIs in time domain, and 2) transforming the data array to range-Doppler domain via an azimuth FFT (cf. detail on the right side of **Figure 7.4**). The objective of this algorithm is to increase the number of range bins of the training data by a factor of L (i.e., the training data contain $K \cdot L \times f_{a,CPI}$ range-Doppler samples).

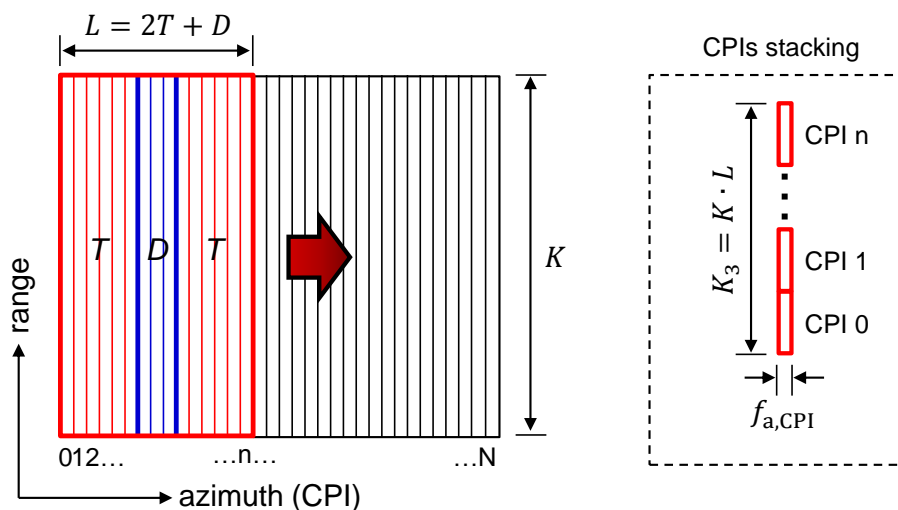


Figure 7.4. Principle of algorithm 3 (novel). The training data (red box) are composed by L CPIs and are updated as the window slides over azimuth. The CPIs D are processed by the PD STAP.

The main steps of this algorithm are listed below:

1. Select the data patch with L CPIs by partitioning the multi-channel data in time domain, in the azimuth direction;
2. Build the training data array by stacking the L CPIs;
3. Estimate the CCM according to Equation (3.5), using $K = K_3 = K \cdot L$;
4. Apply the PD STAP processor on the training data and estimate the CFAR detection threshold η_{hete} ;
5. Apply the PD STAP processor on the CPIs D and detect the moving targets using the CFAR detection threshold η_{hete} . Finally, estimate the parameters of the moving targets;
6. Obtain the next D CPIs and go back to Step 1.

The use of the MTSR module (cf. Section 7.4.5) is very promising in this case, since the “clean” training data still contain enough samples for estimating reliable CFAR detection thresholds. However, this algorithm does not take into account the clutter change over range since all the available range bins K are used. Algorithm 4 is presented in the next section as an alternative solution to this issue.

7.4.4 Algorithm 4 (Novel)

The principle of this algorithm is shown in **Figure 7.5**. As it can be seen, the data patches are processed as the moving window slides over slant range and azimuth. It is assumed that the data patches are partitioned without overlap in slant range.

This algorithm works similarly to algorithm 3, whereas it presents the flexibility to change the number of range bins n_r' of the moving window for taking into account the clutter change over slant range. In this sense, the training data (red box in **Figure 7.5**) contain $L = 2T + D$ truncated CPIs, where only $n_r' < K$ range bins are used.

Similarly to algorithm 3, the training data array is built by stacking the L CPIs in time domain and then transforming the data array to range-Doppler domain via an azimuth FFT (cf. detail on the right side of **Figure 7.5**). The CCM is estimated according to

Equation (3.5), considering $K = K_4 = n'_r \cdot L$. The use of the MTSR module is also promising in this algorithm.

It is important to mention that the length of the moving window (i.e., the choice of the parameters D , T and n'_r) plays a big role for the CCM estimation. The impact caused by different moving window lengths are shown and discussed in Section 7.5.2 based on measured data. The comparison among all algorithms is presented in Section 7.5.5.

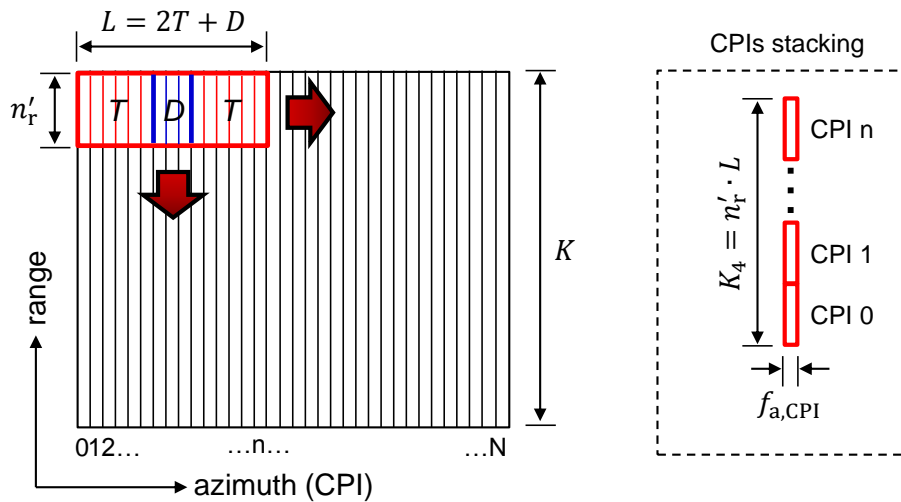


Figure 7.5. Principle of algorithm 4 (novel). The training data (in red) are updated as the window slides over slant range and azimuth. The truncated CPIs D are processed by the PD STAP.

7.4.5 Module for Moving Target Signal Rejection (MTSR)

The Moving Target Signal Rejection (MTSR) is an optional module that can be applied on all previously described algorithms. The objective is to remove undesired range bins of the training data that contain moving target signals and strong scatterers, which would negatively influence on the CCM estimation as well as on the CFAR threshold computation. The principle of the MTSR module is similar to the GIP test presented in [126], including a comparable increase of the processing time. However, in this case the threshold is not based on the amplitude, but rather on the number of azimuth lines (or range bins) to be rejected.

Figure 7.6 shows on the left side a simplified workflow of the proposed MTSR module, where four main steps are carried out:

- Step 1: the PD STAP processor is applied on the original uncleaned training data in order to obtain the range bins of the moving targets. These range bins are stored in the memory and are rejected from the training data only in Step 4;
- Step 2: the magnitudes of all samples contained in the uncleaned training data are sorted (e.g., in descending order);
- Step 3: the number of undesired range bins to be rejected from the uncleaned training data is manually set by the empirical threshold ξ , which needs to be high enough in order to reject at least the range bins of the moving targets;
- Step 4: at first, the undesired range bins of the moving targets (obtained from Step 1) are rejected from the training data. Then, the range bins of the strongest scatterers (sorted in Step 2) are rejected from the training data until the threshold ξ is reached.

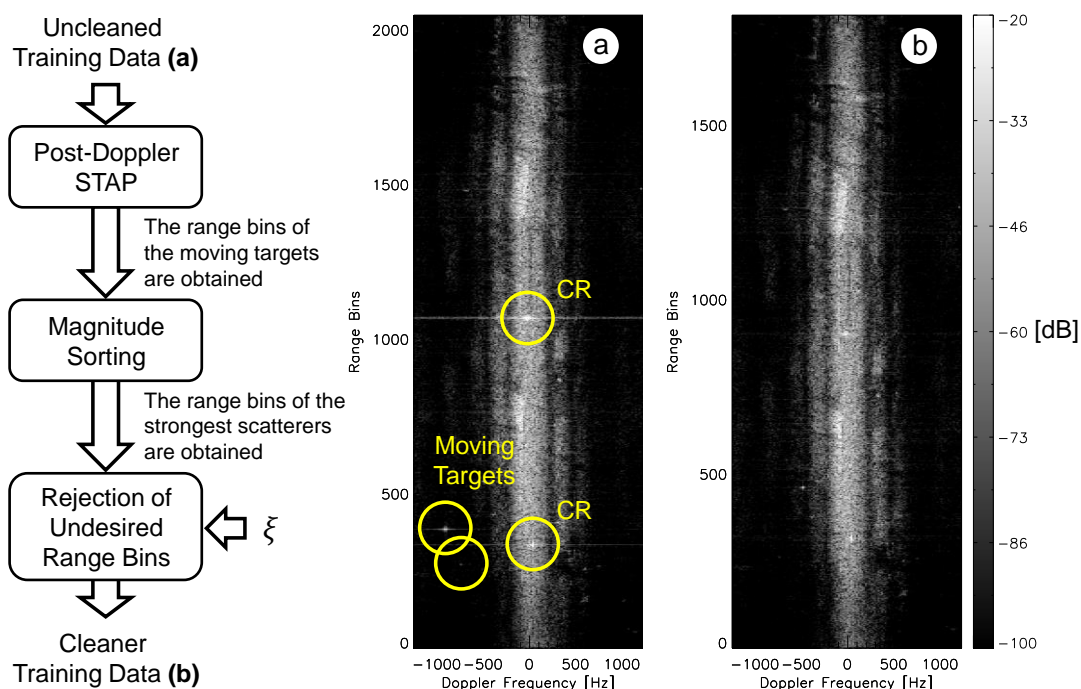


Figure 7.6. Workflow of the proposed MTSR module (left) and an application example based on measured data containing strong scatterers and moving target signals (right). In this example, the sum of the RX channels in range-Doppler domain shows: (a) the uncleaned training data and (b) the cleaner training data obtained after applying the MTSR module. In this case, $\xi = 205$ undesired range bins were rejected. The cleaner training data are used for the CCM estimation.

Exemplarily, **Figure 7.6a** shows an application example where the uncleaned training data (2048 x 128 range-Doppler samples) contained moving target signals and strong scatterers (e.g., corner reflectors – CRs). In this example, the empirical threshold was set to $\xi = 205$ undesired range bins (i.e., $\approx 10\%$ of the total number of available range bins). After applying the MTSR module, the cleaner training data were obtained with 1843 azimuth lines, as shown in **Figure 7.6b**. In this figure, notice that the moving target signals and most of the strong scatterers were rejected (including the CRs). The cleaner training data are used for the CCM estimation.

The experimental results presented in Section 7.5 show that the empirical threshold ξ worked very well for different data sets with different number of moving targets. An analysis of the impacts of the MTSR module on the clutter model using real multi-channel data is presented in Section 7.5.3.

7.5 Experimental Results

In this section, the training data selection algorithms are firstly compared using data takes 1 to 3 (cf. Appendix A), which contained five controlled cars with different positions and velocities. The moving window parameters are evaluated for algorithms 3 and 4, as well as the impact of the MTSR module on the estimated texture parameter and on the CFAR threshold. GMTI results for data take 1 show the main differences among the training data selection algorithms and quantitative comparisons are carried out based on the number of true and false detections, as well as on the estimated probability of false alarm rate. GMTI results are also presented for data take 4 in order to test algorithm 4 (with MTSR) in a real traffic scenario. Finally, experimental results obtained with the fast PD STAP processor (cf. Section 4.4) are shown and discussed.

7.5.1 Experimental Setup

A detailed experiment description of the flight campaign and the radar parameters are presented in [36], [115], and in Appendix A. The data takes were processed using CPIs containing 1024 x 128 range-azimuth samples and the beamformers were

applied using DOA angle steps of 0.05° defined within the 3 dB antenna beamwidth in azimuth. The probability of false alarm rate was set to $P_{fa} = 10^{-6}$.

7.5.2 Moving Window Parameters

The choice of the moving window parameters (D , T and n_r') for algorithms 3 and 4 plays an important role since it defines not only the amount of training data used for the CCM estimation, but also how often the training data are updated. In the following experiments, the data take 1 was processed by algorithms 3 and 4 (with MTSR), where different moving window lengths were applied. The PD STAP processor with road map information was used in the following experiments for counting the number of detections relocated to the airport's runway.

Experiment 1: Parameters D and T

In this experiment, the data take 1 was repeatedly processed by algorithm 3 (with MTSR) using different moving window lengths (i.e., varying the parameters D and T). All available range bins K were considered. **Figure 7.7a** shows the number of true detections of cars 1 to 4 (i.e., $\text{True}_{\#1-4}$) as a function of the parameters D and T . These detections could be counted as true since the velocities and the positions of the cars were known. The detections of car 5 were not counted since it moved off-road and thus its detections were discarded after applying the road map information.

Figure 7.7b shows the number of false detections relocated to the runway as a function of the parameters D and T . In this case, the numbers of false detections were obtained by subtracting the number of true detections ($\text{True}_{\#1-4}$) from the number of total detections. **Figure 7.7** shows that both the number of true and false detections increases proportionally with the length of the moving window. For instance, a good compromise can be achieved when $D = 15$ and $T = 12$, where 450 true detections and only 2 false detections were obtained. Therefore, these parameters were chosen for the moving window applied on algorithms 3 to 4, so that $L = 2T + D = 39$ CPIs, which corresponds to approximately two seconds of data acquisition.

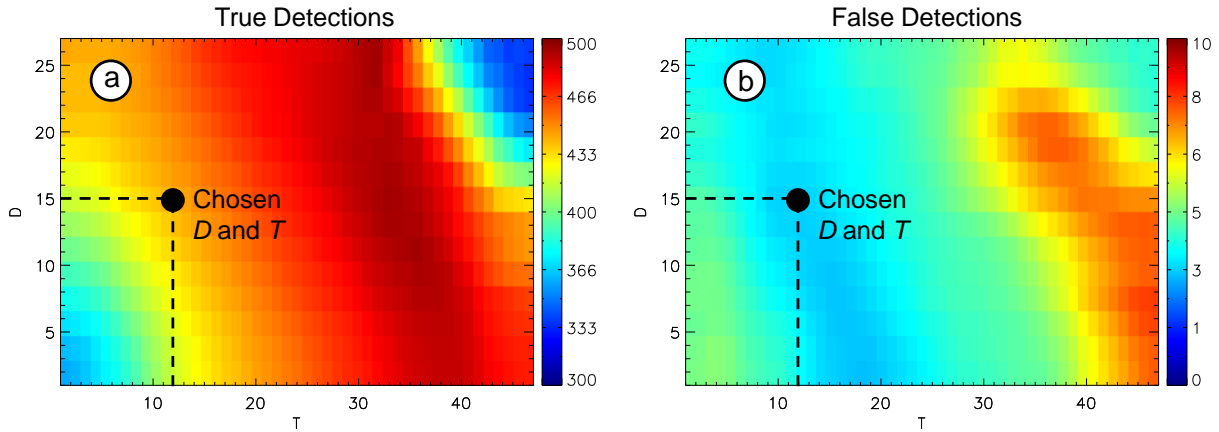


Figure 7.7. Number of detections relocated to the runway as function of parameters D and T : (a) true detections ($\text{True}_{\#1-4}$); (b) false detections ($\text{Relocated} - \text{True}_{\#1-4}$). All available range bins K were used.

Experiment 2: Number of Range Bins

In this experiment, the data take 1 was repeatedly processed by algorithm 4 (with MTSR) assuming $D = 15$ and $T = 12$, and varying the number of range bins n'_r of the moving window. Once more, only the detections from cars 1 to 4 were counted as true ($\text{True}_{\#1-4}$).

Figure 7.8a shows that the number of detections (all, relocated and true) obtained from each moving window. As it can be seen, the levels increased as the number of range bins n'_r increased, reaching the peak at $n'_r = 512$. In other words, up to this point ($n'_r \leq 512$) the CCM estimation benefited from the increase of training data. Beyond this point ($n'_r > 512$), algorithm 4 lost its robustness against the clutter change over range. As a result, the number of detections (all, relocated and true) started decreasing. Note that the numbers of range bins n'_r were applied as a power of two, since the window moved without overlap over range.

The same trend is observed in the percentages of detections shown in **Figure 7.8b**, calculated using the values from **Figure 7.8a**. Moreover, the results obtained with data takes 2 and 3 followed the same trend as for data take 1, whose results are shown in **Figure 7.7** and **Figure 7.8**.

The chosen parameter for algorithm 4 was $n'_r = 512$, which is used for obtaining the results presented in the next sections.

The results obtained from experiments 1 and 2 pointed out the impact of the moving window parameters on the SAR data. In reality, the most suitable moving window parameters depend on the scene and on the aircraft's motion. The parameters chosen for data take 1 (i.e., $D = 15$, $T = 12$ and $n'_r = 512$) are also applied for processing the other data takes considered in this doctoral thesis (cf. Appendix A).

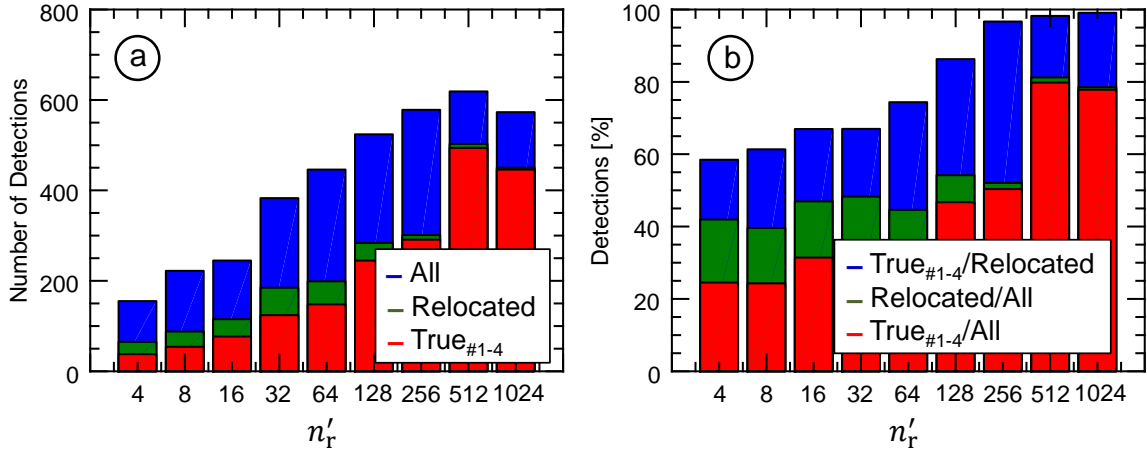


Figure 7.8. (a) Number and (b) percentage of detections as function of the number of range bins n'_r of the moving window. It was assumed the parameters $D = 15$ and $T = 12$, so that $L = 2T + D = 39$ CPIs ($\cong 2$ s of data acquisition).

7.5.3 Impact of MTSR on Clutter Model

In this section, the conventional algorithm 1 was used to process the data take 1. As described in Section 7.4.1, this algorithm estimates the CCM (and therefore the texture parameter and the CFAR detection threshold) once per CPI. In other words, by using this algorithm, it is possible to verify the variation of the texture and the CFAR threshold over time (1 CPI ≈ 0.05 s of data). In this experiment, $\xi = 205$ undesired range bins were rejected from the training data when the MTSR module was applied.

Figure 7.9a shows the texture variation over time with and without applying the MTSR module. As expected, high texture values (i.e., more homogeneous) were obtained after applying the MTSR module since strong scatterers and moving target signals were removed from the training data. In addition, the texture variation over time was smoother when the MTSR module was applied.

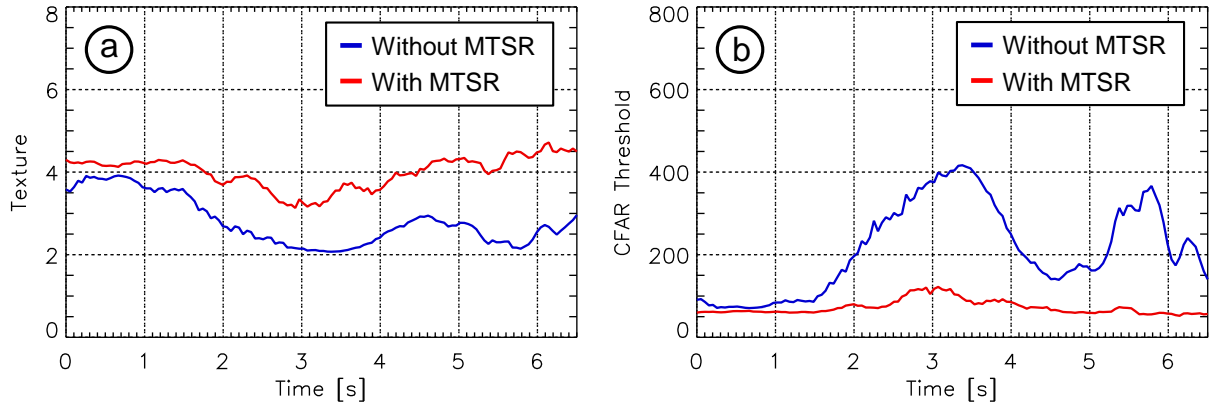


Figure 7.9. Impact of the MTSR module on the heterogeneous clutter model: (a) texture parameter ν and (b) CFAR detection threshold η_{hete} . In this case, algorithm 1 was used to process the data take 1.

Figure 7.9b shows the CFAR threshold variation over time with and without applying the MTSR module. As pointed out in Section 3.4.2, it is possible to note that the lower the texture (i.e., the more heterogeneous), the higher the CFAR threshold. In this sense, the decrease of the CFAR threshold after applying the MTSR module was expected since the texture values were higher. Besides, the CFAR threshold variation was much smoother after applying the MTSR module.

For data take 1, it is pointed out that the runway with cars 1 to 4 was located in the center of the image (i.e., around 3.3 s of data). Therefore, around this time instant, it is possible to notice in **Figure 7.9** that the texture values reached its minimum (i.e., most heterogeneous point) and the CFAR thresholds reached its maximum.

The MTSR module has the benefit to make the texture and the CFAR threshold less sensitive to moving target signals and strong unsuppressed scatterers. However, the MTSR module increases the processing time since the PD STAP core needs to be applied on the training data for detecting the range bins that contain moving target signals.

7.5.4 GMTI Results for Data Take 1

The PD STAP detections obtained by algorithms 1 to 4 are shown in **Figure 7.10**. In this figure, the colors of the detections are related to their absolute ground range velocities. In **Figure 7.10e**, a detail is shown for algorithm 4 in order to demonstrate

the relocation of the targets to the road axis of the OSM, carried out by the PD STAP processor with road map information [59]. In this case, the radar detections are shown before (circles) and after (triangles) relocation using the OSM database, where the center of the runway (white line) was considered as road axis. The triangles point to the moving direction of the cars and the thin yellow lines connect the PD STAP detections to their closest road points on the OSM road axis.

It can be seen from **Figure 7.10** that:

- Algorithm 1 could not detect car 3. Indeed, in this case all available samples of the CPI were used as training data (i.e., including moving target signals and strong scatterers), which lead to the self-whitening of car 3;
- Algorithm 2 was able to detect all the cars several times, whereas it presented by far the highest number of false detections. Indeed, this algorithm used the most reduced amount of training data for the CCM estimation (128 range bins). In addition, moving target signals and strong scatterers contained in the training data worsened the performance of this algorithm;
- Algorithm 3 was able to detect all the cars, presenting a very clean overall result. This result is explained by the large amount of training data used for CCM estimation ($L = 39$ CPIs and $n_r = 1024$ range bins). Thus, even without applying the MTSR module, reliable CFAR thresholds could be estimated for discarding most of the false detections;
- Algorithm 4 had a very similar result as algorithm 3, whereas in this case more detections were obtained from the slow cars 1 and 3. In this case, the amount of training data used for the CCM estimation was still large enough ($L = 39$ CPIs and $n'_r = 512$ range bins) for estimating reliable CFAR thresholds. Moreover, the moving window took into account the clutter change over range.

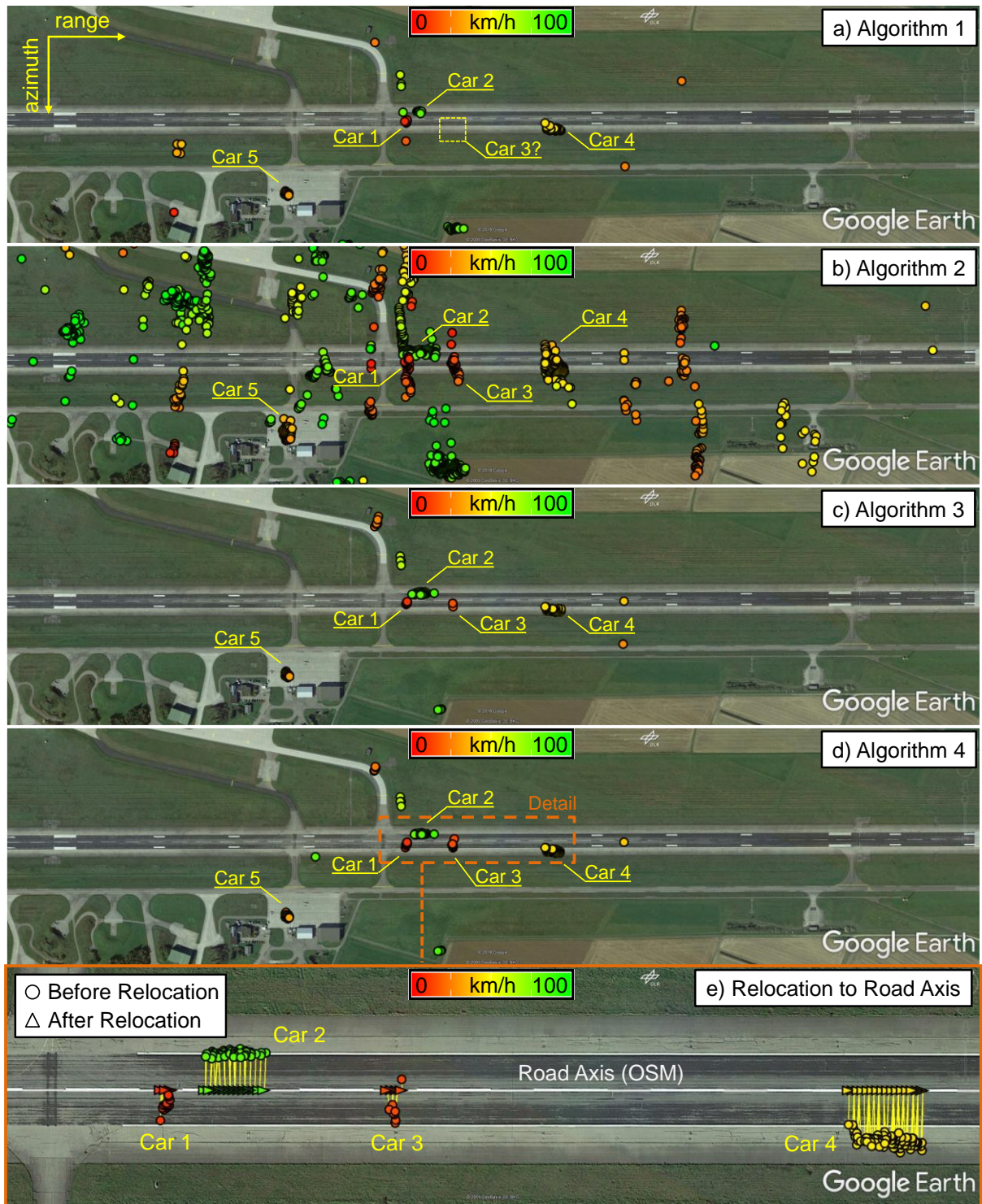


Figure 7.10. Google Earth images overlaid with PD STAP detections. Algorithms 1 to 4 (without MTSR) were applied for selecting the training data for the CCM estimation. The detail (orange box) shows the relocation of the detections (circles) to their closest OSM road points (triangles) [59], [58] using the algorithm 4 (without MTSR). The center of the runway (white line) was the OSM road axis.

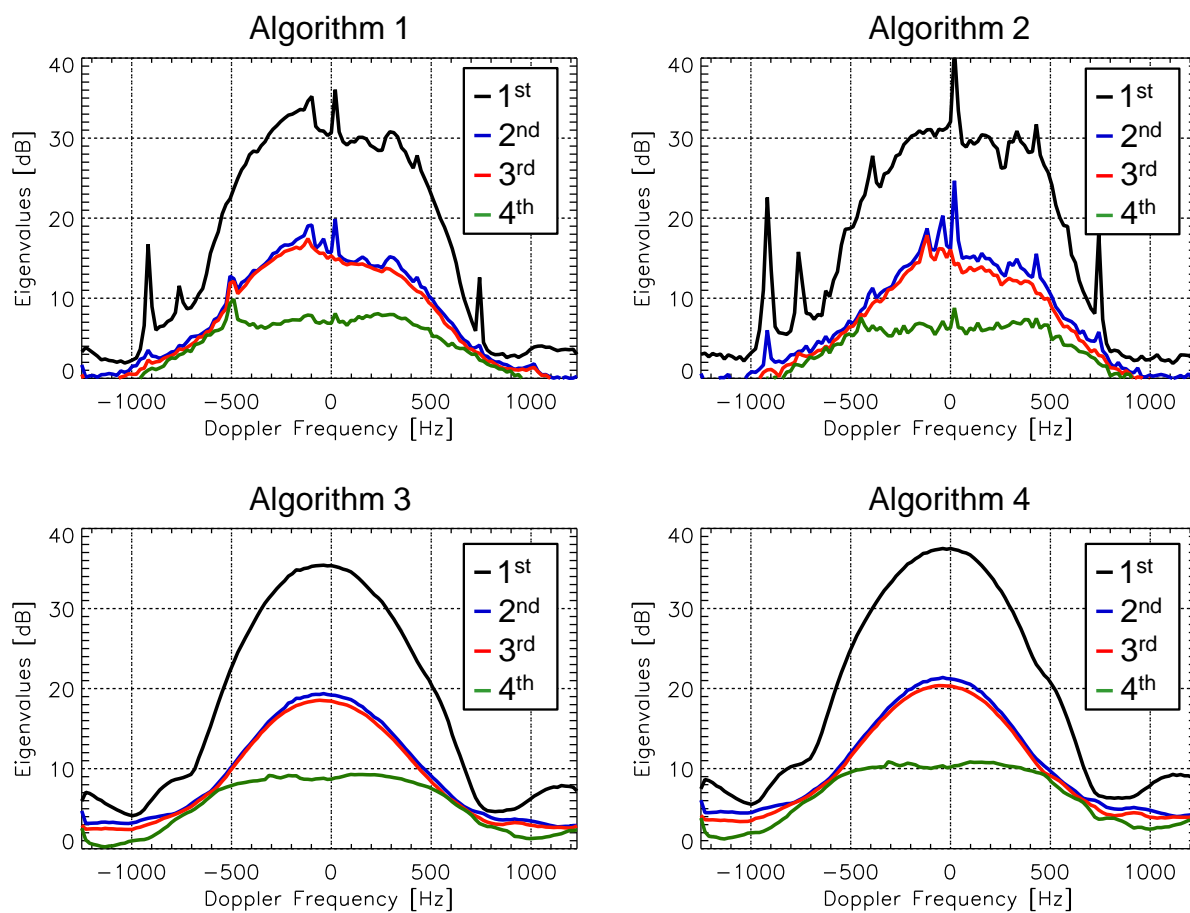


Figure 7.11. Eigenvalues obtained from the training data selected by algorithms 1 to 4 (without MTSR) for the CCM estimation.

Figure 7.11 shows the eigenvalues (normalized to the noise power) obtained from the training data selected by the four algorithms for the CCM estimation. In this case, the processed data patch contained part of the runway where the cars 1 to 4 moved, so that the impact of the moving target signals can be verified in the eigenvalue distributions. For algorithms 1 and 2, the eigenvalue distributions exhibited spikes due to the influence of strong scatterers and moving target signals. The highly contaminated eigenvalue distributions obtained for algorithm 2 explain why this algorithm presented the highest number of false detections (cf. **Figure 7.10b**). In contrast, the eigenvalue distributions obtained by algorithms 3 and 4 were very smooth due to the large amount of training data used by these algorithms.

The eigenvalue distributions can also be useful for verifying the clutter suppression capability of the PD STAP processor, which in this case is given by the highest

difference between the first and the second eigenvalues (≈ 15 dB). The clutter suppression capability could be further improved, for instance, by using more sophisticated digital channel calibration techniques [116]. However, this is out of the scope for this doctoral thesis. The fourth eigenvalue is in the noise power level.

The benefits of the MTSR module can be verified through the ground range velocities histograms of the PD STAP detections, shown in **Figure 7.12**. This figure also allows to compare the amount of false (blue bars) and true detections (red bars) obtained for all algorithms. Once more, the true detections (i.e., $\text{True}_{\#1-5}$) could be counted since the positions and the velocities of all cars were known a priori.

It can be seen from **Figure 7.12** that:

- Algorithm 1 benefited from the MTSR especially because car 3 was detected (i.e., its self-whitening was solved after selecting the training data with the MTSR module). Nevertheless, note that in this case the number of true and false detections increased;
- Algorithm 2 did not benefit from the MTSR since its amount of training data was further decreased. As a result, car 1 was barely detected and car 3 was not detected anymore. In this case, note that the MTSR module decreased both the number of true and false detections;
- Algorithms 3 and 4 benefited from the MTSR and presented the best results. The MTSR module increased the number of true detections (especially from the slower cars 1 and 3), whereas the number of false detections also increased.

In general, all algorithms presented accurate velocities estimates of all cars. The estimated positions were also accurate considering that the cars 1 to 4 moved on the edges of the runway (cf. Appendix A).

This section showed that the MTSR module increased the number of true and false detections for algorithms 1, 3 and 4. In contrast, the number of true and false detections for algorithm 2 decreased. A quantitative comparison among all algorithms is presented in Section 7.5.5, highlighting the pros and cons of the MTSR module.

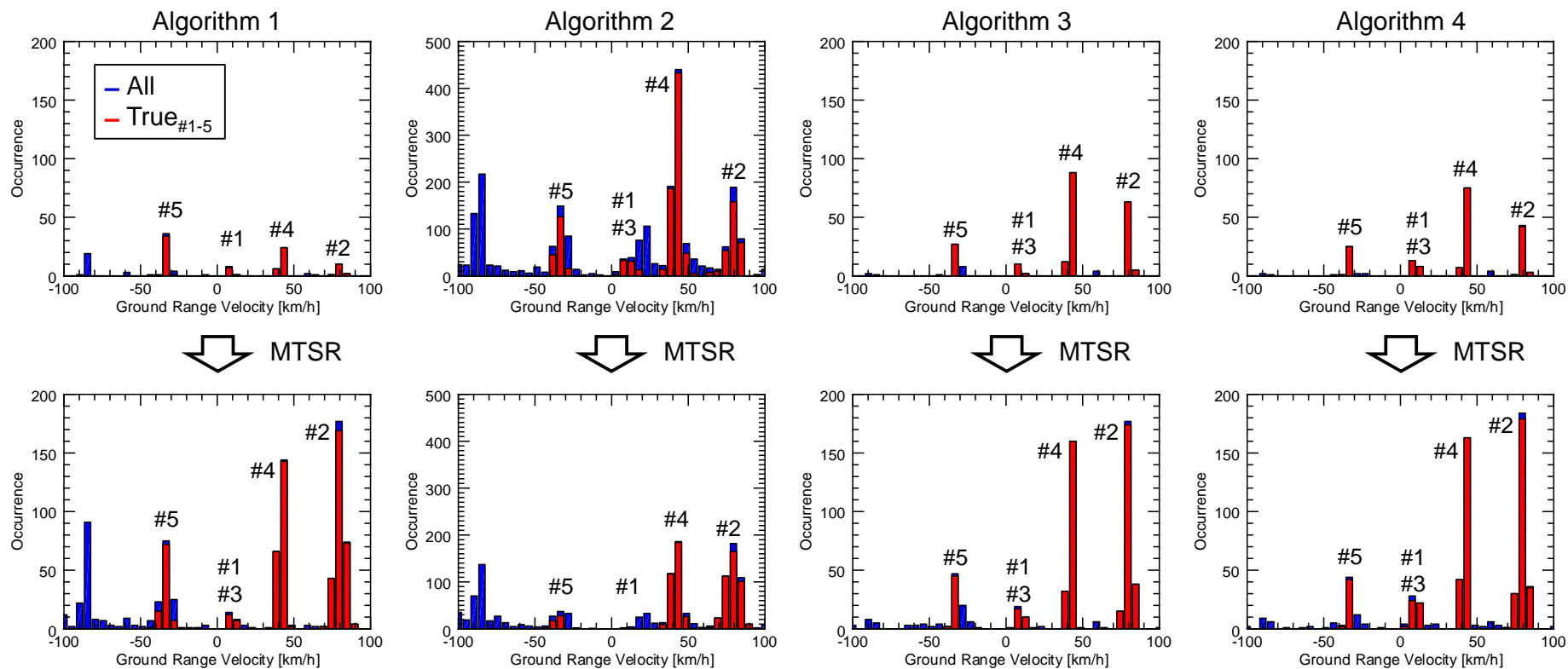


Figure 7.12. Ground range velocity histograms of the detections obtained by algorithms 1 to 4: all (blue bars) and true (red bars) detections. The detections obtained from cars 1 to 5 are numbered in the histograms. In this experiment, the data take 1 was processed.

7.5.5 Quantitative Comparisons for Data Takes 1 to 3

Quantitative comparisons among the training data selection algorithms are shown in **Table 7.1**, **Table 7.2** and **Table 7.3**, which summarize for data takes 1 to 3:

- The number of all detections obtained by the PD STAP processor;
- The number of relocated detections to the runway. This number was counted by using the PD STAP processor with a priori knowledge information (i.e., operational mode 2, cf. Chapter 4). Notice that for data takes 1 and 2 only the cars 1 to 4 were relocated to the runway since car 5 moved off-road;
- The number of true detections. This number was counted since the positions of the cars were known a priori for the data takes 1, 2 and 3;
- The estimated probability of false alarm \hat{P}_{fa} , which is shown with respect to the desired probability of false alarm of the CFAR detector (i.e., $\hat{P}_{fa} = 10^{-6}$);
- The percentage of true detections relocated to the runway. This quantity is very helpful for comparing all training data selection algorithms, with and without applying the MTSR module.

The probability of false alarm \hat{P}_{fa} was estimated according to:

$$\hat{P}_{fa} = \frac{\text{All-True}_{\#1-5}}{N_a \cdot K}, \quad (7.1)$$

where the numbers of processed range and azimuth samples (K and N_a , respectively) of the data takes 1 to 3 are (cf. Appendix A):

- Data take 1: $K = 1024$, $N_a = 16384$;
- Data take 2: $K = 1024$, $N_a = 32768$;
- Data take 3: $K = 1024$, $N_a = 32768$.

TABLE 7.1
NUMBER OF DETECTIONS FROM DATA TAKE 1 (RUNWAY AT 90°)

Algorithm	All	Relocated	True (#1-4)	True (#1-5)	\hat{P}_{fa} [$\times 10^{-6}$]	True _{#1-4} /Relocated [%]
1	134	53	51	77	3.40	96.23
2	2470	1195	1073	1208	75.22	89.79
3	223	181	180	203	1.19	99.45
4	188	151	149	171	1.01	98.68
1 (MTSR)	880	539	522	593	17.11	96.85
2 (MTSR)	1439	834	760	800	38.09	91.13
3 (MTSR)	573	450	448	487	5.13	99.55
4 (MTSR)	625	507	502	537	5.25	99.01

TABLE 7.2
NUMBER OF DETECTIONS FROM DATA TAKE 2 (RUNWAY AT 45°)

Algorithm	All	Relocated	True (#1-4)	True (#1-5)	\hat{P}_{fa} [$\times 10^{-6}$]	True _{#1-4} /Relocated [%]
1	457	100	86	101	10.61	86.00
2	6897	1819	1574	2150	141.47	86.53
3	396	188	182	269	3.78	96.81
4	388	106	105	150	7.09	99.06
1 (MTSR)	3052	932	806	1423	48.55	86.48
2 (MTSR)	3905	1153	1006	1434	73.64	87.25
3 (MTSR)	1102	589	586	900	6.02	99.49
4 (MTSR)	957	498	497	690	7.96	99.80

TABLE 7.3
NUMBER OF DETECTIONS FROM DATA TAKE 3 (RUNWAY AT 30°)

Algorithm	All	Relocated	True (#1-5)	\hat{P}_{fa} [$\times 10^{-6}$]	True _{#1-5} /Relocated [%]
1	478	350	243	7.00	69.43
2	3328	1985	1606	51.32	80.91
3	302	224	193	3.25	86.16
4	223	135	115	3.22	85.19
1 (MTSR)	1869	1270	972	26.73	76.54
2 (MTSR)	1752	1076	884	25.87	82.16
3 (MTSR)	431	342	312	3.54	91.23
4 (MTSR)	282	187	169	3.37	90.38

From **Table 7.1**, **Table 7.2** and **Table 7.3**, it can be seen that:

- The MTSR module increased the \hat{P}_{fa} of algorithms 1, 3 and 4 for all data takes. In other words, it means that the number of false detections increased more than the number of true detections. However, it was shown in Section 7.5.4 that the MTSR module applied on algorithm 1 avoided the self-whitening of car 3. Thus, since the \hat{P}_{fa} obtained for algorithms 3 and 4 after applying the MTSR were tolerable, the MTSR is recommended for algorithms 1, 3 and 4;
- The MTSR module decreased the \hat{P}_{fa} of algorithm 2 on all data takes by nearly the half, which at a first glance looks as an improvement. However, several true detections were lost after applying the MTSR module (e.g., car 3 was not detected) and this algorithm presented the worst \hat{P}_{fa} . Thus, the MTSR module is not recommended for algorithm 2;
- The last column shows the percentage of true detections that remained in the final image after applying a priori knowledge information. In this case, the MTSR module applied on algorithms 3 and 4 presented the best results for all data takes. In the worst case scenario (for data take 3), 90% of the detections were true by using algorithm 4 with MTSR. These values show the great potential of the PD STAP processor with a priori knowledge information [59], [58].

The amount of training data is of great importance for the CCM estimation. In this sense, it was expected that the proposed algorithms 3 and 4 presented the best \hat{P}_{fa} and the best percentages of true detections for all data takes.

Additionally, it is pointed out that a threshold was applied in order to reject detections with SCNRs lower than 10 dB, as described in [63].

7.5.6 GMTI Results for Data Take 4

The PD STAP processor with a priori knowledge information (i.e., operational mode 2, cf. Chapter 4) was applied on a data patch obtained from data take 4 (2048 x 16384 range-azimuth samples, where part of the highway A7 was contained with several vehicles of opportunity. Algorithm 4 (with MTSR) was applied for selecting the training data for the CCM estimation and the moving window parameters were: $D = 15$, $T = 12$ and $n'_r = 512$ (as discussed in Section 7.5.2). The probability of false alarm rate was set to $P_{fa} = 10^{-6}$.

Figure 7.13 shows the GMTI results, where the moving cars are depicted as colored triangles pointing to their heading directions and the highway A7 is shown in white. The colors are related to the absolute velocities of the cars on the road v_{road} , estimated according to Equation (3.19). The information box in **Figure 7.13** shows some examples of parameters that are obtained for each car on the highway.

For instance, it is possible to verify the traffic situation in both directions of the highway A7 according to the ground range velocity histograms of the PD STAP detections, as shown in **Figure 7.14a**. This figure shows the histograms of the total (blue bars) and the relocated (red bars) detections on the highway. As it can be seen, the traffic towards Ulm (i.e., positive ground range velocities) was more intense than the traffic towards Memmingen (i.e., negative ground range velocities).

It is also possible to verify the histograms of the SCNR of the PD STAP detections, as shown in **Figure 7.14b**. This figure shows the histograms of the total (blue bars) and the relocated (red bars) detections on the highway A7. In both cases, the mean SCNR of the cars was about 27 dB. Once more, it is pointed out that a threshold was applied in order to reject detections with SCNRs lower than 10 dB [63].

No ground truth data were available in this experiment and thus it was not possible to compute the percentage of true detections, the probability of false alarm and the errors of the estimated velocities and positions. Nevertheless, the estimated velocities obtained on the highway A7 were reasonable.

Finally, it can be seen from **Figure 7.10** and **Figure 7.13** that the PD STAP processor was able to detect each single car several times, revealing the potential of this processor for traffic monitoring applications. It has to be pointed out that no clustering or tracking algorithms were applied in this experiment for refining the GMTI results.

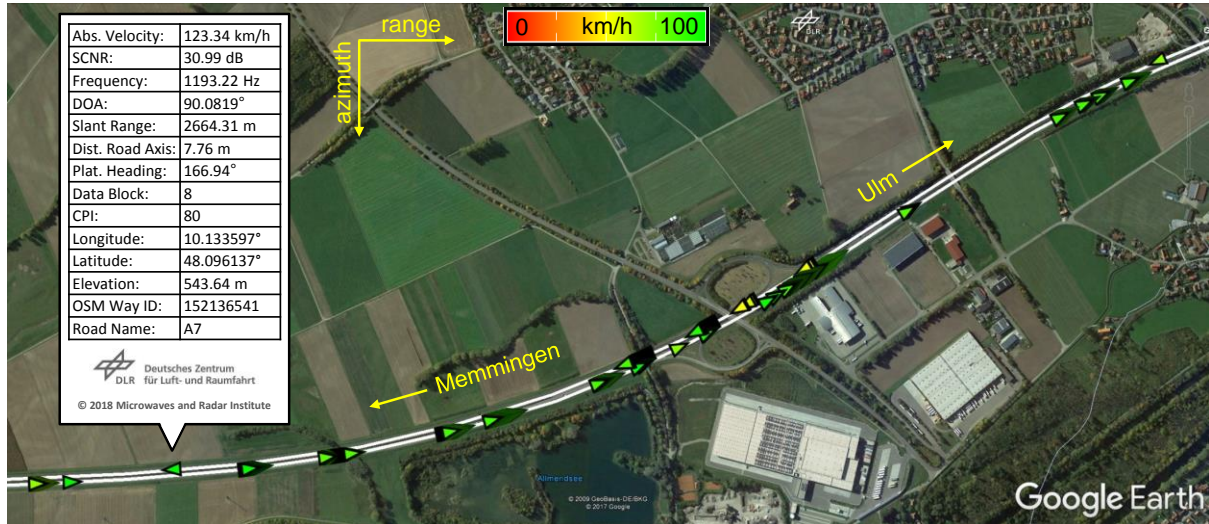


Figure 7.13. Real traffic on the highway A7. The OSM road axis is shown in white and the cars (triangles) are color coded according to their absolute velocities on the road. The cars were detected and their parameters were automatically estimated using the PD STAP processor with a priori knowledge information [59], [58]. Algorithm 4 (with MTSR) was used for training data selection.

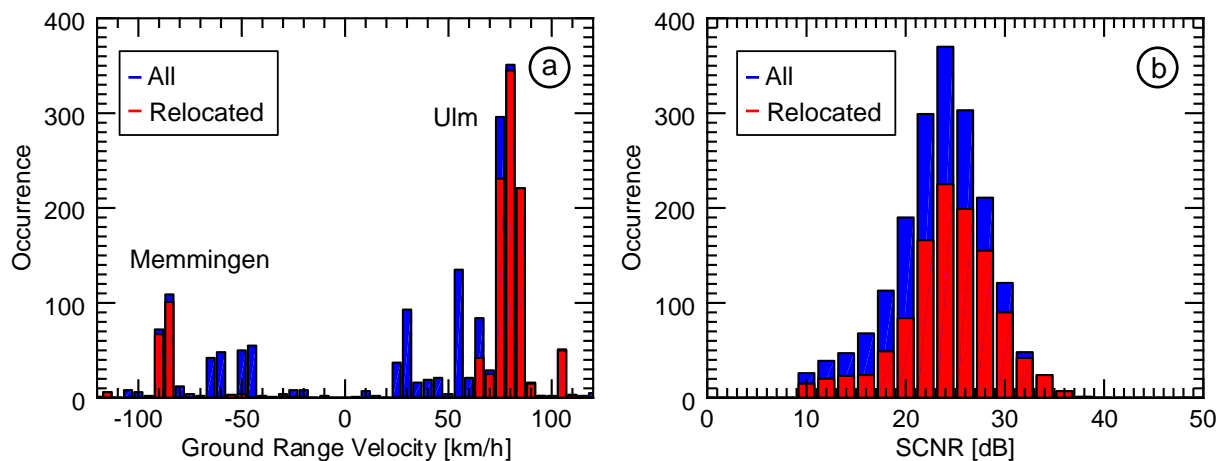


Figure 7.14. Histograms obtained from real traffic in highway A7: (a) ground range velocities and (b) SCNRs of all (blue bars) and relocated detections on the highway (red bars).

7.5.7 GMTI Results Using the Fast PD STAP Processor

This section presents the first experimental results obtained with the fast PD STAP processor (i.e., operational mode 3, cf. Section 4.4) according to data takes 1 and 4. Algorithm 4 (with MTSR) was applied for selecting the training data for the CCM estimation and the moving window parameters were: $D = 15$, $T = 12$ and $n'_t = 512$ (as discussed in Section 7.5.2). The probability of false alarm rate was set to $P_{fa} = 10^{-6}$. The content of this section was submitted for a journal publication [61].

7.5.7.1 Controlled Vehicles

The fast PD STAP processor was firstly tested according to data take 1 (cf. Appendix A), which contains 1024×16384 range-azimuth samples and five cars with controlled movement and speed.

The optical image of the scene is shown in **Figure 7.15**, where the considered cars (numbered from 1 to 5) and the corner reflector (CR) are indicated. It is pointed out that the cars 1 to 4 moved on the edges of the airport's runway, while car 5 moved off-road in circles. Moreover, the runway contained 945 road points from where 128 azimuth samples were selected for each road point. Thus, only a single CPI containing 945×128 samples needed to be processed by the PD STAP core (i.e., 0.72% of the total available data). The selected data for processing are depicted in the yellow box in **Figure 7.15a**.

Figure 7.15b shows the data selected along the airport's runway in Doppler domain before clutter cancellation, where the clutter bandwidth can be seen centered at zero-Doppler. **Figure 7.15c** shows the same data after clutter cancellation, where it can be seen that the region outside of the clutter bandwidth could not be suppressed due to the noise. **Figure 7.15d** shows the binary map of the detected targets, where the signals from all cars as well as from the CR can be clearly recognized. Although the CR is a stationary target, its SCNR exceeds the CFAR detection threshold for different Doppler frequencies. This response is expected and it visibly differs from the response of a moving target signal.

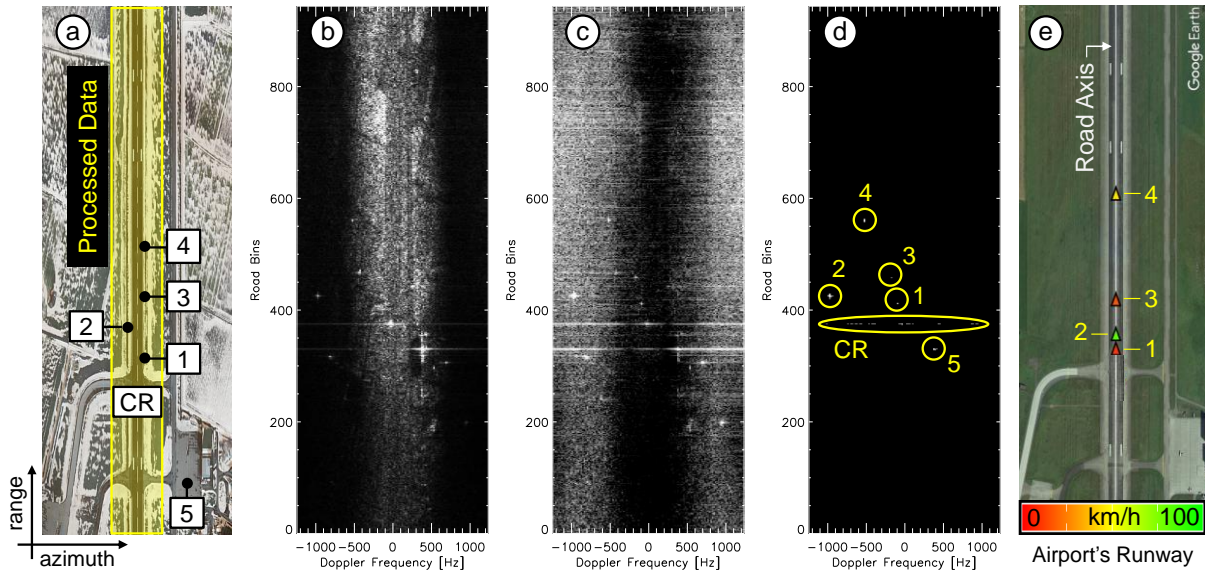


Figure 7.15. Results obtained from data take 1 (cf. Appendix A): (a) optical image of the runway; (b) road-Doppler image before clutter cancellation; (c) road-Doppler image after clutter cancellation; (d) binary detection map (controlled cars numbered from 1 to 5); and (e) final GMTI results.

Figure 7.15e shows the final GMTI results, where the false detections were discarded and the true detections from cars 1 to 4 were relocated to the OSM road axis (white line located at the center of the runway). In this figure, the triangles point to the moving directions of the cars and the colors indicate their absolute velocities on the runway, estimated according to Equation (3.19). It has to be mentioned that car 5 was discarded as a false detection in the Error Models and Decision block since it moved off-road.

The estimated velocities and positions from cars 1 to 4 agreed very well with the measurements shown in [127], [128] with a standard deviation smaller than 5 km/h. Therefore, the fast PD STAP processor was able to detect both slow and fast vehicles.

The data selected along the runway (yellow box in **Figure 7.15a**) were processed using only one DOA angle steered at the broadside direction of the antenna array, which was sufficient for detecting all moving vehicles. Optionally, the selected data could be processed using multiple DOA angles in order to increase the number of moving target detections, as verified in Section 8.4.2.

As a comparison, the PD STAP processor with a priori knowledge information (i.e., operational mode 2, cf. Section 4.3) [59] was applied on the same data take, where all the available SAR data were processed. This processor was also able to detect the cars 1 to 5, whereas the processing time was nearly 37 times longer than the fast PD STAP processor presented in this chapter. Indeed, this processing time factor is data dependent and therefore further work is needed considering other data takes with different number of roads and moving vehicles. This evaluation is foreseen for the next experiments with the novel DLR's DBFSAR system [129], which had its maiden flight in November 2016 and is not yet fully operational with respect to the MTI imaging mode. Anyhow, this result acknowledges the great potential of the proposed processor towards real-time traffic monitoring.

7.5.7.2 Real Traffic

The fast PD STAP processor was also applied on a patch obtained from data take 4 (cf. Appendix A), which contains 1024×16384 range-azimuth samples where a part of the highway A7 is located with several vehicles of opportunity.

Figure 7.16 shows the final GMTI results obtained by processing the data take 4 using only one DOA angle (steered to the broadside direction of the antenna array axis, i.e., $\Psi_{\text{DOA,array}} = 90^\circ$) and using five DOA angles defined within the 3 dB antenna beamwidth in azimuth $\theta_{\text{az,3dB}} = 5.25^\circ$ (cf. Section 3.6.1), i.e., $\Psi_{\text{DOA,array}} = (87.37^\circ, 88.95^\circ, 90.00^\circ, 91.05^\circ, 92.62^\circ)$. In **Figure 7.16**, the moving vehicles are depicted as colored triangles pointing to their moving directions and the OSM road axes are shown in white. The colors indicate the absolute velocities of the vehicles on the roads estimated according to Equation (3.19) and the information box shows examples of parameters that can be displayed for each vehicle.

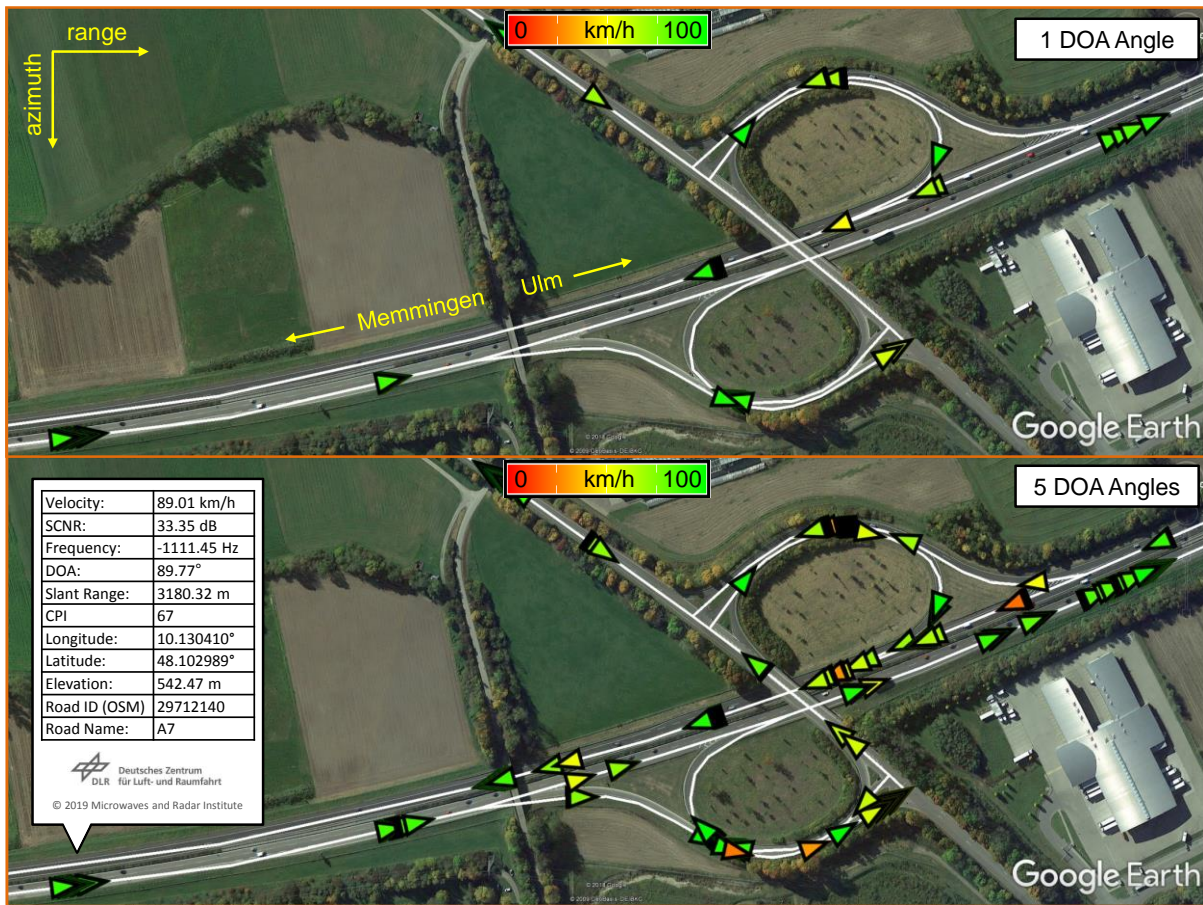


Figure 7.16. Real traffic on the highway A7 towards Ulm and Memmingen. The vehicles were detected and their parameters were automatically estimated using the fast PD STAP processor considering one and five DOA angles.

It is clearly visible that much less detections were obtained by processing the data taken using only one DOA angle and some vehicles could not even be detected in this case. Although much more detections can be obtained using multiple DOA angles, this operation can impact on the real-time capability of the system since more computational time is required.

It can also be seen that the fast PD STAP processor was able to detect some moving vehicles several times, which reveals the potential of this processor for civilian traffic monitoring applications. It is pointed out that no clustering or tracking algorithms were applied in this experiment for refining the GMTI results.

Unfortunately, no ground truth data were available in this experiment and thus it is not possible to determine the probability of false alarm as well as the errors of the estimated velocities and positions. Even so, the estimated velocities of the vehicles on the highway A7 were reasonable.

To conclude, the GMTI results shown in **Figure 7.16** demonstrate how an airborne SAR system could be helpful for evaluating the traffic situation in an area of interest (e.g., on the highway A7 towards Ulm and Memmingen). As mentioned in Chapter 1, in reality such traffic data could supplement the information acquired by the road sensors and be used in research for improving traffic models or as information source for road traffic statistics [17]. Besides, in some cases (e.g., in rural and primary roads without enough sensor installations or in large scale events and catastrophes) an airborne SAR system could be the only source of traffic data.

7.6 Chapter Summary

This chapter compares four training data selection algorithms for CCM estimation: two conventional that are used as reference (algorithms 1 and 2), and two novel (algorithms 3 and 4). Besides, a module for moving target signals rejection (MTSR) is presented for removing undesired range bins of the training data that contain strong scatterers and moving target signals. The four algorithms are firstly applied on the PD STAP processors without and with a priori knowledge information (operational modes 1 and 2, cf. Chapter 4), in both cases using measured data acquired by the DLR's system F-SAR. In the experiments with controlled vehicles (i.e., data takes 1 to 3, cf. Appendix A), it is shown that the two novel algorithms (3 and 4) outperform the conventional ones (1 and 2) by presenting lower probabilities of false alarm rates as well as higher percentages of true detections. For the novel algorithms, the MTSR module increases the number of true detections (avoiding the self-whitening of the moving targets) and keeps a tolerable probability of false alarm rate. Even in the worst case scenario, 90% of the detections that remained in the final image were true. Algorithm 4 (with MTSR) is recommended for traffic monitoring not only because it

is able to collect enough samples for estimating reliable CFAR detection thresholds, but also because it takes into account the clutter change over slant range.

The experimental results obtained by combining algorithm 4 (with MTSR) with the fast PD STAP processor (operational mode 3, cf. Chapter 4) show that this processor can detect both slow and fast targets with very good accuracy, and can discard most of the false detections that lie far from the roads. For data take 1 (cf. Appendix A), the fast PD STAP processor detected all cars and was 37 times faster than the PD STAP processor with a priori knowledge information (operational mode 2, cf. Chapter 4) that processed all the available SAR data. For data take 4 (cf. Appendix A), the fast PD STAP processor detected some vehicles moving on the highway A7 several times with reasonable velocity estimates and much more detections were obtained by processing the selected data using multiple DOA angles, revealing the potential of this processor for traffic monitoring applications using the DLR's system F-SAR.

8 Conclusion

This chapter concludes the doctoral thesis with an overview of the achieved results as well as an outlook on further research.

8.1 Discussion and Summary of Results

STAP techniques have been employed by robust state-of-the-art GMTI processors due to their very good clutter cancellation as well as their accurate target's line-of-sight and position estimation capabilities. A step forward is presented in this doctoral thesis, where the powerful PD STAP technique is fused with two freely available databases: a road map obtained from the OSM and a DEM obtained from the SRTM. This novel combination is shown to be very promising for traffic monitoring. The main features of the PD STAP technique are presented in Chapter 3, including the clutter models used for the estimation of CFAR detection thresholds, the performance model as well as the limitations regarding DOA angle ambiguities and line-of-sight blind velocities.

The proposed PD STAP processor has three operational modes (cf. Chapter 4). The first mode comprises the conventional PD STAP processor without a priori knowledge information, which is able to detect also vehicles moving off-road. This mode can be helpful for areas where the road information is unavailable. The second mode uses a priori knowledge information for assigning the true vehicles to their correct positions on the roads as well as for rejecting detections that lie far from roads, which includes vehicles moving off-road. This mode is especially suitable for non-real-time traffic monitoring since all available SAR data need to be processed. The third mode is a faster processing version of the second mode, where the a priori known OSM database is employed for selecting only the relevant data along the roads to be processed by the computationally expensive PD STAP core. As a result, the amount of processed data (and therefore the overall processing time) can be decreased significantly, paving the way for real-time traffic monitoring applications.

For the PD STAP with a priori knowledge information (operational modes 2 and 3), a decision needs to be made for each detected target in order to verify whether it is a

vehicle moving with high probability on the road or not. This decision is carried out based on a robust algorithm that combines two positioning error models: one for the moving targets and one for the OSM road points (cf. Chapter 5). This novel algorithm takes into account several error sources that are essential for obtaining reliable results.

Another topic of utmost importance is data calibration, which is essential for detecting the moving targets and for estimating their positions and velocities accurately. In this sense, an efficient data calibration algorithm is presented and discussed in Chapter 6. The algorithm corrects not only the residual ATI phase and the magnitude offsets of the RX channels, but also the Doppler centroid variation over slant range (i.e., by removing the “J-Hook” effect) and time by using the antenna array’s attitude angles: yaw, pitch and roll. Experimental GMTI results show that the lack of data calibration affects not only the position and the velocity estimates of the moving targets, but it also prevents the estimation of accurate CFAR detection thresholds. Without data calibration, several false detections are obtained due to systematic phase errors that extend along range and azimuth. The novel data calibration algorithm is faster than state-of-the-art ones (for instance, the digital channel balancing [48], [116]) and works very well for data takes containing different number of roads and moving vehicles.

The clutter cancellation capability achieved with PD STAP depends strongly on the quality of the training data selected for the clutter covariance matrix estimation. In this sense, it is highly important to select training data free of moving targets and strong discrete signals. Novel training data selection strategies are presented and compared in Chapter 7, including a robust module for moving target signals rejection that removes undesired range bins of the training data containing strong scatterers and moving target signals. GMTI results and quantitative comparisons lead to the recommendation of Algorithm 4 (cf. Section 7.4.4) for traffic monitoring not only because it is able to collect enough training data for estimating reliable CFAR detection thresholds, but also because it is robust against the clutter change over slant range.

Chapter 7 also presents experimental results obtained according to four data takes that include scenarios with controlled vehicles as well as real traffic. The results show that

the proposed PD STAP processor can detect both slow and fast targets (moving from 7 km/h up to 110 km/h in the particular experiments) with velocity accuracy better than 10 km/h. Moreover, the use of a priori knowledge information indeed allows discarding most of the false detections that lie far from the roads. In the real traffic scenario, it is shown that some moving vehicles can be detected several times with reasonable velocity estimates. It has to be mentioned that no clustering or tracking algorithms are applied for refining the GMTI results. Finally, it is shown that the fast PD STAP processor (operational mode 3) can be 37 times faster than the PD STAP processor with a priori knowledge information (operational mode 2). This processing time reduction by a factor is data dependent and shows the potential of the fast PD STAP towards real-time traffic monitoring.

In light of the presented results, this doctoral thesis is considered to be successful in its objectives, having introduced, evaluated and tested a novel PD STAP processor with a priori knowledge information that is suitable for many traffic monitoring applications using the DLR's airborne system F-SAR.

8.2 Outlook of Future Work

The following major topics are suggested for ongoing research:

1. The experimental results show that the novel PD STAP processor is able to detect the same moving target several times under different DOA angles defined within the 3 dB antenna beamwidth in azimuth, which increases the target's probability of detection. Nevertheless, vehicles that move close to each other and with similar velocities are hardly distinguished or separated, which is very often the case in major highways (cf. **Figure 7.16**, mainly at the bottom). Clustering and tracking algorithms are recommended in this case for further improving the results (e.g., [130], [131]);
2. The novel PD STAP processor can be combined with tracking information and inverse SAR (ISAR) imaging techniques in order to refocus moving vehicles with very high resolution [132];

3. It is pointed out in Section 6.7 that the ATI phase offsets are estimated from the measured data through the interferograms obtained among the RX channels, where processing time is demanded for coregistering the multi-channel data. An alternative for speeding up the calibration algorithm consists in two main steps: 1) estimate the ATI phase offsets only once from the interferograms (i.e., using co-registration) and 2) correct the ATI phase offset variations using the aircraft's attitude angles (yaw, pitch and roll) obtained from the IMU system and the attitude angle offsets ($\Delta\theta_{\text{YAW}}$, $\Delta\theta_{\text{PITCH}}$ and $\Delta\theta_{\text{ROLL}}$) caused mainly by the antenna lever arms;
4. The overall processing time can be significantly reduced by means of topology optimization. For instance, the code of the novel PD STAP processor can be adapted for a particular processor (e.g., a graphic processing unit) and the computationally expensive functions that are independent from each other and are constantly repeated can be structured for parallel processing;
5. For the fast PD STAP processor (operational mode 3), further work is suggested in order to explore additional strategies for training data selection. For instance, the OSM database could be used for selecting the training data along the roads and the MTSR module could be applied in order to remove undesired range bins containing moving targets and strong discrete signals (cf. Section 7.4.5);
6. The PD STAP processor can be tested with circular SAR data [87], where the illumination time of the moving targets is much longer than the stripmap SAR data takes evaluated in this doctoral thesis. To the author's knowledge, this is a hot topic that has not been much explored in the literature so far;
7. Traffic monitoring using multi-channel spaceborne SAR systems is a hot topic [28]–[30] that is motivated especially by the possibility of large coverage in a global scale. Yet, some major challenges and drawbacks need to be addressed. From the geometry point of view, the long distance between the satellite and the scene causes the SNR of moving targets to be very low, especially for passenger cars with an RCS of only a few square meters [133]. In addition, spaceborne SAR systems are generally not suitable for real time traffic and

infrastructure monitoring since their revisit times can be in the order of a few days [110]. From the architecture point of view, spaceborne SAR systems typically have a limited number of RX channels due to high costs, and robust GMTI algorithms require at least three RX channels for performing clutter cancellation and target parameter estimation accurately. Examples of state-of-the-art GMTI techniques for spaceborne SAR systems are known as Imaging STAP (ISTAP) and Extended DPCA (EDPCA) [32], [134]–[136]. In this sense, the a priori knowledge information framework presented in Chapter 4 can be combined with ISTAP or EDPCA in order to process only the relevant SAR data in the region of roads, thus decreasing the processing time significantly. In addition, the true vehicles can be assigned to their correct positions on the roads and the false detections can be recognized and rejected;

8. The interest in bi-static STAP has been growing largely in order to improve the moving target detection and the image capabilities (e.g., ISAR-like images of the moving targets can be obtained for their recognition and classification). A major challenge of bi-static STAP consists in strong clutter non-stationarity introduced by the geometry, which degrades the quality of the training data and thus the STAP performance is reduced considerably due to covariance matrix estimation error. Robust algorithms have been proposed for improving the bi-static STAP performance [137]–[140] and can be combined with the a priori knowledge information framework presented in Chapter 4 for obtaining a novel and enhanced version of the PD STAP processor proposed in this thesis.

In a further step, it is also interesting to investigate a multi-static spaceborne scenario, where one or several geostationary satellites are used as transmitters and a fleet of smaller satellites (e.g., flying in low or medium Earth orbits) are used as receivers. For instance, the geostationary satellites could be already existing television or communication satellites and not necessarily dedicated radar satellites.

Appendix A: F-SAR System

A.1 Overview

The DLR's F-SAR (*Flugzeug-SAR*) is a state-of-the-art airborne SAR system that has replaced the well-known E-SAR (Experimental-SAR) [141], [142] in order to accomplish the increasing demands of the remote sensing community, especially for acquiring data simultaneously at different frequencies and polarizations, as well as for very high range resolution. The F-SAR improved the quality of the already existing products and delivered totally new product types, supporting the development of innovative approaches in environmental research and the design of future Earth observation satellite missions. In addition, the simultaneous data acquisition in several frequency bands reduced the operation time and costs.

The SAR sensor is installed and operated onboard the DLR's aircraft Dornier DO228-212, a small STOL (short take-off and landing) aircraft that had its maiden test flight in November 2006. The main design feature of this system is the fully polarimetric operation in up to five frequency bands (X, C, S, L and P) with the possibility to acquire the data simultaneously in different bands and polarizations. The F-SAR was built using commercial off-the-shelf components and subsystems, whereas design-critical parts (e.g., its antennas) were developed and built by DLR [40].

The antenna mount is located on the right side of the aircraft and holds seven right-looking planar array antennas (three X-band, one C-band, two S-band and one L-band), as shown in **Figure A.1**. It can be seen in this figure that the F-SAR has across-track interferometers in X-band (pair of antennas X_1, X_2) and in S-band (pair of antennas S_1, S_2), as well as an along-track interferometer in X-band (pair of antennas X_2, X_3). The P-band antenna is mounted under the nose of the aircraft due to its size. Moreover, it is pointed out that the data cannot be acquired simultaneously in S- and C- bands because the subsystem is shared. The primary technical specifications of the F-SAR system are summarized in **Table A.1** [40], [128].

Detail: position of the antennas

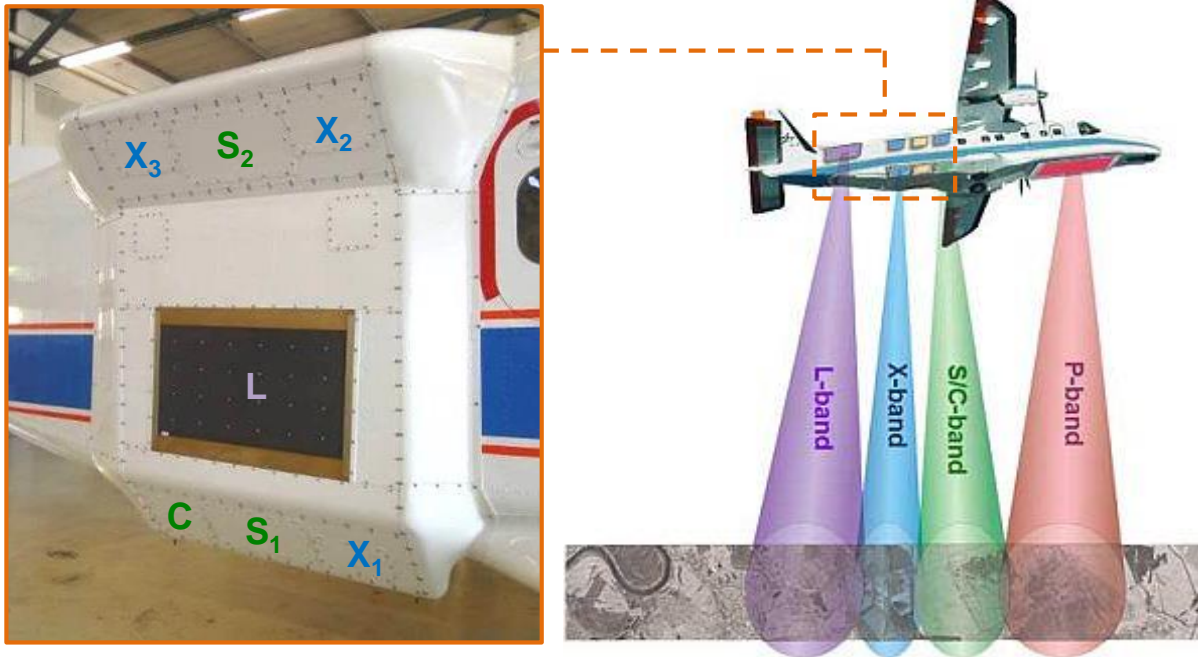


Figure A.1. F-SAR system onboard the DLR's aircraft Dornier DO228-212 (modified after [143]). The SAR sensor can acquire the data simultaneously in X-, S- (or C-), L- and P-bands. The positions of the right-looking dual polarized antennas in the aircraft's fuselage are shown in the detail (modified after [144]).

TABLE A.1
F-SAR TECHNICAL SPECIFICATIONS [40], [128].

Band	X	C	S	L	P
Carrier frequency [MHz]	9600	5300	3250	1325	350/450
Max. PRF [Hz]	5000	5000	5000	10000	10000
Polarization	all bands are fully polarimetric				
Max. bandwidth [MHz]	760	400	300	150	100/50
Transmitted power [kW]	2.50	2.20	2.20	0.90	0.90
Max. number of receive channels	4	2	2	2	2
Max slant-range resolution [m]	0.2	0.4	0.5	1.0	1.5
Azimuth resolution [m]	0.2	0.3	0.35	0.4	1.5
Max. data rates [MB/s]	247 (per channel)				
Swath width [km]	1 to 5 (depending on the flight altitude)				
Sampling [bits]	8 bit real, 1000 Msamples/s				

A.2 GMTI Configuration

The ability to perform fully polarimetric single-pass interferometry in X-band using both across and along-track antenna configurations makes the F-SAR a powerful tool for GMTI applications. **Figure A.2** shows the X-band along-track antenna setup. As it can be seen, the front-end of the system has two units with down-converters and analog-to-digital converters (ADC), so that two antennas can receive simultaneously. The number of receive channels can be extended to four by applying the antenna AS technique [93], whereas the effective PRF is reduced to the half of the system's one (i.e., from 5000 Hz to 2500 Hz per RX channel) [127]. It has also to be mentioned that the F-SAR system has a flat antenna array that does not allow electronic or gimbal-based zero-Doppler beam steering. Therefore, the motion of the aircraft plays an important role during the data processing in order to obtain accurate detection, position and velocity estimates. This problem is solved by using the data calibration technique presented in Chapter 6.

With the F-SAR onboard, the aircraft is able to fly at a maximum altitude of 6100 m above sea level with an average ground speed of 90 m/s during data acquisition. The endurance of the aircraft ranges from 2.5 to 5 h depending on its configuration [145]. The F-SAR usually covers off-nadir angles from 25° to 60° with the possibility to adapt the range according to the application (covering from 60° to 85° for long stand-off imaging or from 0° to 25° for sounding or steep incidence experiments) [144].

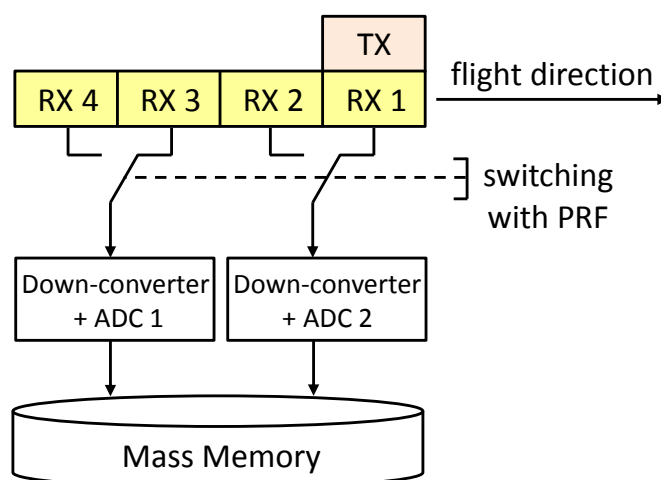


Figure A.2. X-band along-track antenna setup considering the AS technique (modified after [115]).

A.3 Flight Campaigns

The F-SAR system has an experimental GMTI mode, where four RX channels and X-band are employed for evaluating different GMTI algorithms with respect to their capabilities for traffic monitoring [36], [78].

The first GMTI experiments using the F-SAR system were conducted in February 2007 over the Memmingen area, in Germany. **Figure A.3** shows the radar's electronic units and the antenna pod that was mounted at the bottom of the F-SAR's fuselage together with a camera, so that optical images were obtained simultaneously with the radar data [115]. As a result from this flight campaign, several multi-channel radar data takes were obtained from scenarios with ground controlled vehicles as well as from real traffic in major highways.

This section presents four data takes that were used in the scope of this doctoral thesis. The system and the geometry parameters are summarized in **Table A.2**, and a detailed report including all GMTI experiments of this flight campaign is presented in [115].

TABLE A.2
MAIN SYSTEM AND GEOMETRY PARAMETERS FOR GMTI EXPERIMENTS

Parameter	Symbol	Value
Speed of light	c	2.9979×10^8 m/s
Platform velocity	v_p	90 m/s
Number of receive channels (in AS mode)	M	4
Effective PRF (in AS mode)	PRF	2500 Hz
Range sampling frequency	f_r	125 MHz
Azimuth resolution	δ_{az}	0.036 m
Slant-range resolution	δ_r	1.198 m
Effective along-track baseline	d_a	0.1 m
Incidence angle	θ_i	25° to 63°
Radar Wavelength	λ	0.03125 m
TX antenna length	L_a	0.3 m
Flight altitude above ground	h	2200 m



Figure A.3. F-SAR instruments (X-, C-, S-band systems and the antenna pod) before the installation onboard the Dornier DO228-212 aircraft for the first GMTI experiments in February 2007 [146].

Figure A.4 shows the optical Google Earth image where the regions of the data takes are depicted in yellow. The region of data takes 1 to 3 includes the Memmingen's airport, where GMTI experiments considering vehicles with controlled speed were carried out on the airport's runway, which is approximately 3 km long. The region of data take 4 includes a part of the highway A7, where GMTI experiments for real traffic were carried out considering several vehicles of opportunity.

Figure A.5 shows the experimental setup of data takes 1 to 3. The optical image of the Allgäu airport's runway is shown on the left, where five controlled common passenger cars were moving. On the right, the positions and the velocities of the cars are shown for each data take, where the angle of the runway with respect to the flight path was also different. Note that car 5 moved off-road (in circles) in data takes 1 and 2. It is pointed out that the cars 1, 2 and 4 were equipped with radar reflectors in order to enhance their RCS and car 4 had a DGPS receiver for retrieving reliable geographical reference positions and velocities. The data takes 1 to 3 are especially important for evaluating the estimation accuracy of the target's position and velocity, since the positions and the velocities of the vehicles were known a priori.

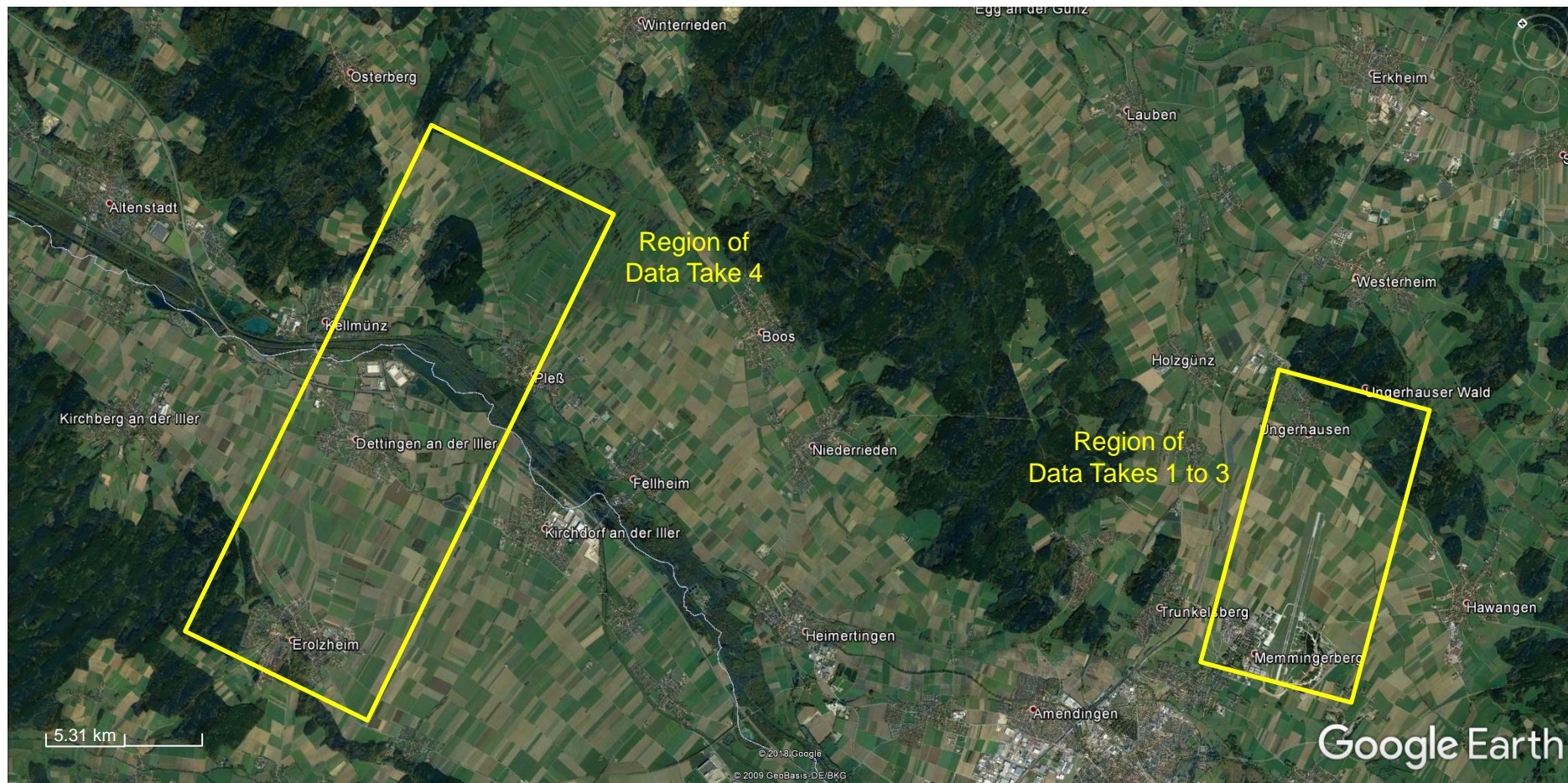


Figure A.4. Optical Google Earth image showing the regions where the data takes were acquired by the DLR's F-SAR system.

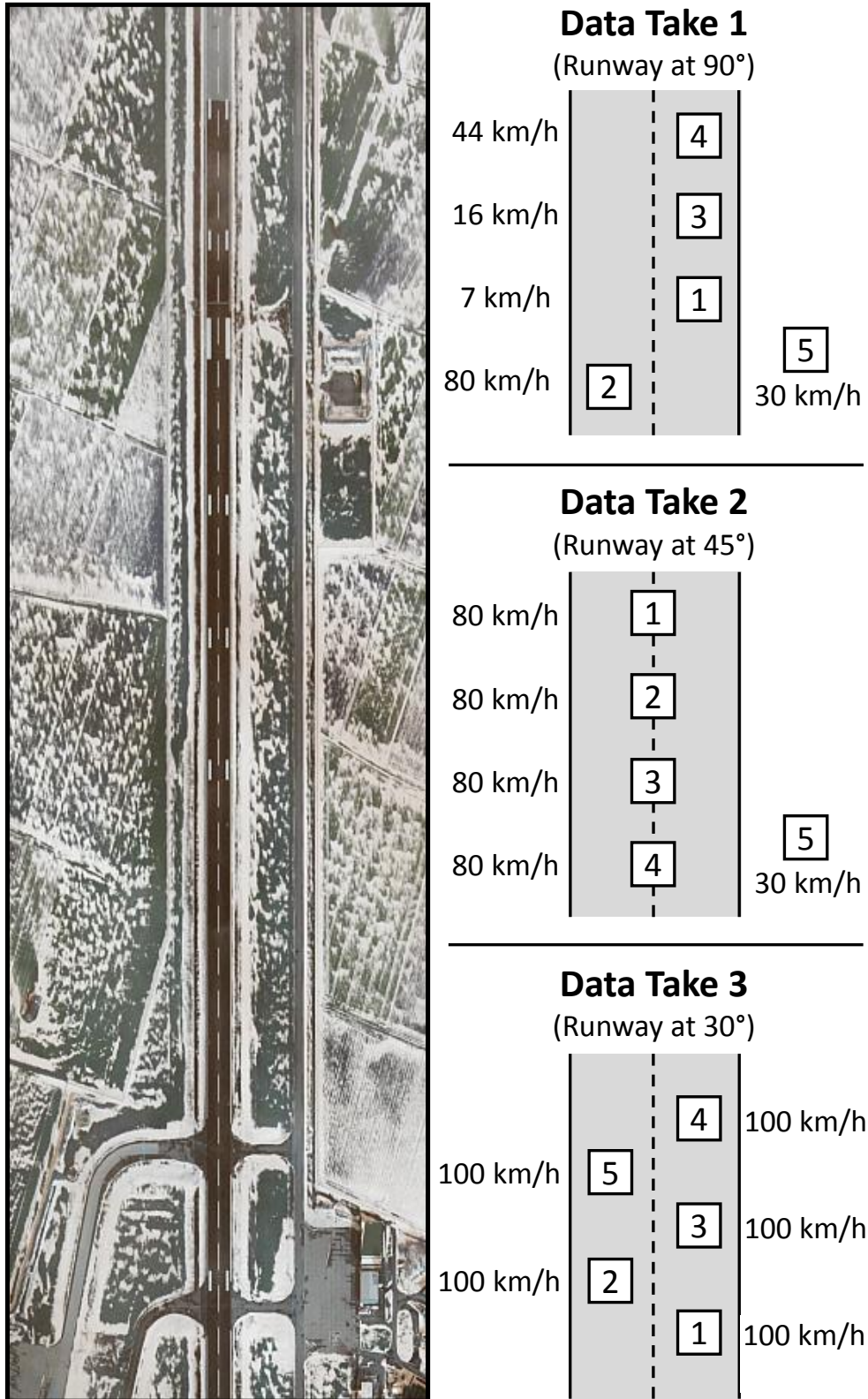


Figure A.5. Flight campaign over the Allgäu airport in Memmingen in February 2007: optical image of the airport's runway (left); desired positions and velocities of the controlled cars for data takes 1 to 3 (right). Notice that the angle of the runway with respect to the flight path changes for each data take.

Figure A.6 shows the radar image from data take 4 obtained in the vicinity of Memmingen. As it can be seen, this data take contains areas of forests, crop fields, villages and a lake, being especially useful for evaluating the heterogeneous clutter model used by the CFAR detector presented in Chapter 3. The data patch containing the highway A7 is processed separately in many experiments of this doctoral thesis, since it is especially helpful for evaluating the PD STAP in a real-traffic scenario.

Finally, **Table A.3** shows the numbers of the processed range and azimuth samples of all data takes, including the approximated dimensions of the illuminated scenes.

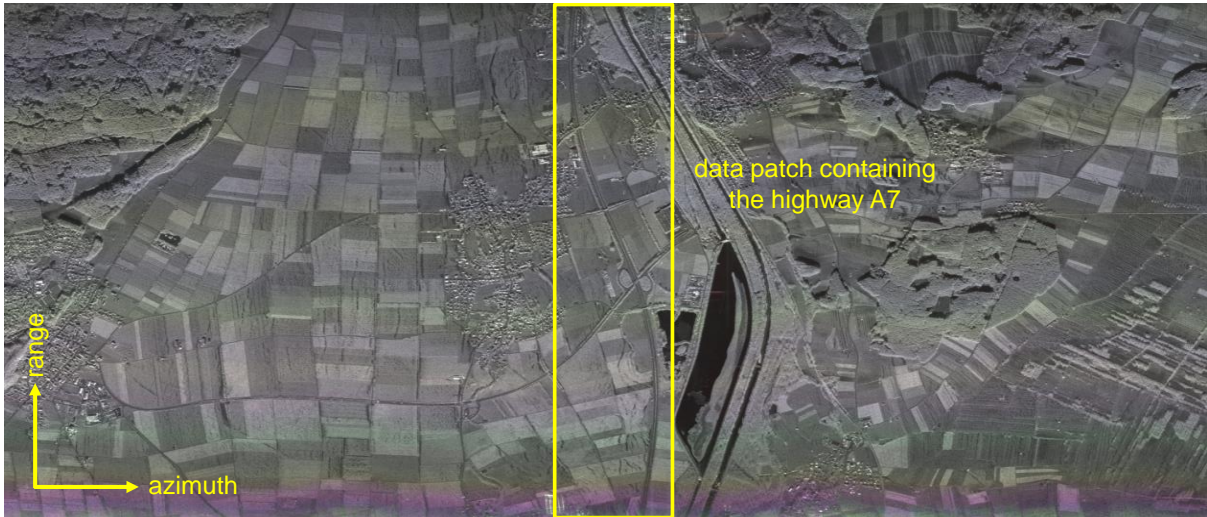


Figure A.6. Radar image from data take 4. The data patch containing the highway A7 is useful for evaluating the PD STAP in a real-traffic scenario.

TABLE A.3
NUMBER OF SAMPLES AND ILLUMINATED SCENE DIMENSIONS OF DATA TAKES 1 TO 4

Data Take	1	2	3	4	4 (patch)
Azimuth samples (N_a)	16384	32768	32768	262144	16384
Range Samples (K)	1024	1024	1024	2048	2048
Size in azimuth (m)	596	1192	1153	9361	584
Size in slant range (m)	1226	1226	1226	2454	2454
Size in ground range (m)	1917	1923	1921	3485	3485

Appendix B: Log of Roads in Germany

The construction of roads generally takes into account that each lane is wide enough to accommodate standard sized vehicles plus a margin of error. In reality, the choices regarding the number of lanes as well as the lane widths depend on many factors (e.g., vehicles type and speed, traffic volume, slope of the roads, curves, etc). Furthermore, both the number and the width of road lanes may change throughout the extension of the same road (for instance, urban road lanes can be narrowed for encouraging drivers to reduce speed or to allocate cycle lanes). Therefore, a robust positioning error model for the roads is needed taking into account proper assumptions for all error sources.

The positioning error model of the OSM road points is presented in Chapter 5, where it is pointed out the need for estimating important road features, for instance:

- The mean number of lanes (\bar{n}_{lanes}) and its standard deviation ($\sigma_{n_{\text{lanes}}}$);
- The mean lanes width (\bar{w}_{lanes}) and its standard deviation ($\sigma_{w_{\text{lanes}}}$).

These parameters were estimated empirically considering 16 roads from different types (urban and rural) and selected from all states of Germany. The road log is presented in **Table B.1**, where it is shown the number of lanes (n_{lanes}) and the lanes width (w_{lanes}) obtained for each indexed road i . These quantities were measured manually at a freely chosen point of each road by using Google Maps [147]. The state codes are referred in table according to [148].

The mean values are obtained according to:

$$\bar{n}_{\text{lanes}} = \frac{1}{N} \sum_{i=1}^N n_{\text{lanes}}^i \cong 2.5, \quad (\text{B.1})$$

$$\bar{w}_{\text{lanes}} = \frac{1}{N} \sum_{i=1}^N w_{\text{lanes}}^i \cong 3.2 \text{ m}, \quad (\text{B.2})$$

where $N = 16$ denotes the total number of roads contained in the log.

The standard deviations are obtained according to:

$$\sigma_{n_{\text{lanes}}} = \sqrt{\sigma_{n_{\text{lanes}}}^2} = \sqrt{\frac{1}{N} \sum_{i=1}^N (n_{\text{lanes}}^i - \bar{n}_{\text{lanes}})^2} \cong 0.9, \quad (\text{B.3})$$

$$\sigma_{w_{\text{lanes}}} = \sqrt{\sigma_{w_{\text{lanes}}}^2} = \sqrt{\frac{1}{N} \sum_{i=1}^N (w_{\text{lanes}}^i - \bar{w}_{\text{lanes}})^2} \cong 0.5 \text{ m}. \quad (\text{B.4})$$

The results obtained from Equations (B.1) to (B.4) are applied in the positioning error model of the OSM road points presented in Chapter 5.

TABLE B.1
LOG OF ROADS IN GERMANY

Index i	Road Name	City	State Code	n_{lanes}	w_{lanes} [m]
1	Römerstraße	Heidelberg	BW	3	2.9
2	Fürther Straße	Nuremberg	BY	2	3.2
3	Holzmarktstraße	Berlin	BE	3	3.3
4	Bahnhofstraße	Cottbus	BB	2	3.1
5	Hämmweg	Bremerhaven	HB	2	3.1
6	Willy-Brandt-Straße	Hamburg	HH	3	3.0
7	Am Römerhof	Frankfurt	HE	3	3.2
8	Hamburger Straße	Braunschweig	NI	2	3.1
9	Liebnitzstraße	Güstrow	MV	4	3.5
10	Altstraße	Aachen	NW	2	2.9
11	Königstraße	Kaiserslautern	RP	2	3.2
12	Johannesstraße	Neunkirchen	SL	2	3.3
13	Theaterstraße	Chemnitz	SN	3	3.3
14	Sachsenring	Magdeburg	ST	2	3.1
15	Friedrich-Ebert-Straße	Flensburg	SH	3	3.1
16	Käthe-Kollwitz-Straße	Erfurt	TH	2	3.6

Bibliography

- [1] B. of T. S. U.S. Department of Transportation, “Transportation Statistics Annual Report (TSAR) 2017,” Washington, DC, USA, 2017.
- [2] Eurostat, “Panorama of Transport,” Luxembourg, 2009.
- [3] P. e A. C. (MTPA) Ministério dos Transportes and Empresa de Planejamento e Logística (EPL), “Anuário Estatístico de Transportes (AET),” Brasília, Brazil, 2017.
- [4] J. Leitloff, D. Rosenbaum, F. Kurz, O. Meynberg, and P. Reinartz, “An operational system for estimating road traffic information from aerial images,” *Remote Sens.*, vol. 6, no. 11, pp. 11315–11341, 2014.
- [5] V. T. Vu, T. Sjogren, M. I. Pettersson, and M. Dahl, “Measurement of Traffic Flows with SAR - Field Test on the Swedish Road Network,” *Int. Geosci. Remote Sens. Symp.*, vol. 2017, pp. 3321–3324, 2017.
- [6] J. C. Curlander and R. N. McDonough, *Synthetic Aperture Radar: Systems and Signal Processing*. New York, USA: John Wiley & Sons, 1991.
- [7] I. G. Cumming and F. H. Wong, *Digital Processing of Synthetic Aperture Radar Data: Algorithms and Implementation*. Boston, USA: Artech House, 2005.
- [8] F. M. Henderson and A. J. Lewis, *Manual of Remote Sensing: Principles and Applications of Imaging Radar*, 3rd ed. New York: John Wiley & Sons, 1998.
- [9] M. I. Skolnik, *Introduction to Radar Systems*, 3rd ed. New York, USA: McGRAW-HILL, 2012.
- [10] K. Tomiyasu, “Tutorial Review of Synthetic-Aperture Radar (SAR) with Applications to Imaging of the Ocean Surface,” *Proc. IEEE*, vol. 66, no. 5, pp. 563–583, 1978.
- [11] W. M. Brown, “Synthetic Aperture Radar,” *IEEE Trans. Aerosp. Electron. Syst.*, vol. AES-3, no. 2, pp. 217–229, 1967.
- [12] A. Moreira, P. Prats, M. Younis, G. Krieger, I. Hajnsek, and K. Papathanassiou, “A Tutorial on Synthetic Aperture Radar,” *IEEE Geosci. Remote Sens. Mag.*,

- vol. 1, no. 1, pp. 6–43, 2013.
- [13] DLR, “VABENE++: Traffic Management for Large Scale Events and Disasters,” *DLR Website*, 2018. [Online]. Available: <https://verkehrsforschung.dlr.de/en/projects/vabene>. [Accessed: 28-Aug-2018].
- [14] D. Rosigkeit, S. V. Baumgartner, and A. Nottensteiner, “Usability of long term evolution (LTE) in DLR’s research aircraft DO 228-212,” in *German Microwave Conference (GeMiC)*, 2015, pp. 40–43.
- [15] D. Rosigkeit, “Verwendbarkeit von LTE im DLR Forschungsflugzeug DO 228-212,” Technische Hochschule Lübeck, 2015.
- [16] S. V. Baumgartner, D. Rosigkeit, and A. Nottensteiner, “Usability of LTE for Transmitting Radar Data from DLR ’ s Research Aircraft DO 228-212,” in *36th European Telemetry and Test Conference*, 2016, pp. 181–187.
- [17] J. Leitloff, S. Hinz, and U. Stilla, “Vehicle Detection in Very High Resolution Satellite Images of City Areas,” *IEEE Trans. Geosci. Remote Sens.*, vol. 48, no. 7, pp. 2795–2806, 2010.
- [18] P. A. C. Marques and J. M. B. Dias, “Velocity estimation of fast moving targets using a single SAR sensor,” *IEEE Trans. Aerosp. Electron. Syst.*, vol. 41, no. 1, pp. 75–89, 2005.
- [19] P. A. C. Marques and J. M. B. Dias, “Moving Target Processing in SAR spatial domain,” *IEEE Trans. Aerosp. Electron. Syst.*, vol. 43, no. 3, pp. 864–874, 2007.
- [20] P. A. C. Marques, “Directional Moving Target Indication for Civil Traffic Monitoring Using Single Channel SAR,” 2009, pp. 1–4.
- [21] P. A. C. Marques, “SAR-MTI Improvement Using A-Priori Knowledge of the Road Network,” in *European Radar Conference (EURAD)*, 2010, pp. 244–247.
- [22] S. V. Baumgartner and G. Krieger, “Multi-Channel SAR for Ground Moving Target Indication,” in *Academic Press Library in Signal Processing: Communications and Radar Signal Processing*, vol. 2, New York, USA:

- Elsevier, 2014, pp. 911–986.
- [23] J. Dickey, F.R. and M. M. Santa, “Final report on anticlutter techniques,” General Electric Company, Report R65EMH37, 1953.
- [24] R. M. Goldstein and H. A. Zebker, “Interferometric radar measurement of ocean surface currents,” *Nature*, vol. 328, pp. 707–709, 1987.
- [25] S. Chiu, C. H. Gierull, and A. Durak, “Clutter effects on ground moving targets’ interferometric phase,” in *International Geoscience and Remote Sensing Symposium (IGARSS)*, 2005, vol. 4, pp. 2928–2931.
- [26] R. Klemm, *Principles of Space-Time Adaptive Processing*, 3rd ed. The Institution of Engineering and Technology (IET), 2006.
- [27] A. Farina, P. Lombardo, and M. Pirri, “Nonlinear STAP processing,” *Electron. Commun. Eng. J.*, vol. 11, no. 1, pp. 41–48, 1999.
- [28] F. Meyer, S. Hinz, A. Laika, D. Weihing, and R. Bamler, “Performance analysis of the TerraSAR-X Traffic monitoring concept,” *ISPRS J. Photogramm. Remote Sens.*, vol. 61, no. 3–4, pp. 225–242, 2006.
- [29] S. Hinz, F. Meyer, M. Eineder, and R. Bamler, “Traffic monitoring with spaceborne SAR-Theory, simulations, and experiments,” *Comput. Vis. Image Underst.*, vol. 106, no. 2–3, pp. 231–244, 2007.
- [30] S. Suchandt, H. Runge, H. Breit, U. Steinbrecher, A. Kotenkov, and U. Bals, “Automatic extraction of traffic flows using TerraSAR-X along-track interferometry,” *IEEE Trans. Geosci. Remote Sens.*, vol. 48, no. 2, pp. 807–819, 2010.
- [31] C. H. Gierull, I. Sikaneta, and D. Cerutti-Maori, “Two-step detector for RADARSAT-2’s experimental GMTI mode,” *IEEE Trans. Geosci. Remote Sens.*, vol. 51, no. 1, pp. 436–454, 2013.
- [32] D. Cerutti-Maori, I. Sikaneta, and C. H. Gierull, “Optimum SAR/GMTI processing and its application to the radar satellite RADARSAT-2 for Traffic Monitoring,” *IEEE Trans. Geosci. Remote Sens.*, vol. 50, no. 10, pp. 3868–

- 3881, 2012.
- [33] S. V. Baumgartner and G. Krieger, “Dual-platform large along-track baseline GMTI,” *IEEE Trans. Geosci. Remote Sens.*, vol. 54, no. 3, pp. 1554–1574, 2016.
- [34] F. Kurz, O. Meynberg, D. Rosenbaum, S. Türmer, P. Reinartz, and M. Schroeder, “Low-cost optical camera system for disaster monitoring,” in *ISPRS Congress*, 2012, vol. 39, pp. 33–37.
- [35] D. Cerutti-Maori, J. Klare, A. R. Brenner, and J. H. G. Ender, “Wide-Area Traffic Monitoring With the SAR/GMTI System PAMIR,” *IEEE Trans. Geosci. Remote Sens.*, vol. 46, no. 10, pp. 3019–3030, 2008.
- [36] S. V. Baumgartner and G. Krieger, “Fast GMTI algorithm for traffic monitoring based on a priori knowledge,” *IEEE Trans. Geosci. Remote Sens.*, vol. 50, no. 11, pp. 4626–4641, 2012.
- [37] “OpenStreetMap,” 2018. [Online]. Available: <http://www.openstreetmap.org>. [Accessed: 10-Nov-2018].
- [38] S. V. Baumgartner and G. Krieger, “A Priori Knowledge-Based Post-Doppler STAP For Traffic Monitoring Applications,” in *International Geoscience and Remote Sensing Symposium (IGARSS)*, 2012, pp. 6087–6090.
- [39] D. Weihing, S. Suchandt, S. Hinz, H. Runge, and R. Bamler, “Traffic Parameter Estimation Using TerraSAR-X Data,” in *International Society for Photogrammetry and Remote Sensing*, 2008, no. 2, pp. 153–156.
- [40] A. Reigber *et al.*, “Very-high-resolution airborne synthetic aperture radar imaging: signal processing and applications,” *Proc. IEEE*, vol. 101, no. 3, pp. 759–783, 2013.
- [41] R. Horn, A. Nottensteiner, and R. Scheiber, “F-SAR – DLR’s advanced airborne SAR system onboard DO228,” in *Proceedings of the European Conference on Synthetic Aperture Radar (EUSAR)*, 2008, vol. 4, pp. 1–4.
- [42] H. A. Zebker, S. N. Madsen, J. Martin, G. Alberti, S. Vetrella, and A. Cucci,

- “The TOPSAR interferometric radar topographic mapping instrument,” *IEEE Trans. Geosci. Remote Sens.*, vol. 30, no. 5, pp. 933–940, 1992.
- [43] S. Hensley, K. Wheeler, G. Sadowy, C. Jones, S. Shaffer, and H. Zebker, “The UAVSAR instrument: description and first results,” in *IEEE Radar Conference*, 2008, pp. 1–6.
- [44] F. Holecz, P. Pasquali, J. Moreira, and D. Nuesch, “Rigorous Radiometric Calibration of Airborne AeS-1 InSAR data,” in *International Geoscience and Remote Sensing Symposium (IGARSS)*, 1998, pp. 2442–2444.
- [45] A. L. Gray and P. J. Farris-Manning, “Repeat-Pass Interferometry with Airborne Synthetic Aperture Radar,” *IEEE Trans. Geosci. Remote Sens.*, vol. 31, no. 1, pp. 180–191, 1993.
- [46] J. Hippler, “Ultrahigh Resolution X-Band SAR Images with SmartRadar,” in *European Conference on Synthetic Aperture Radar (EUSAR)*, 2012, pp. 426–428.
- [47] J. H. G. Ender and A. R. Brenner, “PAMIR - A Wideband Phased Array SAR/MTI System,” in *European Conference on Synthetic Aperture Radar (EUSAR)*, 2002, pp. 157–162.
- [48] J. H. G. Ender, “The Airborne Experimental Multi-Channel SAR-System AER-II,” in *European Conference on Synthetic Aperture Radar (EUSAR)*, 1996, pp. 49–52.
- [49] E. L. Christensen *et al.*, “EMISAR: An Absolutely Calibrated Polarimetric L- and C-band SAR,” *IEEE Trans. Geosci. Remote Sens.*, vol. 36, no. 6, pp. 1852–1865, 1998.
- [50] H. Hellsten, L. M. Ulander, A. Gustavsson, and B. Larsson, “Development of VHF CARABAS II SAR,” in *SPIE Aerospace/Defense Sensing and Controls*, 1996, pp. 48–60.
- [51] P. Dubois-Fernandez *et al.*, “The ONERA RAMSES SAR System,” in *IEEE International Geoscience and Remote Sensing Symposium*, 2002, pp. 1723–

- 1725.
- [52] G. Bonin and P. Dreuillet, “The Airborne SAR-System SETHI: Airborne Microwave Remote Sensing Imaging System,” in *European Conference on Synthetic Aperture Radar (EUSAR)*, 2008, pp. 1–4.
- [53] S. Uratsuka *et al.*, “High-resolution dual-bands interferometric and polarimetric airborne SAR (Pi-SAR) and its applications,” in *International Geoscience and Remote Sensing Symposium (IGARSS)*, 2002, pp. 1720–1722.
- [54] T. Matsuoka, T. Umehara, A. Nadai, and T. Kobayashi, “Calibration of the High Performance Airborne SAR System (Pi-SAR2),” in *International Geoscience and Remote Sensing Symposium (IGARSS)*, 2009, pp. 582–585.
- [55] E. Rodriguez *et al.*, “An assessment of the SRTM topographic products,” Pasadena, CA, USA, 2005.
- [56] T. Farr *et al.*, “The shuttle radar topography mission,” *Rev. Geophys.*, vol. 45, no. 2005, pp. 1–33, 2007.
- [57] Harris Geospatial Solutions, “IDL: Discover What’s in Your Data,” *Harris Geospatial Solutions*, 215AD. [Online]. Available: http://exelis.http.internapcdn.net/exelis/pdfs/7-15_IDL_Brochure_H_VIS15-01_rearrange_low_res.pdf. [Accessed: 30-Aug-2018].
- [58] A. B. C. Silva and S. V. Baumgartner, “STAP moving target position estimation accuracy improvement and false detection recognition using a priori road information,” in *International Radar Symposium (IRS)*, 2017, pp. 1–7.
- [59] A. B. C. Silva and S. V. Baumgartner, “Novel post-Doppler STAP with a priori knowledge information for traffic monitoring applications : basic idea and first results,” *Advances Radio Sci.*, vol. 15, pp. 77–82, 2017.
- [60] A. B. C. Silva, S. V. Baumgartner, and G. Krieger, “Training Data Selection and Update for Airborne Post-Doppler STAP,” *IEEE Trans. Geosci. Remote Sens.*, vol. 57, no. 8, pp. 5626–5641, 2019.
- [61] A. B. C. Silva, S. V. Baumgartner, and A. Moreira, “Fast Post-Doppler STAP

- with Road Map for Traffic Monitoring,” *Adv. Radio Sci.*, vol. 17, pp. 137–143, 2019.
- [62] S. K. Joshi, S. V Baumgartner, A. B. C. Silva, and G. Krieger, “Range-Doppler Based CFAR Ship Detection with Automatic Training Data Selection,” *Remote Sens.*, vol. 11, no. 11, p. 36, 2019.
- [63] A. B. C. Silva and S. V. Baumgartner, “A Priori Knowledge-Based STAP for Traffic Monitoring Applications: First Results,” in *European Conference on Synthetic Aperture Radar (EUSAR)*, 2016, pp. 211–215.
- [64] A. B. C. Silva and S. V. Baumgartner, “Training Data Selection and Update for Airborne Post-Doppler Space-Time Adaptive Processing,” in *European Conference on Synthetic Aperture Radar (EUSAR)*, 2018, pp. 1285–1290.
- [65] A. B. C. Silva, S. V. Baumgartner, and A. Moreira, “Fast Post-Doppler STAP with Road Map for Traffic Monitoring,” in *Kleinheubacher Tagung*, 2018, pp. 1–4.
- [66] A. B. C. Silva and S. V. Baumgartner, “Novel post-Doppler STAP with a priori knowledge information for traffic monitoring applications,” in *Kleinheubacher Tagung*, 2016, pp. 1–6.
- [67] S. V. Baumgartner, A. B. C. Silva, and R. Que, “Meilensteinbericht MST 3303: Der STAP Verkehrsprozessor läuft auf dem Onboard- Prozessor und ist präoperationell einsetzbar,” Oberpfaffenhofen, Germany, 2016.
- [68] S. V. Baumgartner, A. B. C. Silva, and R. Que, “Meilensteinbericht MST 3304: Der kombinierte „A Priori Knowledge-Based STAP Verkehrsprozessor“ läuft auf dem Onboard-Prozessor und ist präoperationell einsetzbar,” Oberpfaffenhofen, Germany, 2016.
- [69] C. Hülsmeier, “Verfahren, um entfernte metallische Gegenstände mittels elektrischer wellen einem Beobachter zu melden,” German Patent 165546, filed 1904, published 1905.
- [70] W. Holpp, “The Century of Radar - from Christian Hülsmeier to Shuttle Radar

- Topography Mission,” *EADS Deutschland GmbH*. [Online]. Available: https://www.100-jahre-radar.fraunhofer.de/vortraege/Holpp-The_Century_of_Radar.pdf. [Accessed: 30-Aug-2018].
- [71] C. A. Wiley, “Pulsed Doppler Radar Methods and Apparatus,” US Patent 3196436, filed 1954, published 1965.
- [72] F. Gini and M. Rangaswamy, *Knowledge Based Radar Detection, Tracking and Classification*. John Wiley & Sons, 2008.
- [73] S. V. Baumgartner, “Circular and Polarimetric ISAR Imaging of Ships Using Airborne SAR Sensors,” in *European Conference on Synthetic Aperture Radar (EUSAR)*, 2018, pp. 116–121.
- [74] J. Harris, “On the Use of Windows for Harmonic Analysis with the Discrete Fourier Transform,” *Proc. IEEE*, vol. 66, no. 1, pp. 51–83, 1978.
- [75] C. Wu, “A Digital System to Produce Imagery from SAR Data,” in *AIAA Conference: System Design Driven by Sensors*, 1976, pp. 1–5.
- [76] A. Moreira, J. Mittermayer, and R. Scheiber, “Extended chirp scaling algorithm for air- and spaceborne SAR data processing in stripmap and ScanSAR imaging modes,” *IEEE Trans. Geosci. Remote Sens.*, vol. 34, no. 5, pp. 1123–1136, 1996.
- [77] S. V. Baumgartner, M. Gabele, G. Krieger, K. H. Bethke, and S. Zuev, “Impact of road vehicle accelerations on SAR-GMTI motion parameter estimation,” in *International Radar Symposium (IRS)*, 2006, pp. 1–4.
- [78] S. V. Baumgartner and G. Krieger, “Acceleration-independent along-track velocity estimation of moving targets,” *IET Radar, Sonar Navig.*, vol. 4, no. 3, pp. 474–487, 2010.
- [79] DLR, “TerraSAR-X: Germany’s Radar Eye in Space,” *DLR Website*, 2009. [Online]. Available: https://www.dlr.de/dlr/en/desktopdefault.aspx/tabid-10377/565_read-436/#/gallery/350. [Accessed: 11-Oct-2018].
- [80] W. Pitz and D. Miller, “The TerraSAR-X Satellite,” *IEEE Trans. Geosci.*

- Remote Sens.*, vol. 48, no. 2, pp. 615–622, 2010.
- [81] R. Werninghaus and S. Buckreuss, “The TerraSAR-X Mission and System Design,” *IEEE Trans. Geosci. Remote Sens.*, vol. 48, no. 2, pp. 606–614, 2010.
- [82] W. L. Melvin, “A STAP overview,” *IEEE Aerosp. Electron. Syst. Mag.*, vol. 19, no. 1, pp. 19–35, 2004.
- [83] W. L. Melvin, “Space-Time Adaptive Processing for Radar,” in *Academic Press Library in Signal Processing: Volume 2 Communications and Radar Signal Processing*, 1st ed., vol. 2, New York, USA: Elsevier Masson SAS, 2014, pp. 595–665.
- [84] W. Bürger, “Space-Time Adaptive Processing: Fundamentals,” *Adv. Radar Signal Data Process.*, pp. 1–14, 2006.
- [85] J. R. Guerci, *Space-Time Adaptive Processing for Radar*, 1st ed., no. 1. Norwood, MA, USA: Artech House, 2003.
- [86] R. C. DiPietro, “Extended factored space-time processing for airborne radar systems,” in *Asilomar Conference on Signals, Systems & Computers*, 1992, pp. 425–430.
- [87] E. Casalini, D. Henke, and E. Meier, “GMTI in Circular Sar Data Using STAP,” in *Sensor Signal Processing for Defence*, 2016, pp. 1–5.
- [88] J. H. G. Ender, “Space-time processing for multichannel synthetic aperture radar,” *Electron. Commun. Eng. J.*, vol. 11, no. 1, pp. 29–38, 1999.
- [89] J. H. G. Ender, C. H. Gierull, and D. Cerutti-Maori, “Improved space-based moving target indication via alternate transmission and receiver switching,” *IEEE Trans. Geosci. Remote Sens.*, vol. 46, no. 12, pp. 3960–3974, 2008.
- [90] F. C. Robey, D. R. Fuhrmann, E. J. Kelly, and R. Nitzberg, “A CFAR Adaptive Matched Filter Detector,” *IEEE Trans. Aerosp. Electron. Syst.*, vol. 28, no. 1, pp. 208–216, 1992.
- [91] I.S.Reed, J.D.Mallett, and L.E.Brennan, “Rapid Convergence Rate in Adaptive Arrays,” *IEEE Trans. Aerosp. Electron. Syst.*, vol. 10, no. 6, pp. 853–863, 1974.

- [92] F. Gini and M. Greco, "Covariance matrix estimation for CFAR detection in correlated heavy tailed clutter," *Signal Processing*, vol. 82, pp. 1847–1859, 2002.
- [93] D. Cerutti-Maori, C. H. Gierull, and J. H. G. Ender, "Experimental verification of SAR-GMTI improvement through antenna switching," *IEEE Trans. Geosci. Remote Sens.*, vol. 48, no. 4 PART 2, pp. 2066–2075, 2010.
- [94] T. F. Ayoub, A. M. Haimovich, and M. L. Pugh, "Reduced-Rank STAP for High PRF Radar," *IEEE Trans. Aerosp. Electron. Syst.*, vol. 35, no. 3, pp. 953–962, 1999.
- [95] P. Lombardo and F. Colone, "A Dual Adaptive Channel STAP Scheme for Target Detection and DOA Estimation," in *International Conference on Radar*, 2003, pp. 115–120.
- [96] R. Kohlleppel, "Ground moving target tracking with space-time adaptive radar," Universitaet Siegen, 2014.
- [97] R. B. Langley, "The UTM Grid System," *GPS World*, vol. 9, no. 2, pp. 46–50, 1998.
- [98] C. H. Gierull, "Statistical analysis of multilook SAR interferograms for CFAR detection of ground moving targets," *IEEE Trans. Geosci. Remote Sens.*, vol. 42, no. 4, pp. 691–701, 2004.
- [99] I. S. Gradshteyn and I. M. Ryzhik, *Table of Integrals, Series, and Products*, 7th ed. San Diego, CA, USA: Elsevier, 2007.
- [100] K. H. Bethke *et al.*, "Air- and spaceborne monitoring of road traffic using SAR moving target indication-Project TRAMRAD," *ISPRS J. Photogramm. Remote Sens.*, vol. 61, pp. 243–259, 2006.
- [101] S. V. Baumgartner, S. Bertl, P. Lopez-Dekker, P. Laskowski, C. Schaefer, and R. Klein, "MTI-SAR: Preliminary System Concepts Definition, Trade-Off and Performance Assessment for Land and Ocean Based MTI Applications," ESTEC Contract Number 4000105042, 2015.

- [102] S. V. Baumgartner *et al.*, “MTI-SAR : MTI Multi-channel Techniques Survey and Scenario Definition,” ESTEC Contract No. 4000105042, 2012.
- [103] C. H. Gierull, “Numerical recipes to determine the performance of multi-channel GMTI radars,” Ottawa, Canada, 2011.
- [104] S. V. Baumgartner and G. Krieger, “Simultaneous High-Resolution Wide-Swath SAR Imaging and Ground Moving Target Indication: Processing Approaches and System Concepts,” *IEEE J. Sel. Top. Appl. Earth Obs. Remote Sens.*, vol. 8, no. 11, pp. 5015–5029, 2015.
- [105] K. Sauerwald, “Einführung in GoogleEarth und KML,” 2013. [Online]. Available: <http://landarzar.net/wp-content/uploads/2013/07/KML.pdf>. [Accessed: 17-Aug-2018].
- [106] Google, “Google Earth,” 2018. [Online]. Available: <https://www.google.com/earth/>. [Accessed: 10-Nov-2018].
- [107] Google, “Introduction to Google Earth Engine.” [Online]. Available: <https://www.google.com/earth/outreach/learn/introduction-to-google-earth-engine/>. [Accessed: 17-Aug-2018].
- [108] G. Krieger *et al.*, “TanDEM-X : A Satellite Formation for High-Resolution SAR Interferometry,” *IEEE Trans. Geosci. Remote Sens.*, vol. 45, no. 11, pp. 3317–3341, 2007.
- [109] P. Rizzoli *et al.*, “Generation and performance assessment of the global TanDEM-X digital elevation model,” *ISPRS J. Photogramm. Remote Sens.*, vol. 132, pp. 119–139, 2017.
- [110] S. V. Baumgartner, “Traffic Monitoring with Air- and Spaceborne Synthetic Aperture Radar,” Karlsruher Instituts für Technologie (KIT), 2014.
- [111] R. Baier, “Richtlinien für die Anlage von Stadtstraßen (RASt 06),” Cologne, Germany, 2006.
- [112] Forschungsgesellschaft für Straßen- und Verkehrswesen e.V., “Richtlinien für die Anlage von Autobahnen (RAA),” Cologne, Germany, 2008.

- [113] R. S. Witte and J. S. Witte, *Statistics*, 9th ed. John Wiley & Sons, 2009.
- [114] A. Papoulis, *Probability, Random Variables and Stochastic Processes*, 3rd ed. New York: McGRAW-HILL, 1991.
- [115] S. V. Baumgartner, “TRAMRAD GMTI-Experimente mit F-SAR,” Oberpfaffenhofen, Germany, 2006.
- [116] C. H. Gierull, “Digital Channel Balancing of Along-Track Interferometric SAR Data,” Ottawa, Canada, 2003.
- [117] A. Bertetich, “Investigation of Multi-Channel SAR Calibration Methods for Real-Time Traffic Monitoring,” Opera Universitaria di Trento, 2010.
- [118] G. K. Borsari, “Mitigating Effects on STAP Processing Caused by an Inclined Array,” *IEEE Natl. Radar Conf.*, pp. 135–140, 1998.
- [119] C. Wu, J. C. Curlander, and A. Di Cenzo, “Determination of spacecraft attitude using synthetic aperture radar data,” *Am. Inst. Aeronaut. Astronaut.*, pp. 57–60, 1980.
- [120] R. Bamler, “Doppler Frequency Estimation and the Cramér-Rao Bound,” *IEEE Trans. Geosci. Remote Sens.*, vol. 29, no. 3, pp. 385–390, 1991.
- [121] J. A. Nelder and R. Mead, “A simplex method for function minimization,” *Comput. J.*, vol. 7, no. 4, pp. 308–313, 1965.
- [122] M. J. D. Powell, “An efficient method for finding the minimum of a function of several variables without calculating derivatives,” *Comput. J.*, vol. 7, no. 2, pp. 155–162, 1964.
- [123] J. Ward, “Space-Time Adaptive Processing for Airborne Radar,” Massachusetts, USA, 1994.
- [124] W. L. Melvin and G. A. Showman, “An approach to knowledge-aided covariance estimation,” *IEEE Trans. Aerosp. Electron. Syst.*, vol. 42, no. 3, pp. 1021–1041, 2006.
- [125] J. Bang, W. Melvin, and A. Lanterman, “Model-based clutter cancellation based

- on enhanced knowledge-aided parametric covariance estimation,” *IEEE Trans. Aerosp. Electron. Syst.*, vol. 51, no. 1, pp. 154–166, 2015.
- [126] S. Gelli, A. Bacci, E. Giusti, M. Martorella, and F. Berizzi, “Effectiveness of Knowledge-Based STAP in Ground Targets Detection with Real Dataset,” in *IET Radar*, 2017, pp. 1–5.
- [127] S. V. Baumgartner *et al.*, “Digital beamforming and traffic monitoring using the new F-SAR system of DLR,” in *International Radar Symposium (IRS)*, 2007, pp. 1–5.
- [128] A. Reigber *et al.*, “Current status of DLR’s new F-SAR sensor,” in *European Conference on Synthetic Aperture Radar (EUSAR)*, 2010, pp. 1078–1081.
- [129] A. Reigber *et al.*, “DBFSAR: An airborne very high-resolution digital beamforming SAR system,” in *European Radar Conference (EURAD)*, 2017, pp. 175–178.
- [130] D. Henke, E. Mendez Dominguez, D. Small, M. E. Schaepman, and E. Meier, “Moving Target Tracking in Single- and Multichannel SAR,” *IEEE Trans. Geosci. Remote Sens.*, vol. 53, no. 6, pp. 3146–3159, 2015.
- [131] S. K. Joshi and S. V. Baumgartner, “Sea clutter model comparison for ship detection using single channel airborne raw SAR data Sea clutter modelling,” in *European Conference on Synthetic Aperture Radar (EUSAR)*, 2018, pp. 731–735.
- [132] V. C. Chen and H. Ling, *Time Frequency Transforms for Radar Imaging And Signal Analysis*, 1st ed. Boston, USA: Artech House, 2002.
- [133] G. Palubinskas and H. Runge, “Radar Signatures of a Passenger Car,” *IEEE Geosci. Remote Sens. Lett.*, vol. 4, no. 4, pp. 644–648, 2007.
- [134] D. Cerutti-Maori and I. Sikaneta, “Optimum GMTI Processing for Space-based SAR/GMTI Systems: Theoretical Derivation,” in *European Conference on Synthetic Aperture Radar (EUSAR)*, 2010, pp. 390–393.
- [135] D. Cerutti-Maori and I. Sikaneta, “Optimum GMTI Processing for Space-based

- SAR/GMTI Systems: Simulation Results,” in *European Conference on Synthetic Aperture Radar (EUSAR)*, 2010, pp. 653–656.
- [136] D. Cerutti-Maori and I. Sikaneta, “A generalization of DPCA processing for multichannel SAR/GMTI radars,” *IEEE Trans. Geosci. Remote Sens.*, vol. 51, no. 1, pp. 560–572, 2013.
- [137] B. Himed, J. H. Michels, and Y. Zhang, “Bistatic STAP Performance Analysis in Radar Applications,” in *IEEE Radar Conference*, 2001, pp. 198–203.
- [138] W. L. Melvin and M. Davis, “Adaptive Cancellation Method for Geometry-Induced Nonstationary Bistatic Clutter Environments,” *IEEE Trans. Aerosp. Electron. Syst.*, vol. 43, no. 2, pp. 651–672, 2007.
- [139] D. Cristallini and I. Walterscheid, “Joint Monostatic and Bistatic STAP for Improved SAR-GMTI Capabilities,” *IEEE Trans. Geosci. Remote Sens.*, vol. 54, no. 3, pp. 1834–1848, 2016.
- [140] S. Gelli, A. Bacci, M. Martorella, and F. Berizzi, “Knowledge-Aided STAP Approach for Bistatic Ground Moving Target Imaging,” in *International Radar Symposium (IRS)*, 2017, pp. 1–10.
- [141] DLR, “E-SAR: The Experimental Airborne SAR System of DLR,” Oberpfaffenhofen, Germany, 2018.
- [142] R. Scheiber, A. Reigber, A. Ulbricht, K. Papathanassiou, R. Horn, and A. Moreira, “Overview of Interferometric Data Acquisition and Processing Modes of the Experimental Airborne SAR System of DLR,” in *IEEE Geoscience and Remote Sensing Symposium (IGARSS)*, 1999, pp. 35–37.
- [143] R. Horn, A. Nottensteiner, A. Reigber, J. Fischer, and R. Scheiber, “F-SAR - DLR’s new multifrequency polarimetric airborne SAR,” in *International Geoscience and Remote Sensing Symposium (IGARSS)*, 2009, pp. 902–905.
- [144] A. Reigber *et al.*, “Performance of the P-band subsystem and the X-band interferometer of the F-SAR airborne SAR instrument,” in *International Geoscience and Remote Sensing Symposium (IGARSS)*, 2012, pp. 5037–5040.

- [145] DLR, “F-SAR: Airborne SAR Remote Sensing,” Oberpfaffenhofen, Germany, 2018.
- [146] R. Burkhart, “Dornier DO228-212 - DLR.” [Online]. Available: <https://www.airliners.net/>. [Accessed: 09-Oct-2018].
- [147] “Google Maps.” [Online]. Available: <https://www.google.de/maps>. [Accessed: 10-Nov-2018].
- [148] Bundesministerium für Bildung und Forschung (BMBF), “Bildung und Forschung in Zahlen 2017,” Bonn, Deutschland, 2017.
- [149] F. De Zan and A. M. Guarnieri, “TOPSAR: Terrain observation by progressive scans,” *IEEE Trans. Geosci. Remote Sens.*, vol. 44, no. 9, pp. 2352–2360, 2006.
- [150] Y. Li, T. Wang, B. Liu, L. Yang, and G. Bi, “Ground Moving Target Imaging and Motion Parameter Estimation with Airborne Dual-Channel CSSAR,” *IEEE Trans. Geosci. Remote Sens.*, vol. 55, no. 9, pp. 5242–5253, 2017.
- [151] O. Ponce, P. Prats, R. Scheiber, A. Reigber, and A. Moreira, “First Airborne Demonstration of Holographic SAR Tomography With Fully Polarimetric Multicircular Acquisitions at L-Band,” *IEEE Trans. Geosci. Remote Sens.*, vol. 54, no. 10, pp. 6170–6196, 2016.
- [152] M. Villano, G. Krieger, and A. Moreira, “A novel processing strategy for staggered SAR,” *IEEE Geosci. Remote Sens. Lett.*, vol. 11, no. 11, pp. 1891–1895, 2014.

Curriculum Vitae

Personal Data

Name	André Barros Cardoso da Silva
Date of Birth	November 16, 1986
Place of Birth	Taubaté, São Paulo, Brazil
Nationality	Brazilian, Portuguese

Education and Professional Experience

- Since **Research Scientist**
Mar 2019 Microwaves and Radar Institute of the German Aerospace Center (DLR) in Oberpfaffenhofen, Germany.
- Sep 2014– **PhD Fellow**
Feb 2019 Scholarship holder of the German Academic Exchange Service (DAAD) at the Microwaves and Radar Institute of the German Aerospace Center (DLR) in Oberpfaffenhofen, Germany.
- Jan 2012 – **Research Engineer**
Aug 2014 Aeronautics Technological Institute (ITA), São José dos Campos, Brazil.
▪ Development of a GMTI processor for single and multi-channel SAR.
- Jan 2012 – **Master of Science Degree** in Electronic and Computer Engineering.
Dec 2013 Aeronautics Technological Institute (ITA), São José dos Campos, Brazil.
Thesis: “Moving targets detection and velocity estimation using multilook SAR images”.
- Jun 2011 – **Research Intern**
Dec 2011 Aeronautics Technological Institute (ITA), São José dos Campos, Brazil.
▪ Accomplishment of an electrical test plan for the telemetry and telecommand transponders (engineering and flight models) for the Brazilian university microsatellite ITASAT.
- Jan 2010 – **Research Engineer**
Apr 2014 Brazilian Antarctic Station “Comandante Ferraz” (EACF), Antarctica.
▪ Five expeditions on summer seasons (228 days in total) working with atmospheric radars and data collection platforms designed for climate change research and environmental monitoring.

- Jan 2009 – **Undergraduate Researcher**
Dec 2009 University of Taubaté (UNITAU), Taubaté, Brazil.
Topic: “Fishing Vessels Monitoring System Using Brazilian Satellites”.
- Jan 2008 – **Undergraduate Researcher**
Dec 2008 University of Taubaté (UNITAU), Taubaté, Brazil.
Topic: “GPS Locator with Advanced Encryption Standard (AES) Data Ciphering”.
- Jan 2005 – **Engineering Intern**
Dec 2009 Brazilian National Institute for Space Research (INPE), São José dos Campos, Brazil.
 - Development, assembly and tests of data collection platforms and S-band tracking stations for the Brazilian Environmental Data Collection System (SBCDA) satellites;
 - Tests of antennas propagation and RF circuits for the satellites CBERS 3&4 (China–Brazil Earth Resources Satellite program).
- Jan 2005 – **Bachelor Degree** in Telecommunication Engineering.
Dec 2009 University of Taubaté (UNITAU), Taubaté, Brazil.
 - With honors - *Summa cum Laude*;
 - Honorable mention in Telecommunication.
- Jan 2002 – **Electronics Technician**
Dec 2004 Everardo Passos Technical School (ETEP), São José dos Campos, Brazil.
 - Member of the Brazilian team at the “FIRST Robotics Competition 2004”, Trenton, New Jersey, USA.

Awards

- Feb 2010 | *CREA-SP Professional Formation Award*, granted for first-class students in engineering courses by the Brazilian Regional Council of Engineering and Architecture of São Paulo state (CREA-SP).

Oberpfaffenhofen, November 2019.



André Barros Cardoso da Silva